

Potential for light emission

Investigations into quantum dots as phosphors and in light-emitting electrochemical cells

Ubbink, R.F.

DOI

[10.4233/uuid:427d8131-50fd-422c-a81f-77ba82aaaae4e](https://doi.org/10.4233/uuid:427d8131-50fd-422c-a81f-77ba82aaaae4e)

Publication date

2025

Document Version

Final published version

Citation (APA)

Ubbink, R. F. (2025). *Potential for light emission: Investigations into quantum dots as phosphors and in light-emitting electrochemical cells*. [Dissertation (TU Delft), Delft University of Technology].
<https://doi.org/10.4233/uuid:427d8131-50fd-422c-a81f-77ba82aaaae4e>

Important note

To cite this publication, please use the final published version (if applicable).
Please check the document version above.

Copyright

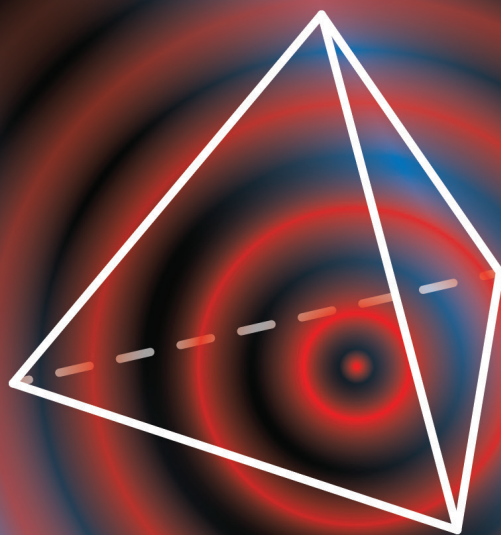
Other than for strictly personal use, it is not permitted to download, forward or distribute the text or part of it, without the consent of the author(s) and/or copyright holder(s), unless the work is under an open content license such as Creative Commons.

Takedown policy

Please contact us and provide details if you believe this document breaches copyrights.
We will remove access to the work immediately and investigate your claim.

Potential for light emission

Investigations into quantum dots as phosphors
and in light-emitting electrochemical cells



Reinout Floris Ubbink

Potential for light emission

Investigations into quantum dots as phosphors
and in light-emitting electrochemical cells

Reinout Floris Ubbink

Potential for light emission

Investigations into quantum dots as phosphors
and in light-emitting electrochemical cells

Dissertation

for the purpose of obtaining the degree of doctor
at Delft University of Technology
by the authority of the Rector Magnificus Prof.dr.ir. T.H.J.J. van der Hagen
chair of the Board for Doctorates

to be defended publicly on
Wednesday 19 March 2025 at 15:00 o' clock

by

Reinout Floris UBBINK

Master of Science in Materials Science and Engineering,
Delft University of Technology, the Netherlands
born in Cambridge, United Kingdom

This dissertation has been approved by the promotor.

Prof. dr. A. J. Houtepen
Dr. ir. T. J. Savenije

Delft University of Technology, promotor
Delft University of Technology, promotor

Composition of the doctoral committee:

Rector Magnificus,
Prof. dr. A. J. Houtepen
Dr. ir. T. J. Savenije

chairperson
Delft University of Technology, promotor
Delft University of Technology, promotor

Independent members:

Prof. dr. F.M. Mulder
Prof. dr. Johan Padding
Dr. C. de Mello-Donega
Prof. dr. I.M.N. Groot

Delft University of Technology
Delft University of Technology
Utrecht University
Leiden University

Other members:

Dr. E.R.H. van Eck

Radboud University

This work received financial support from the Dutch Research Council (NWO) through Open Technology Programme, project nr. 17188 – Quantum Dots for Advanced Lighting Applications. The project was partly financed by Lumileds.



ISBN: 978-94-6473-743-1

Copyright © 2025 Reinout Floris Ubbink

Cover designed by Reinout Floris Ubbink

Printed by Ipskamp printing, the Netherlands

An electronic version of this thesis is available at: <http://repository.tudelft.nl>

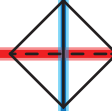
*“Since beginningless time darkness thrives in the void,
but always yields to purifying light.”*

- ATLA, s3e19

Table of contents

Chapter 1	1
Quantum dots in light-emitting applications	
Chapter 2	9
InP colloidal quantum dots for visible and near-infrared photonics	
Chapter 3	53
A water-free in-situ HF treatment for ultra-bright InP quantum dots	
Chapter 4	87
Phosphorus Oxidation Controls Epitaxial Shell Growth in InP/ZnSe Quantum Dots	
Chapter 5	115
Electrochemically Doped Quantum Dot Light-emitting Electrochemical Cells without Charge Injection Layers	
Chapter 6	141
Numerical Model to Simulate Electrochemical Charging of Nanocrystal Films	
Chapter 7	167
Where do the Electrons Go? Studying Loss Processes in the Electrochemical Charging of Semiconductor Nanomaterials	
Summary	194
Samenvatting	198
Acknowledgements	204
List of publications	208
Curriculum vitae	209

1



Quantum dots in
light-emitting applications

1.1 Introduction

Because most people have access to light at any time of day and year at will, the importance of lighting technology can easily be underappreciated. Lighting technologies are used in an crucial array of applications. The most obvious application is general lighting, which allows surgeons to operate indoors, makes it possible to safely drive a car on a winter morning, and may give young children some comfort at night. A second vital application of lighting technology is in displays such as computer screens, smartphones and televisions. Finally, more high-tech lighting applications such as lasers are less widespread, but often used in manufacturing, research and telecommunication. While each of these applications has very different requirements and specifics, they all have two things in common: all applications emit light in the visible part of the electromagnetic spectrum, and all of them may in some manner be improved by incorporating quantum dots as a light-emitting material.

1.2 Quantum dots

Quantum dots (QDs) are nanoparticles made of semiconductor materials. Like other semiconductors, QDs can emit light if an electron is present in the conduction band and a hole in the valence band. This excited electron can radiatively recombine with the hole to produce a photon. Unlike bulk semiconductor crystals, which possess a material-specific band gap, the electronic structure of quantum dots is influenced by quantum confinement effects: when the size of semiconductor particles is reduced to the nanometer scale, electron wavefunctions in the material are confined by the edges of the crystal, akin to the common 'particle in a box' model. Like a particle in a box, more quantum confinement leads to an increase in the difference between the energy levels, which translates to a larger band gap in quantum dots compared to the bulk version of the same materials. InP nanocrystals of different sizes are shown side by side in Figure 1.1 to illustrate this effect.



Figure 1.1. Solutions of indium phosphide-based nanoparticles of increasing size from left to right. As the size of the nanoparticles increases, the band gap of the indium phosphide decreases. This means the light emitted by these nanoparticles has a lower energy and is thus more towards the red side of the spectrum. *Photo taken by the author.*

The smaller the nanoparticles become (to the left of Figure 1.1), the more pronounced the quantum confinement effect is. This results in the first important property of quantum dots: their band gap is size-dependent. This also means that any optical characteristics that depend on the band gap, most notably the wavelengths of absorbed and emitted light, also depend on their size. By tuning the size of quantum dots, it becomes possible to produce a material that emits light at a specific desired wavelength, and thus at a specific color. This effect is clear in Figure 1.1, where the smallest QDs emit blue light, while the larger QDs to the right emit green, yellow, orange and red light. A second important feature of quantum dots is that their emission spectra can be very narrow, translating to a high color purity of the emitted light.

Because of these two properties, the use of quantum dots could lead to improvements in the aforementioned lighting applications. Modern lamps are based on blue bulk gallium nitride LEDs, which are very power-efficient, but rely on converter materials (called phosphors) to convert this blue light into green and red in order to produce light of a warm-white color. During this conversion losses can occur if blue light is converted to invisible infrared light by a converter material with too wide an emission spectrum. Since quantum dots possess very color-pure emission, they would convert all blue light to visible red light, thus resulting in less losses and an energy saving of widely used white LED lamps. In display applications, a similar conversion from blue to red light can be used, or quantum dots could be more directly used for converting electricity into light. Either way the color purity provided by quantum dots is especially important in displays, since higher color purity allows the production of higher-gamut displays, which translates to more realistic and vibrant colors on the display. Quantum dot-based televisions are actually already commercially available at this moment. Finally, quantum dots could be used in laser applications, where the color tunability of quantum dots would allow the generation of laser light of any color.

1.3 Loss mechanisms in QDs

For use in lighting applications, in addition to the aforementioned narrow linewidth, there are two other important requirements for quantum dots: energy efficiency and stability. First, all the energy that is put into the quantum dots should be converted to light. The efficiency of the light production of quantum dots is determined by measuring the photoluminescence quantum yield (PLQY), which is defined as the amount of photons emitted divided by the amount of photons absorbed. Typically quantum yields over 95% are required for applications. Theoretical, perfect QD nanocrystals are expected to exhibit a PLQY of 100%, but in reality, this is hard to achieve because nanocrystals are rarely perfect. Real nanocrystals suffer from atomic defects, which are usually present on the surface of the crystals. These defects can lead to energy states in the band gap of the material (called trap states), which in turn lead to non-radiative recombination of the excited electrons and thus to a drop in PLQY. A schematic showing both radiative recombination and recombination via traps is shown in Figure 1.2.

Another type of loss mechanism that can take place in applications is chemical loss of electrons. In this case, no direct defects may be present on the QDs, but electrons are still lost due to chemical reactions.

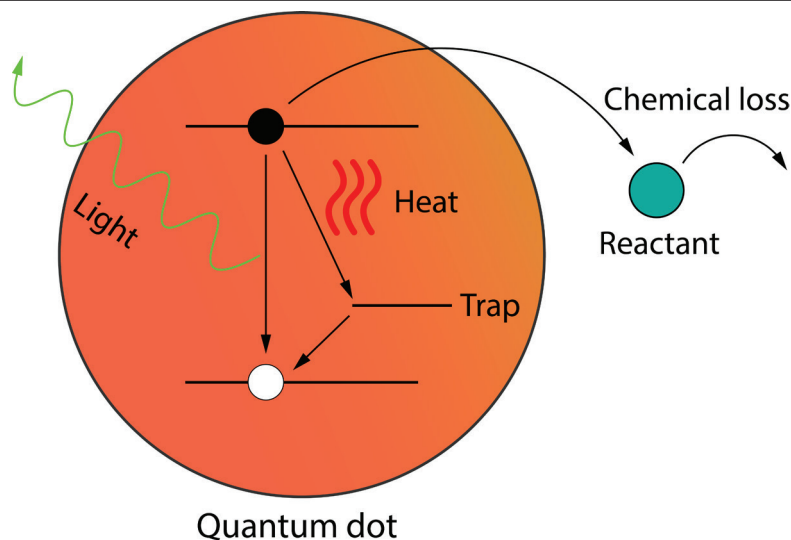


Figure 1.2. Schematic of radiative recombination and loss processes in quantum dots. The quantum dot is in an excited state, with an electron (black) in a high energy level and a hole (white) in a lower energy level. The electron and hole can recombine directly and emit light (radiative recombination). If there is an energy level available in the band gap of the QD (a trap state), the electron and hole can recombine via this trap state, releasing only heat. Electrons and holes can also be lost to chemical reactions. These chemical reactions can be with other reactants around the QD, or with part of the QD themselves. In the latter case, these reactions can lead to instability and degradation of the QDs.

These can be reactions with other compounds (shown in Figure 1.2) or reactions where part of the QD itself reacts. When part of the QD itself is involved in the reaction, this may lead to degradation of the QDs, for instance by creating additional trap states which decrease the PLQY. This relates the second important requirement of QDs for use in applications, their stability. QDs need to maintain their high PLQY over years under high illumination density and elevated temperatures, especially for high-intensity applications such as lasers and car headlights. This means that little or no new atomic defects should develop over time. Since chemical reactions can lead to degradation of the QDs on the long term, avoiding them is crucial for commercial use of QDs. Whether or not the QD is degraded, chemical loss of electrons or holes always leads to a loss of efficiency of the lighting device they occur in.

For both non-radiative recombination due to atomic defects and chemical loss of electrons, little is known about the actual chemical specifics of the processes. Understanding what kinds of defects and chemical reactions can occur on and in QDs is key to understanding how to prevent or remove them. In this thesis, both these types of loss mechanisms will be investigated.

1.3.1 Atomic defects on InP

With regards to atomic defects, we will focus specifically on indium phosphide (InP), as it is the most promising RoHS-compliant material for making quantum dots for lighting applications. It has been shown that InP QDs can be made with emission in the entirety of the visible spectrum, ranging from blue to red (Figure 1.1), with a narrow emission linewidth and thus high color purity. However, it is not yet fully understood which types of atomic defects can be present on InP quantum dots. In order to be able to produce stable InP QDs with near-100% PLQY, it is necessary to examine the types of defects that can be present and what their effect is on the PLQY and the stability of the QDs. With that information, synthesis methods can be devised that either remove these defects or prevent them from forming in the first place.

In QD materials, atomic defects are most often found on the surface of the nanocrystals. Unbound ions at the crystal surface and contaminations formed during the synthesis (for example oxides) can both be present at the surface and lead to trap states. To remove these defects, two different strategies may be employed. First is chemical treatment of the surface. With this technique chemical reactions are performed on the nanocrystals with the goal of fixing as many defects as possible. Another technique is to add a so-called shell layer of a different material around the QDs. In this case the original surface is replaced by an interface and a new outer surface is created, which then should have a lower trap density. Both these techniques are explored in detail in this thesis.

In case of the addition of a shell layer, the interface that is formed between the core and shell material is still a likely location for defects to form. To limit the amount of defects that are formed at the interface, the choice of shelling material is crucial. In the case of InP as a core QD material, the only (ROHS-compliant) shelling materials that have been used to successfully increase the PLQY to near-100% are ZnSe and ZnS. However, using these materials for the shell layer leads to a complicated interface because of the difference in charge of the lattice ions compared to InP. In addition, oxidized contaminations are often found on the InP core/shell interface, with conflicting reports on their effects on the optical properties of the QDs.

In this thesis, we set out to identify which atomic defects are present on both the InP QD surface and the InP/ZnSe core/shell interface. We then examine what the effect of the different atomic defects is on the optical properties of the QDs. We use a variety of structural analysis techniques, but rely most heavily on solid state nuclear magnetic resonance (ssNMR). In ssNMR, the chemical environment of atomic species is probed by measuring the response of atomic nuclei to radio pulses in a very strong magnetic field. ssNMR can distinguish different chemical species from each much better than any other technique and even provides numerous measurements to probe the proximity and interactions between different species. However, ssNMR measurements can only be performed on a select set of atomic nuclei. Luckily, ^{31}P is among these, making ssNMR an excellent tool to investigate the atomic structure of InP. With regards to the shell material, ^{77}Se can be measured. This selenium isotope is only 7.6% abundant (compared to 100% for ^{31}P). Additionally, ^{17}O , present in atomic defects at the InP/ZnSe interface has an abundance of only 0.04%. By creating shells with enriched ^{77}Se (99%) and ^{17}O (70%), we

are however able to use ssNMR techniques to their full potential on the shell material and InP/ZnSe interface as well in this thesis.

1.3.2 Chemical loss of electrons in QD materials

For investigating chemical loss of electrons from QDs, we will take a more general approach and look at different QD materials. We use electrochemistry to inject electrons into the QDs without injecting holes in a process called electrochemical charging. Since these electrons cannot recombine, they will stay in the QDs for a long time. QDs that are electrochemically charged in this way provide interesting opportunities for use in lighting devices such as lasers or light-emitting electrochemical cells as long as the electrons are stable in the QDs. Because the electrons are in the QDs for extended times, this technique also allows us to study the chemical loss reactions that they can partake in. To improve our understanding of the loss processes, we simulate the electrochemical charging process using drift-diffusion simulations. These simulations allow us to track the motion of electrons and other charges in the system. In addition, we can model different types of chemical reactions that the electrons can partake in. By comparing these simulations to experiments we identify what different chemical loss processes would look like in practice. We then compare which loss processes are likely to occur in various QD materials, including InP QDs.

1.4 Outline of this thesis

Chapter 2 provides an extensive literature overview on the topic of InP quantum dots.

In chapter 3, the atomic defects on InP core-only particles are central. We show that in-situ generated HF can be used to boost the PLQY of InP core particles from ~0% to 85%. The treated QDs are then analyzed using a variety of optical and structural analysis techniques and compared to untreated InP cores. Based on the structural changes after the treatment, we identify that the surface is partly covered with indium fluoride (InF_3). This suggests that after the treatment, a better passivation of dangling phosphorus bonds is achieved through passivation with small InF_3 species. Because InF_3 is so small, more of these species can fit on the InP surface compared to native ligands, resulting in better passivation. Additionally, ssNMR and density functional theory (DFT) results indicate that unlike often assumed in literature, not all oxidized species on the InP surface lead to trap states, and specifically the presence of PO_4^{3-} is not harmful for the PLQY.

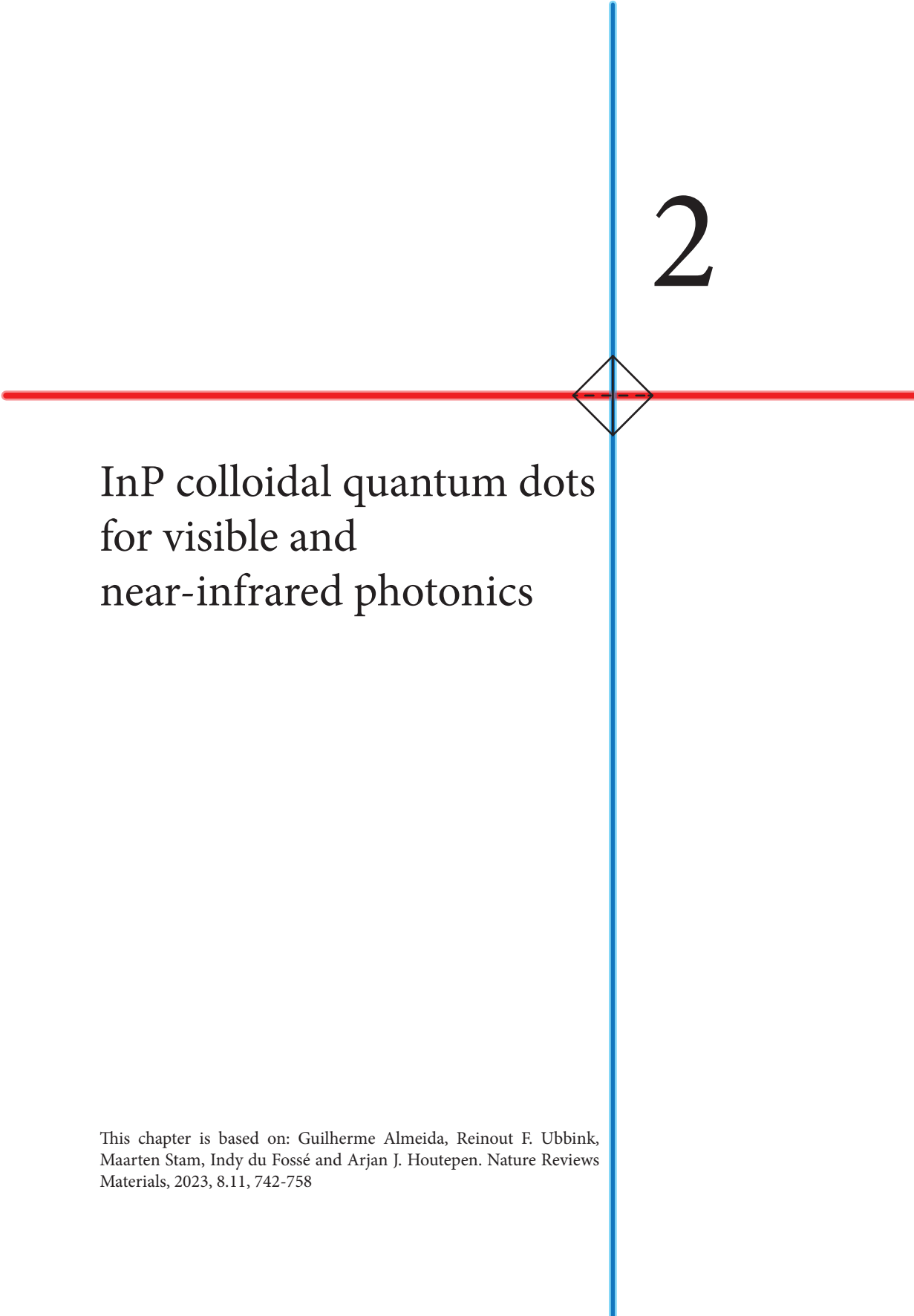
In chapter 4 we continue the investigation of defects on InP QDs, shifting the focus to InP/ZnSe/ZnS core-shell particles. Here we use advanced ^{31}P , ^{77}Se and ^{17}O ssNMR techniques to investigate the InP/ZnSe interface. We find that PO_4^{3-} species found on the cores are still present at the InP/ZnSe interface after the shelling procedure. Near-unity PLQY values are obtained even with ~5 PO_4^{3-} moieties per QD. We then oxidize the InP cores on purpose using molecular oxygen. This results in a strongly increased amount of PO_4^{3-} , which is the only product of the reaction of InP with molecular oxygen. After growing ZnSe shells on the oxidized InP cores, the PLQY of the InP/ZnSe is significantly lower than that of the particles without the oxidized interface. ^{77}Se ssNMR measurements show a decreased amount of selenium at interface positions in the oxidized sample. High-resolution TEM measurements reveal different crystal orientations of the core and shell when the interface

is oxidized. These results indicate that excessive oxidation disrupts the growth of an epitaxial ZnSe interface on top of the InP core.

In chapter 5 we see how QDs are used in actual light-emitting devices called light-emitting electrochemical cells (LECs). By producing these novel devices for the first time with QDs, we show that both electron and hole injection into QDs can be achieved by incorporating ions in the active layer to effectively lower the injection barriers. Results from experiments and drift-diffusion simulations are combined to characterize the device and show the working mechanism. We show that while hole injection is achieved in our QD-based LECs, further improvement of hole injection could improve device performance in the future.

In chapter 6 we use drift-diffusion simulations to closely analyze electrochemical charging and doping of QD films. We find that the doping density that can be obtained in a film depends both on the applied potential and the amount of supporting electrolyte that is present, and we show that electrochemical doping of QD films cannot be described by earlier theory of electrochemical processes.

Finally in chapter 7 we extend the drift-diffusion simulations to include non-ideal processes by including electrochemical side-reactions. By combining experimental and computational data, we identify which loss processes can take place and how different types of QD materials are affected by these processes. First, we show that chemical loss of electrons to redox-active species can be reversible or irreversible depending on the reduction potential of the redox-active species. Next, we analyze loss of electrons to molecular oxygen. We find that loss to oxygen is always fully irreversible, because the reduced oxygen undergoes irreversible chemical reactions after scavenging an electron from the QDs. Finally, we model reactions where the QDs themselves are reduced. We find this type of reduction reaction is the most likely candidate for the irreversible loss of electrons observed in InP and CdSe QDs.



2

InP colloidal quantum dots for visible and near-infrared photonics

This chapter is based on: Guilherme Almeida, Reinout F. Ubbink, Maarten Stam, Indy du Fossé and Arjan J. Houtepen. *Nature Reviews Materials*, 2023, 8.11, 742-758



2.1 Introduction

The development of semiconductor technologies has had a formidable and revolutionizing impact on our civilization over the past 50 years, in particular through electronic and photonic applications. A well-known feature of semiconductors is that their electronic and optical properties depend not only on their composition and structure but also on their size and shape when confined to the nanometer scale, due to quantum mechanical effects.¹⁻⁶ Owing to their tunable energy landscapes, quantized signatures and efficient luminescence, semiconductor nanostructures (a.k.a. quantum dots, wires or wells) have been widely explored at a fundamental level and can be found in electronic and photonic technologies as common as transistors or light emitting diodes.

The emergence of surfactant-assisted syntheses of colloidal nanocrystals has allowed the fabrication an enormous variety of semiconductor nanostructures with remarkable precision in terms of composition, structure and morphology, in a freestanding colloidal form, which confers great versatility for further integration, and in high yields.⁷⁻¹¹ Over the past three decades, the understanding, fabrication, design, performance, stability and applicability of colloidal quantum dots, wires and wells have evolved impressively, and with an increasing number of functionalities, they have become valuable materials for a growing number of photonic technologies such as lighting, displays, lasers, quantum information, solar energy converters, infrared cameras, security inks, theranostics etc.¹¹⁻²⁵

InP based quantum dots (QDs) have raised considerable interest for photonic technologies operating in the visible and near-infrared regions, because of their wide spectral tunability, strong light absorption, efficient luminescence, high carrier mobility and compliance with safety regulations on consumer devices. Recent developments in their fabrication and design have led to considerable quality improvements. InP QDs can already be found integrated as down-converting phosphors in commercial displays, and are also being considered for other applications as their qualities improve and expand.

In this chapter we review the growing field of InP based QDs from its genesis in the mid-1990s to date, encompassing relevant knowledge from other QDs and from III-V semiconductors as a whole, with the aim of providing a comprehensive but concise account of the fundamentals, progress and challenges in this broad field. First we cover the electronic and optical properties of InP QDs. Then we explore their synthesis methods, the occurrence of electronic defects and their passivation, InP based QD hetero-structures and finally the various photonics applications of these QDs.

2.2 General properties of InP

InP is a semiconductor that usually crystallizes in the zinc blende structure. It is considered a relatively covalent semiconductor and has a direct band gap of ca. 1.35 eV in its bulk form (see table 2.1).²⁶ The band gap is formed between valence orbitals with bonding character and conduction orbitals with antibonding character. Specifically, its valence band edge is characterized by a strong contribution from phosphorus 3p orbitals while the conduction band edge has a more mixed character, with the largest contribution coming from the indium 5s orbitals, as well as a lower density of states (see Figure 2.1A).²⁷ Its band structure is characterized by direct transitions from light, heavy and split-off hole states,²⁸⁻³⁰ and its

absorption coefficient is relatively strong ($>10^4 \text{ cm}^{-1}$ at 1.4 eV) as shown in Figure 2.1B.

Table 2.1. Structural, mechanical and optoelectronic properties of selected bulk semiconductors in the zinc blende or wurtzite (w) structure.³¹⁻³⁶ Lattice constant (a), band gap (E_g), valence band energy (E_{VB}) vs. vacuum, effective density of states (DOS) at the valence band (VB) and conduction band (CB), effective mass of electrons (m_e) and holes (m_h),* absorption coefficient (α) at 2.50 eV, Debye temperature (T_D), bulk modulus (B_s) and the Phillips iconicity (PI, a larger/smaller value characterizes a more ionic/covalent lattice). *lh and hh stand for light holes and heavy holes respectively; for GaP two m_e values are given (longitudinal and transversal) because the surfaces of equal energies are ellipsoids.

Material	a (Å)	E_g (eV)	E_{VB} (eV)	DOS (VB) (#/eV)	DOS (CB) (#/eV)	m_e	m_h (lh/hh)	α ($\times 10^5 \text{ cm}^{-1}$)	T_D (K)	B_s (GPa)	PI
InN(w)	3.53 /5.69	2	6.43	5.3×10^{19}	9.0×10^{17}	0.11	0.27/1.63	1.21	660	140	
GaP	5.45	2.26	5.51	1.9×10^{19}	1.8×10^{19}	1.12 /0.22	0.14/0.79	0.01	445	88	0.33
InP	5.87	1.34	5.17	1.1×10^{19}	5.7×10^{17}	0.08	0.6/0.089	1.30	425	71	0.42
GaAs	5.65	1.42	4.98	9.0×10^{17}	4.7×10^{17}	0.063	0.51/0.082	0.99	360	75	0.31
InAs	6.06	0.35	4.69	6.6×10^{18}	8.7×10^{16}	0.023	0.41/0.026	4.53	280	58	0.36
CdSe	4.30	1.7	4.75			0.13	0.45	1.21			0.70
ZnSe	5.67	2.82	5.98			0.14	0.6	-			0.63
ZnS	5.41	3.68	6.53			0.28	-	-			0.62

Owing to the quantum size effect,¹⁻⁶ the band gap of InP can be tuned from the near-infrared (1.3 eV) up to the violet (ca. 2.7 eV) by confining InP to a fraction of its Bohr radius (ca. 10 nm). The relationship between band gap and volume for InP quantum dots is reported in Figure 2.1C.³⁷ Although the individual band/edge shifts are not fully established, it's been suggested that the conduction band levels are more sensitive to quantum confinement than the valence levels, based on simple effective mass arguments and confirmed by more advanced computations (see table 2.1 for effective masses).³⁸⁻⁴⁰

At room temperature, luminescence linewidths of ca. 50 meV have been observed from a single InP QD emitting in the red, and ca. 80 meV for smaller green emitting dots (Figure 2.1D).³⁷ For applications such as displays, narrow emission linewidths from QD ensembles is required. While the emission linewidth of a single QD is size-dependent and limited by ultra-fast structural dynamics and electron-phonon coupling (EPC),⁴¹⁻⁴⁹ which are, in turn, exacerbated by the presence of electronic traps^{50, 51}, the linewidths of an ensemble of QDs is further broadened by its size distribution. Narrower linewidths may be obtainable in samples with higher QY as well as in core-shell structures, discussed ahead in sections 2.4 and 2.5.

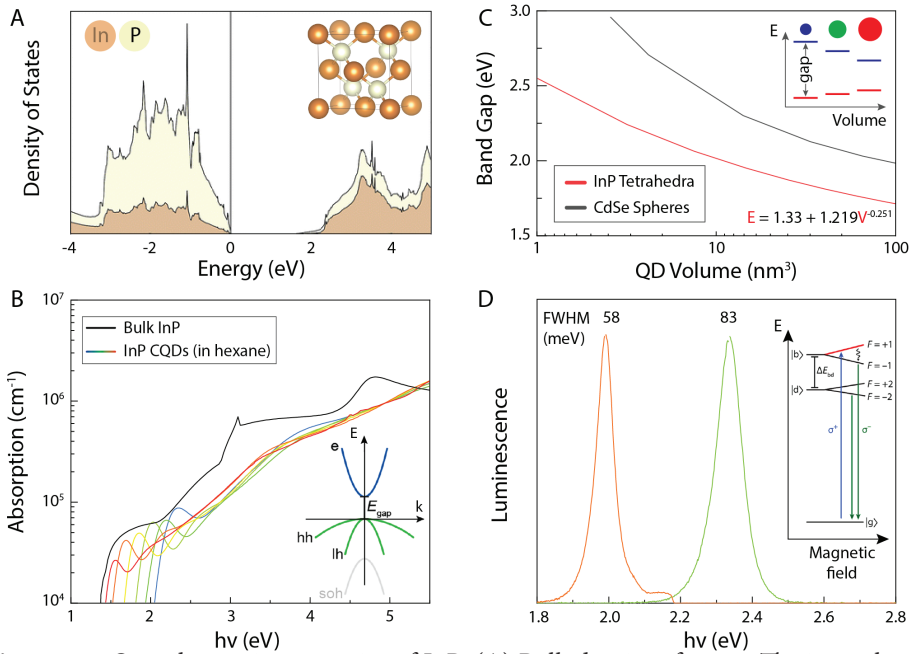


Figure 2.1. Optoelectronic properties of InP: (A) Bulk density of states. The inset shows the zincblende unit cell.²⁷ (B) Absorption coefficients of bulk InP and of InP QDs with edge lengths ranging from 1.5 to 4.0 nm. The inset shows a simplified band structure.⁵² (C) Band gap vs. QD volume for InP tetrahedra and CdSe spheres. The inset illustrates the shift of the band edge levels of InP with quantum confinement.⁵² (D) Room temperature photoluminescence spectra of single InP QDs emitting in the red and in the green exhibiting linewidths of approximately 58 and 83 meV, respectively. The inset shows fine structure splitting at 4 K. lh, light hole; hh, heavy hole; soh, splitoff hole.^{52, 53}

We note that in QDs, the electron-hole exchange interaction causes the splitting of degenerate electron-hole pair configurations into various states.⁵⁴ Briefly, in zinc-blende QDs like InP, the conduction band edge is formed by a double degenerate electron level, while the valence band edge is formed by a fourfold degenerate hole level. Exchange interactions between these levels, combined with shape anisotropy, gives rise to an exciton fine structure, with a $F = \pm 2$ dark lowest exciton state, separated by 2-9 meV from a $F = \pm 1$ bright state (depicted in the inset of Figure 2.1D, data from core/shell QDs).⁵³⁻⁵⁵ At room temperature the emission comes from the thermally populated high energy bright exciton state. In principle this fine-structure splitting is similar to that observed in other tetrahedral binary semiconductors like CdSe. However, it has been shown that the fine structure in InP QDs is particularly insensitive to shape anisotropy. This is attributed to the particular ratio of the light hole over the heavy hole effective mass.^{55, 56} In InP this ratio is 0.149, close to the value of 0.14 where the exciton fine structure is predicted by Efros *et al.* to be least sensitive to shape anisotropy.⁵⁷ As a consequence, the exciton remains nearly isotropic even for prolate or oblate InP QDs. This explains why mixing of the low energy dark exciton with the higher energy bright exciton does not occur in magnetic fields,⁵⁶

and why the bright exciton is found to consist of a doublet in single particle cryogenic PL measurements⁵⁵.

The luminescence of QDs is typically limited by electronic traps arising from structural defects and by Auger processes that take place in the multi-exciton and charged regimes (of relevance for applications such as LEDs or lasers).^{13, 58} There has been great progress in mitigating trap-related losses in InP QDs but much less so in solving Auger losses, as discussed in sections 2.4-2.6. This is extremely relevant as InP QDs emitting in the visible exhibit bi-exciton lifetimes of 5 to 60 ps, i.e. 3-4 orders of magnitude shorter than the single exciton lifetime.³⁷ In addition, Auger processes produce energetic carriers that can lead to irreversible redox chemistry and device degradation.

Finally, for particular applications (such as coherent single-photon emission), QDs with relatively long coherence times are required. Although it is known that the coherence times of QDs can be limited by structural dynamics and EPC,^{41, 43, 59, 60} and also by fine-structure related transitions,^{54, 61-63} no studies of the coherence time have been conducted on InP QDs.

How the structural and optoelectronic properties of InP-based QDs relate and can be engineered will be further discussed in the following sections. This is, however, not always straightforward to assess due to the fact that in QD ensembles not all the QDs are exactly the same (in terms of size, shape, composition, structure, surface coverage) which leads to a distribution in optoelectronic properties, and also due to the difficulties inherent to physical characterization at such small scales.

2.3 Synthesis of Colloidal InP QDs

A variety of protocols have been put forward to synthesize InP QDs.⁶⁴⁻⁸³ InP QDs are generally produced by reacting an In^{3+} salt with a P^{3-} source in a liquid medium and in presence of ions/molecules termed ligands that bind to the surface of QDs providing colloidal stability. Alternatively, the P^{3-} ion may also be formed in-situ by reducing a phosphorus compound in a higher oxidation state. After many years of research into the synthesis of InP QDs, two surfactant-assisted syntheses in non-polar solvents, have attracted most popularity and are currently employed in industrial-scale manufacturing.

The first one, summarized in Figure 2.2A, consists of the reaction of indium (III) alkanooates of general formula $\text{In}[\text{RCOO}]_3$ (R being an alkylic chain, typically C_{14-18}) with an organic silyl phosphine of general formula $\text{P}(\text{SiR}_3)_3$ (R=alkyl or aryl, typically CH_3) at temperatures up to 300 °C,^{67, 84-87} leading to QDs capped by alkanooates (whether SiR_3 groups are also present on the surface remains unclear)⁸⁸. At elevated temperatures this route delivers the most monodisperse InP QDs, and impressive results in terms of linewidths have been obtained by adding trioctylphosphine (TOP, *vide infra*) to the synthesis (see Figures 2.2B and 2.2C).⁷⁵⁻⁷⁷ However, this route is prone to several unwanted side-reactions. For instance, free carboxylic acids left from the preparation of the indium alkanooate precursor can react with InP QDs forming PH_3 ,⁸⁹ react with $\text{P}(\text{SiR}_3)_3$ leading to a series of phosphorus precursors of varying reactivity,^{90, 91} or condense into ketones releasing water molecules which can then oxidize InP QDs and/or react with indium alkanooates to form

In_2O_3 particles^{88,92}. In this regard, adding a base (such as TOP), keeping the temperature low, or purifying the indium alkanoate precursor all seem beneficial. Nevertheless, indium alkanoates themselves may also be prone to other side-reactions as recently pointed out by Li and coworkers⁹³. In addition, the silyl phosphine precursors used are pyrophoric, making them hard to handle and expensive.

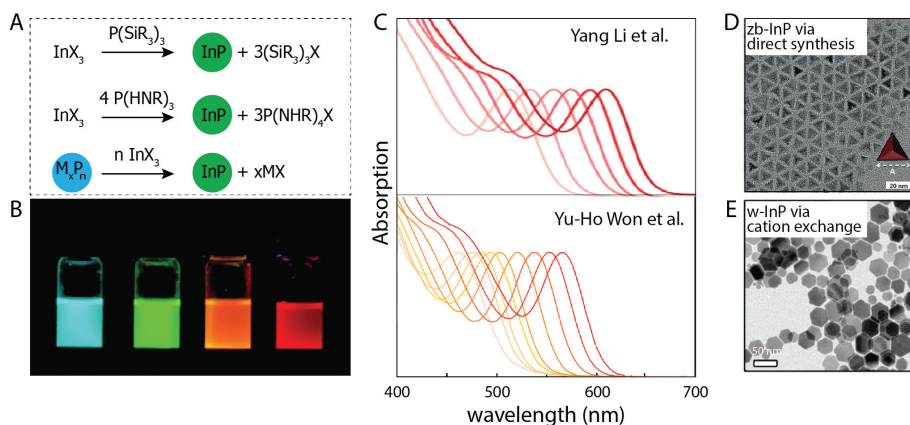


Figure 2.2. (A) InP QDs can be prepared by reacting an InX_3 salt (in which X is a generic monovalent anion such as Cl^- , RCO_2^- , etc.) with (top) an organic silyl phosphine $\text{P}(\text{SiR}_2)_3$ or with (middle) an aminophosphine $\text{P}(\text{HNR})_3$ in the presence of a reducing agent (such as the aminophosphine itself). Alternatively, InP QDs can also be prepared by transforming (cation exchanging) other metal phosphide nanocrystals into InP QDs. (B) Photograph (under UV light) of samples prepared within our group. (C) Absorption spectra of monodisperse InP QDs with band gaps spanning the visible range prepared using silyl phosphines.^{77,93} (D) Electron micrographs of zincblende InP QDs with tetrahedral shape.⁸⁰ (E) Electron micrograph of wurtzite InP QDs in the form of platelets.⁹⁴

The second common route to prepare InP QDs, also summarized in Figure 2.2A, is based on the reaction of indium (+III) halides (typically InCl_3) with aminophosphines, of general formula $\text{P}^{3+}(\text{HNR})_3$ (typically formed in-situ by the reaction of primary alkyl amines RNH_2 with $\text{P}(\text{NR}_2)_3$ precursors) that act simultaneously as a P-source and as reducing agent.⁷⁹⁻⁸¹ It leads to the formation of QDs capped by halide ions and alkylamines. Alternatively, P^{3+}X_3 (X= Cl, Br or I) or Indium (+I) halides may also be employed as precursors.⁹⁵⁻⁹⁷ Although this route hasn't been studied as much and is yet to deliver as monodisperse QDs,⁹⁸ it is definitely more cost-attractive.

Although the two aforementioned synthetic routes employ different chemicals, it is not clear how these affect the growth mechanism and the reaction kinetics or the morphology of the resulting InP QDs. This might be due to the fact that oxidation of InP QDs during the synthesis has been a major obstacle in the study of growth kinetics and it was only recently that a few groups have circumvented it by employing reducing atmospheres (see section 2.4).⁹⁹⁻¹⁰¹ Nevertheless, studies have revealed that the growth of InP QDs using indium carboxylates and $\text{P}(\text{SiR}_2)_3$ precursors proceeds via the formation and ripening of cluster

intermediates¹⁰²⁻¹⁰⁸ whose structure has been identified,¹⁰⁹ and also that these clusters can be employed as single source precursors for synthesizing InP QDs^{76, 103}. Also noteworthy are the first attempts at determining and controlling the reaction kinetics using various aminophosphines,¹¹⁰ the investigation of nucleation and growth through computational methods,¹¹¹ and the successful development of continuous production methods¹¹²⁻¹¹⁸.

Shape-wise, it seems that both routes yield InP QDs that appear triangular in electron micrographs, suggesting that they adopt a tetrahedral shape, as shown in Figure 2.2D. Recently, a study employing the aminophosphine route, claimed that the tetrahedral shape of large-sized InP QDs stems from smaller InP QDs with tetrapod shape whose arms are enclosed by (110) facets.¹¹⁹ Interestingly, a certain degree of control over the tetrapod shape could also be achieved. This was rationalized in another recent paper by Kim and coworkers in which the authors argue that in order to fulfil the requirement of charge neutrality with common monovalent ligands, (100) facets are unlikely to be expressed in cation-rich InP QDs and that a (111) termination is more favorable, in line with the tetrahedral shape observed experimentally.⁴⁰ Following this line of reasoning the authors mention that other possible shapes include truncated pyramids and small-sized cuboctahedrons with (100), (111) and (-111) facets. DFT calculations by Yoo *et al.* also show that both bare and ligand-terminated (111) facets exhibit a lower surface energy than (100) facets.¹²⁰

It has also been shown that Ga and As substituted alloys of InP can be synthesized using variations of the aforementioned routes.¹²¹⁻¹²⁵ However, control over morphology and structure of InP based QDs through direct synthesis remains an outstanding challenge.¹²⁶ Nonetheless, they can still be prepared indirectly, i.e. by transforming (cation exchanging) other metal phosphide nanocrystals into InP QDs while preserving the original phase and morphology, as illustrated in Figure 2.2A. In this way, hexagonal (wurtzite) InP platelets, shown in Figure 2.2E, and InP rods could be successfully prepared from their Cu_3P analogues.^{94, 127-129} As pointed out by Koh *et al.*, control over the exchange rate is important to ensure that single crystalline InP QDs are obtained.¹²⁷

Finally, we note that surface ligands play a key role not only in the synthesis, colloidal stability and self-assembly of QDs, but also in many of their optoelectronic properties (e.g. trap passivation, electron-phonon coupling, carrier delocalization, film conductivity etc.) as well in their surface functionalization.

2.4 Defects and Trap Passivation

As-synthesized InP QDs typically exhibit weak luminescence efficiencies, of a few percent at most (often <1%). Nevertheless, QDs with near unity efficiencies have recently been prepared through defect passivation and shelling approaches. The study of defects in InP materials (QDs, thin films etc.) is a subject of broad interest; various types of defects have been identified, and many passivation and mitigation strategies have been proposed (see Figure 2.3). In this section, oxidation and etching, surface states and Z-type passivation, doping, heterovalent interfaces and strain in InP QDs are reviewed.



2.4.1. Oxidation and etching

III-V semiconductors, including InP, are well known to be prone to oxidation and this is often cited as limiting their growth and their luminescence efficiency.^{77, 100, 130-138} Oxygen is known to adsorb dissociatively on (bulk) InP surfaces¹³⁹⁻¹⁴² and Zhang and coworkers identified the formation of In-O-P and PO_x species ($x>1$) at room temperatures and at oxygen pressures as low as 5 μbar and 5 mbar, respectively, highlighting the strong reactivity of the phosphide anion towards oxidation. At higher temperatures, further structural transformations were observed, including the bridging of PO_x units at ca. 200 °C and the development of a thick indium oxide layer at temperature above 300 °C underlining the diffusion of oxygen.^{141, 143} Water also appears to adsorb dissociatively^{141, 144} and to lead to the formation of In-O-P and PO_x species upon mild heating (100 °C). The formation of In-O-In species can also occur and is more likely upon exposure to oxygen than to water.¹⁴¹

This poses difficulties for the synthesis (and shelling) of InP QDs^{90, 92, 99, 145, 146} and in fact the presence of hydroxyl groups¹⁴⁷ and of oxidized phosphorus have been reported^{88, 133, 134, 136, 148, 149} as depicted in Figure 2.3A-D. Although the sources of oxidation and types of oxidative defects are likely various, their impacts on the electronic structure of InP QDs remain unclear. While the absence of oxidized species often appears to be correlated with increased luminescence efficiency,^{77, 134-136, 138, 150} opposite results have also been observed^{145, 151-157}.

Computational studies are especially suitable to elucidate the effects of oxidation, even though research has mainly been limited to flat (001) surfaces without ligands.^{140, 143, 158-162} Some of these studies report the appearance of trap states upon oxidation,^{140, 143, 158, 162, 163} but the underlying mechanisms that lead to trap formation are not entirely understood. For example, Santosh and coworkers reported that only substitutional oxygen atoms produced trap states, while In-O-P and In-O-In moieties formed by oxygen adsorption did not lead to trap formation.¹⁴⁰ In contrast, in their study on oxygen adsorption on (001) GaP and InP surfaces,¹⁵⁸ Wood and coworkers found that strained In-O-In moieties can give rise to hole traps. Additionally, In-O-In, In-[OH]-In and In-In were found to give electron traps if the In-atoms have unsaturated bonds. In-O-P bridges are generally believed not to lead to trap states,^{158, 161} although Wood and coworkers did observe an increased number of levels near the VB edge.¹⁵⁸ These results indicate that trap formation is highly dependent on the exact configuration of the oxidized species. Indeed, computations on ligand passivated QD models by Ubbink and coworkers found that hole traps are formed by PO_2 moieties, but not by PO_3 and PO_4 .⁸⁹ The effect of polyphosphates remained uncertain due to their unclear oxidation state (leading to n-doping of the QDs), and the large number of possible surface reconstructions. In addition, Park *et al.* have investigated the effect of various metal oxide shells around InP QDs and found evidence for localized defect-like states near their surface in InP/InO, InP/GaO, and InP/AlO core-shell systems but not in InP/CdO and InP/ZnO.¹⁶⁴ Although these results do not cover the entire range of possible oxidated species, they do show that oxidation does not necessarily have detrimental effects, which may explain the seemingly contradictory reports on the effects of InP oxidation.

In spite of all this, oxide-free InP QDs can be prepared either under strict reaction

conditions or by employing hydrogen atmosphere as was recently demonstrated,^{100, 101} but researchers have also looked at how to remove oxidative defects with post-synthetic treatments.

A popular post-synthetic treatment is etching with hydrogen fluoride (HF), as depicted in Figures 2.3E and 2.3F. HF etching was used to clean and expose the surface of InP thin films as early as the 1960's¹⁶⁵. Clark *et al.* later showed that HF etching produced a completely oxide-free InP surface, whereas they were not able to achieve this using other etching agents¹⁶⁶. The application of the HF treatment to InP QD was first reported on by Mičić *et al.* The authors observed an increase in luminescence after applying the treatment, proposing that the fluoride ions fill phosphorus vacancies on the surface and also replace oxygen in the oxide layer.¹³² Since then multiple publications have been made on HF etching, reporting different mechanisms for trap passivation.

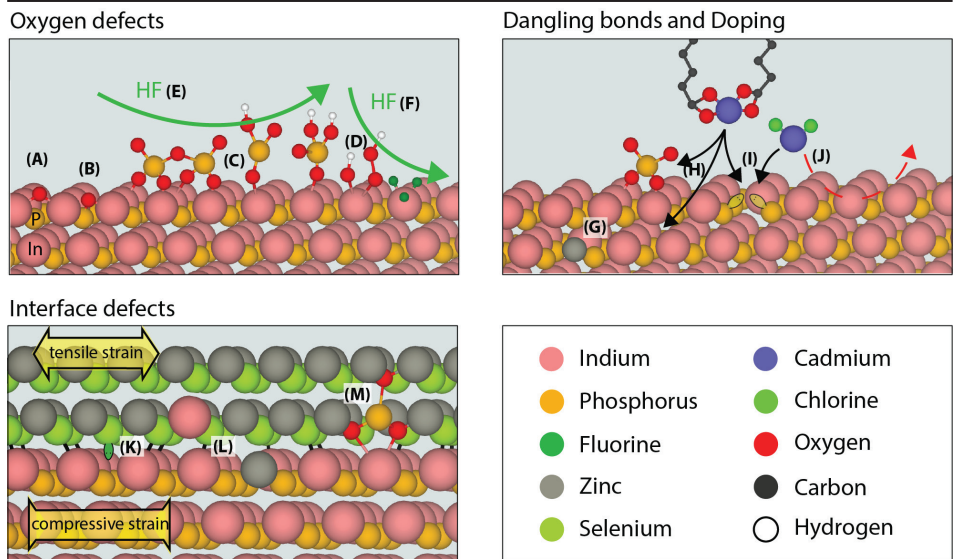


Figure 2.3. Documented structural defects in InP QDs and possible repair mechanisms. Oxygen defects include (A) In-O-In moieties,^{140, 141, 158} (B) In-O-P moieties,^{140, 141, 143, 144, 158, 161} (C) PO_x moieties,^{88, 89, 133, 134, 136, 141, 143, 148, 149} (D) In-OH and In-OOH moieties.^{147, 158, 169} Several mechanisms have been proposed for the passivation of oxygen defects using HF including (E) the breaking of PO_x into smaller PO_3 and PO_4 units⁸⁹ or (F) the replacement of Inbound hydroxide groups by fluoride anions¹⁶⁹ (G) Lattice doping^{82, 135, 171-179} and (H) Incorporation of Cd in surface and subsurface¹⁷¹. (I) Dangling phosphorus bonds can be healed via Ztype passivation^{89, 176, 180-183} but (J) Z-type exchange is also possible.^{184, 185} In coreshell structures, (K) straininduced interfacial defects,^{173, 186-191} (L) mixed interfaces^{178, 192-196} and (M) interfacial oxides^{88, 133, 152} may also occur.

Adam, Talapin and colleagues proposed that the increased luminescence after applying an HF treatment under illumination should be ascribed to removal of the phosphorus as PF_3 , leaving an indium-rich surface that could be better passivated by ligands.^{167, 168} Elimination of phosphorus dangling bonds by fluoride was also supported by transient

absorption results from Yang *et al.*¹³⁷. Alivisatos *et al.* instead ascribed the increased QY after HF exposure to the passivation of indium dangling bonds after they observed an exchange of carboxylate ligands for fluoride ions after the treatment.¹⁶⁹ They also observed that the HF treatment appeared to remove indium (oxo)hydroxides that were present on the nanocrystal surface. Removal of oxygen by means of HF was again reported by Jang *et al.* and Li *et al.*, although they claimed that PO_x species were removed rather than indium hydroxides^{77, 170}. Which types of oxides can be removed by HF treatment and in what way this removal affects the optical properties of nano-InP remains an open question. Recently, Ubbink *et al.* found that HF reacts with InP forming InF_3 (Z-type ligand, see following section) and PH_3 , and breaks up polyphosphate species into smaller PO_4 and PO_3 units. While removal of polyphosphates was correlated with a higher luminescence efficiency, PO_4 and PO_3 species remained present on the surface of highly luminescent HF-treated samples, indicating that only some oxidized species form traps.⁸⁹ Downsides to the HF treatment are the etching of InP itself and the spectral changes observed after treatment, in addition to the dangers associated with HF.

Because of the hazardous nature of HF, alternative fluorination strategies have also been proposed. Strousse and Lovinggood found that adding fluoride-rich ionic compound during the synthesis under microwave illumination strongly improved the quantum yield of the particles.¹⁹⁷ Post-synthetic treatment with fluoride-containing ionic liquids was also found to increase luminescence.¹⁸⁵ Hughes and colleagues ascribed this to the passivation of electrons traps when fluoride binds dangling indium bonds.

2.4.2 Surface states and Z-type passivation

The main suspect for trap states in quantum dots has always been dangling bonds, i.e. under-coordinated atoms at the surface of nanocrystals. Early theoretical calculations by Fu and Zunger¹⁸¹ predicted the existence of both electron and hole traps on the surface of InP QDs as a result of In and P dangling bonds, respectively. The traps appear to become “deeper” as the QD size is reduced, due to the shift of the band-edges. These conclusions are also corroborated by Cho *et al.*¹⁹⁸ Additionally, Dümbsgen *et al.* show that the formation of trap states due to undercoordinated surface atoms depends shape of the QD.¹⁸⁰ In their work, cuboctahedral and In(111)terminated tetrahedral models are deprived of a surface capping moiety to simulate undercoordinated surface atoms. For cuboctahedrons, it was found that surface reconstruction prevents, in most cases, the formation of hole and electron traps. However, tetrahedral shaped models are prone to form localized trap states within the band gap resulting from undercoordinated In and P atoms.

One way to investigate the passivation of surface anions is through treatment of the particles with metal salts also known as Z-type ligands (depicted in Figure 2.3I).^{171, 182, 184, 199}

²⁰⁰ Stein and colleagues found that treatment of InP with Z-type ligands led to an increase in quantum yield (to 19 % for Zn carboxylates and 49% for Cd oleate) and attributed this to the passivation of dangling phosphorus bonds.¹⁸² Kirkwood *et al.* proposed the same passivation mechanism after obtaining PLQYs of 11% for InP treated with CdCl_2 .¹⁹⁹ On the other hand, Hughes *et al.* hypothesized that Cd^{2+} or Zn^{2+} can replace surface In^{3+} ions (Z-type exchange, depicted in Figure 2.3J) relieving steric pressure on the surface and allowing for a more complete passivation, thus reducing trap states.²⁰⁰ Calvin *et al.* also

found support for the exchange mechanism by following the treatment of InP with metal halides using isothermal titration calorimetry.¹⁸⁴ However, Hanrahan and coworkers have shown that cadmium carboxylate Z-type ligands can bind both to phosphorus as well as phosphate that is present on the (sub)surface of InP nanoparticles, suggesting that the mechanism behind Z-type passivation may be more involved than previously thought (see Figure 2.3H and 2.3I).¹⁷¹ Nevertheless, Ubbink *et al.* have recently shown that a simple Z-type passivation procedure with InF_3 leads to higher quantum yields if the QDs are free of oxidized phosphorus species, specifically polyphosphates.⁸⁹

Surface reconstructions may also play an important role in the creation or removal of surface states. In bulk solid state physics, it is well known that surfaces that are directly obtained from cleaving the bulk material are often not stable and will reconstruct.²⁰¹ For example, studies on GaAs surfaces have shown that the Ga-terminated (111) facet will reconstruct by creating Ga-vacancies.²⁰² As-terminated (-1-1-1) facets are more complicated and different reconstructions based on vacancies,²⁰³ or As-trimers have been proposed.²⁰⁴ Although these reconstructions are relatively well understood for bulk surfaces, it is currently unclear if they also take place on the QD surface. One study by Voznyy *et al.* on CdSe QDs did show that surface vacancies are necessary for the delocalization of the HOMO and LUMO levels,²⁰⁵ highlighting the need for further studies on QD surfaces.

2.4.3 Doping

The incorporation of impurities into III-V semiconductors has been long pursued for doping purposes.²⁰⁶ The incorporation of cations (other than group III) into InP QDs, however, has been driven by two other reasons: optical doping (i.e. Stokes-shifted emission) or linewidth narrowing. For instance, Thuy *et al.* observed that doping with Eu^{3+} yields multiple emission lines around the red spectral region.²⁰⁷ Doping with Cu^+ has also been studied by a few groups²⁰⁸⁻²¹⁵ and yields a broad emission in the near-infrared-I window (with photoluminescence efficiencies up to 80%) ascribed to hole localization and to structural relaxation around the Cu site.

More common is the introduction of Zn^{2+} ions during the synthesis of InP QDs in order to obtain QDs with narrower (ensemble) linewidths.^{172, 173, 216} However, aliovalent impurities such as Zn^{2+} are known dopants for III-V semiconductors,^{174-177, 217} and appear to be incorporated and to diffuse into InP QDs (as illustrated in Figure 2.3G).^{171, 218} Through various spectroscopic analyses Janke *et al.* concluded that the incorporation of Zn introduces shallow hole states and associated lattice disorder.¹⁷⁶ Moreover, results by Li *et al.* and Shen *et al.* suggest that the incorporation of Zn in the InP core limits the performance of core-shell structures (see following sections).^{135, 178} Nevertheless, PLQYs of ca. 90% have been reported for both InP and $\text{In}(\text{Zn})\text{P}^{82, 135, 157, 179, 219-221}$ QDs shelled with $\text{ZnSe}_{1-x}\text{S}_x$, $\text{In}(\text{Zn})\text{P}$ standing for InP QDs incorporating Zn in the InP lattice.

2.4.4 Heterovalent core-shell interfaces

Epitaxial growth of II-VI on III-V semiconductors (including InP QDs) has been extensively investigated (see section 2.5). The heterovalent nature of such interfaces introduces complexity and it is worthwhile to highlight some observations from works

on lattice matched GaAs/ZnSe (001) polar junctions. First, we note the efforts to reduce the density of stacking faults in the ZnSe overlayers.^{222, 223} Second, computational studies have shown that an abrupt interface is thermodynamically unstable and that a mixed and/or a defected interface is energetically favored (Figure 2.3L).^{192, 224} In fact, there is also experimental support for the existence of mixed and defected interfaces in samples with a low density of stacking faults.¹⁹⁴ Furthermore Deng *et al.* have shown that the composition of stable mixed interfaces is orientation dependent.¹⁹⁵

As mentioned earlier and as will be discussed in detail ahead, coating InP QDs with ZnSe_{1-x}S_x shells allows the synthesis of highly efficient and stable emitters. A few studies have highlighted the importance of achieving a balanced stoichiometry in these III-V / II-VI core / shell systems.^{135, 178, 225, 226} In particular, results from Li *et al.* and Shen *et al.* strongly suggest that a InP/(In,Zn)P/ZnSe interface allows to boost the photoluminescence efficiency of InP/ZnSe_{1-x}S_x QDs beyond 90%,^{178, 196} and according to studies on In(Zn)P QDs, a selenium terminated interface could be important to limit the diffusion of zinc^{227, 228} and sulfur^{135, 226} into the InP cores. Interfaces containing oxidized species have also shown beneficial effects in the performance of InP QDs (Figure 2.3M).^{152, 229}

2.4.5 Strain

In core-shell QDs, strain can arise from the lattice mismatch between core and shell materials and can have several consequences.²³⁰ It can introduce (strain-relieving) defects as depicted in Figure 2.3K,²³¹ alter band offsets,^{232, 233} shift vibrational frequencies,²³⁴ give rise to piezoelectric fields,²³⁵ or even impact the fine structure,²³⁶⁻²³⁸ the electron-phonon coupling,²³⁹ and photon out-coupling²⁴⁰.

However, little is known about strain engineering in InP QDs. In bulk InP, a phase transition (to rock salt) closely followed by a direct-to-indirect transition (as the X band crosses under Γ) are known to occur at lattice contractions of about 3-5 % (ca. 10 GPa),^{186, 187} and similar values are found for InP QDs.^{188, 189, 241} Rafipoor *et al.* showed that in InP / Zn_{1-x}Cd_xSe core-shell systems, strain can be tuned from compressive (InP/ZnSe) to tensile (InP/CdSe) with no strain observed at x ca. 0.4.¹⁹⁰ Computational investigations by Suh *et al.* suggest that even a thin ZnSe can build considerable tensile strain and could lead to a considerable energy shift of the HOMO.¹⁷³ More pronounced effects are found with ZnS shells instead which could be related to its smaller lattice constant but also its larger Young modulus (see table 2.1 for mechanical properties).¹⁹¹ These computational results also point to a decrease in band gap with increasing tensile strain. However, experimental results have shown the opposite trend: in fact a considerable increase in band gap is observed with increasing tensile strain, which could be of potential interest for piezochromic applications.^{188, 189}

2.5 Wave-Function Engineering

Control over the energy landscape is fundamental in quantum dot technologies.^{13, 14} While this might be achievable to a limited extent by tuning the ligands on the surface of the QDs,^{169, 242} shape-control and core-shell structuring offer a more versatile and robust alternative to achieve it, and the latter has been pivotal in the development of performant and stable QDs. In this section, the various InP based core-shell structures considered

thus far are reviewed, namely, type I structures employing II-VI or III-V shells, as well as reverse core-shells and type II structures. It is important to note that one of the key parameters in the classification and in the design of semiconductor hetero-structures is the band offset (see Figures 2.4A and 2.4B). However, determining the band offsets in QD hetero-structures is not straightforward since the degree of quantum confinement needs to be taken into account as well as any interface dipoles.²⁴³ The latter is of particular relevance to heterovalent systems such as InP/ ZnSe_{1-x}S_x core-shell structures, as recently highlighted.²⁴⁴

2.5.1 Type I InP/ZnSe_{1-x}S_x core/shell QDs

At first glance, ZnSe and ZnS seem to exhibit complementary properties for shelling InP. On one hand, ZnSe has a small lattice mismatch (3.4 %) but does not provide a robust type I confinement, especially for smaller InP cores. On the other hand, ZnS ensures a robust type I band alignment (regardless of core size), but has a large lattice mismatch (7.8 %) which appears to broaden the emission of the QDs.²⁴⁵ By finding a balance between the size of the InP core and the composition and structure of the ZnSe_{1-x}S_x shell, these apparent limitations can be overcome, and highly efficient narrow band emitters can be obtained (see Figures 2.4C and 2.4D). For instance, red-emitting InP/ZnSe/ZnS core-shell-shell structures with near unity photoluminescence efficiency and linewidths of 110-130 meV have been demonstrated (including non-blinking QDs),^{77, 135, 170} green emitting InP/ZnSe_{1-x}S_x/ZnS (0.5<x<0.67) hetero-structures with efficiencies around 90 % and slightly broader linewidths (160-210 meV) have also been realized,^{82, 219, 220, 245} while blue emitting systems are, so far, least performant with efficiencies and linewidths of 45 % and 260 meV respectively^{221, 246}. The lower performance of green and blue emitting QDs is not yet clear but could be related to the strain caused by the shell's increased lattice mismatch which is also more problematic for smaller structures as these have less possibilities to relax strain within the material.¹⁹¹ Interfacial strain can be relieved by alloying the ZnSe_{1-x}S_x shell with other divalent cations.^{190, 247} In addition, their efficiency could also be limited by defects in the shell (stacking faults, impurities etc.)^{196, 248-254} while the broader linewidths seem to arise from a combination of synthetic and intrinsic drawbacks inherent to the extremely small sizes of the InP cores (i.e. size distribution requirements, increased homogeneous linewidths etc.). As mentioned in section 2.4, Zn doping of InP cores is widely employed to decrease their linewidths. Although the structure of these QDs remains unclear, blue and green emitting In(Zn)P/ZnSeS core-shell QDs with improved QYs and narrower linewidths have been demonstrated.^{82, 135, 157, 179, 219-221} We note that the structure of InP/ZnSe_{1-x}S_x QDs might also be quite complex as summarized in section 2.4.

Despite their remarkable efficiencies and stabilities, these QDs still have room for improvement. For instance, the relatively thick ZnSe_{1-x}S_x shells impact the compactness of the QDs which can undermine phosphor and lasing applications (see section 2.6). Another limitation, and perhaps more pressing, is their relatively short biexciton lifetimes preventing efficient operation at high exciton density (see section 2.6).⁷⁷ For instance, highly efficient red-emitting InP/ZnSe/ZnS core-shell-shell QDs exhibit exciton lifetimes of 13 ns but biexciton lifetimes of only 50 ps.⁷⁷ In this system, the negative trion is rather long lived (5.3 ns), owing to the delocalization of the electron wave-function into the thick ZnSe shell (3.5 nm),²⁶³ suggesting that the short biexciton lifetime is due to a

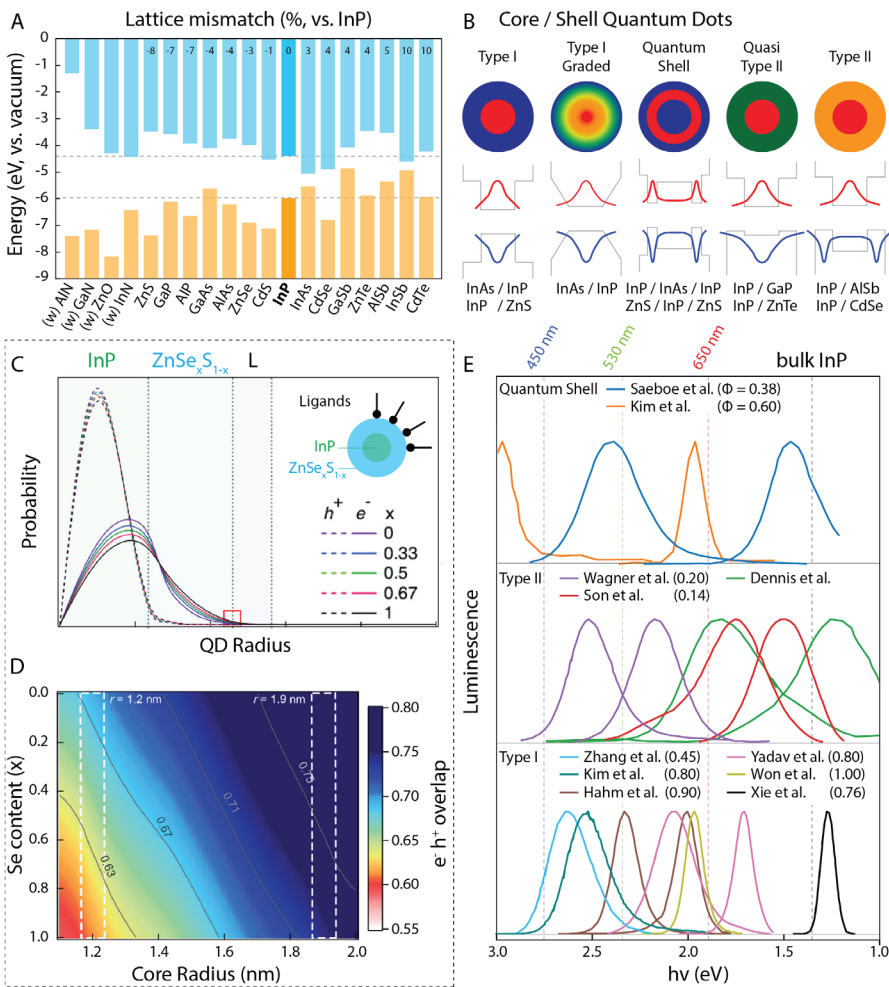


Figure 2.4. InP-based coreshell QDs (A) The band offsets of bulk semiconductors^{32, 255} are usually used as a first approximation in the design of coreshell QD structures. (B) Coreshell structures can be classified into various types according to the (de)localization of electron and hole wavefunctions (the electron and hole probability distribution functions are depicted in red and blue, respectively). In fact, quantum confinement also has an important role in the design, and in InP the conduction levels are thought to be more sensitive to it than the valence band levels. For instance, type I confinement in InP/ZnSe_xS_{1-x} QDs is achieved by (C) employing shells with a large sulfur content and/or (D) by employing larger cores.²⁴⁵ (E) Photoluminescence spectra of selected InP-based core-shell structures emitting in the visible or near infrared, reported efficiencies Φ in parenthesis.^{77, 97, 221, 245, 256-262}

sharp hole confinement. To mitigate this, smoothing the confinement potential using compositionally graded core shells QDs could be an effective approach since it has found enormous success in II-VI QDs. Graded ZnSe_{1-x}S_x shells have been grown on InP QDs and

allowed not only to extend the negative trion lifetimes by ca. 4 times, but also to reduce luminescence intermittency (blinking) and spectral diffusion as the grey state appears to originate from the negative trion itself.^{82, 264, 265} These type of shells should allow to improve the performance and stability of QLEDs as excess electrons often accumulate in the QD layer due to the imbalanced charge injection rates, however they don't fix the sharp hole confinement at the core/shell interface and therefore are unlikely to increase bi-exciton lifetimes.

This raises question marks on whether these type of shells can promote efficient optical gain. Very recently Velosa *et al.* presented a thorough study on the development of gain in InP/ZnSe QDs using transient absorption spectroscopy.²⁶⁶ Their analysis indicated that, at room temperature, gain can be understood as originating from state filling of the lowest electron level with a degeneracy of 2 and of the lowest hole level with an effective degeneracy of 5-10. This effective hole degeneracy is higher than the expected degeneracy of 4, which was attributed to thermal population of higher states in the valence band, perhaps arising from the ZnSe shell. In addition, it was also observed that optical gain was limited to about 10 % of the theoretical maximum value due to a loss of charge carriers at high exciton density attributed to hole trapping. Hole trapping in this system has also been studied in other works.^{251, 267}

2.5.2 The quest for all III-V type I core-shell QDs

In principle, shelling InP with a III-V semiconductor would allow to obtain QDs with dipole-free interfaces and to realize graded core-shell structures in need to mitigate Auger-related losses.²⁶⁸⁻²⁷³ In fact, lasing-quality has been demonstrated using vapor phase grown InP QDs encapsulated by $\text{Al}_x\text{Ga}_{1-x}\text{In}_z\text{P}$ layers.²⁷⁴ However, in the QD field, these systems remain rather unexplored and there might be a number of reasons for this. First, the two evident shelling materials, $\text{In}_{1-x}\text{Ga}_x\text{P}$ and $\text{In}_{1-x}\text{Al}_x\text{P}$, are characterized by a direct to indirect crossovers at x ca. 0.8 and 0.4 respectively, which complicates the prediction of band offsets. Furthermore, whether these materials can effectively provide a type I confinement to InP QDs remains unclear.²⁷⁵⁻²⁷⁸ Second, due to their indirect nature, GaP and AlP shells would strongly reduce the absorption cross section of the QDs. Third, like InP, these materials are also prone to oxidation (see section 2.4) and many Ga precursors appear to react with InP QDs to form $\text{In}_{1-x}\text{Ga}_x\text{P}$ alloys, which poses additional challenges in the growth of core-shell structures.^{256, 257, 279} So far there have been very few reports on these structures, and to be the best of our knowledge the literature is limited to InP/GaP core-shells and mostly in combination with ZnS outer shells.^{256, 280-282} Mixed-anion alloys also remain unexplored but could be another avenue to access wide direct gap shelling materials with a type I band alignment. For example, vapor-phase grown $\text{InP}/\text{GaAs}_{0.6}\text{P}_{0.4}$ dot-in-a-well lasers were recently demonstrated.²⁸³

According to bulk band alignments, InP could also be envisaged as a (type I) shell material for infrared emitting InAs QDs. The development of InAs/InP and $\text{InP}_{1-x}\text{As}_x/\text{InP}$ core-shell QDs emitting in the range of 600-1000 nm was first explored in the works of Xie *et al.* and Kim *et al.* respectively.^{122, 258} Although the photoluminescence efficiencies of these core-shell QDs remained quite low (<5%), subsequent shelling with ZnSe allowed for significant improvement (to ca. 76%). Recently, similar results were obtained by Enright



et al.,²⁸⁴ while Wijaya *et al.* and Zhao *et al.* investigated multi-shell In(Zn)As/In(Zn)P/GaP/ZnS QDs emitting at ca. 800-1000 nm.^{285, 286} In the latter case the photo-luminescence efficiency of the In(Zn)As cores (2.5 %) could be increased to 33, 46, 75% with successive shells, promising results that brighten up prospects for these type of structures.

2.5.3 Reverse core-shell-shell structures

Reverse core-shell-shell structures, also known as *quantum shells* offer further band-gap tunability and room for mitigating Auger losses.²⁸⁷⁻²⁹¹ In this configuration, an InP mid-shell is grown in between a core and an outer shell of wider-gaps, with the band gap being determined by the core size and the shell thickness. For instance, systems such as ZnSe/InP/ZnS and CdTe/InP/ZnS QDs were shown to exhibit tunable and efficient emission across the near infrared I.^{259, 260, 292} However, these structures haven't been much explored, and whether they allow to mitigate Auger processes remains an open question.

2.5.4 Type II and quasi-type II structures

Type II and quasi-type II structures allow for spatial delocalization and separation of electrons and holes within the dot, which, in turn, allows reduction of the band gap and increase of the Stokes shift as well as the carrier lifetimes.²⁹³⁻²⁹⁵ These structures have found interest for photovoltaic and photo-electrochemical cells,²⁹⁶⁻²⁹⁸ photo-catalysis,²⁹⁹ down-converters for solar concentrators,³⁰⁰ and also gain mediums^{301, 302}. For example, Denis *et al.* prepared InP/CdS core-shell QDs emitting in the NIR and showed that both the exciton and biexciton lifetimes increased with increasing shell thickness, with values up to 702 ns and 7 ns respectively.²⁶¹ In addition to this remarkable increase in lifetimes, the charge transfer rate to methylviologen³⁰³ and the multiple exciton generation quantum yield³⁰⁴ are not affected by the quasi-type II band alignment making these QDs interesting for QD based solar cells. Cd-free alternatives have also been developed which expands their potential to biological applications. For instance, InP/ZnTe/ZnSeS QDs emitting in the NIR have been realized, with exciton lifetimes of 387 ns²⁶². InP/ZnO QDs have also been proposed for LEDs^{305, 306}, solar concentrators¹⁵³ and artificial retinas³⁰⁷ although the exciton lifetimes in these structures appear to be shorter, ca. 31 ns. We note that the luminescence efficiency of these type of QDs can be limited by surface traps but in principle this can be mitigated by efficient surface passivation or by growing an outer type I shell.^{306, 308}

2.6 InP QDs in Photonic Technologies

Owing to their tunable band gap, high absorption coefficient, narrow emission linewidths and ROHS compliance, as well as to decades of research, InP quantum dots (QDs) have become of industrial relevance for visible and near-infrared photonic technologies.¹⁴ As shall be discussed in this section, this field has been mainly driven by the development of down-converting and electroluminescent red, green and, to a lesser extent, blue sources. Nevertheless, the tunability of InP QDs is opening an interesting path into near-infrared applications, and QDs also hold potential for generating coherent and quantum light (lasers, single photon, super-fluorescence). In addition, InP QDs can also be employed in other types of photonic applications such as up-conversion or photodetection.

2.6.1 RGB Phosphors

With a bright, narrow and color-tunable emission across the visible spectrum, cyan, green and red QDs have become strong contenders for optical down-conversion in display and lightning technologies. Converting blue light into red or green through a QD film is a simple and efficient way of upgrading a blue LED array into a full color display (Figure 2.5A). Down-converting blue into both red and green light is also interesting for constructing white emitting diodes using a single blue source (Figure 2.5A) and it circumvents both the poor efficiency of green as well as the high cost of red in the three-diode approach to white light generation. In addition, the tunability of QD phosphors enables the generation of customized spectral outputs.

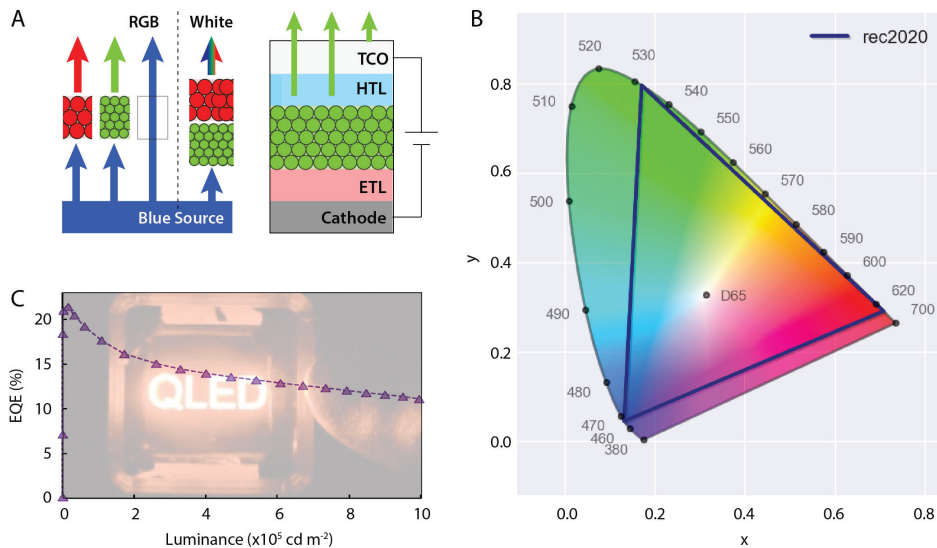


Figure 2.5. InPbased QDs in LEDs. (A) In luminescent down-converting devices, QDs convert blue photons into less energetic photons (such as green or red) shown on the left, whereas in electroluminescent devices QDs convert electrical energy into photons as shown in the right. (B) The high color purity of red InP and green In(Zn)P LEDs is already in close agreement with the requirements for a wide color space of rec2020 standards (the corners of the triangle are the coordinates of highly pure red, green and blue, and D65 represents the coordinates for white light). At low powers, QDs with near-unity photoluminescence efficiencies have been successfully implemented in efficient LEDs. However, at high powers, the efficiency droop remains a problem. This can be clearly seen in (C) the external quantum efficiency of an electroluminescent InP-based QLED as a function of brightness.⁷⁷ EQE: external quantum efficiency, ETL: electron transporting layer, HTL: hole transporting layer, RGB: red, green and blue, TCO: transparent conducting oxide.

For quantum dots to be used as down-converters in high-intensity applications such as LED lamps, strong blue-absorptivity, narrow emission line (color purity), near-unity quantum yield, stability at high photon fluxes (no droop) and at elevated temperatures are all required. Such properties have been obtained for Cd-based type I QDs³⁰⁹, but droop

remains a major challenge in InP based dots²⁵³. Recently, various design strategies have been suggested to mitigate Auger recombination in InP QDs, such as trap passivation¹³⁷ and incorporating a thick mid-shell⁴⁰ or graded shell²⁶⁵. The latter study showed that negative trion Auger recombination can be strongly reduced though potential smoothing in gradient shells, however extended bi-exciton lifetimes remain elusive in these systems. Furthermore, the brightness of InP QDs is limited by the relatively weak blue-absorptivity of thick $\text{ZnSe}_{1-x}\text{S}_x$ shells, and innovative solutions in terms of shell engineering may be required using e.g. more compact shells³¹⁰ or alternative materials³¹¹. Also, smaller InP QDs exhibit wider linewidths and lower efficiencies, although these limitations seem to be surpassed with the incorporation of Zn into the cores.²¹⁹

It was recently shown that red InP QDs can already be a viable on-chip solution for use in white LEDs employing traditional green/yellow phosphors.³¹² An early demonstration of full InP QD white LEDs could also be achieved by avoiding FRET processes between QDs of different colors (sizes), in this case red and green.³¹³ Furthermore, the integration of InP QDs in μLED displays has also been demonstrated.^{17, 314} Finally, InP QDs could also be a solution to the growing interest in cyan-phosphors for healthy-lighting.³¹⁵⁻³¹⁹ It thus seems that commercial use of InP QDs as blue-downconverters in display and lighting technology is close on the horizon. In addition, InP QD phosphors may also be of interest for specialty applications such as custom illumination (e.g. indoors, horticulture), greenhouse roofs and security inks.

2.6.2 Electroluminescent QLEDs

Theoretically, electroluminescence is a more efficient way to obtain light from QDs compared to down-conversion, and there have been many attempts to construct InP QD based LED devices to this end (Figure 2.5A).^{77, 135, 320-325} Electroluminescent QLEDs are particularly interesting for display applications and the high color purity of red InP and green In(Zn)P QLEDs is already in close agreement with the requirements for a wide color space of rec2020 standards (Figure 2.5B).³²⁶ Currently, record efficiencies stand at 22.2% for red¹⁷⁰, 16.3% for green³²⁷ and 2.8% for blue^{328, 329} devices. To construct highly efficient LEDs, a careful choice of device structure and materials is required to ensure exciton confinement inside the QDs in order to prevent parasitic or trap emission in the device (this can be achieved by growing a thick type I shell around the InP cores),³²¹ and a balanced electron and hole injection currents. Compared to II-IV materials, the high-lying valence band edge of InP QDs makes electron (hole) injection comparatively hard (easy).³²¹ Despite the impressive near-limit efficiencies reached in red InP/ZnSe_{1-x}S_x QLEDs, there are still opportunities for further improvements as the efficiency droop at higher operation power is limiting and the lifetime still leaves much to be desired (Figure 2.5C).

2.6.3 Into the infrared

Far-red and near-infrared QDs hold great potential for current and upcoming infrared technologies.^{330, 331} Light sources in this range are increasingly required for applications in biology and medicine,³³²⁻³³⁶ computer vision³³⁷ and data transmission at both short and long (fiber) ranges^{274, 338-340}. Owing to their small size, tunable surface chemistry and processing versatility, infrared QDs extend their application window to e.g. miniaturized

devices such as μ LEDs or photonic chips,^{17,25} nano-imaging,³⁴¹ fluorescent (bio) markers,³⁴² optical sensors and security inks. In addition, infrared QDs with high absorption cross-sections and carrier mobilities are of great interest for infrared detection and imaging technologies³⁴³ and for photovoltaics³⁴⁴.

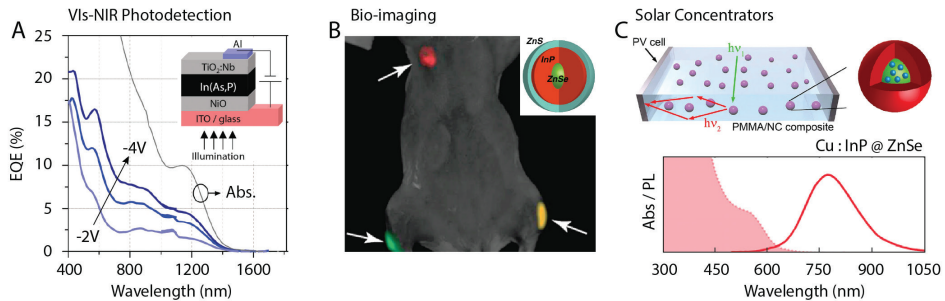


Figure 2.6. Nearinfrared applications of InP QDs. (A) Photodetectors with high external quantum efficiency.³⁴⁵ (B) Bioimaging. In this photograph, QDs are used to probe different parts of a mouse.²⁵⁹ (C) Solar concentrators. With a large Stokes shift, Cu-doped InP QDs down-convert visible photons to infrared photons, which are then guided by a waveguide, such as a polymethyl methacrylate (PMMA) matrix, to solar panels placed on the side.²¹² NC: nanocrystal, NIR: near-infrared, PV: photovoltaic.

In spite of a bulk band gap of 1.35 eV, InP might still well be in competition for applications ranging from the far-red to the short-wave infrared ($< 1\text{eV}$). While the synthesis of large-sized InP QDs remains challenging, examples of InP structures emitting in this range have been reported, namely wurtzite QDs,¹²⁸ reverse hetero-structures, $\text{InP}_{1-x}\text{As}_x$ alloys,^{122, 125} doped QDs, InAs-InP core-shell QDs, together with early demonstrations of *in-vivo* imaging,^{122, 346, 347} solar cells,^{348, 349} LEDs^{285, 286} and photo-detectors³⁴⁵ (see Figure 2.6). In addition, efficient (photon) up-converting systems using InP QDs have also been demonstrated, which further widens the potential of these systems.³⁵⁰ The development of large-sized InP QDs is in reach and is expected to bring the benefits of larger dots along, i.e. higher absorption cross sections, narrower linewidths, longer bi-exciton lifetimes and higher film mobilities (still limited to $< 0.5 \text{ cm}^2 \text{ V}^{-1} \text{ s}^{-1}$)³⁵¹.

In addition, broadband infrared sources based on InP QDs can also be envisaged, either by combining InP QDs emitting at various wavelengths (as in the case of the white LED), or by doping InP with elements such as Cu. As seen in section 2.4, Cu^+ doping results in a broad emission of impressive efficiency, and it is spectrally tunable according to doping concentrations.^{208, 213} With a large Stokes shift, Cu doped InP QDs have also raised interest for luminescent solar concentrators (Figure 2.6C).^{153, 212}

2.6.4 Coherent and Quantum Light

QDs present interesting opportunities as active materials for optical amplifiers, super luminescent diodes and lasers.¹⁹ In fact, optical gain and lasing from QDs have been intensely studied over the past two decades,^{19, 352} and the development of gain in CdSe

is now well understood³⁵³. Given the similar electronic structure of InP and CdSe, one expects the physics of gain to be similar in both materials, however, in InP QDs it remains much less studied. Gain, amplified spontaneous emission and lasing have been observed in InP/ZnSe_{1-x}S_x QDs (see Figure 2.7A-C), but loss processes such as trapping and Auger recombination severely limit gain. In addition, the effective (band-edge) degeneracies in this type of systems remain far from understood (see section 2.5).^{266, 354}

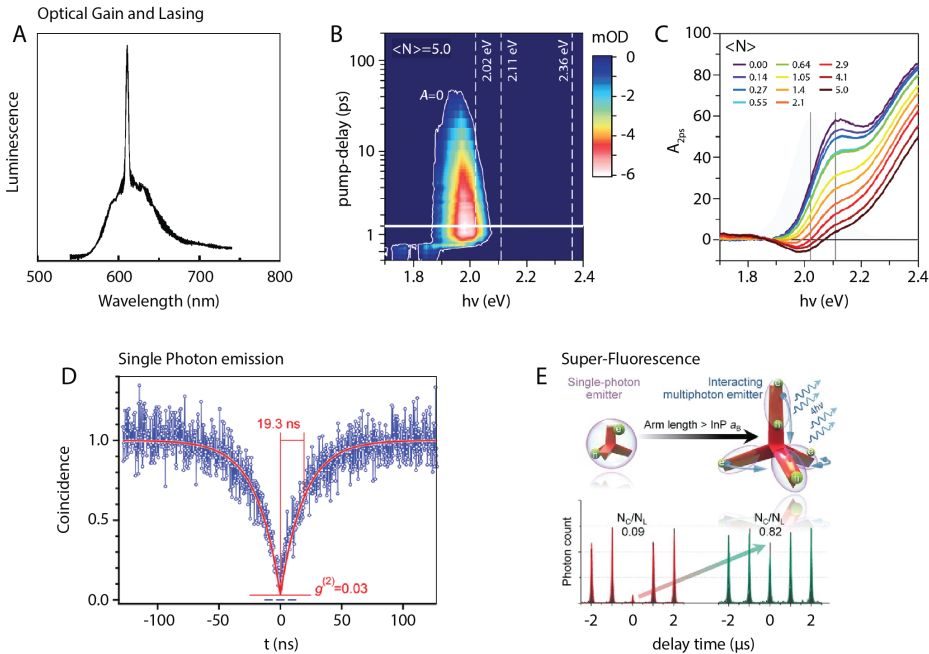


Figure 2.7. Coherent and quantum light sources using InP QDs. (A) Lasing using InP QDs has been demonstrated.³⁵⁴ (B) Ultrafast transient absorption spectroscopy reveals that the multiexcitons remain relatively shortlived.²⁶⁶ (C) Optical gain is also rather weak ($\langle N \rangle$ denotes the average number of excitons per dot and A_{2ps} is the absorption at a pumpprobe delay of 2 ps).²⁶⁶ (D) Highly pure (incoherent) singlephoton emission has also been demonstrated under continuouswave excitation.³⁵⁵ (E) Single InP tetrapods with long arms can emit multiphotons coherently, that is, in a superfluorescent fashion.³⁵⁶ a.u.: arbitrary unit, mOD: milli optical density.

The development of highly efficient InP-based QDs with robust optical performance in the multi-exciton regime and with well-controlled degeneracies is yet to be achieved, and in this regard, further studies on size and shape effects, as well as on compositionally-graded and strain-engineered hetero-structures might be very beneficial.^{236-238, 268-273} Alternatively, type II structures allowing for single-exciton gain could also be envisaged.³⁰¹

Quantum dots are also promising emitters for single-photon and entangled-photon sources.^{340, 357, 358} For efficient generation of undistinguishable single-photons, the optical coherence time needs to approach twice the spontaneous emission lifetime. The

generation of entangled photon pairs, instead, can be achieved through the biexciton-exciton cascade,³⁵⁸⁻³⁶¹ known to occur in InAs QDs.^{362, 363} The development of such light sources employing InP QDs remains an outstanding challenge, with only few studies observing fast dephasing ascribed to phonons,³⁶⁴⁻³⁶⁸ and will require not only improved QD design, but also optimized device architectures and efficient fabrication methods. Nevertheless, high-purity single-photon emission was observed in InP/ZnSe QDs under intense continuous wave pumping (Figure 2.7D), owing to the combination of efficient luminescence and efficient Auger recombination of multi-excitons, highlighting the potential of these systems for on-demand (incoherent) single photon sources operating at room-temperature.³⁵⁵

Finally, super luminescence from QD arrays has also been subject of recent research.^{369, 370} Although InP QD arrays have not been investigated in this regard, super luminescence was observed, remarkably, from a single tetrapod shaped InP QD with long arms and ascribed to excitons in different arms interacting via quantum tunneling (Figure 2.7E).³⁵⁶

2.7 Outlook

The quality of InP QDs has improved and expanded considerably, especially over the past decade. Today, InP QDs emitting in the visible are manufactured at industrial scale for the LED market. However, their quality is still lagging behind that of II-VI or halide perovskite QDs in many aspects, and is also below what is desirable for applications, including LEDs; in other words their current commercial appeal still lies, to a good extent, in their compliance (in terms of elemental composition) with current regulations on consumer electronics. Improving the quality and competitiveness of InP based QDs is therefore key to cement and further their technological impact.

References

1. Dingle, R.; Wiegmann, W.; Henry, C. H., Quantum States of Confined Carriers in Very Thin $\text{Al}_x\text{Ga}_{1-x}\text{As-GaAs-Al}_x\text{Ga}_{1-x}\text{As}$ Heterostructures. *Physical Review Letters* **1974**, 33 (14), 827-830.
2. Sakaki, H., Scattering Suppression and High-Mobility Effect of Size-Quantized Electrons in Ultrafine Semiconductor Wire Structures. *Japanese Journal of Applied Physics* **1980**, 19 (12), 735-738.
3. Ekimov, A.; Onushchenko, A., Quantum size effect in three-dimensional microscopic semiconductor crystals. *Jetp Letters* **1981**, 34, 345.
4. A. L. Efros; Efros, A. L., Interband Absorption of Light in a Semiconductor Sphere. *Soviet Physics - Semiconductors* **1982**, 16, 772-775.
5. Brus, L. E., A simple model for the ionization potential, electron affinity, and aqueous redox potentials of small semiconductor crystallites. *The Journal of Chemical Physics* **1983**, 79 (11), 5566-5571.
6. Brus, L. E., Electron-electron and electron-hole interactions in small semiconductor crystallites: The size dependence of the lowest excited electronic state. *The Journal of Chemical Physics* **1984**, 80 (9), 4403-4409.
7. Meyer, M.; Wallberg, C.; Kurihara, K.; Fendler, J. H., Photosensitized charge separation and hydrogen production in reversed micelle entrapped platinized colloidal cadmium sulphide. *Journal of the Chemical Society, Chemical Communications* **1984**, (2), 90-91.
8. Murray, C. B.; Norris, D. J.; Bawendi, M. G., Synthesis and characterization of nearly monodisperse CdE (E = sulfur, selenium, tellurium) semiconductor nanocrystallites. *Journal*



- of the American Chemical Society **1993**, 115 (19), 8706-8715.
9. Yin, Y.; Alivisatos, A. P., Colloidal nanocrystal synthesis and the organic–inorganic interface. *Nature* **2005**, 437 (7059), 664–670.
 10. Calvin, J. J.; Brewer, A. S.; Alivisatos, A. P., The role of organic ligand shell structures in colloidal nanocrystal synthesis. *Nature Synthesis* **2022**, 1 (2), 127–137.
 11. Kovalenko, M. V.; Manna, L.; Cabot, A.; Hens, Z.; Talapin, D. V.; Kagan, C. R.; Klimov, V. I.; Rogach, A. L.; Reiss, P.; Milliron, D. J.; Guyot-Sionnest, P.; Konstantatos, G.; Parak, W. J.; Hyeon, T.; Korgel, B. A.; Murray, C. B.; Heiss, W., Prospects of Nanoscience with Nanocrystals. *ACS Nano* **2015**, 9 (2), 1012–1057.
 12. Efros, A. L.; Brus, L. E., Nanocrystal Quantum Dots: From Discovery to Modern Development. *ACS Nano* **2021**, 15, 6192–6210.
 13. Pietryga, J. M.; Park, Y.-S.; Lim, J.; Fidler, A. F.; Bae, W. K.; Brovelli, S.; Klimov, V. I., Spectroscopic and Device Aspects of Nanocrystal Quantum Dots. *Chemical Reviews* **2016**, 116 (18), 10513–10622.
 14. García de Arquer, F. P.; Talapin, D. V.; Klimov, V. I.; Arakawa, Y.; Bayer, M.; Sargent, E. H., Semiconductor quantum dots: Technological progress and future challenges. *Science* **2021**, 373 (6555), eaaz8541.
 15. Liu, M.; Yazdani, N.; Yarema, M.; Jansen, M.; Wood, V.; Sargent, E. H., Colloidal quantum dot electronics. *Nature Electronics* **2021**, 4 (8), 548–558.
 16. Rhee, S.; Kim, K.; Roh, J.; Kwak, J., Recent Progress in High-Luminance Quantum Dot Light-Emitting Diodes. *Curr. Opt. Photon.* **2020**, 4 (3), 161–173.
 17. Liu, Z.; Lin, C.-H.; Hyun, B.-R.; Sher, C.-W.; Lv, Z.; Luo, B.; Jiang, F.; Wu, T.; Ho, C.-H.; Kuo, H.-C.; He, J.-H., Micro-light-emitting diodes with quantum dots in display technology. *Light: Science & Applications* **2020**, 9 (1), 83.
 18. Nannen, E.; Frohleiks, J.; Gellner, S., Light-Emitting Electrochemical Cells Based on Color-Tunable Inorganic Colloidal Quantum Dots. *Advanced Functional Materials* **2020**, 30 (33), 1907349.
 19. Park, Y.-S.; Roh, J.; Diroll, B. T.; Schaller, R. D.; Klimov, V. I., Colloidal quantum dot lasers. *Nature Reviews Materials* **2021**, 6, 382–401.
 20. Jung, H.; Ahn, N.; Klimov, V. I., Prospects and challenges of colloidal quantum dot laser diodes. *Nature Photonics* **2021**, 15 (9), 643–655.
 21. Pejović, V.; Georgitzikis, E.; Lee, J.; Lieberman, I.; Cheyns, D.; Heremans, P.; Malinowski, P. E., Infrared Colloidal Quantum Dot Image Sensors. *IEEE Transactions on Electron Devices* **2022**, 69 (6), 2840–2850.
 22. Nakotte, T.; Munyan, S. G.; Murphy, J. W.; Hawks, S. A.; Kang, S.; Han, J.; Hiszpanski, A. M., Colloidal quantum dot based infrared detectors: extending to the mid-infrared and moving from the lab to the field. *Journal of Materials Chemistry C* **2022**, 10 (3), 790–804.
 23. Kagan, C. R.; Bassett, L. C.; Murray, C. B.; Thompson, S. M., Colloidal Quantum Dots as Platforms for Quantum Information Science. *Chemical Reviews* **2021**, 121 (5), 3186–3233.
 24. Chen, J.; Rong, K., Nanophotonic devices and circuits based on colloidal quantum dots. *Materials Chemistry Frontiers* **2021**, 5 (12), 4502–4537.
 25. Chen, M.; Lu, L.; Yu, H.; Li, C.; Zhao, N., Integration of Colloidal Quantum Dots with Photonic Structures for Optoelectronic and Optical Devices. *Advanced Science* **2021**, 8 (18), 2101560.
 26. Adachi, S., *Handbook on Physical Properties of Semiconductors*. Springer: 2004; Vol. 2.
 27. Abdollahi, A.; Golzan, M. M.; Aghayar, K., First-principles investigation of electronic properties of Al_xIn_{1-x}P semiconductor alloy. *Journal of Materials Science* **2016**, 51 (15), 7343–7354.
 28. Braunstein, R.; Kane, E. O., The valence band structure of the III–V compounds. *Journal of Physics and Chemistry of Solids* **1962**, 23 (10), 1423–1431.
 29. Vurgaftman, I.; Meyer, J. R.; Ram-Mohan, L. R., Band parameters for III–V compound

- semiconductors and their alloys. *Journal of Applied Physics* **2001**, 89 (11), 5815-5875.
30. Kim, Y.-S.; Marsman, M.; Kresse, G.; Tran, F.; Blaha, P., Towards efficient band structure and effective mass calculations for III-V direct band-gap semiconductors. *Physical Review B* **2010**, 82 (20), 205212.
 31. Kwok, N., *Complete Guide to Semiconductor Devices*. Wiley-IEEE Press: 2002.
 32. Van de Walle, C. G.; Neugebauer, J., Universal alignment of hydrogen levels in semiconductors, insulators and solutions. *Nature* **2003**, 423 (6940), 626-628.
 33. Adachi, S., *The Handbook on Optical Constants of Semiconductors*. WORLD SCIENTIFIC: 2012; p 632.
 34. Catlow, C. R. A.; Stoneham, A. M., Ionicity in solids. *Journal of Physics C: Solid State Physics* **1983**, 16 (22), 4321.
 35. Christensen, N. E.; Satpathy, S.; Pawlowska, Z., Bonding and ionicity in semiconductors. *Physical Review B* **1987**, 36 (2), 1032-1050.
 36. Tripathy, S. K.; Pattanaik, A., Optical and electronic properties of some semiconductors from energy gaps. *Optical Materials* **2016**, 53, 123-133.
 37. Almeida, G. e. a., Size-dependent Optical Properties of InP CQDs. *To be published* **2023**.
 38. Franceschetti, A.; Fu, H.; Wang, L. W.; Zunger, A., Many-body pseudopotential theory of excitons in InP and CdSe quantum dots. *Physical Review B* **1999**, 60 (3), 1819-1829.
 39. Efros, A. L.; Rosen, M., The Electronic Structure of Semiconductor Nanocrystals. *Annual Review of Materials Science* **2000**, 30 (1), 475-521.
 40. Dübngben, K. C.; Zito, J.; Infante, I.; Hens, Z., Shape, Electronic Structure, and Trap States in Indium Phosphide Quantum Dots. *Chemistry of Materials* **2021**, 33, 6885-6896.
 41. Krauss, T. D.; Wise, F. W., Coherent Acoustic Phonons in a Semiconductor Quantum Dot. *Physical Review Letters* **1997**, 79 (25), 5102-5105.
 42. Besombes, L.; Kheng, K.; Marsal, L.; Mariette, H., Acoustic phonon broadening mechanism in single quantum dot emission. *Physical Review B* **2001**, 63 (15), 155307.
 43. *Semiconductor Quantum Dots: Physics, Spectroscopy and Applications*. Springer: 2002.
 44. Bozyigit, D.; Yazdani, N.; Yarema, M.; Yarema, O.; Lin, W. M. M.; Volk, S.; Vuttivorakulchai, K.; Luisier, M.; Juranyi, F.; Wood, V., Soft surfaces of nanomaterials enable strong phonon interactions. *Nature* **2016**, 531 (7596), 618-622.
 45. Cui, J.; Beyler, A. P.; Coropceanu, I.; Cleary, L.; Avila, T. R.; Chen, Y.; Cordero, J. M.; Heathcote, S. L.; Harris, D. K.; Chen, O.; Cao, J.; Bawendi, M. G., Evolution of the Single-Nanocrystal Photoluminescence Linewidth with Size and Shell: Implications for Exciton-Phonon Coupling and the Optimization of Spectral Linewidths. *Nano Letters* **2016**, 16 (1), 289-296.
 46. Kirschner, M. S.; Hannah, D. C.; Diroll, B. T.; Zhang, X.; Wagner, M. J.; Hayes, D.; Chang, A. Y.; Rowland, C. E.; Lethiec, C. M.; Schatz, G. C.; Chen, L. X.; Schaller, R. D., Transient Melting and Recrystallization of Semiconductor Nanocrystals Under Multiple Electron-Hole Pair Excitation. *Nano Letters* **2017**, 17 (9), 5314-5320.
 47. Yazdani, N.; Bozyigit, D.; Vuttivorakulchai, K.; Luisier, M.; Infante, I.; Wood, V., Tuning Electron-Phonon Interactions in Nanocrystals through Surface Termination. *Nano Letters* **2018**, 18 (4), 2233-2242.
 48. Yazdani, N.; Volk, S.; Yarema, O.; Yarema, M.; Wood, V., Size, Ligand, and Defect-Dependent Electron-Phonon Coupling in Chalcogenide and Perovskite Nanocrystals and Its Impact on Luminescence Line Widths. *ACS Photonics* **2020**, 7 (5), 1088-1095.
 49. Kang, S.; Kim, Y.; Jang, E.; Kang, Y.; Han, S., Fundamental limit of emission linewidth of quantum dots: ab initio study on CdSe nanocrystals. *ACS Applied Materials & Interfaces* **2020**, 12, 22012-22018.
 50. Guzelurk, B.; Cotts, B. L.; Jasrasaria, D.; Philbin, J. P.; Hanifi, D. A.; Koscher, B. A.; Balan, A. D.; Curling, E.; Zajac, M.; Park, S.; Yazdani, N.; Nyby, C.; Kamysbayev, V.; Fischer, S.; Nett, Z.; Shen, X.; Kozina, M. E.; Lin, M.-F.; Reid, A. H.; Weathersby, S. P.; Schaller, R. D.;



- Wood, V.; Wang, X.; Dionne, J. A.; Talapin, D. V.; Alivisatos, A. P.; Salleo, A.; Rabani, E.; Lindenberg, A. M., Dynamic lattice distortions driven by surface trapping in semiconductor nanocrystals. *Nature Communications* **2021**, *12* (1), 1860.
51. Monreal, R. C., Electron-phonon interaction in the dynamics of trap filling in quantum dots. *Physical Review B* **2021**, *104* (18), 184304.
 52. Almeida, G.; van der Poll, L.; Evers, W. H.; Szoboszlai, E.; Vonk, S. J. W.; Rabouw, F. T.; Houtepen, A. J., Size-Dependent Optical Properties of InP Colloidal Quantum Dots. *Nano Letters* **2023**, *23* (18), 8697-8703.
 53. Brodu, A.; Ballottin, M. V.; Buhot, J.; van Harten, E. J.; Dupont, D.; La Porta, A.; Prins, P. T.; Tessier, M. D.; Versteegh, M. A. M.; Zwiller, V.; Bals, S.; Hens, Z.; Rabouw, F. T.; Christianen, P. C. M.; de Mello Donega, C.; Vanmaekelbergh, D., Exciton Fine Structure and Lattice Dynamics in InP/ZnSe Core/Shell Quantum Dots. *ACS Photonics* **2018**, *5* (8), 3353-3362.
 54. Kim, J.; Wong, C. Y.; Scholes, G. D., Exciton Fine Structure and Spin Relaxation in Semiconductor Colloidal Quantum Dots. *Accounts of Chemical Research* **2009**, *42* (8), 1037-1046.
 55. Brodu, A.; Chandrasekaran, V.; Scarpelli, L.; Buhot, J.; Masia, F.; Ballottin, M. V.; Severijnen, M.; Tessier, M. D.; Dupont, D.; Rabouw, F. T.; Christianen, P. C. M.; de Mello Donega, C.; Vanmaekelbergh, D.; Langbein, W.; Hens, Z., Fine Structure of Nearly Isotropic Bright Excitons in InP/ZnSe Colloidal Quantum Dots. *The Journal of Physical Chemistry Letters* **2019**, *10* (18), 5468-5475.
 56. Brodu, A.; Tessier, M. D.; Canneson, D.; Dupont, D.; Ballottin, M. V.; Christianen, P. C. M.; de Mello Donega, C.; Hens, Z.; Yakovlev, D. R.; Bayer, M.; Vanmaekelbergh, D.; Biadala, L., Hyperfine Interactions and Slow Spin Dynamics in Quasi-isotropic InP-based Core/Shell Colloidal Nanocrystals. *ACS Nano* **2019**, *13* (9), 10201-10209.
 57. Efros, A. L.; Rosen, M.; Kuno, M.; Nirmal, M.; Norris, D. J.; Bawendi, M., Band-edge exciton in quantum dots of semiconductors with a degenerate valence band: Dark and bright exciton states. *Physical Review B* **1996**, *54* (7), 4843-4856.
 58. Melnychuk, C.; Guyot-Sionnest, P., Multicarrier Dynamics in Quantum Dots. *Chemical Reviews* **2021**.
 59. Takagahara, T., Electron-phonon interactions and excitonic dephasing in semiconductor nanocrystals. *Physical Review Letters* **1993**, *71* (21), 3577-3580.
 60. Borri, P.; Langbein, W.; Woggon, U.; Stavarache, V.; Reuter, D.; Wieck, A. D., Exciton dephasing via phonon interactions in InAs quantum dots: Dependence on quantum confinement. *Physical Review B* **2005**, *71* (11), 115328.
 61. Masia, F.; Accanto, N.; Langbein, W.; Borri, P., Spin-Flip Limited Exciton Dephasing in CdSe/ZnS Colloidal Quantum Dots. *Physical Review Letters* **2012**, *108* (8), 087401.
 62. Accanto, N.; Masia, F.; Moreels, I.; Hens, Z.; Langbein, W.; Borri, P., Engineering the Spin-Flip Limited Exciton Dephasing in Colloidal CdSe/CdS Quantum Dots. *ACS Nano* **2012**, *6* (6), 5227-5233.
 63. Fumani, A. K.; Berezovsky, J., Magnetic-field-dependent spin decoherence and dephasing in room-temperature CdSe nanocrystal quantum dots. *Physical Review B* **2013**, *88* (15), 155316.
 64. Micic, O. I.; Curtis, C. J.; Jones, K. M.; Sprague, J. R.; Nozik, A. J., Synthesis and Characterization of InP Quantum Dots. *The Journal of Physical Chemistry* **1994**, *98* (19), 4966-4969.
 65. Guzelian, A. A.; Katari, J. E. B.; Kadavanich, A. V.; Banin, U.; Hamad, K.; Juban, E.; Alivisatos, A. P.; Wolters, R. H.; Arnold, C. C.; Heath, J. R., Synthesis of Size-Selected, Surface-Passivated InP Nanocrystals. *The Journal of Physical Chemistry* **1996**, *100* (17), 7212-7219.
 66. Mičić, O. I.; Jones, K. M.; Cahill, A.; Nozik, A. J., Optical, Electronic, and Structural

- Properties of Uncoupled and Close-Packed Arrays of InP Quantum Dots. *The Journal of Physical Chemistry B* **1998**, *102* (49), 9791-9796.
67. Battaglia, D.; Peng, X., Formation of High Quality InP and InAs Nanocrystals in a Noncoordinating Solvent. *Nano Letters* **2002**, *2* (9), 1027-1030.
 68. Talapin, D. V.; Rogach, A. L.; Mekis, I.; Haubold, S.; Kornowski, A.; Haase, M.; Weller, H., Synthesis and surface modification of amino-stabilized CdSe, CdTe and InP nanocrystals. *Colloids and Surfaces A: Physicochemical and Engineering Aspects* **2002**, *202* (2), 145-154.
 69. Gao, S.; Lu, J.; Chen, N.; Zhao, Y.; Xie, Y., Aqueous synthesis of III-V semiconductor GaP and InP exhibiting pronounced quantum confinement. *Chemical Communications* **2002**, (24), 3064-3065.
 70. Jun, K.-W.; Khanna, P. K.; Hong, K.-B.; Baeg, J.-O.; Suh, Y.-D., Synthesis of InP nanocrystals from indium chloride and sodium phosphide by solution route. *Materials Chemistry and Physics* **2006**, *96* (2), 494-497.
 71. Gerbec, J. A.; Magana, D.; Washington, A.; Strouse, G. F., Microwave-Enhanced Reaction Rates for Nanoparticle Synthesis. *Journal of the American Chemical Society* **2005**, *127* (45), 15791-15800.
 72. Xu, S.; Kumar, S.; Nann, T., Rapid Synthesis of High-Quality InP Nanocrystals. *Journal of the American Chemical Society* **2006**, *128* (4), 1054-1055.
 73. Xie, R.; Battaglia, D.; Peng, X., Colloidal InP Nanocrystals as Efficient Emitters Covering Blue to Near-Infrared. *Journal of the American Chemical Society* **2007**, *129* (50), 15432-15433.
 74. Li, L.; Protière, M.; Reiss, P., Economic Synthesis of High Quality InP Nanocrystals Using Calcium Phosphide as the Phosphorus Precursor. *Chemistry of Materials* **2008**, *20* (8), 2621-2623.
 75. Harris, D. K.; Bawendi, M. G., Improved Precursor Chemistry for the Synthesis of III-V Quantum Dots. *Journal of the American Chemical Society* **2012**, *134* (50), 20211-20213.
 76. Xu, Z.; Li, Y.; Li, J.; Pu, C.; Zhou, J.; Lv, L.; Peng, X., Formation of size-tunable and nearly monodisperse InP nanocrystals: Chemical reactions and controlled synthesis. *Chemistry of Materials* **2019**, *31* (14), 5331-5341.
 77. Won, Y.-H.; Cho, O.; Kim, T.; Chung, D.-Y.; Kim, T.; Chung, H.; Jang, H.; Lee, J.; Kim, D.; Jang, E., Highly efficient and stable InP/ZnSe/ZnS quantum dot light-emitting diodes. *Nature* **2019**, *575* (7784), 634-638.
 78. Achorn, O. B.; Franke, D.; Bawendi, M. G., Seedless Continuous Injection Synthesis of Indium Phosphide Quantum Dots as a Route to Large Size and Low Size Dispersity. *Chemistry of Materials* **2020**, *32* (15), 6532-6539.
 79. Song, W.-S.; Lee, H.-S.; Lee, J. C.; Jang, D. S.; Choi, Y.; Choi, M.; Yang, H. J. J. o. N. R., Amine-derived synthetic approach to color-tunable InP/ZnS quantum dots with high fluorescent qualities. **2013**, *15* (6), 1750.
 80. Kim, K.; Yoo, D.; Choi, H.; Tamang, S.; Ko, J.-H.; Kim, S.; Kim, Y.-H.; Jeong, S., Halide-Amine Co-Passivated Indium Phosphide Colloidal Quantum Dots in Tetrahedral Shape. **2016**, *55* (11), 3714-3718.
 81. Tessier, M. D.; De Nolf, K.; Dupont, D.; Sinnaeve, D.; De Roo, J.; Hens, Z., Aminophosphines: A Double Role in the Synthesis of Colloidal Indium Phosphide Quantum Dots. *Journal of the American Chemical Society* **2016**, *138* (18), 5923-5929.
 82. Jo, J.-H.; Jo, D.-Y.; Lee, S.-H.; Yoon, S.-Y.; Lim, H.-B.; Lee, B.-J.; Do, Y. R.; Yang, H., InP-Based Quantum Dots Having an InP Core, Composition-Gradient ZnSeS Inner Shell, and ZnS Outer Shell with Sharp, Bright Emissivity, and Blue Absorptivity for Display Devices. *ACS Applied Nano Materials* **2020**, *3*, 1972-1980.
 83. Liu, Z.; Kumbhar, A.; Xu, D.; Zhang, J.; Sun, Z.; Fang, J., Coreduction Colloidal Synthesis of III-V Nanocrystals: The Case of InP. *Angewandte Chemie International Edition* **2008**, *47* (19), 3540-3542.



84. Joung, S.; Yoon, S.; Han, C.-S.; Kim, Y.; Jeong, S., Facile synthesis of uniform large-sized InP nanocrystal quantum dots using tris(tert-butyltrimethylsilyl)phosphine. *Nanoscale Research Letters* **2012**, 7 (1), 93.
85. Gary, D. C.; Glassy, B. A.; Cossairt, B. M., Investigation of Indium Phosphide Quantum Dot Nucleation and Growth Utilizing Triarylsilylphosphine Precursors. *Chemistry of Materials* **2014**, 26 (4), 1734-1744.
86. Chandrasiri, H. B.; Kim, E. B.; Snee, P. T., Sterically Encumbered Tris(trialkylsilyl) Phosphine Precursors for Quantum Dot Synthesis. *Inorganic Chemistry* **2020**.
87. Wells, R. L.; Pitt, C. G.; McPhail, A. T.; Purdy, A. P.; Shafieezad, S.; Hallock, R. B., The use of tris(trimethylsilyl)arsine to prepare gallium arsenide and indium arsenide. *Chemistry of Materials* **1989**, 1 (1), 4-6.
88. Virieux, H.; Le Troedec, M.; Cros-Gagneux, A.; Ojo, W.-S.; Delpech, F.; Nayral, C.; Martinez, H.; Chaudret, B., InP/ZnS Nanocrystals: Coupling NMR and XPS for Fine Surface and Interface Description. *Journal of the American Chemical Society* **2012**, 134 (48), 19701-19708.
89. Ubbink, R. F.; Almeida, G.; Iziyi, H.; du Fossé, I.; Verkleij, R.; Ganapathy, S.; van Eck, E. R. H.; Houtepen, A. J., A Water-Free In Situ HF Treatment for Ultrabright InP Quantum Dots. *Chemistry of Materials* **2022**, 34, 10093-10103.
90. Gary, D. C.; Cossairt, B. M., Role of Acid in Precursor Conversion During InP Quantum Dot Synthesis. *Chemistry of Materials* **2013**, 25 (12), 2463-2469.
91. Angelé, L.; Dreyfuss, S.; Dubertret, B.; Mézailles, N., Synthesis of Monodisperse InP Quantum Dots: Use of an Acid-Free Indium Carboxylate Precursor. *Inorganic Chemistry* **2021**, 60 (4), 2271-2278.
92. Narayanaswamy, A.; Xu, H.; Pradhan, N.; Kim, M.; Peng, X., Formation of Nearly Monodisperse In₂O₃ Nanodots and Oriented-Attached Nanoflowers: Hydrolysis and Alcoholysis vs Pyrolysis. *Journal of the American Chemical Society* **2006**, 128 (31), 10310-10319.
93. Li, Y.; Hou, X.; Shen, Y.; Dai, N.; Peng, X., Tuning the Reactivity of Indium Alkanoates by Tertiary Organophosphines for the Synthesis of Indium-Based Quantum Dots. *Chemistry of Materials* **2021**, 33 (23), 9348-9356.
94. De Trizio, L.; Gaspari, R.; Bertoni, G.; Kriegel, I.; Moretti, L.; Scotognella, F.; Maserati, L.; Zhang, Y.; Messina, G. C.; Prato, M.; Marras, S.; Cavalli, A.; Manna, L., Cu₃-xP Nanocrystals as a Material Platform for Near-Infrared Plasmonics and Cation Exchange Reactions. *Chemistry of Materials* **2015**, 27 (3), 1120-1128.
95. Zhao, T.; Oh, N.; Jishkariani, D.; Zhang, M.; Wang, H.; Li, N.; Lee, J. D.; Zeng, C.; Muduli, M.; Choi, H.-J.; Su, D.; Murray, C. B.; Kagan, C. R., General Synthetic Route to High-Quality Colloidal III-V Semiconductor Quantum Dots Based on Pnictogen Chlorides. *Journal of the American Chemical Society* **2019**, 141 (38), 15145-15152.
96. Ginterseder, M.; Franke, D.; Perkinson, C. F.; Wang, L.; Hansen, E. C.; Bawendi, M. G., Scalable Synthesis of InAs Quantum Dots Mediated through Indium Redox Chemistry. *Journal of the American Chemical Society* **2020**, 142, 4088-4092.
97. Yadav, R.; Kwon, Y.; Rivaux, C.; Saint-Pierre, C.; Ling, W. L.; Reiss, P., Narrow Near-Infrared Emission from InP QDs Synthesized with Indium(I) Halides and Aminophosphine. *Journal of the American Chemical Society* **2023**, (145), 5070-5891.
98. Valleix, R.; Cisnetti, F.; Okuno, H.; Boutinaud, P.; Chadeyron, G.; Boyer, D., Size-Controlled Indium Phosphide Quantum Dots for Bright and Tunable Light Emission by Simple Hindered Diamine Addition. *ACS Applied Nano Materials* **2021**, 4, 11105-11114.
99. Xie, L.; Harris, D. K.; Bawendi, M. G.; Jensen, K. F., Effect of Trace Water on the Growth of Indium Phosphide Quantum Dots. *Chemistry of Materials* **2015**, 27 (14), 5058-5063.
100. Baquero, E. A.; Virieux, H.; Swain, R. A.; Gillet, A.; Cros-Gagneux, A.; Coppel, Y.; Chaudret, B.; Nayral, C.; Delpech, F., Synthesis of Oxide-Free InP Quantum Dots: Surface

- Control and H₂-Assisted Growth. *Chemistry of Materials* **2017**, *29* (22), 9623-9627.
101. Calvin, J. J.; Kaufman, T. M.; Sedlak, A. B.; Crook, M. F.; Alivisatos, A. P., Observation of ordered organic capping ligands on semiconducting quantum dots via powder X-ray diffraction. *Nature Communications* **2021**, *12* (1), 2663.
 102. Allen, P. M.; Walker, B. J.; Bawendi, M. G., Mechanistic Insights into the Formation of InP Quantum Dots. **2010**, *49* (4), 760-762.
 103. Gary, D. C.; Terban, M. W.; Billinge, S. J. L.; Cossairt, B. M., Two-Step Nucleation and Growth of InP Quantum Dots via Magic-Sized Cluster Intermediates. *Chemistry of Materials* **2015**, *27* (4), 1432-1441.
 104. Cossairt, B. M., Shining Light on Indium Phosphide Quantum Dots: Understanding the Interplay among Precursor Conversion, Nucleation, and Growth. *Chemistry of Materials* **2016**, *28* (20), 7181-7189.
 105. Xie, L.; Shen, Y.; Franke, D.; Sebastián, V.; Bawendi, M. G.; Jensen, K. F., Characterization of Indium Phosphide Quantum Dot Growth Intermediates Using MALDI-TOF Mass Spectrometry. *Journal of the American Chemical Society* **2016**, *138* (41), 13469-13472.
 106. Gary, D. C.; Petrone, A.; Li, X.; Cossairt, B. M., Investigating the role of amine in InP nanocrystal synthesis: destabilizing cluster intermediates by Z-type ligand displacement. *Chemical Communications* **2017**, *53* (1), 161-164.
 107. Friedfeld, M. R.; Johnson, D. A.; Cossairt, B. M., Conversion of InP Clusters to Quantum Dots. *Inorganic Chemistry* **2019**, *58* (1), 803-810.
 108. Kwon, Y.; Oh, J.; Lee, E.; Lee, S. H.; Agnes, A.; Bang, G.; Kim, J.; Kim, D.; Kim, S., Evolution from unimolecular to colloidal-quantum-dot-like character in chlorine or zinc incorporated InP magic size clusters. *Nature Communications* **2020**, *11* (1), 3127.
 109. Gary, D. C.; Flowers, S. E.; Kaminsky, W.; Petrone, A.; Li, X.; Cossairt, B. M., Single-Crystal and Electronic Structure of a 1.3 nm Indium Phosphide Nanocluster. *Journal of the American Chemical Society* **2016**, *138* (5), 1510-1513.
 110. McMurtry, B. M.; Qian, K.; Teglassi, J. K.; Swarnakar, A. K.; De Roo, J.; Owen, J. S., Continuous Nucleation and Size Dependent Growth Kinetics of Indium Phosphide Nanocrystals. *Chemistry of Materials* **2020**.
 111. Zhao, Q.; Kulik, H. J., Electronic Structure Origins of Surface-Dependent Growth in III-V Quantum Dots. *Chemistry of Materials* **2018**, *30* (20), 7154-7165.
 112. Baek, J.; Allen, P. M.; Bawendi, M. G.; Jensen, K. F., Investigation of Indium Phosphide Nanocrystal Synthesis Using a High-Temperature and High-Pressure Continuous Flow Microreactor. *Angewandte Chemie International Edition* **2011**, *50* (3), 627-630.
 113. Kim, K.; Jeong, S.; Woo, J. Y.; Han, C.-S., Successive and large-scale synthesis of InP/ZnS quantum dots in a hybrid reactor and their application to white LEDs. *Nanotechnology* **2012**, *23* (6), 065602.
 114. Ippen, C.; Schneider, B.; Pries, C.; Kröpke, S.; Greco, T.; Holländer, A., Large-scale synthesis of high quality InP quantum dots in a continuous flow-reactor under supercritical conditions. *Nanotechnology* **2015**, *26* (8), 085604.
 115. Baek, J.; Shen, Y.; Lignos, I.; Bawendi, M. G.; Jensen, K. F., Multistage Microfluidic Platform for the Continuous Synthesis of III-V Core/Shell Quantum Dots. *Angewandte Chemie International Edition* **2018**, *57* (34), 10915-10918.
 116. Vikram, A.; Kumar, V.; Ramesh, U.; Balakrishnan, K.; Oh, N.; Deshpande, K.; Ewers, T.; Trefonas, P.; Shim, M.; Kenis, P. J. A., A Millifluidic Reactor System for Multistep Continuous Synthesis of InP/ZnSeS Nanoparticles. *ChemNanoMat* **2018**, *4* (9), 943-953.
 117. Lignos, I.; Mo, Y.; Carayannopoulos, L.; Ginterseder, M.; Bawendi, M. G.; Jensen, K. F., A high-temperature continuous stirred-tank reactor cascade for the multistep synthesis of InP/ZnS quantum dots. *Reaction Chemistry & Engineering* **2021**, *6* (3), 459-464.
 118. Okamoto, A.; Toda, S.; Hirakawa, M.; Bai, H.; Tanaka, M.; Seino, S.; Nakagawa, T.; Murakami, H., Narrowing of the Particle Size Distribution of InP Quantum Dots for Green



- Light Emission by Synthesis in Micro-Flow Reactor. *ChemistrySelect* **2022**, 7 (6), e202104215.
119. Kim, Y.; Choi, H.; Lee, Y.; Koh, W.-k.; Cho, E.; Kim, T.; Kim, H.; Kim, Y.-H.; Jeong, H. Y.; Jeong, S., Tailored growth of single-crystalline InP tetrapods. *Nature Communications* **2021**, 12 (1), 4454.
 120. Yoo, H.; Lee, K.-S.; Nahm, S.; Hwang, G. W.; Kim, S., Predicting ligand-dependent nanocrystal shapes of InP quantum dots and their electronic structures. *Applied Surface Science* **2022**, 578, 151972.
 121. Micic, O. I.; Sprague, J. R.; Curtis, C. J.; Jones, K. M.; Machol, J. L.; Nozik, A. J.; Giessen, H.; Fluegel, B.; Mohs, G.; Peyghambarian, N., Synthesis and Characterization of InP, GaP, and GaInP2 Quantum Dots. *The Journal of Physical Chemistry* **1995**, 99 (19), 7754-7759.
 122. Kim, S.-W.; Zimmer, J. P.; Ohnishi, S.; Tracy, J. B.; Frangioni, J. V.; Bawendi, M. G., Engineering InAsxP1-x/InP/ZnSe III–V Alloyed Core/Shell Quantum Dots for the Near-Infrared. *Journal of the American Chemical Society* **2005**, 127 (30), 10526-10532.
 123. Joo, J.; Choi, Y.; Suh, Y.-H.; Lee, C.-L.; Bae, J.; Park, J., Synthesis and characterization of In1-xGaxP@ZnS alloy core-shell type colloidal quantum dots. *Journal of Industrial and Engineering Chemistry* **2020**, 88, 106-110.
 124. Kim, Y.; Yang, K.; Lee, S., Highly luminescent blue-emitting In1-xGaxP@ZnS quantum dots and their applications in QLEDs with inverted structure. *Journal of Materials Chemistry C* **2020**, 8 (23), 7679-7687.
 125. Leemans, J.; Dümbgen, K. C.; Minjauw, M. M.; Zhao, Q.; Vantomme, A.; Infante, I.; Detavernier, C.; Hens, Z., Acid-Base Mediated Ligand Exchange on Near-Infrared Absorbing, Indium-Based III–V Colloidal Quantum Dots. *Journal of the American Chemical Society* **2021**, 143, 4290–4301.
 126. Yarema, M.; Kovalenko, M. V., Colloidal Synthesis of InSb Nanocrystals with Controlled Polymorphism Using Indium and Antimony Amides. *Chemistry of Materials* **2013**, 25 (9), 1788-1792.
 127. Koh, S.; Kim, W. D.; Bae, W. K.; Lee, Y. K.; Lee, D. C., Controlling Ion-Exchange Balance and Morphology in Cation Exchange from Cu3-xP Nanoplatelets into InP Crystals. *Chemistry of Materials* **2019**, 31 (6), 1990-2001.
 128. Stone, D.; Koley, S.; Remennik, S.; Asor, L.; Panfil, Y. E.; Naor, T.; Banin, U., Luminescent Anisotropic Wurtzite InP Nanocrystals. *Nano Letters* **2021**, 21 (23), 10032-10039.
 129. Shan, X.; Li, B.; Ji, B., Synthesis of Wurtzite In and Ga Phosphide Quantum Dots Through Cation Exchange Reactions. *Chemistry of Materials* **2021**, 33 (13), 5223-5232.
 130. Rosenberg, A. J., The oxidation of intermetallic compounds—III: The room-temperature oxidation of AIIIBv compounds. *Journal of Physics and Chemistry of Solids* **1960**, 14, 175-180.
 131. Hollinger, G.; Bergignat, E.; Joseph, J.; Robach, Y., On the nature of oxides on InP surfaces. *Journal of Vacuum Science & Technology A* **1985**, 3 (6), 2082-2088.
 132. Mičić, O. I.; Sprague, J.; Lu, Z.; Nozik, A. J., Highly efficient band-edge emission from InP quantum dots. *Applied Physics Letters* **1996**, 68 (22), 3150-3152.
 133. Cros-Gagneux, A.; Delpech, F.; Nayral, C.; Cornejo, A.; Coppel, Y.; Chaudret, B., Surface chemistry of InP quantum dots: a comprehensive study. *Journal of the American Chemical Society* **2010**, 132 (51), 18147-18157.
 134. Cossairt, B. M.; Stein, J. L.; Holden, W. M.; Seidler, G. T., 4-1: Invited Paper: Role of Phosphorus Oxidation in Controlling the Luminescent Properties of Indium Phosphide Quantum Dots. **2018**, 49 (1), 21-24.
 135. Clarke, M. T.; Viscomi, F. N.; Chamberlain, T. W.; Hondow, N.; Adawi, A. M.; Sturge, J.; Erwin, S. C.; Bouillard, J.-S. G.; Tamang, S.; Stasiuk, G. J., Synthesis of super bright indium phosphide colloidal quantum dots through thermal diffusion. *Communications Chemistry* **2019**, 2 (1), 36.
 136. Vikram, A.; Zahid, A.; Bhargava, S. S.; Jang, H.; Sutrisno, A.; Khare, A.; Trefonas, P.; Shim,

- M.; Kenis, P. J. A., Unraveling the Origin of Interfacial Oxidation of InP-Based Quantum Dots: Implications for Bioimaging and Optoelectronics. *ACS Applied Nano Materials* **2020**, *3* (12), 12325-12333.
137. Yang, W.; Yang, Y.; Kaledin, A. L.; He, S.; Jin, T.; McBride, J. R.; Lian, T., Surface passivation extends single and biexciton lifetimes of InP quantum dots. *Chemical Science* **2020**, *11* (22), 5779-5789.
138. Pu, Y.-C.; Fan, H.-C.; Chang, J.-C.; Chen, Y.-H.; Tseng, S.-W., Effects of Interfacial Oxidative Layer Removal on Charge Carrier Recombination Dynamics in InP/ZnSexS1-x Core/Shell Quantum Dots. *The Journal of Physical Chemistry Letters* **2021**, 7194-7200.
139. Chen, G.; Visbeck, S. B.; Law, D. C.; Hicks, R. F., Structure-sensitive oxidation of the indium phosphide (001) surface. *Journal of Applied Physics* **2002**, *91* (11), 9362-9367.
140. Santosh, K.; Wang, W.; Dong, H.; Xiong, K.; Longo, R. C.; Wallace, R. M.; Cho, K. J. J. o. A. P., First principles study on InP (001)-(2 × 4) surface oxidation. **2013**, *113* (10), 103705.
141. May, M. M.; Lewerenz, H.-J.; Hannappel, T., Optical in Situ Study of InP(100) Surface Chemistry: Dissociative Adsorption of Water and Oxygen. *The Journal of Physical Chemistry C* **2014**, *118* (33), 19032-19041.
142. Ruiz Alvarado, I. A.; Karmo, M.; Runge, E.; Schmidt, W. G., InP and AlInP(001)(2 × 4) Surface Oxidation from Density Functional Theory. *ACS Omega* **2021**, *6* (9), 6297-6304.
143. Zhang, X.; Ogitsu, T.; Wood, B. C.; Pham, T. A.; Ptasinska, S., Oxidation-Induced Polymerization of InP Surface and Implications for Optoelectronic Applications. *The Journal of Physical Chemistry C* **2019**, *123* (51), 30893-30902.
144. Wood, B. C.; Schwegler, E.; Choi, W. I.; Ogitsu, T., Surface Chemistry of GaP(001) and InP(001) in Contact with Water. *The Journal of Physical Chemistry C* **2014**, *118* (2), 1062-1070.
145. Ramasamy, P.; Kim, B.; Lee, M.-S.; Lee, J.-S., Beneficial effects of water in the colloidal synthesis of InP/ZnS core-shell quantum dots for optoelectronic applications. *Nanoscale* **2016**, *8* (39), 17159-17168.
146. Vikram, A.; Zahid, A.; Bhargava, S. S.; Keating, L. P.; Sutrisno, A.; Khare, A.; Trefonas, P.; Shim, M.; Kenis, P. J. A., Mechanistic Insights into Size-Focused Growth of Indium Phosphide Nanocrystals in the Presence of Trace Water. *Chemistry of Materials* **2020**, *32* (8), 3577-3584.
147. Baquero, E. A.; Ojo, W.-S.; Coppel, Y.; Chaudret, B.; Urbaszek, B.; Nayral, C.; Delpech, F., Identifying short surface ligands on metal phosphide quantum dots. *Physical Chemistry Chemical Physics* **2016**, *18* (26), 17330-17334.
148. Tomaselli, M.; Yarger, J. L.; Jr., M. B.; Havlin, R. H.; deGraw, D.; Pines, A.; Alivisatos, A. P., NMR study of InP quantum dots: Surface structure and size effects. *The Journal of Chemical Physics* **1999**, *110* (18), 8861-8864.
149. Stein, J. L.; Holden, W. M.; Venkatesh, A.; Mundy, M. E.; Rossini, A. J.; Seidler, G. T.; Cossairt, B. M., Probing surface defects of InP quantum dots using phosphorus Ka and Kβ x-ray emission spectroscopy. *Chemistry of Materials* **2018**, *30* (18), 6377-6388.
150. Calvin, J. J.; Swabeck, J. K.; Sedlak, A. B.; Kim, Y.; Jang, E.; Alivisatos, A. P., Thermodynamic Investigation of Increased Luminescence in Indium Phosphide Quantum Dots by Treatment with Metal Halide Salts. *Journal of the American Chemical Society* **2020**.
151. Protière, M.; Reiss, P., Amine-induced growth of an In2O3 shell on colloidal InP nanocrystals. *Chemical Communications* **2007**, (23), 2417-2419.
152. Tessier, M. D.; Baquero, E. A.; Dupont, D.; Grigel, V.; Bladt, E.; Bals, S.; Coppel, Y.; Hens, Z.; Nayral, C.; Delpech, F., Interfacial Oxidation and Photoluminescence of InP-Based Core/Shell Quantum Dots. *Chemistry of Materials* **2018**, *30* (19), 6877-6883.
153. Sadeghi, S.; Bahmani Jalali, H.; Melikov, R.; Ganesh Kumar, B.; Mohammadi Aria, M.; Ow-Yang, C. W.; Nizamoglu, S., Stokes-Shift-Engineered Indium Phosphide Quantum Dots for Efficient Luminescent Solar Concentrators. *ACS Applied Materials & Interfaces* **2018**, *10*



- (15), 12975-12982.
154. Kim, K.; Suh, Y.-H.; Kim, D.; Choi, Y.; Bang, E.; Kim, B. H.; Park, J., Zinc Oxo Clusters Improve the Optoelectronic Properties on Indium Phosphide Quantum Dots. *Chemistry of Materials* **2020**, *32* (7), 2795-2802.
 155. Granada-Ramirez, D. A.; Arias-Cerón, J. S.; Pérez-González, M.; Luna-Arias, J. P.; Cruz-Orea, A.; Rodríguez-Fragoso, P.; Herrera-Pérez, J. L.; Gómez-Herrera, M. L.; Tomás, S. A.; Vázquez-Hernández, F.; Durán-Ledezma, A. A.; Mendoza-Alvarez, J. G., Chemical synthesis and optical, structural, and surface characterization of InP-In₂O₃ quantum dots. *Applied Surface Science* **2020**, *530*, 147294.
 156. Eren, G. O.; Sadeghi, S.; Bahmani Jalali, H.; Ritter, M.; Han, M.; Baylam, I.; Melikov, R.; Onal, A.; Oz, F.; Sahin, M.; Ow-Yang, C. W.; Sennaroglu, A.; Lechner, R. T.; Nizamoglu, S., Cadmium-Free and Efficient Type-II InP/ZnO/ZnS Quantum Dots and Their Application for LEDs. *ACS Applied Materials & Interfaces* **2021**, *13*, 32022–32030.
 157. Van Avermaet, H.; Schiettecatte, P.; Hinz, S.; Giordano, L.; Ferrari, F.; Nayral, C.; Delpech, F.; Maultzsch, J.; Lange, H.; Hens, Z., Full-Spectrum InP-Based Quantum Dots with Near-Unity Photoluminescence Quantum Efficiency. *ACS Nano* **2022**.
 158. Wood, B. C.; Ogitsu, T.; Schwegler, E., Local structural models of complex oxygen-and hydroxyl-rich GaP/InP (001) surfaces. *The Journal of Chemical Physics* **2012**, *136* (6), 064705.
 159. Wood, B. C.; Schwegler, E.; Choi, W. I.; Ogitsu, T., Surface chemistry of GaP (001) and InP (001) in contact with water. *The Journal of Physical Chemistry C* **2014**, *118* (2), 1062-1070.
 160. Pham, T. A.; Zhang, X.; Wood, B. C.; Prendergast, D.; Ptasinska, S.; Ogitsu, T. J. T. J. o. P. C. L., Integrating Ab initio simulations and X-ray photoelectron spectroscopy: Toward a realistic description of oxidized solid/liquid interfaces. **2018**, *9* (1), 194-203.
 161. Zhang, X.; Pham, T. A.; Ogitsu, T.; Wood, B. C.; Ptasinska, S., Modulation of surface bonding topology: Oxygen bridges on OH-terminated InP (001). *The Journal of Physical Chemistry C* **2020**, *124* (5), 3196-3203.
 162. Ruiz Alvarado, I. A.; Karmo, M.; Runge, E.; Schmidt, W. G., InP and AlInP (001)(2× 4) Surface Oxidation from Density Functional Theory. *ACS omega* **2021**, *6* (9), 6297-6304.
 163. Berwanger, M.; Schoenhalz, A. L.; Dos Santos, C. L.; Piquini, P., Oxidation of InP nanowires: a first principles molecular dynamics study. *Physical Chemistry Chemical Physics* **2016**, *18* (45), 31101-31106.
 164. Park, N.; Beck, R. A.; Hoang, K. K.; Ladd, D. M.; Abramson, J. E.; Rivera-Maldonado, R. A.; Nguyen, H. A.; Monahan, M.; Seidler, G. T.; Toney, M. F.; Li, X.; Cossairt, B. M., Colloidal, Room-Temperature Growth of Metal Oxide Shells on InP Quantum Dots. *Inorganic Chemistry* **2023**, *62* (17), 6674-6687.
 165. Gatos, H. C.; Lavine, M. C., Characteristics of the {111} surfaces of the III-V intermetallic compounds. *Journal of the Electrochemical Society* **1960**, *107* (5), 427.
 166. Clark, D.; Fok, T.; Roberts, G.; Sykes, R., An investigation by electron spectroscopy for chemical analysis of chemical treatments of the (100) surface of n-type InP epitaxial layers for Langmuir film deposition. *Thin Solid Films* **1980**, *70* (2), 261-283.
 167. Adam, S.; Talapin, D.; Borchert, H.; Lobo, A.; McGinley, C.; De Castro, A.; Haase, M.; Weller, H.; Möller, T., The effect of nanocrystal surface structure on the luminescence properties: Photoemission study of HF-etched InP nanocrystals. *The Journal of chemical physics* **2005**, *123* (8), 084706.
 168. Talapin, D. V.; Gaponik, N.; Borchert, H.; Rogach, A. L.; Haase, M.; Weller, H., Etching of Colloidal InP Nanocrystals with Fluorides: Photochemical Nature of the Process Resulting in High Photoluminescence Efficiency. *The Journal of Physical Chemistry B* **2002**, *106* (49), 12659-12663.
 169. Kim, T.-G.; Zherebetsky, D.; Bekenstein, Y.; Oh, M. H.; Wang, L.-W.; Jang, E.; Alivisatos, A. P., Trap passivation in indium-based quantum dots through surface fluorination: mechanism and applications. *ACS nano* **2018**, *12* (11), 11529-11540.

170. Li, H.; Zhang, W.; Bian, Y.; Ahn, T. K.; Shen, H.; Ji, B., ZnF₂-Assisted Synthesis of Highly Luminescent InP/ZnSe/ZnS Quantum Dots for Efficient and Stable Electroluminescence. *Nano Letters* **2022**, *10*, 4067–4073.
171. Hanrahan, M. P.; Stein, J. L.; Park, N.; Cossairt, B. M.; Rossini, A. J., Elucidating the Location of Cd²⁺ in Post-synthetically Treated InP Quantum Dots Using Dynamic Nuclear Polarization ³¹P and ¹¹³Cd Solid-State NMR Spectroscopy. *The Journal of Physical Chemistry C* **2021**, *125* (5), 2956–2965.
172. Thuy, U. T. D.; Reiss, P.; Liem, N. Q., Luminescence properties of In(Zn)P alloy core/ZnS shell quantum dots. *Applied Physics Letters* **2010**, *97* (19), 193104.
173. Suh, Y.-H.; Lee, S.; Jung, S.-M.; Bang, S. Y.; Yang, J.; Fan, X.-B.; Zhan, S.; Samarakoon, C.; Jo, J.-W.; Kim, Y.; Choi, H. W.; Occhipinti, L. G.; Lee, T. H.; Shin, D.-W.; Kim, J. M., Engineering Core Size of InP Quantum Dot with Incipient ZnS for Blue Emission. *Advanced Optical Materials* **2022**, *10* (7), 2102372.
174. Mahajan, S.; Bonner, W. A.; Chin, A. K.; Miller, D. C., The characterization of highly-zinc-doped InP crystals. *Applied Physics Letters* **1979**, *35* (2), 165–168.
175. van Gorp, G. J.; van Dongen, T.; Fontijn, G. M.; Jacobs, J. M.; Tjaden, D. L. A., Interstitial and substitutional Zn in InP and InGaAsP. *Journal of Applied Physics* **1989**, *65* (2), 553–560.
176. Janke, E. M.; Williams, N. E.; She, C.; Zherebetsky, D.; Hudson, M. H.; Wang, L.; Gosztola, D. J.; Schaller, R. D.; Lee, B.; Sun, C.; Engel, G. S.; Talapin, D. V., Origin of Broad Emission Spectra in InP Quantum Dots: Contributions from Structural and Electronic Disorder. *Journal of the American Chemical Society* **2018**, *140* (46), 15791–15803.
177. Asor, L.; Liu, J.; Ossia, Y.; Tripathi, D. C.; Tessler, N.; Frenkel, A. I.; Banin, U., InAs Nanocrystals with Robust p-Type Doping. *Advanced Functional Materials* **2021**, *31* (6), 2007456.
178. Shen, C.; Zhu, Y.; Li, Z.; Li, J.; Tao, H.; Zou, J.; Xu, X.; Xu, G., Highly luminescent InP–In(Zn)P/ZnSe/ZnS core/shell/shell colloidal quantum dots with tunable emissions synthesized based on growth-doping. *Journal of Materials Chemistry C* **2021**, *9*, 9599–9609.
179. Yu, P.; Cao, S.; Shan, Y.; Bi, Y.; Hu, Y.; Zeng, R.; Zou, B.; Wang, Y.; Zhao, J., Highly efficient green InP-based quantum dot light-emitting diodes regulated by inner alloyed shell component. *Light: Science & Applications* **2022**, *11* (1), 162.
180. Dümbsgen, K. C.; Zito, J.; Infante, I.; Hens, Z., Shape, Electronic Structure, and Trap States in Indium Phosphide Quantum Dots. *Chemistry of Materials* **2021**, *33* (17), 6885–6896.
181. Fu, H.; Zunger, A., InP quantum dots: Electronic structure, surface effects, and the redshifted emission. *Physical Review B* **1997**, *56* (3), 1496–1508.
182. Stein, J. L.; Mader, E. A.; Cossairt, B. M., Luminescent InP quantum dots with tunable emission by post-synthetic modification with lewis acids. *The journal of physical chemistry letters* **2016**, *7* (7), 1315–1320.
183. Kirkwood, N.; Monchen, J. O. V.; Crisp, R. W.; Grimaldi, G.; Bergstein, H. A. C.; du Fossé, I.; van der Stam, W.; Infante, I.; Houtepen, A. J., Finding and Fixing Traps in II–VI and III–V Colloidal Quantum Dots: The Importance of Z-Type Ligand Passivation. *Journal of the American Chemical Society* **2018**, *140* (46), 15712–15723.
184. Calvin, J. J.; Swabeck, J. K.; Sedlak, A. B.; Kim, Y.; Jang, E.; Alivisatos, A. P., Thermodynamic investigation of increased luminescence in indium phosphide quantum dots by treatment with metal halide salts. *Journal of the American Chemical Society* **2020**, *142* (44), 18897–18906.
185. Hughes, K. E.; Stein, J. L.; Friedfeld, M. R.; Cossairt, B. M.; Gamelin, D. R., Effects of surface chemistry on the photophysics of colloidal InP nanocrystals. *ACS nano* **2019**, *13* (12), 14198–14207.
186. Kobayashi, T.; Aoki, K.; Yamamoto, K., Pressure dependence of optical absorption in InP at 77 K. *Physica B+C* **1986**, *139–140*, 537–540.
187. Gorczyca, I.; Christensen, N. E.; Alouani, M., Calculated optical and structural properties of



- InP under pressure. *Physical Review B* **1989**, 39 (11), 7705-7712.
188. Lee, C.-J.; Mizel, A.; Banin, U.; Cohen, M. L.; Alivisatos, A. P., Observation of pressure-induced direct-to-indirect band gap transition in InP nanocrystals. *The Journal of Chemical Physics* **2000**, 113 (5), 2016-2020.
 189. Liu, H.; Wang, Y.; Yang, X.; Zhao, X.; Wang, K.; Wu, M.; Zuo, X.; Yang, W.; Sui, Y.; Zou, B., Pressure-stimulus-responsive behaviors of core-shell InP/ZnSe nanocrystals: remarkable piezochromic luminescence and structural assembly. *Nanoscale* **2022**, 14, 7530-7537.
 190. Rafipoor, M.; Dupont, D.; Tornatzky, H.; Tessier, M. D.; Maultzsch, J.; Hens, Z.; Lange, H., Strain Engineering in InP/(Zn,Cd)Se Core/Shell Quantum Dots. *Chemistry of Materials* **2018**, 30 (13), 4393-4400.
 191. Rafipoor, M.; Tornatzky, H.; Dupont, D.; Maultzsch, J.; Tessier, M. D.; Hens, Z.; Lange, H., Strain in InP/ZnSe, S core/shell quantum dots from lattice mismatch and shell thickness—Material stiffness influence. *The Journal of Chemical Physics* **2019**, 151 (15), 154704.
 192. Kley, A.; Neugebauer, J., Atomic and electronic structure of the GaAs/ZnSe(001) interface. *Physical Review B* **1994**, 50 (12), 8616-8628.
 193. Stroppa, A.; Peressi, M., ZnSe/GaAs (001) heterostructures with defected interfaces: Structural, thermodynamic, and electronic properties. *Physical Review B* **2005**, 72 (24), 245304.
 194. Colli, A.; Carlino, E.; Pelucchi, E.; Grillo, V.; Franciosi, A., Local interface composition and native stacking fault density in ZnSe/GaAs(001) heterostructures. *Journal of Applied Physics* **2004**, 96 (5), 2592-2602.
 195. Deng, H.-X.; Luo, J.-W.; Wei, S.-H., Chemical trends of stability and band alignment of lattice-matched II-VI/III-V semiconductor interfaces. *Physical Review B* **2015**, 91 (7), 075315.
 196. Li, Y.; Hou, X.; Dai, X.; Yao, Z.; Lv, L.; Jin, Y.; Peng, X., Stoichiometry-Controlled InP-Based Quantum Dots: Synthesis, Photoluminescence, and Electroluminescence. *Journal of the American Chemical Society* **2019**, 141 (16), 6448-6452.
 197. Lovingood, D. D.; Strouse, G. F., Microwave induced in-situ active ion etching of growing InP nanocrystals. *Nano letters* **2008**, 8 (10), 3394-3397.
 198. Cho, E.; Kim, T.; Choi, S.-m.; Jang, H.; Min, K.; Jang, E., Optical Characteristics of the Surface Defects in InP Colloidal Quantum Dots for Highly Efficient Light-Emitting Applications. *ACS Applied Nano Materials* **2018**, 1 (12), 7106-7114.
 199. Kirkwood, N.; Monchen, J. O.; Crisp, R. W.; Grimaldi, G.; Bergstein, H. A.; Du Fossé, I.; Van Der Stam, W.; Infante, I.; Houtepen, A. J., Finding and fixing traps in II-VI and III-V colloidal quantum dots: the importance of Z-type ligand passivation. *Journal of the American Chemical Society* **2018**, 140 (46), 15712-15723.
 200. Hughes, K. E.; Stein, J. L.; Friedfeld, M. R.; Cossairt, B. M.; Gamelin, D. R., Effects of Surface Chemistry on the Photophysics of Colloidal InP Nanocrystals. *ACS Nano* **2019**, 13, 14198-14207.
 201. Duke, C., Semiconductor surface reconstruction: The structural chemistry of two-dimensional surface compounds. *Chemical Reviews* **1996**, 96 (4), 1237-1260.
 202. Chadi, D., Vacancy-induced 2×2 reconstruction of the Ga (111) surface of GaAs. *Physical Review Letters* **1984**, 52 (21), 1911.
 203. Chadi, D., Atomic structure of the (2×2) reconstructed GaAs $(1^{-} 1^{-} 1^{-})$ surface: A multivacancy model. *Physical Review Letters* **1986**, 57 (1), 102.
 204. Biegelsen, D.; Bringans, R.; Northrup, J.; Swartz, L., Reconstructions of GaAs $(1\ 1\ 1)$ surfaces observed by scanning tunneling microscopy. *Physical Review Letters* **1990**, 65 (4), 452.
 205. Voznyy, O.; Sargent, E., Atomistic model of fluorescence intermittency of colloidal quantum dots. *Physical Review Letters* **2014**, 112 (15), 157401.
 206. Schubert, E. F., *Doping in III-V Semiconductors*. Cambridge University Press: Cambridge, 1993.

207. Thuy, U. T. D.; Maurice, A.; Liem, N. Q.; Reiss, P., Europium doped In(Zn)P/ZnS colloidal quantum dots. *Dalton Transactions* **2013**, 42 (35), 12606-12610.
208. Xie, R.; Peng, X., Synthesis of Cu-Doped InP Nanocrystals (d-dots) with ZnSe Diffusion Barrier as Efficient and Color-Tunable NIR Emitters. *Journal of the American Chemical Society* **2009**, 131 (30), 10645-10651.
209. Knowles, K. E.; Nelson, H. D.; Kilburn, T. B.; Gamelin, D. R., Singlet-Triplet Splittings in the Luminescent Excited States of Colloidal Cu⁺:CdSe, Cu⁺:InP, and CuInS₂ Nanocrystals: Charge-Transfer Configurations and Self-Trapped Excitons. *Journal of the American Chemical Society* **2015**, 137 (40), 13138-13147.
210. Hassan, A.; Zhang, X.; Liu, C.; Snee, P. T., Electronic Structure and Dynamics of Copper-Doped Indium Phosphide Nanocrystals Studied with Time-Resolved X-ray Absorption and Large-Scale DFT Calculations. *The Journal of Physical Chemistry C* **2018**, 122 (20), 11145-11151.
211. Kim, H.-J.; Jo, J.-H.; Yoon, S.-Y.; Jo, D.-Y.; Kim, H.-S.; Park, B.; Yang, H., Emission Enhancement of Cu-Doped InP Quantum Dots through Double Shelling Scheme. **2019**, 12 (14), 2267.
212. Sadeghi, S.; Bahmani Jalali, H.; Srivastava, S. B.; Melikov, R.; Baylam, I.; Sennaroglu, A.; Nizamoglu, S., High-Performance, Large-Area, and Ecofriendly Luminescent Solar Concentrators Using Copper-Doped InP Quantum Dots. *iScience* **2020**, 23 (7), 101272.
213. Mundy, M. E.; Eagle, F. W.; Hughes, K. E.; Gamelin, D. R.; Cossairt, B. M., Synthesis and Spectroscopy of Emissive, Surface-Modified, Copper-Doped Indium Phosphide Nanocrystals. *ACS Materials Letters* **2020**, 2 (6), 576-581.
214. Kim, J.; Choi, H. S.; Wedel, A.; Yoon, S.-Y.; Jo, J.-H.; Kim, H.-M.; Han, C.-J.; Song, H.-J.; Yi, J.-M.; Jang, J.-S.; Zschiesche, H.; Lee, B.-J.; Park, K.; Yang, H., Highly luminescent near-infrared Cu-doped InP quantum dots with a Zn-Cu-In-S/ZnS double shell scheme. *Journal of Materials Chemistry C* **2021**, 9 (12), 4330-4337.
215. Prins, P. T.; Spruijt, D. A. W.; Mangnus, M. J. J.; Rabouw, F. T.; Vanmaekelbergh, D.; de Mello Donega, C.; Geiregat, P., Slow Hole Localization and Fast Electron Cooling in Cu-Doped InP/ZnSe Quantum Dots. *The Journal of Physical Chemistry Letters* **2022**, 9950-9956.
216. Koh, S.; Eom, T.; Kim, W. D.; Lee, K.; Lee, D.; Lee, Y. K.; Kim, H.; Bae, W. K.; Lee, D. C., Zinc-Phosphorus Complex Working as an Atomic Valve for Colloidal Growth of Monodisperse Indium Phosphide Quantum Dots. *Chemistry of Materials* **2017**, 29 (15), 6346-6355.
217. Asor, L.; Liu, J.; Xiang, S.; Tessler, N.; Frenkel, A. I.; Banin, U., Zn-doped P-type InAs Nanocrystal Quantum Dots. *Advanced Materials* **2022**, 35, 2208332.
218. Kirkwood, N.; De Backer, A.; Altantzis, T.; Winckelmans, N.; Longo, A.; Antolinez, F. V.; Rabouw, F. T.; De Trizio, L.; Geuchies, J. J.; Mulder, J. T.; Renaud, N.; Bals, S.; Manna, L.; Houtepen, A. J., Locating and Controlling the Zn Content in In(Zn)P Quantum Dots. *Chemistry of Materials* **2020**, 32 (1), 557-565.
219. Kim, Y.; Ham, S.; Jang, H.; Min, J. H.; Chung, H.; Lee, J.; Kim, D.; Jang, E., Bright and Uniform Green Light Emitting InP/ZnSe/ZnS Quantum Dots for Wide Color Gamut Displays. *ACS Applied Nano Materials* **2019**, 2 (3), 1496-1504.
220. Liu, P.; Lou, Y.; Ding, S.; Zhang, W.; Wu, Z.; Yang, H.; Xu, B.; Wang, K.; Sun, X. W., Green InP/ZnSeS/ZnS Core Multi-Shelled Quantum Dots Synthesized with Aminophosphine for Effective Display Applications. *Advanced Functional Materials* **2021**, 31, 2008453.
221. Zhang, W.; Tan, Y.; Duan, X.; Zhao, F.; Liu, H.; Chen, W.; Liu, P.; Liu, X.; Wang, K.; Zhang, Z.; Sun, X. W., High Quantum Yield Blue InP/ZnS/ZnS Quantum Dots Based on Bromine Passivation for Efficient Blue Light-Emitting Diodes. *Advanced Optical Materials* **2022**, 10 (15), 2200685.
222. Heun, S.; Paggel, J. J.; Sorba, L.; Rubini, S.; Franciosi, A.; Bonard, J. M.; Ganière, J. D., Interface composition and stacking fault density in II-VI/III-V heterostructures. *Applied*



- Physics Letters* **1997**, *70* (2), 237-239.
223. Colli, A.; Pelucchi, E.; Franciosi, A., Controlling the native stacking fault density in II-VI/III-V heterostructures. *Applied Physics Letters* **2003**, *83* (1), 81-83.
 224. Stroppa, A.; Peressi, M., $\text{ZnSe/GaAs}(001)$ heterostructures with defected interfaces: Structural, thermodynamic, and electronic properties. *Physical Review B* **2005**, *72* (24), 245304.
 225. Park, N.; Eagle, F. W.; DeLarme, A. J.; Monahan, M.; LoCurto, T.; Beck, R.; Li, X.; Cossairt, B. M., Tuning the interfacial stoichiometry of InP core and InP/ZnSe core/shell quantum dots. *The Journal of Chemical Physics* **2021**, *155* (8), 084701.
 226. Cho, D.-Y.; Xi, L.; Boothroyd, C.; Kardynal, B.; Lam, Y. M., The role of ion exchange in the passivation of In(Zn)P nanocrystals with ZnS. *Scientific Reports* **2016**, *6* (1), 22818.
 227. Sun, Z.; Wu, Q.; Wang, S.; Cao, F.; Wang, Y.; Li, L.; Wang, H.; Kong, L.; Yan, L.; Yang, X., Suppressing the Cation Exchange at the Core/Shell Interface of InP Quantum Dots by a Selenium Shielding Layer Enables Efficient Green Light-Emitting Diodes. *ACS Applied Materials & Interfaces* **2022**, *14*, 15401-15406.
 228. Wu, Q.; Cao, F.; Wang, S.; Wang, Y.; Sun, Z.; Feng, J.; Liu, Y.; Wang, L.; Cao, Q.; Li, Y.; Wei, B.; Wong, W.-Y.; Yang, X., Quasi-Shell-Growth Strategy Achieves Stable and Efficient Green InP Quantum Dot Light-Emitting Diodes. *Advanced Science* **2022**, *n/a* (n/a), 2200959.
 229. Park, N.; Cossairt, B., Colloidal, Room Temperature Growth of Metal Oxide Shells on InP Quantum Dots. *ChemRxiv* **2023**.
 230. Jang, Y.; Shapiro, A.; Isarov, M.; Rubin-Brusilovski, A.; Safran, A.; Budniak, A. K.; Horani, E.; Dehnel, J.; Sashchiuk, A.; Lifshitz, E., Interface control of electronic and optical properties in IV-VI and II-VI core/shell colloidal quantum dots: a review. *Chemical Communications* **2017**, *53* (6), 1002-1024.
 231. Chen, X.; Lou, Y.; Samia, A. C.; Burda, C., Coherency Strain Effects on the Optical Response of Core/Shell Heteronanostructures. *Nano Letters* **2003**, *3* (6), 799-803.
 232. Jing, L.; Kershaw, S. V.; Kipp, T.; Kalytchuk, S.; Ding, K.; Zeng, J.; Jiao, M.; Sun, X.; Mews, A.; Rogach, A. L.; Gao, M., Insight into Strain Effects on Band Alignment Shifts, Carrier Localization and Recombination Kinetics in CdTe/CdS Core/Shell Quantum Dots. *Journal of the American Chemical Society* **2015**, *137* (5), 2073-2084.
 233. Smith, A. M.; Mohs, A. M.; Nie, S., Tuning the optical and electronic properties of colloidal nanocrystals by lattice strain. *Nature Nanotechnology* **2009**, *4* (1), 56-63.
 234. Han, P.; Bester, G., Heavy strain conditions in colloidal core-shell quantum dots and their consequences on the vibrational properties from ab initio calculations. *Physical Review B* **2015**, *92* (12), 125438.
 235. Park, S.-H.; Cho, Y.-H., Strain and piezoelectric potential effects on optical properties in CdSe/CdS core/shell quantum dots. *Journal of Applied Physics* **2011**, *109* (11), 113103.
 236. Yablonovitch, E.; Kane, E., Reduction of lasing threshold current density by the lowering of valence band effective mass. *Journal of Lightwave Technology* **1986**, *4* (5), 504-506.
 237. Fan, F.; Voznyy, O.; Sabatini, R. P.; Bicanic, K. T.; Adachi, M. M.; McBride, J. R.; Reid, K. R.; Park, Y.-S.; Li, X.; Jain, A.; Quintero-Bermudez, R.; Saravanapavanantham, M.; Liu, M.; Korkusinski, M.; Hawrylak, P.; Klimov, V. I.; Rosenthal, S. J.; Hoogland, S.; Sargent, E. H., Continuous-wave lasing in colloidal quantum dot solids enabled by facet-selective epitaxy. *Nature* **2017**, *544* (7648), 75-79.
 238. Park, Y.-S.; Lim, J.; Klimov, V. I., Asymmetrically strained quantum dots with non-fluctuating single-dot emission spectra and subthermal room-temperature linewidths. *Nature Materials* **2019**, *18* (3), 249-255.
 239. Wang, L.; Bai, J.; Zhang, T.; Huang, X.; Hou, T.; Xu, B.; Li, D.; Li, Q.; Jin, X.; Wang, Y.; Zhang, X.; Song, Y., Controlling the emission linewidths of alloy quantum dots with asymmetric strain. *Journal of Colloid and Interface Science* **2022**, *624*, 287-295.
 240. Song, Y.; Liu, R.; Wang, Z.; Xu, H.; Ma, Y.; Fan, F.; Voznyy, O.; Du, J., Enhanced emission

- directivity from asymmetrically strained colloidal quantum dots. *Science Advances* **8** (8), eabl8219.
241. Díaz, J. G.; Bryant, G. W.; Jaskólski, W.; Zielinski, M., Theory of InP nanocrystals under pressure. *Physical Review B* **2007**, *75* (24), 245433.
 242. Frederick, M. T.; Amin, V. A.; Cass, L. C.; Weiss, E. A., A Molecule to Detect and Perturb the Confinement of Charge Carriers in Quantum Dots. *Nano Letters* **2011**, *11* (12), 5455-5460.
 243. Harrison, W. A.; Tersoff, J., Tight-binding theory of heterojunction band lineups and interface dipoles. *Journal of Vacuum Science & Technology B: Microelectronics Processing and Phenomena* **1986**, *4* (4), 1068-1073.
 244. Jeong, B. G.; Chang, J. H.; Hahm, D.; Rhee, S.; Park, M.; Lee, S.; Kim, Y.; Shin, D.; Park, J. W.; Lee, C.; Lee, D. C.; Park, K.; Hwang, E.; Bae, W. K., Interface polarization in heterovalent core-shell nanocrystals. *Nature Materials* **2021**, *21*, 246-252.
 245. Hahm, D.; Chang, J. H.; Jeong, B. G.; Park, P.; Kim, J.; Lee, S.; Choi, J.; Kim, W. D.; Rhee, S.; Lim, J.; Lee, D. C.; Lee, C.; Char, K.; Bae, W. K., Design Principle for Bright, Robust, and Color-Pure InP/ZnSe_{1-x}/ZnS Heterostructures. *Chemistry of Materials* **2019**, *31* (9), 3476-3484.
 246. Yang, Y.; Li, J.; Li, J.; Huang, J.; Li, Q.; Zhang, Y.; Dai, H.; Yao, J., Optical control of terahertz plasmon-induced transparency based on hybrid CsPbBr₃ quantum dot metasurfaces. *Opt. Express* **2020**, *28* (16), 24047-24055.
 247. Mulder, J. T.; Kirkwood, N.; De Trizio, L.; Li, C.; Bals, S.; Manna, L.; Houtepen, A. J., Developing Lattice Matched ZnMgSe Shells on InZnP Quantum Dots for Phosphor Applications. *ACS Applied Nano Materials* **2020**, *3* (4), 3859-3867.
 248. Orfield, N. J.; McBride, J. R.; Keene, J. D.; Davis, L. M.; Rosenthal, S. J., Correlation of Atomic Structure and Photoluminescence of the Same Quantum Dot: Pinpointing Surface and Internal Defects That Inhibit Photoluminescence. *ACS Nano* **2015**, *9* (1), 831-839.
 249. Kim, T.; Kim, K.-H.; Kim, S.; Choi, S.-M.; Jang, H.; Seo, H.-K.; Lee, H.; Chung, D.-Y.; Jang, E., Efficient and stable blue quantum dot light-emitting diode. *Nature* **2020**, *586* (7829), 385-389.
 250. Cavanaugh, P.; Jen-La Plante, I.; Ippen, C.; Ma, R.; Kelley, D. F.; Kelley, A. M., Resonance Raman Study of Shell Morphology in InP/ZnSe/ZnS Core/Shell/Shell Nanocrystals. *The Journal of Physical Chemistry C* **2021**, *125* (19), 10549-10557.
 251. Nguyen, A. T.; Jen-La Plante, I.; Ippen, C.; Ma, R.; Kelley, D. F., Extremely Slow Trap-Mediated Hole Relaxation in Room-Temperature InP/ZnSe/ZnS Quantum Dots. *The Journal of Physical Chemistry C* **2021**, *125*, 4110-4118.
 252. Cavanaugh, P.; Sun, H.; Jen-La Plante, I.; Bautista, M. J.; Ippen, C.; Ma, R.; Kelley, A. M.; Kelley, D. F., Radiative dynamics and delayed emission in pure and doped InP/ZnSe/ZnS quantum dots. *The Journal of Chemical Physics* **2021**, *155* (24), 244705.
 253. Nguyen, A. T.; Cavanaugh, P.; Plante, I. J.-L.; Ippen, C.; Ma, R.; Kelley, D. F., Auger dynamics in InP/ZnSe/ZnS quantum dots having pure and doped shells. *The Journal of Physical Chemistry C* **2021**, *125* (28), 15405-15414.
 254. Sun, H.; Cavanaugh, P.; Jen-La Plante, I.; Ippen, C.; Bautista, M.; Ma, R.; Kelley, D. F., Biexciton and trion dynamics in InP/ZnSe/ZnS quantum dots. *The Journal of Chemical Physics* **2022**, *156* (5), 054703.
 255. Hinuma, Y.; Grüneis, A.; Kresse, G.; Oba, F., Band alignment of semiconductors from density-functional theory and many-body perturbation theory. *Physical Review B* **2014**, *90* (15), 155405.
 256. Wegner, K. D.; Pouget, S.; Ling, W. L.; Carrière, M.; Reiss, P., Gallium – a versatile element for tuning the photoluminescence properties of InP quantum dots. *Chemical Communications* **2019**, *55* (11), 1663-1666.
 257. Kim, K.-H.; Jo, J.-H.; Jo, D.-Y.; Han, C.-Y.; Yoon, S.-Y.; Kim, Y.; Kim, Y.-H.; Ko, Y. H.; Kim, S. W.; Lee, C.; Yang, H., Cation-Exchange-Derived InGaP Alloy Quantum Dots toward Blue



- Emissivity. *Chemistry of Materials* **2020**, 32 (8), 3537-3544.
258. Xie, R.; Chen, K.; Chen, X.; Peng, X., InAs/InP/ZnSe core/shell/shell quantum dots as near-infrared emitters: Bright, narrow-band, non-cadmium containing, and biocompatible. *Nano Research* **2008**, 1 (6), 457-464.
 259. Saeboe, A. M.; Nikiforov, A. Y.; Toufanian, R.; Kays, J. C.; Chern, M.; Casas, J. P.; Han, K.; Piryatinski, A.; Jones, D.; Dennis, A. M., Extending the Near-Infrared Emission Range of Indium Phosphide Quantum Dots for Multiplexed In Vivo Imaging. *Nano Letters* **2021**, 21 (7), 3271-3279.
 260. Kim, S.; Park, J.; Kim, T.; Jang, E.; Jun, S.; Jang, H.; Kim, B.; Kim, S.-W., Reverse Type-I ZnSe/InP/ZnS Core/Shell/Shell Nanocrystals: Cadmium-Free Quantum Dots for Visible Luminescence. *Small* **2011**, 7 (1), 70-73.
 261. Dennis, A. M.; Mangum, B. D.; Piryatinski, A.; Park, Y.-S.; Hannah, D. C.; Casson, J. L.; Williams, D. J.; Schaller, R. D.; Htoon, H.; Hollingsworth, J. A., Suppressed Blinking and Auger Recombination in Near-Infrared Type-II InP/CdS Nanocrystal Quantum Dots. *Nano Letters* **2012**, 12 (11), 5545-5551.
 262. Son, M.; Kim, S.; Lee, Y.; Bang, J., Synthesis of near-infrared-emitting type-II In(Zn)P/ZnTe (core/shell) quantum dots. *Journal of Alloys and Compounds* **2021**, 886, 161233.
 263. Kim, T.; Won, Y.-H.; Jang, E.; Kim, D., Negative Trion Auger Recombination in Highly Luminescent InP/ZnSe/ZnS Quantum Dots. *Nano Letters* **2021**, 21, 2111-2116.
 264. Lee, S. H.; Kim, Y.; Jang, H.; Min, J. H.; Oh, J.; Jang, E.; Kim, D., The effects of discrete and gradient mid-shell structures on the photoluminescence of single InP quantum dots. *Nanoscale* **2019**, 11 (48), 23251-23258.
 265. Lee, Y.; Jo, D.-Y.; Kim, T.; Jo, J.-H.; Park, J.; Yang, H.; Kim, D., Effectual interface and defect engineering for auger recombination suppression in bright InP/ZnSeS/ZnS quantum dots. *ACS Applied Materials & Interfaces* **2022**, 14 (10), 12479-12487.
 266. Sousa Velosa, F.; Van Avermaet, H.; Schiettecatte, P.; Mingabudinova, L.; Geiregat, P.; Hens, Z., State Filling and Stimulated Emission by Colloidal InP/ZnSe Core/Shell Quantum Dots. *Advanced Optical Materials* **2022**, 10 (18), 2200328.
 267. Kelley, A. M.; Cavanaugh, P.; Sun, H.; Wang, X.; Bautista, M. J.; Jen-La Plante, I.; Ippen, C.; Kelley, D. F., Identity of the reversible hole traps in InP/ZnSe core/shell quantum dots. *The Journal of Chemical Physics* **2022**, 157 (17), 174701.
 268. Cragg, G. E.; Efros, A. L., Suppression of Auger Processes in Confined Structures. *Nano Letters* **2010**, 10 (1), 313-317.
 269. García-Santamaría, F.; Brovelli, S.; Viswanatha, R.; Hollingsworth, J. A.; Htoon, H.; Crooker, S. A.; Klimov, V. I., Breakdown of Volume Scaling in Auger Recombination in CdSe/CdS Heteronanocrystals: The Role of the Core-Shell Interface. *Nano Letters* **2011**, 11 (2), 687-693.
 270. Park, Y.-S.; Lim, J.; Makarov, N. S.; Klimov, V. I., Effect of Interfacial Alloying versus "Volume Scaling" on Auger Recombination in Compositionally Graded Semiconductor Quantum Dots. *Nano Letters* **2017**, 17 (9), 5607-5613.
 271. Lim, J.; Park, Y.-S.; Wu, K.; Yun, H. J.; Klimov, V. I., Droop-Free Colloidal Quantum Dot Light-Emitting Diodes. *Nano Letters* **2018**, 18 (10), 6645-6653.
 272. Park, Y.-S.; Bae, W. K.; Baker, T.; Lim, J.; Klimov, V. I., Effect of Auger Recombination on Lasing in Heterostructured Quantum Dots with Engineered Core/Shell Interfaces. *Nano Letters* **2015**, 15 (11), 7319-7328.
 273. Roh, J.; Park, Y.-S.; Lim, J.; Klimov, V. I., Optically pumped colloidal-quantum-dot lasing in LED-like devices with an integrated optical cavity. *Nature Communications* **2020**, 11 (1), 271.
 274. Al-Ghamdi, M. S.; Smowton, P. M.; Shutts, S.; Blood, P.; Beanland, R.; Krysa, A. B., Absorption, Gain, and Threshold in InP/AlGaInP Quantum Dot Laser Diodes. *IEEE Journal of Quantum Electronics* **2013**, 49 (4), 389-394.
 275. C. H. Shen, S. A. S., M. J. Peanasky, C. P. Kuo, OMVPE Growth of AlGaInP for High Efficiency

- Visible Light Emitting Diodes. In *High Brightness Light Emitting Diodes*, G. Stringfellow, M. C., Ed. Elsevier: 1997; pp 97-149.
276. Gessmann, T.; Schubert, E. F., High-efficiency AlGaInP light-emitting diodes for solid-state lighting applications. *Journal of Applied Physics* **2004**, *95* (5), 2203-2216.
 277. Meier, L.; Braun, C.; Hannappel, T.; Schmidt, W. G., Band Alignment at Ga_xIn_{1-x}P/Al_yIn_{1-y}P Alloy Interfaces from Hybrid Density Functional Theory Calculations. *physica status solidi (b)* **2021**, *258* (2), 2000463.
 278. Zhang, X. H.; Chua, S. J.; Fan, W. J., Band offsets at GaInP/AlGaInP(001) heterostructures lattice matched to GaAs. *Applied Physics Letters* **1998**, *73* (8), 1098-1100.
 279. Srivastava, V.; Kamysbayev, V.; Hong, L.; Dunietz, E.; Klie, R. F.; Talapin, D. V., Colloidal Chemistry in Molten Salts: Synthesis of Luminescent In_{1-x}Ga_xP and In_{1-x}Ga_xAs Quantum Dots. *Journal of the American Chemical Society* **2018**, *140* (38), 12144-12151.
 280. Kim, S.; Kim, T.; Kang, M.; Kwak, S. K.; Yoo, T. W.; Park, L. S.; Yang, I.; Hwang, S.; Lee, J. E.; Kim, S. K.; Kim, S.-W., Highly Luminescent InP/GaP/ZnS Nanocrystals and Their Application to White Light-Emitting Diodes. *Journal of the American Chemical Society* **2012**, *134* (8), 3804-3809.
 281. Lee, W. L., C.; Kim, B.; Choi, Y.; Chae, H., Synthesis of Blue-Emissive InP/GaP/ZnS Quantum Dots via Controlling the Reaction Kinetics of Shell Growth and Length of Capping Ligands. *Nanomaterials* **2020**, *10*, 2171.
 282. Xu, Y.; Lv, Y.; Wu, R.; Shen, H.; Yang, H.; Zhang, H.; Li, J.; Li, L. S., Preparation of Highly Stable and Photoluminescent Cadmium-Free InP/GaP/ZnS Core/Shell Quantum Dots and Application to Quantitative Immunoassay. *Particle & Particle Systems Characterization* **2020**, *37*, 1900441.
 283. Luo, W.; Lin, L.; Huang, J.; Lin, Q.; Lau, K. M., Electrically pumped InP/GaAsP quantum dot lasers grown on (001) Si emitting at 750 nm. *Opt. Express* **2022**, *30* (22), 40750-40755.
 284. Enright, M. J.; Jasarasaria, D.; Hanchard, M. M.; Needell, D. R.; Phelan, M. E.; Weinberg, D.; McDowell, B. E.; Hsiao, H.-W.; Akbari, H.; Kottwitz, M.; Potter, M. M.; Wong, J.; Zuo, J.-M.; Atwater, H. A.; Rabani, E.; Nuzzo, R. G., Role of Atomic Structure on Exciton Dynamics and Photoluminescence in NIR Emissive InAs/InP/ZnSe Quantum Dots. *The Journal of Physical Chemistry C* **2022**, *126* (17), 7576-7587.
 285. Wijaya, H.; Darwan, D.; Zhao, X.; Ong, E. W. Y.; Lim, K. R. G.; Wang, T.; Lim, L. J.; Khoo, K. H.; Tan, Z.-K., Efficient Near-Infrared Light-Emitting Diodes based on In(Zn)As-In(Zn)P-GaP-ZnS Quantum Dots. *Advanced Functional Materials* **2020**, *30* (4), 1906483.
 286. Zhao, X.; Lim, L. J.; Ang, S. S.; Tan, Z.-K., Efficient Short-Wave Infrared Light-Emitting Diodes based on Heavy-Metal-Free Quantum Dots. *Advanced Materials* **2022**, *34*, 2206409.
 287. Eychmüller, A.; Mews, A.; Weller, H., A quantum dot quantum well: CdS/HgS/CdS. *Chemical Physics Letters* **1993**, *208* (1), 59-62.
 288. Jeong, B. G.; Park, Y.-S.; Chang, J. H.; Cho, I.; Kim, J. K.; Kim, H.; Char, K.; Cho, J.; Klimov, V. I.; Park, P.; Lee, D. C.; Bae, W. K., Colloidal Spherical Quantum Wells with Near-Unity Photoluminescence Quantum Yield and Suppressed Blinking. *ACS Nano* **2016**, *10* (10), 9297-9305.
 289. Nagamine, G.; Jeong, B. G.; Ferreira, T. A. C.; Chang, J. H.; Park, K.; Lee, D. C.; Bae, W. K.; Padilha, L. A., Efficient Optical Gain in Spherical Quantum Wells Enabled by Engineering Biexciton Interactions. *ACS Photonics* **2020**, *7* (8), 2252-2264.
 290. Rreza, I.; Yang, H.; Hamachi, L.; Campos, M.; Hull, T.; Treadway, J.; Kurtin, J.; Chan, E. M.; Owen, J. S., Performance of Spherical Quantum Well Down Converters in Solid State Lighting. *ACS Applied Materials & Interfaces* **2021**, *13* (10), 12191-12197.
 291. Cassidy, J.; Diroll, B. T.; Mondal, N.; Berkinsky, D. B.; Zhao, K.; Harankahage, D.; Porotnikov, D.; Gately, R.; Khon, D.; Proppe, A.; Bawendi, M. G.; Schaller, R. D.; Malko, A. V.; Zamkov, M., Quantum Shells Boost the Optical Gain of Lasing Media. *ACS Nano* **2022**, *16*, 3017-3026.



292. Kim, S.; Shim, W.; Seo, H.; Hyun Bae, J.; Sung, J.; Choi, S. H.; Moon, W. K.; Lee, G.; Lee, B.; Kim, S.-W., Bandgap engineered reverse type-I CdTe/InP/ZnS core-shell nanocrystals for the near-infrared. *Chemical Communications* **2009**, (10), 1267-1269.
293. Kim, S.; Lim, Y. T.; Soltesz, E. G.; De Grand, A. M.; Lee, J.; Nakayama, A.; Parker, J. A.; Mihaljevic, T.; Laurence, R. G.; Dor, D. M.; Cohn, L. H.; Bawendi, M. G.; Frangioni, J. V., Near-infrared fluorescent type II quantum dots for sentinel lymph node mapping. *Nature Biotechnology* **2004**, *22* (1), 93-97.
294. Kim, S.; Fisher, B.; Eisler, H.-J.; Bawendi, M., Type-II Quantum Dots: CdTe/CdSe(Core/Shell) and CdSe/ZnTe(Core/Shell) Heterostructures. *Journal of the American Chemical Society* **2003**, *125* (38), 11466-11467.
295. de Mello Donegá, C., Formation of nanoscale spatially indirect excitons: Evolution of the type-II optical character of CdTe/CdSe heteronanocrystals. *Physical Review B* **2010**, *81* (16), 165303.
296. Gur, I.; Fromer, N. A.; Geier, M. L.; Alivisatos, A. P., Air-Stable All-Inorganic Nanocrystal Solar Cells Processed from Solution. *Science* **2005**, *310* (5747), 462-465.
297. Simi, N. J.; Bernadsha, S. B.; Thomas, A.; Ison, V. V., Quantum dot sensitized solar cells using type-II CdSe-Cu₂Se core-shell QDs. *Results in Optics* **2021**, *4*, 100088.
298. Li, X.; Tong, X.; Yue, S.; Liu, C.; Channa, A. I.; You, Y.; Wang, R.; Long, Z.; Zhang, Z.; Zhao, Z.; Liu, X.-F.; Wang, Z. M., Rational design of colloidal AgGaS₂/CdSeS core/shell quantum dots for solar energy conversion and light detection. *Nano Energy* **2021**, *89*, 106392.
299. Wang, Y.; Wang, Q.; Zhan, X.; Wang, F.; Safdar, M.; He, J., Visible light driven type II heterostructures and their enhanced photocatalysis properties: a review. *Nanoscale* **2013**, *5* (18), 8326-8339.
300. Zhou, Y.; Zhao, H.; Ma, D.; Rosei, F., Harnessing the properties of colloidal quantum dots in luminescent solar concentrators. *Chemical Society Reviews* **2018**, *47* (15), 5866-5890.
301. Klimov, V. I.; Ivanov, S. A.; Nanda, J.; Achermann, M.; Bezel, I.; McGuire, J. A.; Piryatinski, A., Single-exciton optical gain in semiconductor nanocrystals. *Nature* **2007**, *447* (7143), 441-446.
302. Liao, C.; Xu, R.; Xu, Y.; Zhang, C.; Xiao, M.; Zhang, L.; Lu, C.; Cui, Y.; Zhang, J., Ultralow-Threshold Single-Mode Lasing from Phase-Pure CdSe/CdS Core/Shell Quantum Dots. *The Journal of Physical Chemistry Letters* **2016**, *7* (24), 4968-4976.
303. Wu, K.; Song, N.; Liu, Z.; Zhu, H.; Rodríguez-Córdoba, W.; Lian, T., Interfacial Charge Separation and Recombination in InP and Quasi-Type II InP/CdS Core/Shell Quantum Dot-Molecular Acceptor Complexes. *The Journal of Physical Chemistry A* **2013**, *117* (32), 7561-7570.
304. Smith, C. T.; Leontiadou, M. A.; Clark, P. C. J.; Lydon, C.; Savjani, N.; Spencer, B. F.; Flavell, W. R.; O'Brien, P.; Binks, D. J., Multiple Exciton Generation and Dynamics in InP/CdS Colloidal Quantum Dots. *The Journal of Physical Chemistry C* **2017**, *121* (4), 2099-2107.
305. Karatum, O.; Jalali, H. B.; Sadeghi, S.; Melikov, R.; Srivastava, S. B.; Nizamoglu, S., Light-Emitting Devices Based on Type-II InP/ZnO Quantum Dots. *ACS Photonics* **2019**, *6* (4), 939-946.
306. Eren, G. O.; Sadeghi, S.; Bahmani Jalali, H.; Ritter, M.; Han, M.; Baylam, I.; Melikov, R.; Onal, A.; Oz, F.; Sahin, M.; Ow-Yang, C. W.; Sennaroglu, A.; Lechner, R. T.; Nizamoglu, S., Cadmium-Free and Efficient Type-II InP/ZnO/ZnS Quantum Dots and Their Application for LEDs. *ACS Applied Materials & Interfaces* **2021**, *13* (27), 32022-32030.
307. Bahmani Jalali, H.; Mohammadi Aria, M.; Dikbas, U. M.; Sadeghi, S.; Ganesh Kumar, B.; Sahin, M.; Kavakli, I. H.; Ow-Yang, C. W.; Nizamoglu, S., Effective Neural Photostimulation Using Indium-Based Type-II Quantum Dots. *ACS Nano* **2018**, *12* (8), 8104-8114.
308. Karatum, O.; Eren, G. O.; Melikov, R.; Onal, A.; Ow-Yang, C. W.; Sahin, M.; Nizamoglu, S., Quantum dot and electron acceptor nano-heterojunction for photo-induced capacitive

- charge-transfer. *Scientific Reports* **2021**, *11* (1), 2460.
309. Shimizu, K. T.; Böhmer, M.; Estrada, D.; Gangwal, S.; Grabowski, S.; Bechtel, H.; Kang, E.; Vampola, K. J.; Chamberlin, D.; Shchekin, O. B., Toward commercial realization of quantum dot based white light-emitting diodes for general illumination. *Photonics Research* **2017**, *5* (2), A1-A6.
310. Toufanian, R.; Chern, M.; Kong, V. H.; Dennis, A. M., Engineering Brightness-Matched Indium Phosphide Quantum Dots. *Chemistry of Materials* **2021**, *33*, 1964-1975.
311. Dupont, D.; Tessier, M. D.; Smet, P. F.; Hens, Z., Indium Phosphide-Based Quantum Dots with Shell-Enhanced Absorption for Luminescent Down-Conversion. *Advanced Materials* **2017**, *29* (29), 1700686.
312. Karadza, B.; Van Avermaet, H.; Mingabudinova, L.; Hens, Z.; Meuret, Y., Efficient, high-CRI white LEDs by combining traditional phosphors with cadmium-free InP/ZnSe red quantum dots. *Photonics Research* **2022**, *10* (1), 155-165.
313. Lee, S.-H.; Lee, K.-H.; Jo, J.-H.; Park, B.; Kwon, Y.; Jang, H. S.; Yang, H., Remote-type, high-color gamut white light-emitting diode based on InP quantum dot color converters. *Optical Materials Express* **2014**, *4* (7), 1297-1302.
314. Tian, W.; Dou, L.; Jin, Z.; Xiao, J.; Li, J., Full-color micro-LED displays with cadmium-free quantum dots patterned by photolithography technology. *Appl. Opt.* **2020**, *59* (35), 11112-11122.
315. Boivin, D. B.; Duffy, J. F.; Kronauer, R. E.; Czeisler, C. A., Dose-response relationships for resetting of human circadian clock by light. *Nature* **1996**, *379* (6565), 540-542.
316. Pauley, S. M., Lighting for the human circadian clock: recent research indicates that lighting has become a public health issue. *Medical Hypotheses* **2004**, *63* (4), 588-596.
317. Dong, K.; Goyarts, E. C.; Pelle, E.; Trivero, J.; Pernodet, N., Blue light disrupts the circadian rhythm and create damage in skin cells. *International Journal of Cosmetic Science* **2019**, *41* (6), 558-562.
318. Hye Oh, J.; Ji Yang, S.; Rag Do, Y., Healthy, natural, efficient and tunable lighting: four-package white LEDs for optimizing the circadian effect, color quality and vision performance. *Light: Science & Applications* **2014**, *3* (2), e141-e141.
319. Zhu, P.; Zhu, H.; Adhikari, G. C.; Thapa, S., Design of circadian white light-emitting diodes with tunable color temperature and nearly perfect color rendition. *OSA Continuum* **2019**, *2* (8), 2413-2427.
320. Lim, J.; Bae, W. K.; Lee, D.; Nam, M. K.; Jung, J.; Lee, C.; Char, K.; Lee, S., InP@ ZnSeS, core@ composition gradient shell quantum dots with enhanced stability. *Chemistry of Materials* **2011**, *23* (20), 4459-4463.
321. Lim, J.; Park, M.; Bae, W. K.; Lee, D.; Lee, S.; Lee, C.; Char, K., Highly efficient cadmium-free quantum dot light-emitting diodes enabled by the direct formation of excitons within InP@ ZnSeS quantum dots. *ACS nano* **2013**, *7* (10), 9019-9026.
322. Jo, J.-H.; Kim, J.-H.; Lee, K.-H.; Han, C.-Y.; Jang, E.-P.; Do, Y. R.; Yang, H., High-efficiency red electroluminescent device based on multishelled InP quantum dots. *Optics Letters* **2016**, *41* (17), 3984-3987.
323. Cao, F.; Wang, S.; Wang, F.; Wu, Q.; Zhao, D.; Yang, X., A layer-by-layer growth strategy for large-size InP/ZnSe/ZnS core-shell quantum dots enabling high-efficiency light-emitting diodes. *Chemistry of Materials* **2018**, *30* (21), 8002-8007.
324. Zhang, H.; Hu, N.; Zeng, Z.; Lin, Q.; Zhang, F.; Tang, A.; Jia, Y.; Li, L. S.; Shen, H.; Teng, F., High-efficiency green InP quantum dot-based electroluminescent device comprising thick-shell quantum dots. *Advanced Optical Materials* **2019**, *7* (7), 1801602.
325. Iwasaki, Y.; Motomura, G.; Ogura, K.; Tsuzuki, T., Efficient green InP quantum dot light-emitting diodes using suitable organic electron-transporting materials. *Applied Physics Letters* **2020**, *117* (11), 111104.
326. Jang, E.; Kim, Y.; Won, Y.-H.; Jang, H.; Choi, S.-M., Environmentally Friendly InP-Based



Quantum Dots for Efficient Wide Color Gamut Displays. *ACS Energy Letters* **2020**, 1316-1327.

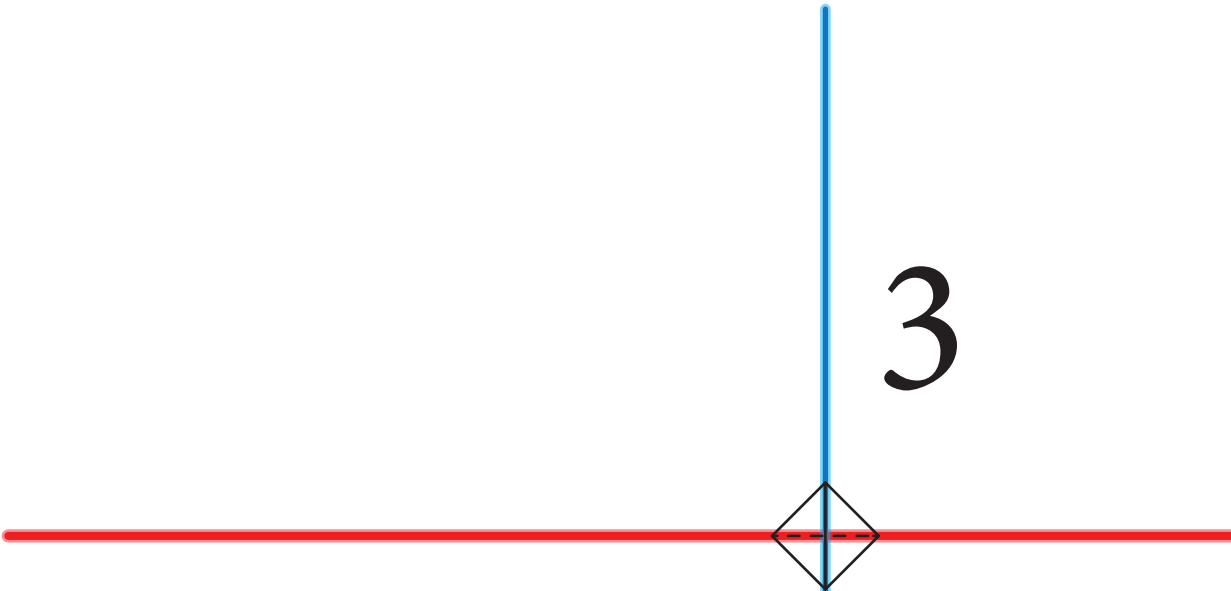
327. Chao, W.-C.; Chiang, T.-H.; Liu, Y.-C.; Huang, Z.-X.; Liao, C.-C.; Chu, C.-H.; Wang, C.-H.; Tseng, H.-W.; Hung, W.-Y.; Chou, P.-T., High efficiency green InP quantum dot light-emitting diodes by balancing electron and hole mobility. *Communications Materials* **2021**, 2 (1), 1-10.
328. Zhang, H.; Ma, X.; Lin, Q.; Zeng, Z.; Wang, H.; Li, L. S.; Shen, H.; Jia, Y.; Du, Z., High-brightness blue InP quantum dot-based electroluminescent devices: the role of shell thickness. *The Journal of Physical Chemistry Letters* **2020**, 11 (3), 960-967.
329. Mei, G.; Tan, Y.; Sun, J.; Wu, D.; Zhang, T.; Liu, H.; Liu, P.; Sun, X. W.; Choy, W. C. H.; Wang, K., Light extraction employing optical tunneling in blue InP quantum dot light-emitting diodes. *Applied Physics Letters* **2022**, 120 (9), 091101.
330. H. Sargent, E., Infrared Quantum Dots. *Advanced Materials* **2005**, 17 (5), 515-522.
331. Lu, H.; Carroll, G. M.; Neale, N. R.; Beard, M. C., Infrared Quantum Dots: Progress, Challenges, and Opportunities. *ACS Nano* **2019**, 13 (2), 939-953.
332. Thimsen, E.; Sadtler, B.; Berezin, M. Y., Shortwave-infrared (SWIR) emitters for biological imaging: a review of challenges and opportunities. *Nanophotonics* **2017**, 6 (5), 1043-1054.
333. Yun, S. H.; Kwok, S. J. J., Light in diagnosis, therapy and surgery. *Nature Biomedical Engineering* **2017**, 1 (1), 0008.
334. Yao, J.; Li, P.; Li, L.; Yang, M., Biochemistry and biomedicine of quantum dots: from biodetection to bioimaging, drug discovery, diagnostics, and therapy. *Acta Biomaterialia* **2018**, 74, 36-55.
335. Zhao, P.; Xu, Q.; Tao, J.; Jin, Z.; Pan, Y.; Yu, C.; Yu, Z., Near infrared quantum dots in biomedical applications: current status and future perspective. *WIREs Nanomedicine and Nanobiotechnology* **2018**, 10 (3), e1483.
336. Lee, G.-H.; Moon, H.; Kim, H.; Lee, G. H.; Kwon, W.; Yoo, S.; Myung, D.; Yun, S. H.; Bao, Z.; Hahn, S. K., Multifunctional materials for implantable and wearable photonic healthcare devices. *Nature Reviews Materials* **2020**, 5 (2), 149-165.
337. Teutsch, M.; Sappa, A. D.; Hammoud, R. I., Computer Vision in the Infrared Spectrum: Challenges and Approaches. *Synthesis Lectures on Computer Vision* **2021**, 10 (2), 1-138.
338. Kahn, J. M.; Barry, J. R., Wireless infrared communications. *Proceedings of the IEEE* **1997**, 85 (2), 265-298.
339. Haffouz, S.; Zeuner, K. D.; Dalacu, D.; Poole, P. J.; Lapointe, J.; Poitras, D.; Mnaymneh, K.; Wu, X.; Couillard, M.; Korkusinski, M.; Schöll, E.; Jöns, K. D.; Zwiller, V.; Williams, R. L., Bright Single InAsP Quantum Dots at Telecom Wavelengths in Position-Controlled InP Nanowires: The Role of the Photonic Waveguide. *Nano Letters* **2018**, 18 (5), 3047-3052.
340. Lu, C.-Y.; Pan, J.-W., Quantum-dot single-photon sources for the quantum internet. *Nature Nanotechnology* **2021**, 16, 1294-1296.
341. Jin, D.; Xi, P.; Wang, B.; Zhang, L.; Enderlein, J.; van Oijen, A. M., Nanoparticles for super-resolution microscopy and single-molecule tracking. *Nature Methods* **2018**, 15 (6), 415-423.
342. Chinnathambi, S.; Shirahata, N., Recent advances on fluorescent biomarkers of near-infrared quantum dots for in vitro and in vivo imaging. *Science and Technology of Advanced Materials* **2019**, 20 (1), 337-355.
343. Tong, X.; Wu, J.; Wang, Z. M., *Quantum Dot Photodetectors*. Springer: 2021.
344. Carey, G. H.; Abdelhady, A. L.; Ning, Z.; Thon, S. M.; Bakr, O. M.; Sargent, E. H., Colloidal Quantum Dot Solar Cells. *Chemical Reviews* **2015**, 115 (23), 12732-12763.
345. Leemans, J.; Pejović, V.; Georgitzikis, E.; Minjauw, M.; Siddik, A. B.; Deng, Y.-H.; Kuang, Y.; Roelkens, G.; Detavernier, C.; Lieberman, I.; Malinowski, P. E.; Cheyons, D.; Hens, Z., Colloidal III-V Quantum Dot Photodiodes for Short-Wave Infrared Photodetection. *Advanced Science* **2022**, 2200844.
346. Saeboe, A. M.; Nikiforov, A. Y.; Toufanian, R.; Kays, J. C.; Chern, M.; Casas, J. P.; Han, K.;

- Piryatinski, A.; Jones, D.; Dennis, A. M., Extending the Near-Infrared Emission Range of Indium Phosphide Quantum Dots for Multiplexed In Vivo Imaging. *Nano Letters* **2021**, *21*, 3271–3279.
347. Zhang, L.; Yang, X.-Q.; An, J.; Zhao, S.-D.; Zhao, T.-Y.; Tan, F.; Cao, Y.-C.; Zhao, Y.-D., In vivo tumor active cancer targeting and CT-fluorescence dual-modal imaging with nanoprobe based on gold nanorods and InP/ZnS quantum dots. *Journal of Materials Chemistry B* **2018**, *6* (17), 2574-2583.
348. Zaban, A.; Mičić, O. I.; Gregg, B. A.; Nozik, A. J., Photosensitization of Nanoporous TiO₂ Electrodes with InP Quantum Dots. *Langmuir* **1998**, *14* (12), 3153-3156.
349. Yang, S.; Zhao, P.; Zhao, X.; Qu, L.; Lai, X., InP and Sn:InP based quantum dot sensitized solar cells. *Journal of Materials Chemistry A* **2015**, *3* (43), 21922-21929.
350. Lai, R.; Sang, Y.; Zhao, Y.; Wu, K., Triplet Sensitization and Photon Upconversion Using InP-Based Quantum Dots. *Journal of the American Chemical Society* **2020**, *142*, 19825-19829.
351. Zhao, T.; Zhao, Q.; Lee, J.; Yang, S.; Wang, H.; Chuang, M.-Y.; He, Y.; Thompson, S. M.; Liu, G.; Oh, N.; Murray, C. B.; Kagan, C. R., Engineering the Surface Chemistry of Colloidal InP Quantum Dots for Charge Transport. *Chemistry of Materials* **2022**, *34* (18), 8306-8315.
352. Klimov, V. I.; Mikhailovsky, A. A.; Xu, S.; Malko, A.; Hollingsworth, J. A.; Leatherdale, C. A.; Eisler, H. J.; Bawendi, M. G., Optical Gain and Stimulated Emission in Nanocrystal Quantum Dots. *Science* **2000**, *290* (5490), 314-317.
353. Geuchies, J. J.; Brynjarsson, B.; Grimaldi, G.; Gudjonsdottir, S.; van der Stam, W.; Evers, W. H.; Houtepen, A. J., Quantitative Electrochemical Control over Optical Gain in Quantum-Dot Solids. *ACS Nano* **2020**, *15*, 377–386.
354. Gao, S.; Zhang, C.; Liu, Y.; Su, H.; Wei, L.; Huang, T.; Dellas, N.; Shang, S.; Mohnney, S. E.; Wang, J.; Xu, J., Lasing from colloidal InP/ZnS quantum dots. *Opt. Express* **2011**, *19* (6), 5528-5535.
355. Chandrasekaran, V.; Tessier, M. D.; Dupont, D.; Geiregat, P.; Hens, Z.; Brainis, E., Nearly Blinking-Free, High-Purity Single-Photon Emission by Colloidal InP/ZnSe Quantum Dots. *Nano Letters* **2017**, *17* (10), 6104-6109.
356. Kim, T.; Kim, Y.; Park, S.; Park, K.; Wang, Z.; Oh, S. H.; Jeong, S.; Kim, D., Shape-Tuned Multi-photon Emitting InP Nanotetrapod. *Advanced Materials* **2022**, *34*, 2110665.
357. Senellart, P.; Solomon, G.; White, A., High-performance semiconductor quantum-dot single-photon sources. *Nature Nanotechnology* **2017**, *12* (11), 1026-1039.
358. Michler, P., *Quantum Dots for Quantum Information Technologies*. 2017.
359. Benson, O.; Santori, C.; Pelton, M.; Yamamoto, Y., Regulated and Entangled Photons from a Single Quantum Dot. *Physical Review Letters* **2000**, *84* (11), 2513-2516.
360. Schimpf, C.; Reindl, M.; Basset, F. B.; Jöns, K. D.; Trotta, R.; Rastelli, A., Quantum dots as potential sources of strongly entangled photons: Perspectives and challenges for applications in quantum networks. *Applied Physics Letters* **2021**, *118* (10), 100502.
361. Trivedi, R.; Fischer, K. A.; Vučković, J.; Müller, K., Generation of Non-Classical Light Using Semiconductor Quantum Dots. *Advanced Quantum Technologies* **2020**, *3* (1), 1900007.
362. Akopian, N.; Lindner, N. H.; Poem, E.; Berlatzky, Y.; Avron, J.; Gershoni, D.; Gerardot, B. D.; Petroff, P. M., Entangled Photon Pairs from Semiconductor Quantum Dots. *Physical Review Letters* **2006**, *96* (13), 130501.
363. Lettner, T.; Gyger, S.; Zeuner, K. D.; Schweickert, L.; Steinhauer, S.; Reuterskiöld Hedlund, C.; Stroj, S.; Rastelli, A.; Hammar, M.; Trotta, R.; Jöns, K. D.; Zwiller, V., Strain-Controlled Quantum Dot Fine Structure for Entangled Photon Generation at 1550 nm. *Nano Letters* **2021**, *21*, 10501-10506.
364. Banin, U.; Cerullo, G.; Guzelian, A. A.; Bardeen, C. J.; Alivisatos, A. P.; Shank, C. V., Quantum confinement and ultrafast dephasing dynamics in InP nanocrystals. *Physical Review B* **1997**, *55* (11), 7059-7067.
365. Ellingson, R. J.; Blackburn, J. L.; Nedeljkovic, J.; Rumbles, G.; Jones, M.; Fu, H.; Nozik, A. J.,



- Theoretical and experimental investigation of electronic structure and relaxation of colloidal nanocrystalline indium phosphide quantum dots. *Physical Review B* **2003**, *67* (7), 075308.
366. Narayanaswamy, A.; Feiner, L. F.; Meijerink, A.; van der Zaag, P. J., The Effect of Temperature and Dot Size on the Spectral Properties of Colloidal InP/ZnS Core–Shell Quantum Dots. *ACS Nano* **2009**, *3* (9), 2539-2546.
367. Huang, T.; Han, P.; Wang, X.; Feng, S.; Sun, W.; Ye, J.; Zhang, Y., Phonon induced pure dephasing process of excitonic state in colloidal semiconductor quantum dots. *Superlattices and Microstructures* **2016**, *92*, 52-59.
368. Brodu, A.; Ballottin, M. V.; Buhot, J.; Dupont, D.; Tessier, M.; Hens, Z.; Rabouw, F. T.; Christianen, P. C. M.; de Mello Donega, C.; Vanmaekelbergh, D., Exciton-phonon coupling in InP quantum dots with ZnS and (Zn, Cd) shells. *Physical Review B* **2020**, *101* (12), 125413.
369. Rainò, G.; Becker, M. A.; Bodnarchuk, M. I.; Mahr, R. F.; Kovalenko, M. V.; Stöferle, T., Superfluorescence from lead halide perovskite quantum dot superlattices. *Nature* **2018**, *563* (7733), 671-675.
370. Grim, J. Q.; Bracker, A. S.; Zalalutdinov, M.; Carter, S. G.; Kozen, A. C.; Kim, M.; Kim, C. S.; Mlack, J. T.; Yakes, M.; Lee, B.; Gammon, D., Scalable in operando strain tuning in nanophotonic waveguides enabling three-quantum-dot superradiance. *Nat Mater* **2019**, *18* (9), 963-969.





A water-free in-situ HF treatment for ultra-bright InP quantum dots

This chapter is based on: Reinout F. Ubbink, Guilherme Almeida, Hodayfa Iziyi, Indy du Fossé, Ruud Verkleij, Swapna Ganapathy, Ernst R. H. van Eck and Arjan J. Houtepen. *Chemistry of Materials*, 2022, 34.22, 10093-10103.



3.1 Introduction

Colloidal quantum dots (QDs) are promising luminescent materials for use in photonic applications such as LEDs, displays and lasers.¹⁻³ With a tunable band gap in the range of 1.3 – 3 eV, InP QDs are an ROHS-compliant alternative to traditional Cd-based QDs for visible and near-infrared applications. Core/shell InP structures have become the industry standard for light-emitting applications, but core-only QDs offer advantages such as high absorptivity of blue light and better charge carrier mobilities when used in e.g. electroluminescent devices. However, as-synthesized InP QDs invariably display low photoluminescence quantum yields (PLQYs), usually attributed to surface oxidation⁴⁻⁸, although an atomistic picture of how oxidation results in trap states is missing. Treatments of InP with hydrogen fluoride (HF) have long been used to increase its luminescence,⁹⁻¹⁵ and HF treatment is still employed in the preparation of highly luminescent core/shell InP/ZnSe/ZnS QDs.^{6, 16, 17} However, the PLQYs of HF treated core InP QDs are typically limited to <50% and the mechanisms through which HF removes or passivates electronic traps remains unclear. On one hand the removal of oxidized phosphorus and trap passivation due to surface fluorination have been suggested.^{6, 16-18} On the other hand most studies have employed aqueous HF even though water is a known source of oxidation and can also have detrimental effects on the PLQYs.¹⁹⁻²²

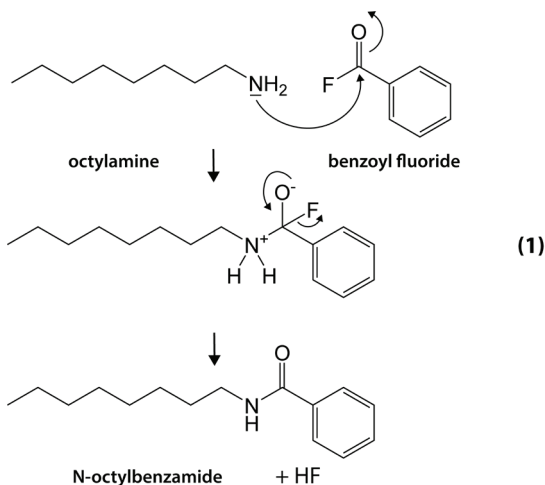
Here we study the reaction of InP QDs with anhydrous HF produced in-situ via the amidation of an acyl fluoride with an alkylamine, which also constitutes a safer alternative to handling HF directly. In this manuscript we refer to this approach as “in-situ HF treatment”. The reaction is investigated through a combination of optical and structural techniques including absorption and photoluminescence spectroscopy, x-ray photoelectron spectroscopy (XPS), x-ray diffraction (XRD) as well as solution and solid state nuclear magnetic resonance (NMR). We find that in-situ HF quickly etches InP QDs via the formation of PH_3 and InF_3 , after which InF_3 binds to the InP surface, passivating dangling phosphorus bonds and increasing quantum yield. Although PLQYs up to 70% can be reached using this in-situ HF treatment and 85% when additional ZnCl_2 Z-type ligands are added, solid-state NMR results show that oxidized phosphorus species (PO_3 and PO_4) remain present on the surface. This suggests that the presence of PO_3 and PO_4 on the InP surface does not lead to trap states, which is further supported by DFT calculations. A conversion of polyphosphates to H_xPO_4 is observed however, indicating that in-situ HF protonates and breaks up polyphosphate species, allowing for further Z-type ligand passivation of the surface. InF_3 and in-situ HF treatments of InP QDs with varying degree of oxidation are shown to support this hypothesis.

3.2 Results and discussion

3.2.1 The in-situ HF treatment

Since standard HF treatments pose a considerable safety hazard and expose the InP QDs to water, we searched for a safer method to deliver HF in an anhydrous way, which could be performed entirely within a glovebox. Herein, we exploit the amidation of acyl fluorides to generate HF in-situ, which is considered to be a rapid exothermic reaction.²³ In particular, benzoyl fluoride is reacted with octylamine in mesitylene. Benzoyl fluoride's phenyl group delocalizes electron density, which makes it highly electrophilic. When combined with octylamine, amidation takes place upon which N-octylbenzamide and

hydrogen fluoride are formed via reaction (1) depicted in Scheme 3.1 and the middle of Figure 3.1A. Although this treatment is performed post-synthesis, we will refer to it as “in-situ HF treatment” to differentiate from regular HF treatments, since the HF is not added directly to the QD solution, but is formed only after the amidation reaction.



Scheme 3.1. The amidation of octylamine and benzoyl fluoride leads to the formation of N-octylbenzamide and hydrogen fluoride (HF).

The formation of N-octylbenzamide after reaction (1) is confirmed using $^1\text{H-NMR}$ as shown in Figure A3.1 in the appendix. When the reaction occurs in the presence of InP QDs (diameter = 2.6 nm), PH_3 is formed as confirmed by solution $^{31}\text{P-NMR}$ (Figure A3.2) and InF_3 is observed as a white precipitate (confirmed by XPS in Figure A3.3). We propose that the InP nanoparticles are etched by the HF according to the simple reaction (2) in Scheme 3.2, wherein InF_3 and PH_3 are formed:



Scheme 3.2. The proposed HF etching reaction of InP.

At intermediate concentrations (around 1000 molecules of benzoyl fluoride per QD), the sample is only partially etched and highly luminescent InP QDs can be obtained (Figure 3.1B). Figure 3.1C shows the absorption spectra of the InP QDs over the course of a typical in-situ HF treatment. Strong etching immediately takes place upon injection of benzoyl fluoride into the octylamine solution containing the QDs, leading to a visible decrease in optical density (Figure 3.1C). The drop in optical density is observed to increase with increasing HF concentration, as can be seen in Figure A3.4, and is in line with a net loss of InP material in accordance with reaction (2). Furthermore, the first absorption peak is initially found slightly blue-shifted (from 476 to 463 nm) and then red-shifts over time as the treatment is continued, suggesting that the particles re-grow after the initial etching.

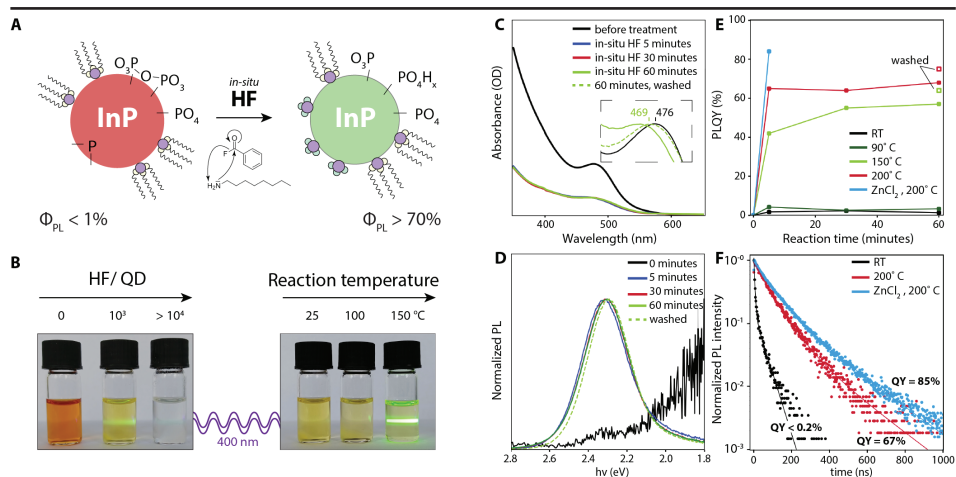


Figure 3.1. Schematic representation and optical characteristics of oxidized InP QDs treated with in-situ HF. As illustrated in panel (A), InP QDs are reacted with HF produced in-situ via the amidation reaction of benzoyl fluoride and octylamine in anhydrous conditions. (B) Photographs of InP QD samples treated with in-situ HF at various concentrations and temperatures reveal that, in certain conditions, highly luminescent samples can be obtained, however strong material losses are also apparent. An optical characterization of aliquots collected over the course of a typical in-situ HF treatment at 150 °C is provided in panels (C-E), namely, (C) absolute absorption spectra (inset shows normalized absorption spectra before and after the treatment), photoluminescence (D) spectra ($\lambda_{ex} = 387$ nm) and (E) PLQYs. In panel (E) we also report the evolution of PLQYs at other reaction temperatures. In the untreated QDs, a weak band edge luminescence and some trap-emission can be observed. Upon HF-treatment a strong drop in absorption quickly occurs and only at reaction temperatures of 150 °C or higher is a strong increase in quantum yield observed. The addition of ZnCl₂:TBP complexes during the treatment leads to even higher quantum yields. Panel (F) shows the time-resolved PL lifetime measurements of samples before and after the in-situ HF treatment. Solid lines show the bi-exponential fits.

Figures 3.1D and 3.1E show the effect of the in-situ HF treatment on the photoluminescence (PL) of the InP QDs. Running the treatment at 150 °C for up to one hour increases the PL quantum yield (PLQY) to 55% and reduces the relative intensity of red tail in the PL, attributed to trap emission.²⁴⁻²⁶ Full-width-half-maxima (FWHM) after the in-situ HF treatment were ~ 70 nm (300 meV), which is typical for InP after HF treatment^{9, 18, 27} and wider than the narrowest emission observed for core InP.¹⁷ Purification of the treated QDs leads to size-selective precipitation (as can be seen by the redshift in absorption in the inset of Figure 3.1C) and to an increase in the PLQY to 64%. Although the quick drop in absorption that happens at the start of the treatment appears temperature-independent, the effect of the HF treatment on the PLQYs appears to be strongly temperature related. As can be seen in Figure 3.1E, both at room temperature and at 90 °C, PLQYs never exceeded 5% regardless of treatment time. At 150 °C a quick rise in PLQY to ca. 40% is observed over the first few minutes and thereafter the PLQY keeps on increasing over

time. At 200 °C even higher quantum yields (>70%) are observed and PLQY evolution appears complete in under 5 minutes. This shows that there is a sizable activation energy for restructuring the surface, possibly related to the removal of the original ligands. We note that the in-situ HF treatment reproducibly results in PLQY values of ~70%, but that a further increase is possible by adding additional ZnCl₂ Z-type ligands to the treatment, which increases the PLQY further to 85%. The addition of ZnCl₂ will be discussed in more detail below. Time-resolved PL measurements (Figure 3.1F) show that longer PL lifetimes are obtained for samples with higher quantum yield. Average lifetimes (see methods for details) increased from 29 ns in untreated QDs to 107 ns after the in-situ HF treatment and 138 ns when ZnCl₂ was added during the treatment.

To disentangle the various chemical processes involved in the in-situ HF method we conducted a series of control experiments. First, the effects of treating InP QDs with either only octylamine or benzoyl fluoride were investigated and are summarized in Figures A3.5 and A3.6 in the appendix. Octylamine barely affects the QDs on its own (Figure A3.5). Benzoyl fluoride treatments, however, were often found to cause the QDs to precipitate from the mesitylene dispersion, which we assign to a reaction of benzoyl fluoride with palmitate ligands, forming anhydrides and fluoride ions (Figure A3.6). This reaction appears to be rather slow with respect to amidation and, unlike the in-situ HF reaction, does not improve the luminescence.

Furthermore, treatments similar to the in-situ HF treatment with benzoylbromide (forming in-situ HBr) and benzoylchloride (forming in-situ HCl) are reported in Figure A3.7. Neither HCl nor HBr increases the PLQY of InP QDs, and at higher concentration they quickly cause full dissolution of all nanocrystals. Treatments with organic Brønsted acids were also attempted (Figure A3.8), but only resulted in small increases in PLQY of 1-2%. It thus seems that the etching reaction (2) can be extended to a variety of protic acids, but among these, only HF has the ability to increase the PLQY of InP quantum dots.

We consider that InF₃, which forms during the HF treatment according to reaction (2), could play an active role in the trap passivation process as a Z-type ligand. Interestingly, treating InP QDs with solid InF₃ powder (hereafter referred to as “pure InF₃ treatment”), increases the PLQY up to 28 % (Figure A3.9). This observation was also reported by Kim *et al.* as well by Calvin and colleagues, although they attempted to dissolve InF₃ in TOP and tetrahydrofuran, respectively.^{18, 28} We note that after our pure InF₃ treatment, the absorption drop that is typical for the in-situ HF treatment is absent. However, the QDs precipitate out of dispersion at high concentrations of InF₃. Furthermore, this treatment also appears temperature activated; only at 150 °C is an increase in quantum yield observed.

Taken together, these observations suggest that several trap passivation mechanisms might be at play during the HF treatment, including passivation or removal of dangling bonds, as well as the potential changes in the surface oxide species. To elucidate structural changes occurring during this in situ HF treatment, we performed a series of analyses.

3.2.2 Structural analysis

To obtain further information on the processes responsible for the increase in

photoluminescence quantum yield, x-ray diffraction (XRD), x-ray photoelectron spectroscopy (XPS) and solution as well as solid state nuclear magnetic resonance (ssNMR) analyses were performed. The XRD patterns of the QDs before and after treatment are shown in Figure A3.10. In both diffractograms peaks that can be indexed to zinc blende InP are observed, as well as a peak at 20° arising from the palmitate ligands.²⁹ The latter peak is strongly reduced after the in situ HF treatment, suggesting that the in-situ HF treatment leaves the InP crystal lattice intact while inducing the removal of a large fraction of the palmitate ligands, in agreement with previous observations by Calvin *et al.* after their HF treatment.²⁹

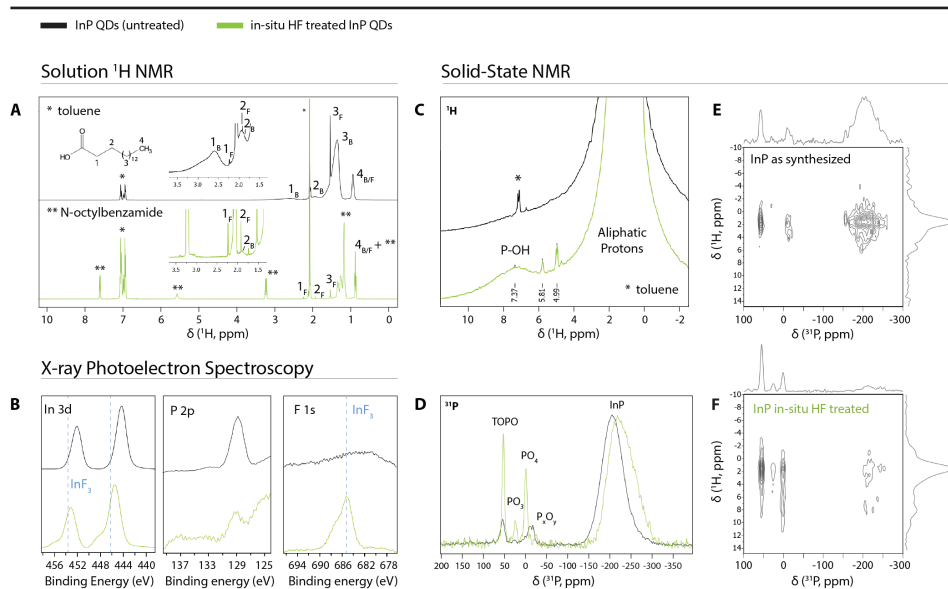
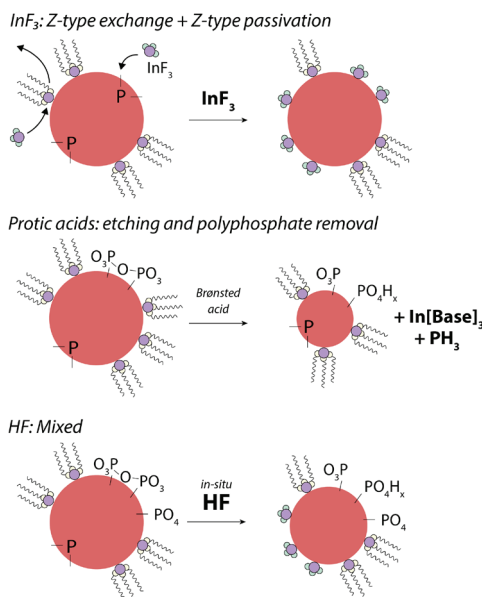


Figure 3.2. Structural characterization of oxidized InP QDs treated with in-situ HF. (A) Solution ^1H nuclear magnetic resonance (NMR) spectra of InP QD dispersions before and after treatment with in-situ HF (solvent: deuterated toluene). Peaks corresponding to palmitate ligands are labeled “B” for species bound to the nanocrystal surface and “F” for free species. A reduction of the bound palmitate fraction is observed after the treatment. (B) XPS spectra of InP QDs before and after the in-situ HF treatment. Part of a plasmon loss peak of the aluminum substrate is visible in the P2p part of the spectrum at lower binding energies. Some of the InP has been converted to InF₃ during the treatment. InF₃ reference peaks were copied from XPS data by Kim *et al.*¹⁸(C-F) Solid state NMR spectra of InP QDs before and after the in-situ HF treatment. (C) ^1H single pulse. (D) ^{31}P single pulse. Spectra are normalized to the intensity of the core InP peak to highlight relative differences between the two samples. (E) $^{31}\text{P}\{^1\text{H}\}$ cross-polarization HETCOR of the QDs before treatment. (F) $^{31}\text{P}\{^1\text{H}\}$ cross-polarization HETCOR of the QDs after the in-situ HF treatment. A CP time of 2 ms was used for both HETCORs. Average ^1H and ^{31}P spectra are plotted at the top and left sides. MAS frequency was 12.5 kHz for all measurements.

The removal of surface ligands is further confirmed using solution ^1H NMR (Figure 3.2A).

In solution NMR, ligands that are bound to the NC surface exhibit broad peaks due to their slow rotational motion (slow tumbling).^{30, 31} As shown in Figure 3.2A, such peaks are clearly seen at 2.60, 1.93, 1.35 and 0.93 ppm for the untreated sample, and belong to the α , β , remaining chain and methyl tail protons of the palmitate ligands, respectively. In addition, some free palmitate is observed as narrow lines at similar resonances. After the HF treatment the same peaks are visible but the intensity of free palmitate relative to bound palmitate has strongly increased, indicating that palmitate ligands have been removed from the InP QD surface.

XPS spectra of the samples are shown in Figure 3.2B. In the spectra before the treatment, typical InP peaks can be observed at 444.4 and 452.2 eV (In 3d) and at 128.8 eV (P 2p). After the treatment, the indium peaks have shifted to higher binding energies and a peak is observed at 485.2 eV corresponding to F1s in InF_3 . This shows that part of the InP has been converted to InF_3 , in accordance with reaction (2). This InF_3 then likely binds to the InP surface during the treatment, replacing $\text{In}(\text{PA})_3$ units. Elemental quantification of the XPS data shows that the P:In ratio is maintained at 1:2, which is typical for InP QDs of this size and shows that both the starting and the treated QDs have an indium-rich surface.³² A F:In ratio of 2:1 is also found. The unchanged P:In ratio indicates that fluoride does not replace phosphide, but rather is bound to indium atoms at the surface of the QDs.



Scheme 3.3. Reaction schemes of three different type of surface treatments of InP QDs. Z-type treatment with InF_3 results in a partial exchange of InPA_3 for InF_3 and passivation of phosphorus dangling bonds. Treatment with protic acids results in etching and polyphosphate removal. The in-situ HF treatment combines these two features.

Taken together, these results show that after the treatment, palmitate ligands have been removed from the surface and have been replaced with fluoride. Kim and colleagues



suggested that the replacement of palmitate with fluoride ions upon HF treatment takes place on the surface of the QDs as the result of a direct acid-base reaction between HF and palmitate¹⁸. We do not exclude that part of the exchange may take place during the initial etching according to this mechanism, where HF can directly protonate palmitate and form InF_3 on the surface. However, after the initial etching has finished and all the HF has reacted, the additional increase in PLQY should be attributed to the partial exchange of $\text{In}(\text{PA})_3$ with the InF_3 that was formed in a Z-type exchange mechanism, as depicted in Scheme 3.3. This hypothesis is in line with the slow and thermally activated increase in PLQY (Figure 3.1D). The results from the pure InF_3 treatment (Figure A3.9) show that while the solubility of InF_3 in mesitylene is presumably low, the exchange of $\text{In}(\text{PA})_3$ with InF_3 can still be facilitated at 150 °C. However, on these QDs, the increase in PLQY after the pure InF_3 treatment is always significantly lower than for in-situ HF treatment, pointing to additional benefits of HF on the InP surface, related to the removal of surface oxides, as discussed next.

3.3.3 Solid state NMR characterization

Solid state NMR (ssNMR) is one of the most powerful tools to investigate the atomic structure of InP QDs and has been used often to investigate oxidized phosphorus species.^{22, 32-35} Through magic angle spinning (MAS), phosphorus and hydrogen species that are in the solid phase and therefore severely broadened in solution NMR can be observed and distinguished. Single pulse spectra give quantitative information on the species that are present, while surface species can be identified by utilizing a cross-polarization (CP) pulse sequence to transfer magnetization from the hydrogen atoms in the ligands to the phosphorus species on the surface. 2D ssNMR techniques such as heteronuclear correlation (HETCOR) can also be performed to obtain information on the spatial proximity of specific species.

Figures 3.2C-F show various ssNMR measurements on InP QDs before and after the in-situ HF treatment. The ^1H solid state spectra are expected to resemble those observed in solution NMR. However, significant broadening should be expected in the solid state spectra, since molecular motion is greatly reduced in the solid state, which cannot be fully compensated for by magic angle spinning. This is indeed observed in the ^1H solid state spectrum of the untreated QDs (Figure 3.2C): apart from a small residual solvent peak, only aliphatic resonances are observed, ascribed to palmitate ligands, similar to the solution ^1H spectrum (Figure 3.2A). After the HF treatment, additional weaker resonances arise. Two sharp ones at 5.0 and 5.8 ppm (ascribed to residual trace water and N-octylbenzamide respectively) and another centered at 7.4 ppm. The latter is much broader than the other two, indicating strong bonding to the surface. Baquero and colleagues earlier observed a peak at a similar frequency, which they ascribed to P-OH with the help of Forward and Back Cross Polarization (FBCP) experiments.³⁵ This species is invisible in solution NMR due to its strong bonding to the surface and low intensity.

In Figure 3.2D, the ^{31}P ssNMR spectra before and after treatment are presented. The core phosphorus atoms in InP QDs are known to give a broad signal around -200 ppm.^{22, 32-35} This broad signal is indeed observed in the QDs before the treatment, and shifts from -198 to -223 ppm upon treatment with HF. We ascribe this shift to the exchange of InPA_3 for

InF₃, DFT studies on small InP complexes provide theoretical support for this observed frequency shift (Figure A3.11). Further downfield in Figure 3.2D resonances can be observed between -20 and +60 ppm. These peaks are enhanced when cross-polarization from hydrogen is employed (Figure A3.12), thus confirming that they are present on the surface, close to the hydrogen atoms of the palmitate ligands. These resonances have often been observed in ³¹P ssNMR spectra on InP QDs and are usually attributed to various surface-oxide complexes. Specifically, the peaks around 0 ppm and 24 ppm are assigned to P(V) (i.e. PO₄³⁻) and P(III) (i.e. PO₃³⁻) complexes^{22, 32, 33} or trioctylphosphine oxide (TOPO),³⁶ while the peak at 53 ppm is assigned either to PO₂³⁻²², or also to TOPO^{33,34}. Since trioctylphosphine (TOP), which can readily be oxidized to TOPO, is employed in our synthesis, we cannot unambiguously assign these observed surface peaks based on only the single pulse and cross-polarization spectra. 2D ³¹P{¹H} HETCOR experiments were therefore performed to help identify the nature of the surface phosphorus resonances. Using this method, phosphorus and hydrogen resonances that have the ability to cross-polarize with each other are selectively shown. In other words, only phosphorus species that are spatially close to hydrogen and vice versa appear in the spectra. A correlation peak between two specific species in the 2D spectrum indicates that those species are spatially close to one another.

³¹P{¹H} HETCOR on the as-synthesized particles (Figure 3.2E) reveals correlations between all phosphorus peaks and the aliphatic hydrogens. No strong correlations can be distinguished between any specific species. This shows that all surface phosphorus species have approximately the same spatial proximity to hydrogen atoms on the ligands.

After the in-situ HF treatment however, two specific correlations can be distinguished (Figure 3.2F). The aliphatic protons correlate with the phosphorus peak at 53 ppm, and the new hydrogen peak at 7.4 ppm that appears after the treatment correlates with the phosphorus peak at 0 ppm. The correlations become even more clear when looking at single slices of the 2D spectrum, as shown in Figure A3.13. These two correlations show spatial proximity of the aforementioned proton and phosphorus species and can help identify the nature of the phosphorus peaks.

First, the peak around 0 ppm is usually ascribed to PO₄ species.^{22,32,37} In the untreated QDs, this peak is positioned more upfield, at -15 ppm. This resonance is typically associated with pyro- or polyphosphates.^{38, 39} Polyphosphates are expected to form on InP surfaces upon oxidation at temperatures around 573 K¹⁹ and could thus be present after InP hot injection synthesis. Upon treatment the resonance narrows down and shifts to 0 ppm, nearly the same value as the chemical shift of the H₃PO₄ reference. Our results thus suggest that polyphosphate species are formed during the high-temperature synthesis, after which they are broken up and protonated during the HF treatment, resulting in H_xPO₄ species and the correlating P-OH peak in the hydrogen spectrum at 7.4 ppm. Secondly, the peak at 24 ppm is usually assigned to PO₃ species.^{22, 32, 33} DFT calculations are in line with this assignment of PO₄ and PO₃, and support the general trend that PO_x species appear at more positive chemical shifts for lower x (Figure A3.11).

Although these DFT calculations suggest that the final peak at 53 ppm may be ascribed



to PO_2 , we argue that it should instead be assigned to TOPO that is formed during the synthesis and bound to the surface of InP QDs, in line with the assignment made by Stein and colleagues.³³ The resonance at 53 ppm is almost identical to that of free TOPO (46 ppm, Figure A3.12). This assignment of TOPO is further supported by additional ssNMR spectra that were obtained after InP syntheses with and without the use of TOP (Figure A3.12). If no TOP is used in the synthesis, no peak is observed at 53 ppm.

After the in-situ HF treatment we observe an increase in the intensity of the resonances in the 60 ppm to -20 ppm range compared to the broad core phosphide peak around -200 ppm (Figure 3.2D). By normalizing both spectra to their respective InP core peak area, the integrals of each species relative to the core InP peak were calculated. Relative integrals of the PO_4 and PO_3 peaks increase from 0.05 to 0.07 and from 0.01 to 0.02 respectively after the in-situ HF treatment. This shows that, surprisingly, the in-situ HF-treatment does not result in a net decrease of the ratio of surface oxidized phosphorous/unoxidized core InP species.

In summary, from ssNMR measurements we observe TOPO, PO_3 and polyphosphate species on the as-synthesized InP surface. While the in-situ HF treatment does not remove all PO_x species, it breaks up polyphosphates into smaller H_xPO_4 species.

3.3.4 Reasons for PLQY increase after the in-situ HF treatment

Based on the aforementioned XPS and NMR results, the first clear effect of the in-situ HF treatment is fluorination of the InP surface. Fluorination of InP QDs has been reported many times, and it is widely accepted that fluorination of InP QDs leads to an increase in the luminescence efficiency^{9, 12, 18, 40, 41}. However, multiple different explanations have been given for this relationship. The first mechanism that was proposed to be responsible for the PLQY increase after the HF treatment was reported by Adam *et al.*¹², who suggested that the passivation of phosphorus dangling bonds by fluoride was the main drive of the increase in PLQY. We support a similar mechanism, but propose that InF_3 units bind the dangling phosphorus bonds as Z-type ligands rather than fluorine alone. Indeed, DFT calculations shows 2-coordinated phosphorus atoms on InP present in-gap states, and also that Z-type passivation removes these in-gap states.⁴² The efficiency of InF_3 compared to the other Z-type ligands such as $\text{In}(\text{PA})_3$ or InCl_3 may be explained by considering steric effects⁴³: bulky species may limit surface coverage of InP QDs. Exchanging part of the indium palmitate for less bulky species like InF_3 allows a higher surface coverage in Z-type ligands and thus a decrease in the number of phosphorus dangling bonds. We note that other works have also proposed that the strong electronegativity of surface fluoride ions could also be related to the high quantum yields.^{18, 44}

Despite the presence of PO_4 and PO_3 surface species after the in-situ HF treatment we observe quantum yields >50%. This seems to contradict reports claiming that removal of oxygen is the most important function of the HF treatment that leads to better luminescence properties.^{6, 16, 17} However, we do observe the removal or conversion of polyphosphates after the in-situ HF treatment. This suggests that only certain types of oxide species, i.e. polyphosphates, hamper the quantum yield. The presence of polyphosphates could introduce trap states directly (i.e. orbitals of the polyphosphate species act as traps) or

could inhibit full passivation of dangling P with Z-type ligands due to their bulky nature. In both cases, polyphosphate removal may be the second important effect of the in-situ HF treatment that leads to higher PLQYs. Compared to traditional HF treatments^{9, 11, 12, 18}, our in-situ HF treatment appears to yield QDs with higher PLQYs. This could be due to the anhydrous nature of the treatment, which limits oxidation of the QDs due to water and thus the formation of new polyphosphates.

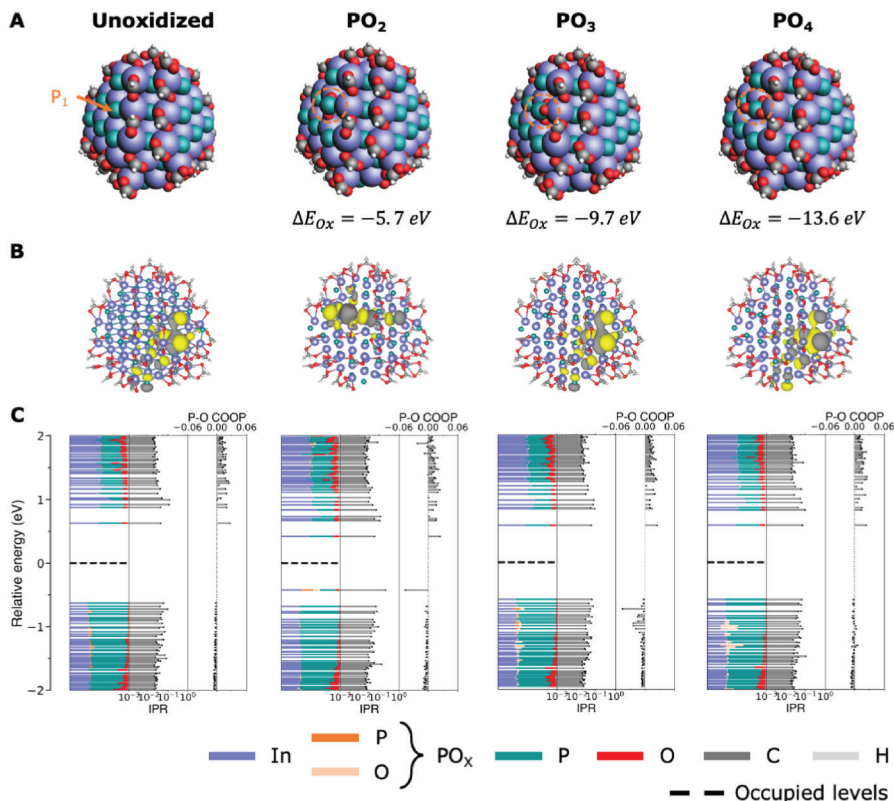


Figure 3.3. Electronic structure (DFT) calculations on InP QDs with surface PO_x^{3-} species ($x = 2, 3, 4$). (A) Structural composition of each system. (B) Contour plot of the highest occupied molecular orbital (HOMO) of each system. (C) Calculated density of states (DOS), inverse participation ratio (IPR) and crystal-orbital overlap population (COOP) of each system.

To test if various PO_x species on the surface cause in gap states we performed DFT calculations on QD model systems, replacing surface P^{3-} species with PO_x^{3-} , with $x = 2, 3, 4$ (Figure 3.3). We find that InP QDs with PO_3^{3-} or PO_4^{3-} on the surface do not present states in their bandgap, even if a large amount (6 units) of PO_4^{3-} is added. This is in line with the observation that high quantum yields can be obtained after the in-situ

HF treatments even though PO_3 or PO_4 species remain present on the surface, and with observations of high quantum yields in InP core/shell structures despite the presence of interfacial PO_4 .^{37,45} In gap states are observed for PO_2^{3-} species, and assigned to the HOMO orbital of the PO_2^{3-} complex, formed by an antibonding combination of the P 3p and O 2p atomic orbitals (Figure A3.14). However, as discussed in the section above, there is no real evidence from the ssNMR spectra that PO_2^{3-} species are present. Rather, the peak at 53 ppm is assigned to TOPO at the surface. It thus seems more likely that the polyphosphates, observed at -15 ppm in the ssNMR spectra of the untreated QDs are associated with trap formation and lower quantum yields. DFT calculations were attempted using P_2O_7 as a model polyphosphate species, but proved inconclusive in showing a correlation between these species and in-gap states (Figure A3.15). Negatively charged or neutral P_2O_7 species led to n-doping of the quantum dots and reduction of surface indium, similar to earlier results on CdX QDs.^{46,47} This resulted in many in-gap states but could be an artifact of the simulation. Additionally, P_2O_7 species appear unstable on the InP surface in simulations, leading to surface reconstructions. A clear atomistic picture of the exact species and arrangement of polyphosphates on the InP QD surface would thus be required to obtain more conclusive information from DFT simulations.

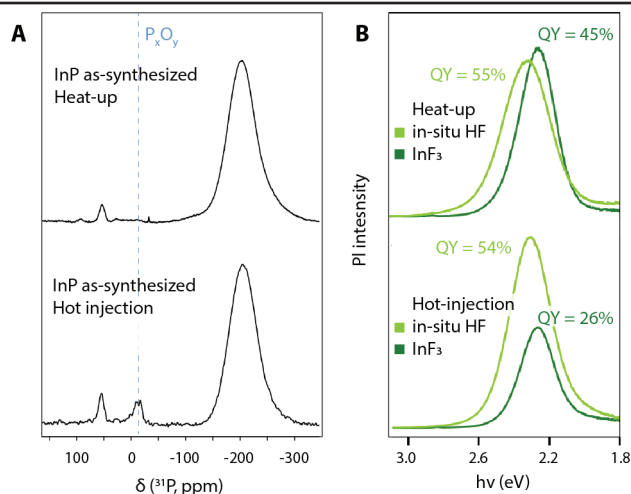


Figure 3.4. Effectiveness of the in-situ HF and of the InF_3 treatments on InP QDs with varying degree of oxidation. (A) ^{31}P ssNMR spectra and (B) photoluminescence spectra and quantum yields. QDs synthesized using the heat-up synthesis do not exhibit polyphosphate peak around -15 ppm in their ^{31}P ssNMR spectra. For these quantum dots, the InF_3 treatment is almost as effective as the in-situ HF treatment in terms of (B) photoluminescence, while a clear difference between the two treatments can be observed for the polyphosphate-containing sample synthesized via hot injection.

Nevertheless, if indeed the polyphosphate species with their peak at -15 ppm are responsible for the low PLQY of the as synthesized InP QDs, it may be expected that higher efficiencies could be reached by performing the pure InF_3 Z-type treatment on QDs without any of these species present on the surface. It is known that the use of carboxylate

precursors can lead to water formation during high temperature InP synthesis, resulting in surface oxidation.³² In an attempt to avoid water formation, we synthesized InP QDs via a heat-up method, which resulted in nearly oxide-free particles. These were then treated with anhydrous InF_3 . The results of this experiment are summarized in Figure 3.4 and are compared with those obtained with the more oxidized particles discussed so far. In Figure 3.4A, the ^{31}P ssNMR spectra of both particles are presented. It is clear that the polyphosphate peak at -15 ppm is only present in the sample synthesized *via* hot injection, and absent in the heat-up sample. When applying the pure InF_3 treatment to both particles, we observe significantly higher quantum yields for the heat-up sample, up to 45%, vs. < 28% for the hot injection sample (Figure 3.4B). These results together with the ssNMR spectra in Figure 3.2 indicate that the removal of polyphosphates in addition to Z-type ligand passivation is necessary to obtain high quantum yields in core InP QDs.

3.3.5 Overcoming the limitations of the HF treatments

The in situ HF treatment offers a safer and easy alternative to standard HF treatments on InP QDs. While it strongly enhances the PLQY it also results in a loss of InP material due to etching, and causes broadening of the optical absorption and emission, which would ideally be prevented by optimizing the reaction conditions. However, the gaseous nature of HF poses difficulties in controlling the kinetics and in the scale up of this high temperature treatment. In fact, according to our in situ HF experiments, a high concentration of HF (~1000 molecules of benzoyl fluoride per QD) is required to obtain QDs with high PLQYs, which comes at the expense of extensive etching. Therefore, the ability to regulate the activity of HF at such high temperatures could be highly desirable. We investigated whether this could be achieved by introducing the base triethylamine in our in-situ HF treatment, as it can bind to HF in a simple acid-base equilibrium and is inert towards benzoyl fluoride and therefore does not interfere with the amidation process. As shown in Figure A3.16, we find that the introduction of triethylamine allows to mitigate the loss of material while still achieving the same increase in PLQY. We expect the slight excess of octylamine in our experiments to also decrease the strength of HF in a similar fashion.

As shown in previous sections, Z-type passivation plays a key role in PLQY improvement. It was also previously shown that treatments with Z-type ligands such as CdCl_2 ⁴³ and both cadmium and zinc carboxylates⁴⁰ can increase the PLQY of InP QDs. Therefore we explored whether providing additional Z-type ligands during the HF treatment would further improve the PLQY of the InP QDs. We observe that running the in situ HF treatment in presence of additional InF_3 powder does not lead to improved PLQYs. InF_3 does not dissolve well in common solvents even when additional L-type ligands like amines or phosphines are added, potentially making the passivation of the surface by additional InF_3 more difficult. In contrast Zn salts like ZnCl_2 can be dissolved with L-type ligands.⁴³ We dissolved ZnCl_2 with tributylphosphine (TBP) in mesitylene and added this to QD dispersion before performing the in situ HF treatment as described above. This results in an increase of the PLQYs up to 85%, as shown in Figure 3.1. This PLQY value is significantly higher than the previous record for core-only InP QDs (54%⁴⁰) and comes close to the most efficient green-emitting InP-based core/shell structures²⁶ and core-only II-IV materials.^{48, 49}

The results presented in this paper demonstrate that highly efficient narrow-band InP QDs can be fabricated through appropriate surface engineering, without the need to grow inorganic shells. These results provide insight into the mechanisms of carrier trapping at the surface of InP QDs, but may also be relevant for the application of core-only InP QDs. For instance, the use of wide bandgap shells reduces the blue absorption in films of core/shell InP QDs, compared to films of core-only InP QDs of the same thickness. The brightness of a film of QDs depends on their PLQY as well as their absorbance and is thus higher for the core-only InP QDs than for core-shell QDs. Further, charge transport is more efficient in core-only QD films, since inorganic shells introduce additional tunnel barriers for electrons and holes. Efficient charge transport is important for applications such as electroluminescent QLED, photodetectors and solar cells. Our work shows that core-only (fluoride terminated) InP QDs could be a lead and cadmium free alternative for use in these applications, although their stability remains to be investigated.

3.3 Conclusion

Using a safe, water-free in-situ HF treatment the quantum yield of InP quantum dots can be increased from <0.1% to up to 70%, and up to 85% when additional Z-type ZnCl_2 ligands are provided. Optical analyses show that in-situ generated HF etches InP QDs to produce InF_3 and PH_3 , resulting in a loss of material and a minor blueshift of the optical properties. Structural analyses show that the in-situ HF treatment does not remove all oxidized phosphorus from the QD surface, but converts polyphosphate species to H_xPO_4 , and results in exchange of surface $\text{In}(\text{PA})_3$ for InF_3 . Based on these results in combination with DFT calculations, phosphorus dangling bonds and the presence of polyphosphates on the surface are suggested to be the sources of traps that cause non-radiative recombination in InP QDs. Removing these traps results in core-only InP QDs with PLQY that is comparable to the best InP/ZnSe/ZnS core/shell/shell QDs.

3.4 Methods

All procedures were executed in an inert atmosphere (Schlenk line or glovebox, $\text{H}_2\text{O} < 0.1$ ppm, $\text{O}_2 < 0.1$ ppm).

Materials

The following materials were purchased from Merck Sigma and used as received: indium acetate (99.99%), palmitic acid (PAH, 99%), trioctylphosphine (TOP, 97%), anhydrous acetone (99.8%), octylamine (99%), anhydrous hexadecane (99%), zinc chloride (ZnCl_2 , 99.999%), tributylphosphine (TBP, 97%) and triethylamine (99.5%). Tris(trimethylsilyl) phosphine (TMSP, 98%, Strem) *Caution: TMSP is a highly pyrophoric substance that can release toxic phosphine gas upon reaction with air*, anhydrous toluene (99.8%, Alfa Aesar), benzoyl fluoride (98%, TCI), didodecylamine (97%, TCI), and indium fluoride (InF_3 , 99.95%, Alfa Aesar) were used as received. 1-Octadecene (ODE, 90%, Merck Sigma) and mesitylene (98%, Merck Sigma) were degassed *in vacuo* at 100°C and room temperature respectively before being stored in a nitrogen-filled glovebox.

Hot-injection synthesis of InP QDs

The synthesis is based on that reported by Won *et al.*⁶ In a typical synthesis, indium acetate (585 mg, 2.00 mmol), palmitic acid (1535 mg, 6.00mmol), and ODE (50 mL) were added

to a 3-neck round-bottom flask. This mixture was degassed in a Schlenk line at 0.1 mbar and 120 °C for 60 minutes, during which indium palmitate ($\text{In}(\text{PA})_3$) formed and acetic acid evaporated under vacuum. Nitrogen gas was then blown over the surface through a needle (rate = 0.4 L/min, pressure ca. 1 bar) and the temperature was raised. At 280 °C, a TMSP solution (5 mL of 0.3 M in TOP) was injected, causing the temperature to drop instantly. The reaction was allowed to run at 260 °C for 12 minutes before being cooled down by air gun. At room temperature, a transparent, dark red dispersion was obtained. The quantum dots were purified by precipitation with anhydrous acetone (5 volume equivalents) and separated by centrifugation (10 minutes at 5000 rpm). After carefully discarding the supernatant, the liquid precipitate containing the QDs was diluted in anhydrous toluene (8 mL). The washing procedure was repeated before obtaining the InP QD stock solution. The concentration of this stock solution (ca. 1.37 mM) was assessed via optical absorption considering an extinction coefficient of $0.45 \text{ cm}^{-1} \mu\text{M}^{-1}$ at 330 nm, which was determined via the Maxwell-Garnett model developed for QDs.⁵⁰

Heat-up synthesis of InP QDs

This procedure is based on the work of Li *et al.*⁵¹ indium acetate (436 mg, 1.5 mmol), palmitic acid (999.9 mg, 3.9 mmol) and ODE (41.4g, 52.5 mL) were combined in a 3-neck round-bottom flask. The mixture was connected to a Schlenk line and N_2 was bubbled through the solution at a rate of 0.3 L/min. The mixture was heated at 150 °C for 30 minutes. During this time, indium palmitate ($\text{In}(\text{PA})_3$) was formed and acetic acid was evaporated away by the gas stream. Then, (i) TOP (6.23g, 7.5 mL) and (ii) TMSP (187 mg, 0.75 mmol) in ODE (9.47 g, 12 mL), were sequentially injected into the $\text{In}(\text{PA})_3$ solution and the temperature was increased to 270 °C and kept at that value for 5 minutes. The flask was then cooled down by air gun to 200 °C, after which a water bath was used to quickly bring it to room temperature, at which point a dark red InP quantum dot dispersion was obtained. The quantum dots were purified in the same way as stated above for the hot injection method.

In-situ HF treatment

Caution: since toxic phosphine gas is formed during this treatment, it should only be performed inside a glovebox or well-ventilated fumehood. In a typical treatment, the InP QD stock dispersion (30 μL , 41 nmol) was first diluted in mesitylene (820 μL) inside a glass vial. The mixture was heated to 150 °C, at which point an (i) octylamine solution (90 μL of 0.64 M in mesitylene, 58 μmol) and a (ii) benzoyl fluoride solution (90 μL of 0.45 M in mesitylene, 41 μmol) were sequentially added. The addition of the benzoyl fluoride triggers a color change in the QD solution from orange to yellow and formation of a colorless vapor can be observed. After 2 minutes, the vial caps were closed, and the mixture was allowed to react at 150 °C for another 58 minutes. For the treatment at 200 °C mesitylene was replaced by hexadecane and octylamine was replaced by didodecylamine. Additionally, the injected volumes of benzoyl fluoride and amine solutions were increased to 130 μL and the cap was added immediately after injection (of benzoyl fluoride) to minimize the effect of evaporation. The quantum dot mixture was then purified through a filter (0.2 μm PTFE), after which 10-20 volume equivalents of anhydrous acetone were added to precipitate the QDs. The mixture was centrifuged for 10 minutes at 6000 rpm, after which the yellow-green precipitate was re-dispersed in toluene.

ZnCl₂ addition

A ZnCl₂ solution (10 μL of 0.64 M, 6.4 μmol) was added to the QD dispersion before starting the in-situ HF treatment which was otherwise performed as stated above, except the added volumes of benzoyl fluoride and amine solution were increased to 150 μL and the treatment only lasted 5 minutes. The ZnCl₂ solution (0.64 M in mesitylene) was prepared by mixing ZnCl₂ (436 mg, 3.2 mmol), TBP (11.2 mmol, 2266 mg) and mesitylene (to a volume of 5 mL) under stirring until fully dissolved. TBP was necessary to dissolve the ZnCl₂ in polar solvents and accurately determine the concentration.

Pure InF₃ treatment

InF₃ (50 mg, 0.29 mmol), mesitylene (1 mL) and the InP QD stock dispersion (30 μL, 41 nmol) were combined in a glass vial. The mixture was stirred at 150 °C for one hour.

Optical characterization

UV-Vis spectra were recorded on a Perkin-Elmer Lambda 365 spectrometer. Fluorescence measurements were recorded on an Edinburgh Instruments FLS980 spectrometer equipped with a PMT 400 detector. Photoluminescence quantum yields were measured in accordance with IUPAC methodology⁵² against a coumarin 102 dye solution in ethanol (purity > 99.8%) at an excitation wavelength of 387 nm (OD at 387 nm for all samples ~0.1). Integrated emission intensities were corrected using a detector calibration curve. Measuring the coumarin 102 quantum yield in an integrating sphere in the same setup gave a value of 99%, but to calculate the quantum yield, the literature value of 95% was considered for the quantum yield of coumarin 102.⁵³ Additionally, a typical in-situ HF+ZnCl₂ treated InP sample was measured in an integrating sphere in the same instrument to have a PLQY of 84% (Figure A3.19), confirming the values obtained in the dye measurements. PL decay traces were collected on a Edinburgh Instruments Lifespec TCSPC setup with a 400 nm pulsed laser. The emission was measured at 540 nm. TRPL traces were fitted with a bi-exponential fitting curve, after which intensity-weighted average lifetimes were calculated by the following equation: $\tau_{ave} = (A_1\tau_1^2 + A_2\tau_2^2)/(A_1\tau_1 + A_2\tau_2)$, where A_n and τ_n are the n^{th} amplitude and lifetime parameters obtained from the bi-exponential fit.⁵⁴

X-Ray Diffraction (XRD)

Samples were prepared by drop casting QD dispersions on zero-diffraction silicon substrates. Diffraction patterns were recorded using a Bruker D8 Advance diffractometer (Cu K α , $\lambda = 0.15406$ nm).

X-Ray Photoelectron Spectroscopy (XPS)

Samples were prepared by drop casting the QD dispersions onto thin aluminum substrates inside a nitrogen filled glovebox and were vacuum-transferred to the instrument to avoid exposure to air. Measurements were performed under UHV (<2e-7 mbar) on a ThermoFisher K-Alpha equipped with Al K α source, radiating with an energy of 1486 eV. A flood gun (Ar) was active during all measurements to prevent charging of the samples.

Solution Nuclear Magnetic Resonance (NMR)

Solution NMR spectra were recorded on an Agilent 400-MR DD2 equipped with a 5 mm ONE NMR Probe and operating at 25 °C. ¹H NMR (399.7 MHz) spectra were collected

with a recycle delay of 1 s in deuterated toluene. Signals were referenced according to the residual methyl peak of toluene-d8 (2.08 ppm). ^{31}P NMR spectra (161.8 MHz) were collected a recycle delay of 1 s in toluene (enriched with toluene-d8). ^{31}P signals were externally referenced to H_3PO_4 .

Solid state Nuclear Magnetic Resonance (ssNMR)

Samples were loaded into 4 mm Zirconia rotors inside an nitrogen filled glovebox ($\text{O}_2 < 0.1$ ppm, $\text{H}_2\text{O} < 0.1$ ppm). Measurements were performed using an Agilent 400 MHz magnet operating at ^1H , ^{31}P and ^{13}C resonance frequencies of 399.9, 161.9 and 100.6 MHz respectively, using a CMX 4.0mm Triple Res T3 SPC400-550. MAS frequency was set to 12.5 kHz for all measurements. One-pulse ^1H MAS spectra were collected with a recycle delay (d1) of 30 s and a 2.5 μs pulse width. One-pulse ^{31}P MAS spectra were collected with a recycle delay (d1) of 10-15 s and a 3.4 μs pulse width. $^1\text{H} \rightarrow ^{31}\text{P}$ CPMAS measurements were performed with a ^1H $\pi/2$ pulse length of 3.4 μs , a CP period of 2 ms and a recycle delay (d1) of 3 s. $^1\text{H} \rightarrow ^{13}\text{C}$ CPMAS measurements were performed with a ^1H $\pi/2$ pulse length of 3.4 μs , a CP period of 1.2 ms and a recycle delay (d1) of 3 s. During all CPMAS measurements, proton decoupling was performed using the Spinal-64 decoupling sequence. $^{31}\text{P}\{^1\text{H}\}$ heteronuclear correlation (HETCOR) measurements were performed with a CP contact time of 2 ms. For each of the 512 transients in the ^1H dimension, 2048 ^{31}P scans were accumulated. A recycle delay of 3 s was applied after each scan. Spectra were referenced to external H_3PO_4 .

Additional ssNMR spectra were collected with a Bruker Ascend 500 magnet (11.7 T) equipped with a NEO console operating at ^1H and ^{31}P resonance frequencies of 500.16 and 202.45 MHz respectively, using a 4 mm three channel DVT MAS probe head from Bruker. Samples were filled into 4 mm Zirconia rotors in an argon filled glovebox ($\text{O}_2 < 0.1$ ppm, $\text{H}_2\text{O} < 0.1$ ppm). InP samples were impregnated into an Al_2O_3 filler. The MAS frequency was set to 8 kHz for all measurements. One-pulse ^{31}P MAS spectra were collected with a recycle delay of 50 s and a 5 μs pulse width. $^1\text{H} \rightarrow ^{31}\text{P}$ CPMAS measurements were performed with a ^1H $\pi/2$ pulse length of 3.85 μs and CP period of 500 μs . 30,000 scans were accumulated with a recycle delay of 2s. Proton decoupling was performed during acquisition using the Spinal-64 decoupling sequence.

Computational methods

Geometry optimization of complexes for NMR were carried out using a PBE exchange correlation functional¹ and a TZ2P basis set. The structure of H_3PO_4 , which is used as the chemical shift reference, was taken directly from the ADF database. Scalar relativistic effects were taken into account by the zeroth-order regular approximation (ZORA). All NMR calculations^{2,3} were carried out using a hybrid PBE0 exchange correlation functional⁷ and TZ2P-J basis set with the inclusion of spin-orbit coupling as implemented in the ADF software package.⁴ Calculations on QD systems were carried out at the DFT level, using a PBE exchange-correlation functional¹ and double- ζ basis set, as implemented in the CP2K quantum chemistry software package.⁵ Relativistic effects were taken into account by using effective core potentials. Geometry optimizations were performed at 0 K and in the gas phase.



To confirm the orbital localization of the trap state, the inverse participation ratio (IPR)^{6,7} of an electronic state is used. We define IPR as:

$$IPR_i = \frac{\sum_a |P_{a,i}|^4}{(\sum_a |P_{a,i}|^2)^2}$$

Where $P_{a,i}$ is the weight of a molecular orbital i on a given atom a expanded in an atomic orbital basis. The IPR can be used to estimate the number of atoms that contribute to an electronic state. The value can range from 1/number of atoms present in the system, meaning the contribution is equally distributed over all atoms, to 1, meaning that the contribution comes from 1 atom.

Crystal-orbital overlap population (COOP) is used to give insight on the bonding or anti-bonding nature of an electronic state.⁸⁻¹⁰ Positive COOP values correspond to a bonding interaction, whereas negative COOP values correspond to an anti-bonding interaction. A value close to 0 is a non-bonding interaction.

IPR & COOP calculations were carried out using the QMFlows Python package.¹¹

References

1. Wu, Z.; Liu, P.; Zhang, W.; Wang, K.; Sun, X. W., Development of InP quantum dot-based light-emitting diodes. *ACS Energy Letters* **2020**, 5 (4), 1095-1106.
2. Coe-Sullivan, S.; Liu, W.; Allen, P.; Steckel, J. S., Quantum dots for LED downconversion in display applications. *ECS Journal of Solid State Science and Technology* **2012**, 2 (2), R3026.
3. Park, Y.-S.; Roh, J.; Diroll, B. T.; Schaller, R. D.; Klimov, V. I., Colloidal quantum dot lasers. *Nature Reviews Materials* **2021**, 6 (5), 382-401.
4. Gary, D. C.; Terban, M. W.; Billinge, S. J.; Cossairt, B. M., Two-step nucleation and growth of InP quantum dots via magic-sized cluster intermediates. *Chemistry of Materials* **2015**, 27 (4), 1432-1441.
5. Tessier, M. D.; De Nolf, K.; Dupont, D.; Sinnave, D.; De Roo, J.; Hens, Z., Aminophosphines: a double role in the synthesis of colloidal indium phosphide quantum dots. *Journal of the American Chemical Society* **2016**, 138 (18), 5923-5929.
6. Won, Y.-H.; Cho, O.; Kim, T.; Chung, D.-Y.; Kim, T.; Chung, H.; Jang, H.; Lee, J.; Kim, D.; Jang, E., Highly efficient and stable InP/ZnSe/ZnS quantum dot light-emitting diodes. *Nature* **2019**, 575 (7784), 634-638.
7. Xu, Z.; Li, Y.; Li, J.; Pu, C.; Zhou, J.; Lv, L.; Peng, X., Formation of size-tunable and nearly monodisperse InP nanocrystals: Chemical reactions and controlled synthesis. *Chemistry of Materials* **2019**, 31 (14), 5331-5341.
8. Achorn, O. B.; Franke, D.; Bawendi, M. G., Seedless continuous injection synthesis of indium phosphide quantum dots as a route to large size and low size dispersity. *Chemistry of Materials* **2020**, 32 (15), 6532-6539.
9. Mičić, O. I.; Sprague, J.; Lu, Z.; Nozik, A. J., Highly efficient band-edge emission from InP quantum dots. *Applied Physics Letters* **1996**, 68 (22), 3150-3152.
10. Mičić, O. I.; Jones, K. M.; Cahill, A.; Nozik, A. J., Optical, electronic, and structural properties of uncoupled and close-packed arrays of InP quantum dots. *The Journal of Physical Chemistry B* **1998**, 102 (49), 9791-9796.
11. Talapin, D. V.; Gaponik, N.; Borchert, H.; Rogach, A. L.; Haase, M.; Weller, H., Etching of colloidal InP nanocrystals with fluorides: photochemical nature of the process resulting

- in high photoluminescence efficiency. *The Journal of Physical Chemistry B* **2002**, *106* (49), 12659-12663.
12. Adam, S.; Talapin, D.; Borchert, H.; Lobo, A.; McGinley, C.; De Castro, A.; Haase, M.; Weller, H.; Möller, T., The effect of nanocrystal surface structure on the luminescence properties: Photoemission study of HF-etched InP nanocrystals. *The Journal of chemical physics* **2005**, *123* (8), 084706.
 13. Clark, D.; Fok, T.; Roberts, G.; Sykes, R., An investigation by electron spectroscopy for chemical analysis of chemical treatments of the (100) surface of n-type InP epitaxial layers for Langmuir film deposition. *Thin Solid Films* **1980**, *70* (2), 261-283.
 14. Gu, Y.; Lin, Z.; Butera, R.; Smentkowski, V.; Waldeck, D., Preparation of self-assembled monolayers on InP. *Langmuir* **1995**, *11* (6), 1849-1851.
 15. Gatos, H. C.; Lavine, M. C., Characteristics of the {111} surfaces of the III-V intermetallic compounds. *Journal of the Electrochemical Society* **1960**, *107* (5), 427.
 16. Pu, Y.-C.; Fan, H.-C.; Chang, J.-C.; Chen, Y.-H.; Tseng, S.-W., Effects of Interfacial Oxidative Layer Removal on Charge Carrier Recombination Dynamics in InP/ZnSe_xS_{1-x} Core/Shell Quantum Dots. *The Journal of Physical Chemistry Letters* **2021**, *12*, 7194-7200.
 17. Li, H.; Zhang, W.; Bian, Y.; Ahn, T. K.; Shen, H.; Ji, B., ZnF₂-Assisted Synthesis of Highly Luminescent InP/ZnSe/ZnS Quantum Dots for Efficient and Stable Electroluminescence. *Nano Letters* **2022**.
 18. Kim, T.-G.; Zhrebetsky, D.; Bekenstein, Y.; Oh, M. H.; Wang, L.-W.; Jang, E.; Alivisatos, A. P., Trap Passivation in Indium-Based Quantum Dots through Surface Fluorination: Mechanism and Applications. *ACS Nano* **2018**, *12* (11), 11529-11540.
 19. Zhang, X.; Ogitsu, T.; Wood, B. C.; Pham, T. A.; Ptasinska, S., Oxidation-Induced Polymerization of InP Surface and Implications for Optoelectronic Applications. *The Journal of Physical Chemistry C* **2019**, *123* (51), 30893-30902.
 20. May, M. M.; Lewerenz, H.-J.; Hannappel, T., Optical in situ study of InP (100) surface chemistry: dissociative adsorption of water and oxygen. *The Journal of Physical Chemistry C* **2014**, *118* (33), 19032-19041.
 21. Wood, B. C.; Schwegler, E.; Choi, W. I.; Ogitsu, T., Surface chemistry of GaP (001) and InP (001) in contact with water. *The Journal of Physical Chemistry C* **2014**, *118* (2), 1062-1070.
 22. Cros-Gagneux, A.; Delpech, F.; Nayral, C.; Cornejo, A.; Coppel, Y.; Chaudret, B., Surface chemistry of InP quantum dots: a comprehensive study. *Journal of the American Chemical Society* **2010**, *132* (51), 18147-18157.
 23. Sonntag, N. O. V., The Reactions of Aliphatic Acid Chlorides. *Chemical Reviews* **1953**, *52* (2), 237-416.
 24. Poles, E.; Selmarten, D. C.; Mičić, O. I.; Nozik, A. J., Anti-Stokes photoluminescence in colloidal semiconductor quantum dots. *Applied physics letters* **1999**, *75* (7), 971-973.
 25. Cho, E.; Kim, T.; Choi, S.-m.; Jang, H.; Min, K.; Jang, E., Optical Characteristics of the Surface Defects in InP Colloidal Quantum Dots for Highly Efficient Light-Emitting Applications. *ACS Applied Nano Materials* **2018**, *1* (12), 7106-7114.
 26. Kim, Y.; Ham, S.; Jang, H.; Min, J. H.; Chung, H.; Lee, J.; Kim, D.; Jang, E., Bright and Uniform Green Light Emitting InP/ZnSe/ZnS Quantum Dots for Wide Color Gamut Displays. *ACS Applied Nano Materials* **2019**, *2* (3), 1496-1504.
 27. Talapin, D. V.; Gaponik, N.; Borchert, H.; Rogach, A. L.; Haase, M.; Weller, H., Etching of Colloidal InP Nanocrystals with Fluorides: Photochemical Nature of the Process Resulting in High Photoluminescence Efficiency. *The Journal of Physical Chemistry B* **2002**, *106* (49), 12659-12663.
 28. Calvin, J. J.; Swabeck, J. K.; Sedlak, A. B.; Kim, Y.; Jang, E.; Alivisatos, A. P., Thermodynamic investigation of increased luminescence in indium phosphide quantum dots by treatment with metal halide salts. *Journal of the American Chemical Society* **2020**, *142* (44), 18897-18906.

29. Calvin, J. J.; Kaufman, T. M.; Sedlak, A. B.; Crook, M. F.; Alivisatos, A. P., Observation of ordered organic capping ligands on semiconducting quantum dots via powder X-ray diffraction. *Nature communications* **2021**, *12* (1), 1-8.
30. Hens, Z.; Moreels, I.; Martins, J. C., In situ ¹H NMR study on the trioctylphosphine oxide capping of colloidal InP nanocrystals. *ChemPhysChem* **2005**, *6* (12), 2578-2584.
31. Moreels, I.; Martins, J. C.; Hens, Z., Solution NMR techniques for investigating colloidal nanocrystal ligands: a case study on trioctylphosphine oxide at InP quantum dots. *Sensors and Actuators B: Chemical* **2007**, *126* (1), 283-288.
32. Virieux, H.; Le Troedec, M.; Cros-Gagneux, A.; Ojo, W.-S.; Delpech, F.; Nayral, C.; Martinez, H.; Chaudret, B., InP/ZnS nanocrystals: coupling NMR and XPS for fine surface and interface description. *Journal of the American Chemical Society* **2012**, *134* (48), 19701-19708.
33. Stein, J. L.; Holden, W. M.; Venkatesh, A.; Mundy, M. E.; Rossini, A. J.; Seidler, G. T.; Cossairt, B. M., Probing surface defects of InP quantum dots using phosphorus K α and K β x-ray emission spectroscopy. *Chemistry of Materials* **2018**, *30* (18), 6377-6388.
34. Tomaselli, M.; Yarger, J.; Bruchez Jr, M.; Havlin, R.; DeGraw, D.; Pines, A.; Alivisatos, A., NMR study of InP quantum dots: Surface structure and size effects. *The Journal of chemical physics* **1999**, *110* (18), 8861-8864.
35. Baquero, E. A.; Ojo, W.-S.; Coppel, Y.; Chaudret, B.; Urbaszek, B.; Nayral, C.; Delpech, F., Identifying short surface ligands on metal phosphide quantum dots. *Physical Chemistry Chemical Physics* **2016**, *18* (26), 17330-17334.
36. Tomaselli, M.; Yarger, J. L.; Jr, M. B.; Havlin, R. H.; deGraw, D.; Pines, A.; Alivisatos, A. P., NMR study of InP quantum dots: Surface structure and size effects. *The Journal of Chemical Physics* **1999**, *110* (18), 8861-8864.
37. Tessier, M. D.; Baquero, E. A.; Dupont, D.; Grigel, V.; Bladt, E.; Bals, S.; Coppel, Y.; Hens, Z.; Nayral, C.; Delpech, F., Interfacial oxidation and photoluminescence of InP-based core/shell quantum dots. *Chemistry of Materials* **2018**, *30* (19), 6877-6883.
38. Cade-Menun, B. J.; Carter, M. R.; James, D. C.; Liu, C. W., Phosphorus forms and chemistry in the soil profile under long-term conservation tillage: A phosphorus-31 nuclear magnetic resonance study. *Journal of Environmental Quality* **2010**, *39* (5), 1647-1656.
39. Sannigrahi, P.; Ingall, E., Polyphosphates as a source of enhanced P fluxes in marine sediments overlain by anoxic waters: Evidence from ³¹P NMR. *Geochemical Transactions* **2005**, *6* (3), 1-8.
40. Hughes, K. E.; Stein, J. L.; Friedfeld, M. R.; Cossairt, B. M.; Gamelin, D. R., Effects of surface chemistry on the photophysics of colloidal InP nanocrystals. *ACS nano* **2019**, *13* (12), 14198-14207.
41. Lovingood, D. D.; Strouse, G. F., Microwave induced in-situ active ion etching of growing InP nanocrystals. *Nano letters* **2008**, *8* (10), 3394-3397.
42. Dümbgen, K. C.; Zito, J.; Infante, I.; Hens, Z., Shape, Electronic Structure, and Trap States in Indium Phosphide Quantum Dots. *Chemistry of Materials* **2021**, *33* (17), 6885-6896.
43. Kirkwood, N.; Monchen, J. O.; Crisp, R. W.; Grimaldi, G.; Bergstein, H. A.; Du Fossé, I.; Van Der Stam, W.; Infante, I.; Houtepen, A. J., Finding and fixing traps in II-VI and III-V colloidal quantum dots: the importance of Z-type ligand passivation. *Journal of the American Chemical Society* **2018**, *140* (46), 15712-15723.
44. Calvin, J. J.; Swabeck, J. K.; Sedlak, A. B.; Kim, Y.; Jang, E.; Alivisatos, A. P., Thermodynamic Investigation of Increased Luminescence in Indium Phosphide Quantum Dots by Treatment with Metal Halide Salts. *Journal of the American Chemical Society* **2020**.
45. Van Avermaet, H.; Schiettecatte, P.; Hinz, S.; Giordano, L.; Ferrari, F.; Nayral, C.; Delpech, F.; Maultzsch, J.; Lange, H.; Hens, Z., Full-Spectrum InP-Based Quantum Dots with Near-Unity Photoluminescence Quantum Efficiency. *ACS nano* **2022**, *16* (6), 9701-9712.
46. Du Fossé, I.; Boehme, S. C.; Infante, I.; Houtepen, A. J., Dynamic Formation of Metal-Based

- Traps in Photoexcited Colloidal Quantum Dots and Their Relevance for Photoluminescence. *Chemistry of Materials* **2021**, 33 (9), 3349-3358.
47. Du Fossé, I.; Ten Brinck, S.; Infante, I.; Houtepen, A. J., Role of surface reduction in the formation of traps in n-doped II–VI semiconductor nanocrystals: How to charge without reducing the surface. *Chemistry of Materials* **2019**, 31 (12), 4575-4583.
 48. Page, R. C.; Espinobarro-Velazquez, D.; Leontiadou, M. A.; Smith, C.; Lewis, E. A.; Haigh, S. J.; Li, C.; Radtke, H.; Pengpad, A.; Bondino, F., Near-Unity Quantum Yields from Chloride Treated CdTe Colloidal Quantum Dots. *small* **2015**, 11 (13), 1548-1554.
 49. Gao, Y.; Peng, X., Photogenerated excitons in plain core CdSe nanocrystals with unity radiative decay in single channel: the effects of surface and ligands. *Journal of the American Chemical Society* **2015**, 137 (12), 4230-4235.
 50. Hens, Z.; Moreels, I., Light absorption by colloidal semiconductor quantum dots. *Journal of Materials Chemistry* **2012**, 22 (21), 10406-10415.
 51. Li, Y.; Hou, X.; Shen, Y.; Dai, N.; Peng, X., Tuning the Reactivity of Indium Alkanoates by Tertiary Organophosphines for the Synthesis of Indium-Based Quantum Dots. *Chemistry of Materials* **2021**, 33 (23), 9348-9356.
 52. Brouwer, A. M., Standards for photoluminescence quantum yield measurements in solution (IUPAC Technical Report). *Pure and Applied Chemistry* **2011**, 83 (12), 2213-2228.
 53. Jones, G.; Jackson, W. R.; Choi, C. Y.; Bergmark, W. R., Solvent effects on emission yield and lifetime for coumarin laser dyes. Requirements for a rotatory decay mechanism. *The Journal of Physical Chemistry* **1985**, 89 (2), 294-300.
 54. Zatoryb, G.; Klak, M., On the choice of proper average lifetime formula for an ensemble of emitters showing non-single exponential photoluminescence decay. *Journal of Physics: Condensed Matter* **2020**, 32 (41), 415902.



Appendix

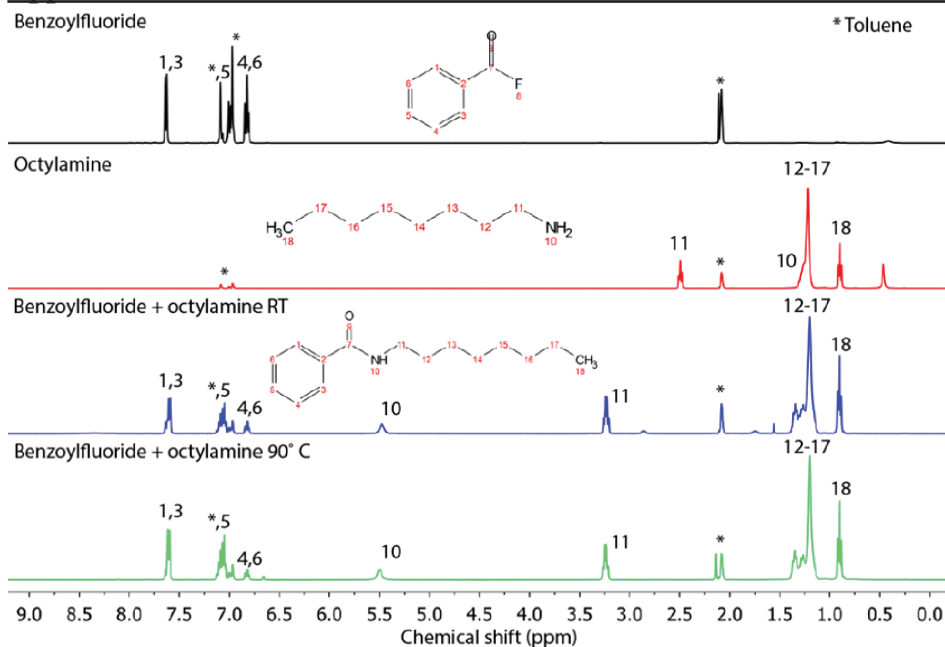


Figure A3.1. Solution ^1H spectra of the compounds used in the in-situ HF treatment, before and after their reaction. Spectra were referenced according to the residual solvent peaks of toluene- d_8 (2.08 ppm). As can be observed from the shift in peak 11 (no residual peak at 2.5 ppm after the reaction), full conversion of the amine is achieved when equimolar amounts are reacted.

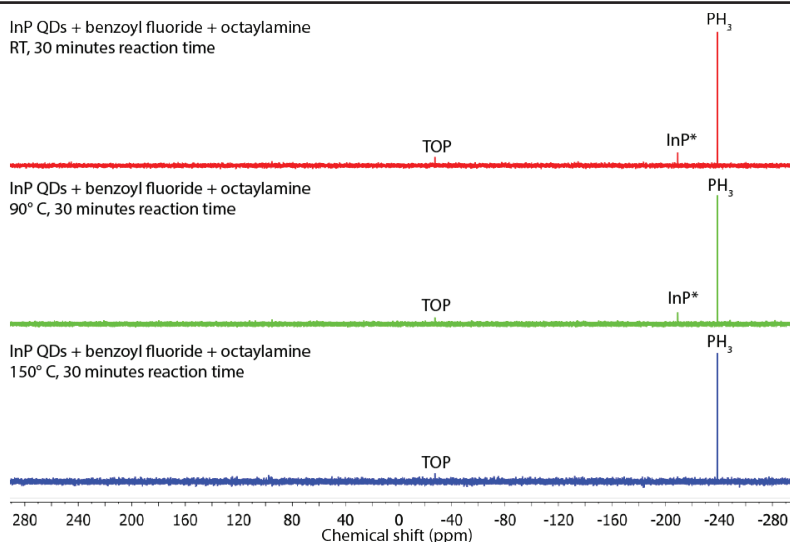


Figure A3.2. Solution ^{31}P NMR spectra of aliquots taken from treatments at different temperatures. The PH_3 peak can clearly be observed at -239 ppm. Free TOP is also present in all spectra at -29 ppm. At -210 ppm, a final peak can be observed, but only in the RT and 90°C spectra. This peak shows at the typical shift of InP (see solid state NMR spectra in Figure A3.10), and is thus ascribed to small InP clusters/complexes in solution.

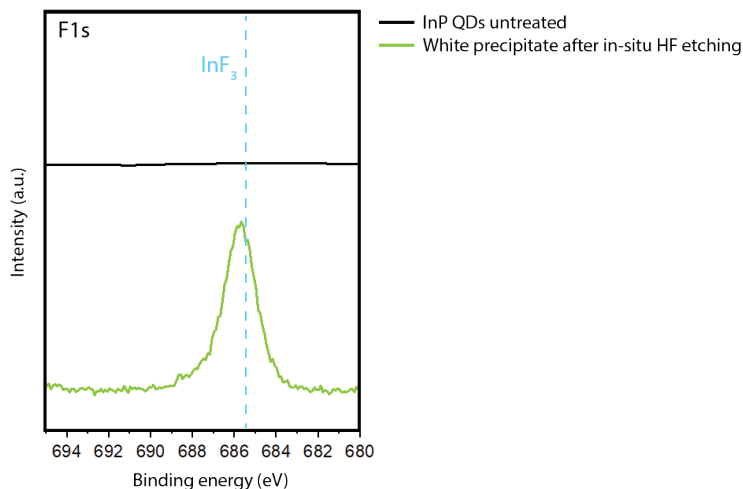


Figure A3.3. F1s XPS spectra of the as-synthesized QDs and the white powder that formed after reacting an excess of in-situ generated HF with InP QDs. All of the InP has been converted to InF_3 during the treatment.

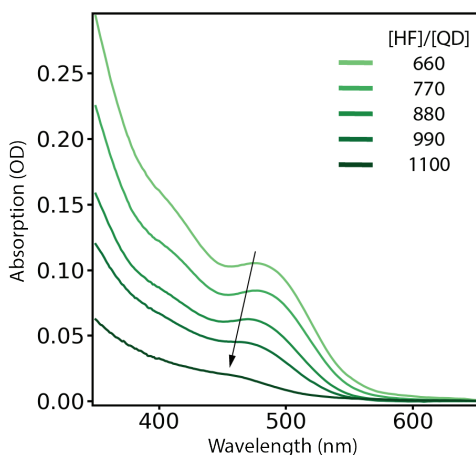


Figure A3.4. Absolute absorption spectra of InP QDs after in-situ HF etching at different concentrations. HF concentration was varied by adjusting both the amount of benzoyl fluoride and octylamine that was added while keeping their ratio consistent. At higher HF concentrations, the first absorption maximum is blueshifted further and a larger drop in the absorption is observed. The highest quantum yields were observed for HF concentrations between 850-1000 molar equivalents.

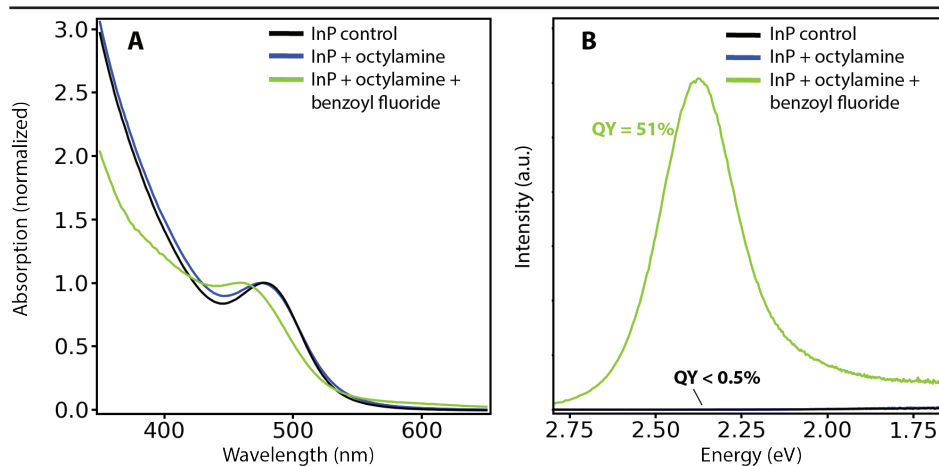


Figure A3.5. Normalized absorption (A) and PL emission (B) spectra of InP treated with octylamine and a combination of octylamine and benzoyl fluoride. $[\text{benzoyl fluoride}]/[\text{QD}] = 1400$, $[\text{octylamine}]/[\text{QD}] = 2000$. Treatments were performed at 150°C for 180 minutes in mesitylene, similar to the in-situ HF treatment.

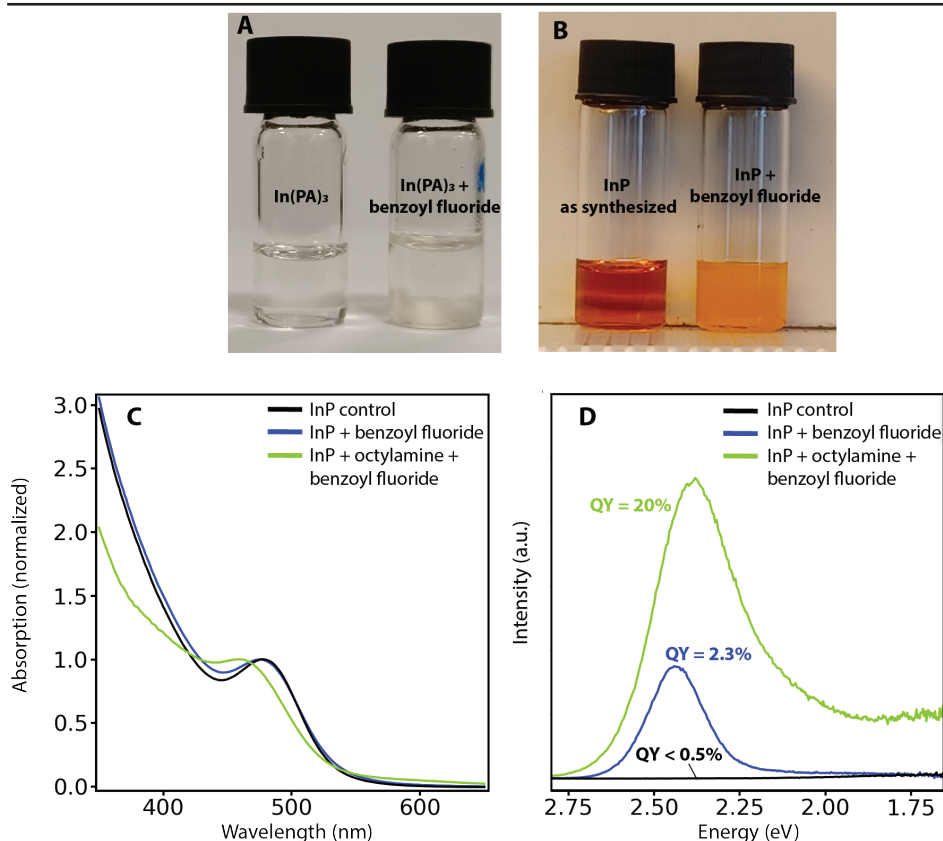


Figure A3.6. Photographs and optical data of InP QDs treated with benzoyl fluoride. Photographs of (A) In(Pa)_3 and (B) InP QDs in toluene before and after reaction with benzoyl fluoride. A precipitate is formed during the reaction of benzoyl fluoride and indium palmitate. The InP QDs have precipitated after the reaction with benzoyl fluoride, indicating a loss of polar surface ligands. Normalized absorption (C) and PL emission (D) spectra of InP treated with benzoyl fluoride and a combination of octylamine and benzoyl fluoride (in-situ HF). $[\text{benzoyl fluoride}]/[\text{QD}] = 1400$, $[\text{octylamine}]/[\text{QD}] = 2000$. The benzoyl fluoride was performed for 10 minutes at 150 °C, while the in-situ HF treatment was performed for 5 minutes at 150 °C.

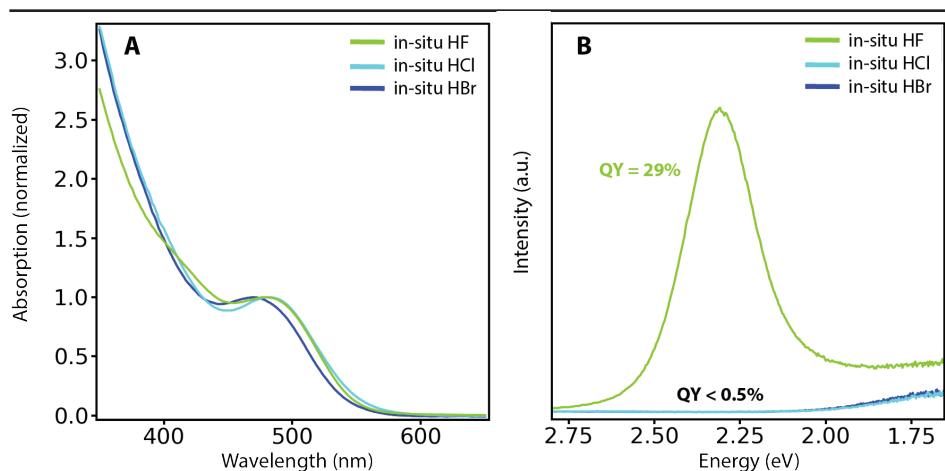


Figure A3.7. Normalized absorption (A) and PL emission (B) spectra of InP treated with different in-situ generated acids. Benzoyl bromide, benzoyl chloride and benzoyl fluoride were used in conjunction with octylamine to produce each of the acids in-situ. $[\text{acyl halogen}]/[\text{QD}] = 700$ for each of the samples. At higher concentrations, HCl and HBr fully dissolved the InP. Treatments were performed at 150°C for 180 minutes in mesitylene, similar to the in-situ HF treatment.

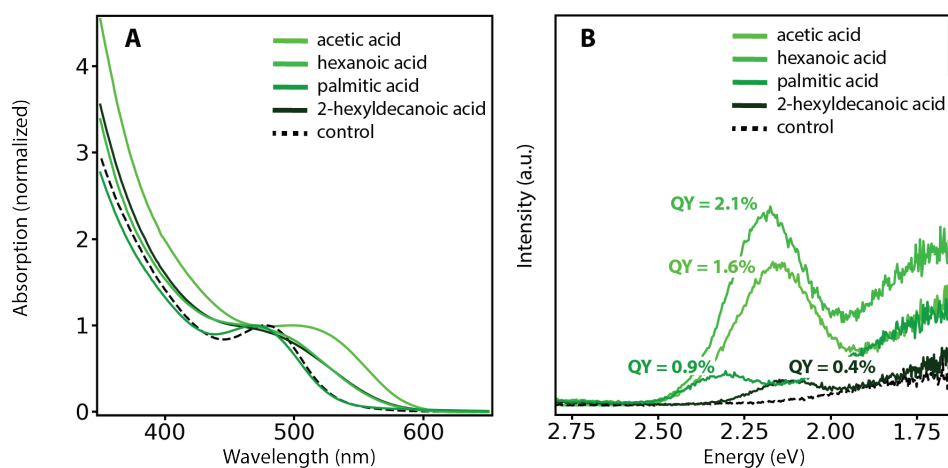


Figure A3.8. Normalized absorption (A) and PL emission (B) spectra of InP treated with different organic acids. $[\text{acid}]/[\text{QD}] = 1000$ for each of the samples. Treatments were performed at 150°C for 180 minutes in mesitylene, similar to the in-situ HF treatment. Modest increases in quantum yield are observed when smaller organic acids are applied.

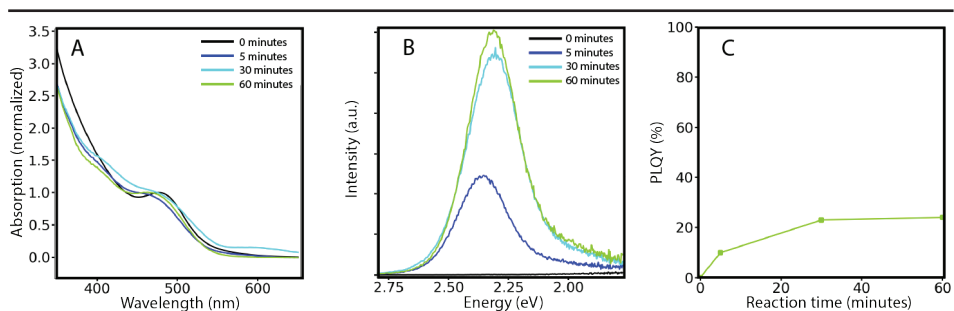


Figure A3.9. Optical data of the InF₃ treatment at 150 °C. (A) normalized absorption curves. (B) PL spectra. (C) photoluminescence quantum yield over time during the treatment. The treatment is performed by adding solid InF₃ to a dilute solution of InP QDs in mesitylene and heating to 150 °C. No additional compounds need to be added.

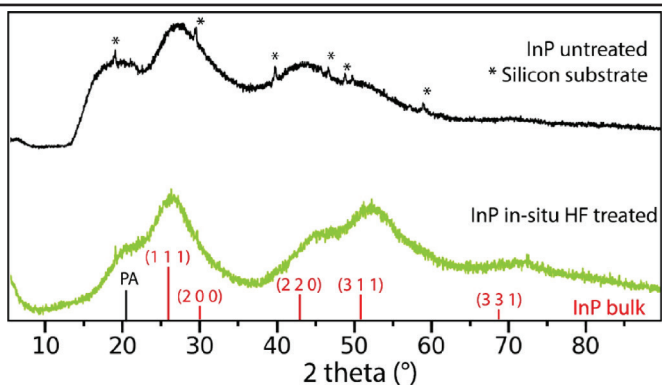


Figure A3.10. X-ray diffraction patterns of InP QDs before and after the in-situ HF treatment. After the treatment the peak at 20°, ascribed to ordered palmitate ligands, is decreased in intensity.

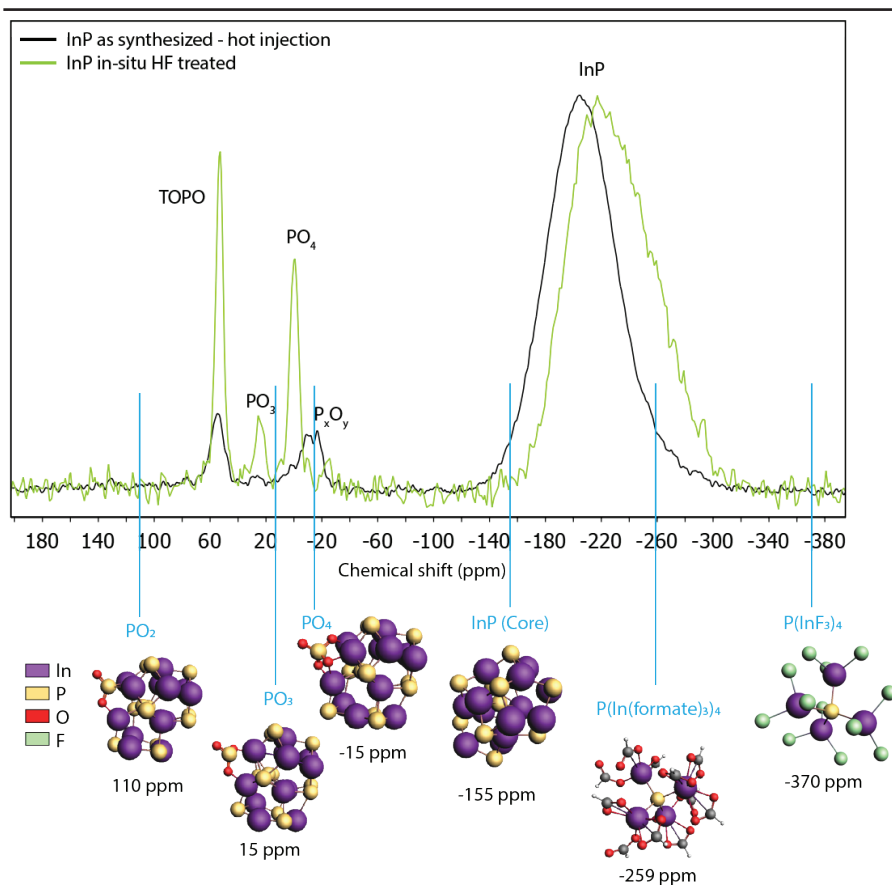


Figure A3.11. ^{31}P NMR shifts of various small InP structures as calculated using DFT. Shifts were referenced using the calculated shift of H_3PO_4 . For PO_x species, lower chemical shift is observed for increasing x , which mirrors experimental observations. P bound to four InF_3 was calculated to have a lower chemical shift than P bound to four $\text{In}(\text{carbonate})_3$. This is in accordance with our observations after the HF treatment, where the ^{31}P chemical shift becomes more negative after $\text{In}(\text{PA})_3$ has been replaced with InF_3 on the InP surface.

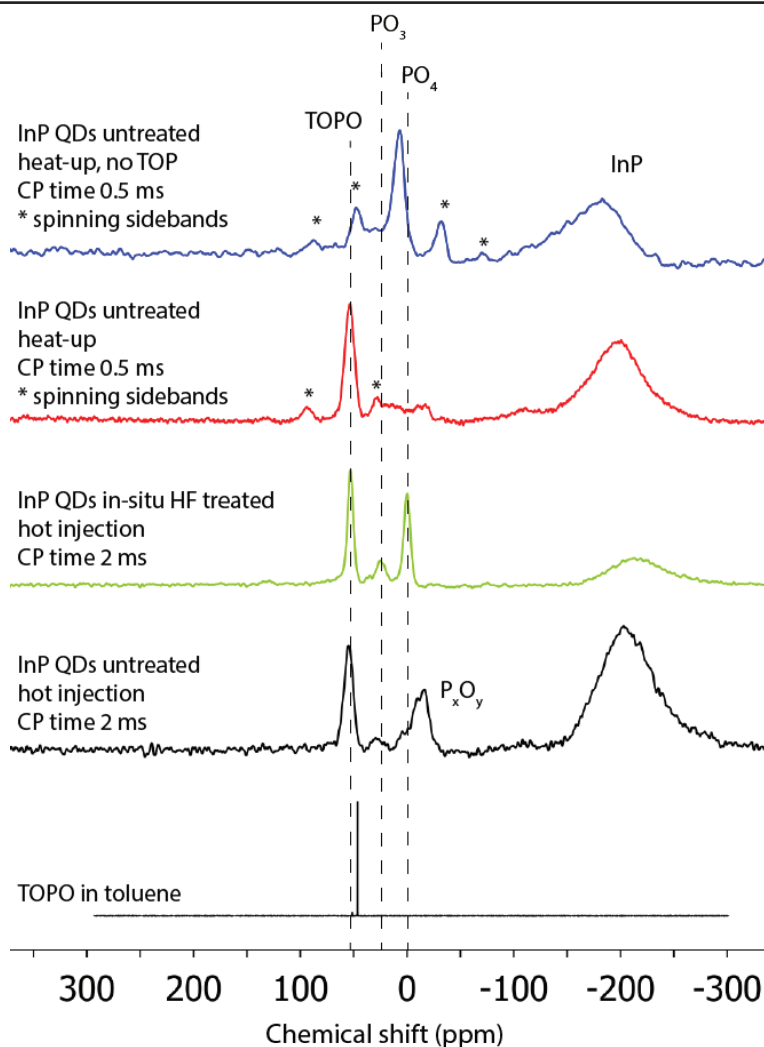


Figure A3.12. $^1\text{H} \rightarrow ^{31}\text{P}$ CPMAS spectra of as-synthesized QDs from heat-up syntheses and QDs from the hot injection synthesis before and after the in-situ HF treatment. The surface peaks in the region of 100 to -20 ppm are enhanced compared to the InP core peak due to proximity to hydrogen atoms. Dashed lines indicate the chemical shifts of PO_4 , PO_3 and TOPO species. TOPO in toluene is provided for reference.

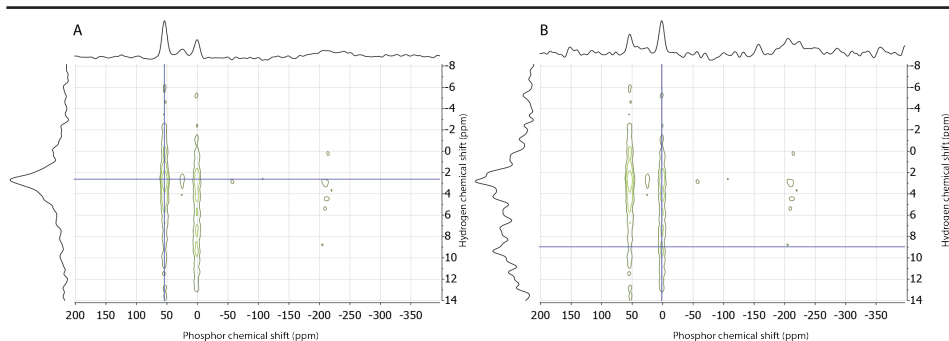


Figure A3.13. Projections of the $^{31}\text{P}\{^1\text{H}\}$ HETCOR spectra after the in-situ HF treatment. The phosphorus slice around ^1H 2.5 ppm shows spatial proximity of the aliphatic protons to the phosphorus peak at 52 ppm. The slice at ^1H 9 ppm shows a correlation between the PO_4 species at 0 ppm and the new, broad, downfield hydrogen peak around 7.5 ppm.

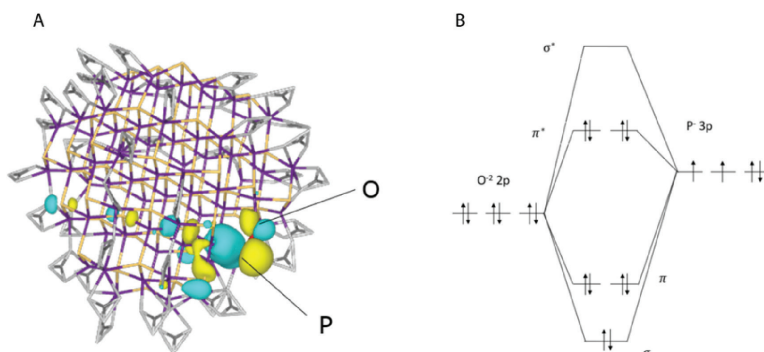


Figure A3.14. (A) Contour plot of the HOMO in the PO_2^{3-} InP QDs DFT simulations. (B) Molecular orbital (MO) of PO_3^{3-} complex. In the DOS InP QDs containing PO_2^{3-} , a state just above the valence band (VB) is formed, with significant contribution from the added oxygen atom as well as the phosphor atom the oxygen is bound to (see Figure 3.4). The IPR value of the trap state of the PO moiety is 0.33, whereas the IPR value of the unoxidized HOMO is 0.1 which shows that the trap state is slightly localized. The contour plot of this localized wave function (A) indicates that it is formed by an anti-bonding combination of p orbitals on the surface P and O atoms. To confirm the anti-bonding nature of the trap state, we use the crystal-orbital overlap population (COOP) analysis. Positive COOP values correspond to a bonding interaction, whereas negative COOP values correspond to an anti-bonding interaction. A value around 0 is a non-bonding interaction. The negative COOP values confirm the anti-bonding nature of the state (see Figure 3.4). Therefore we conjecture that the state inside the bandgap is primarily made up from the anti-bonding orbital of the O 2p orbital and the P 3p orbital. To further confirm this, we set up the molecular orbital (MO) diagram of PO_3^{3-} (B) We see that the highest occupied molecular orbital (HOMO) is indeed a π^* orbital.

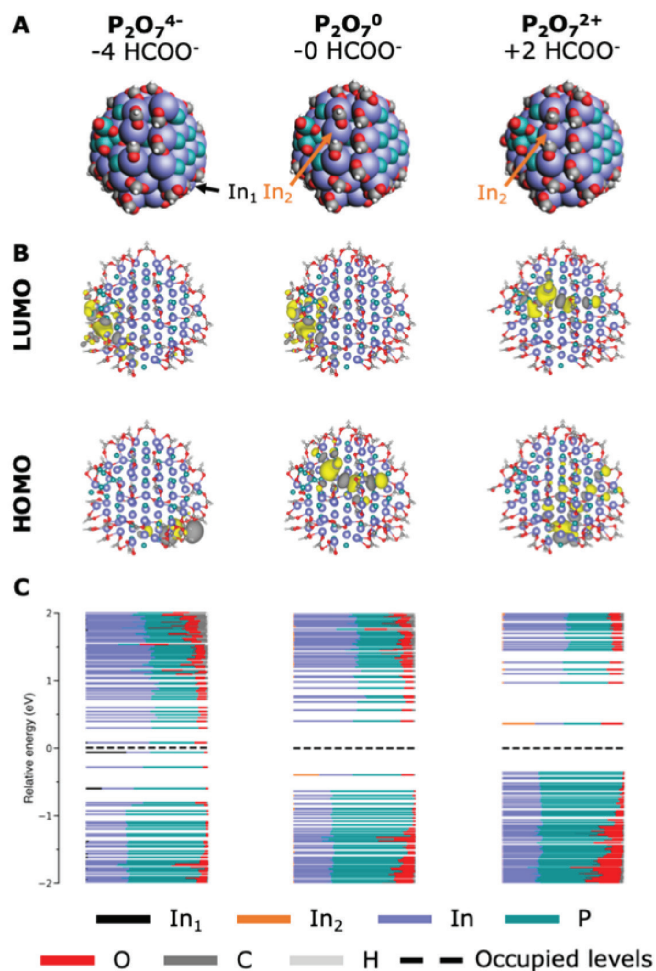


Figure A3.15. DFT calculations on InP QDs containing a P_2O_7 species on the surface. (A) atomic structures after geometry optimization. (B) HOMO and LUMO orbital shapes. (C) DOS plots of the respective structures. Negatively charged and neutral P_2O_7 species result in n-doping of the QD and reduction of indium, similar to earlier results on CdX QDs. Achieving charge neutrality is only possible by adding two additional carbonate ligands, effectively resulting in an unphysical $P_2O_7^{2+}$ species. Furthermore P_2O_7 species are not stable in DFT calculations, resulting in spontaneous surface reconstructions, where $(O_2P)-O-(PO_3)$ units are formed, and one oxygen forms an In-O-P bond instead.

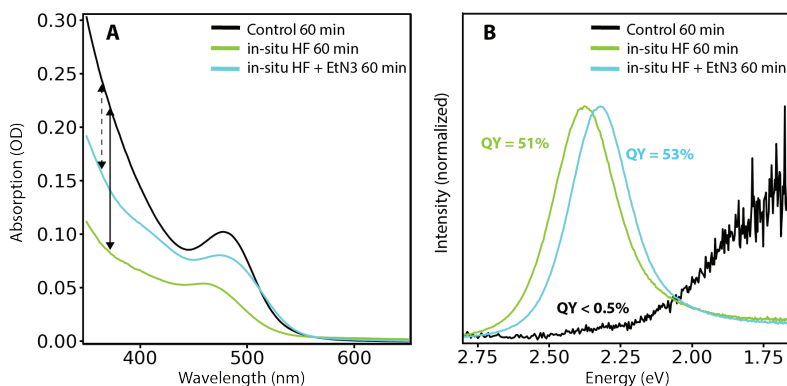


Figure A3.16. Optical data of the in-situ HF treatment and the in-situ HF treatment with added triethylamine at 150 °C, compared to a control sample at 150 °C. Triethylamine was added at the same concentration as the benzoyl fluoride. (A) absolute absorption spectra. (B) PL spectra. Adding triethylamine before starting the treatment results in less HF etching, while achieving the same increase in PLQY. Less InP is converted to InF_3 as can be seen by the reduced absorption drop compared to the HF treatment. There is also no absorption or PL blueshift observed after the treatment.

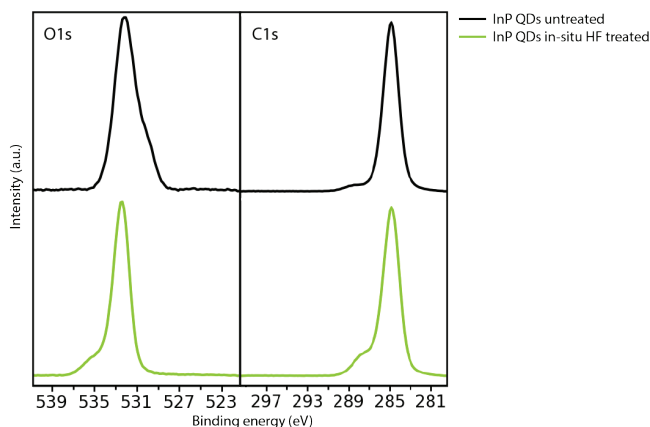


Figure A3.17. O1s and C1s XPS spectra of the InP QDs before and after the in-situ HF treatment. It should be noted that after the in-situ HF treatment, less carbonate ligands are present on the InP surface than before the treatment. The dropcasting procedure of the samples after the treatment also resulted in thinner QD layers with a lower coverage of the substrate. Because of these factors, the signal from contaminations (organic compounds on the substrate) in the O1s and C1s spectra is expected to be higher in the in-situ HF treated samples relative to the untreated samples, which makes a comparison of these spectra difficult.

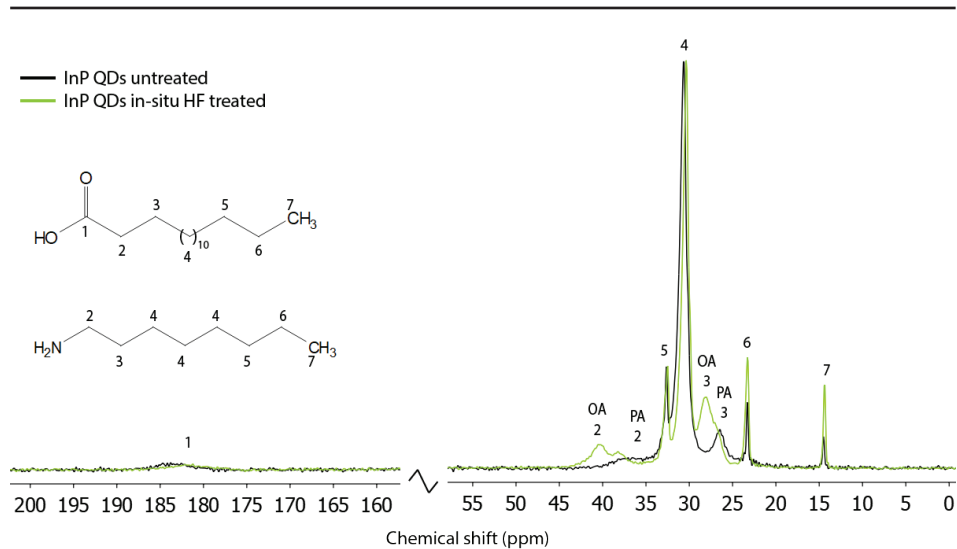


Figure A3.18. ^{13}C ssNMR spectra. After the in-situ HF treatment, octylamine is bound to the surface in addition to some remaining palmitates.

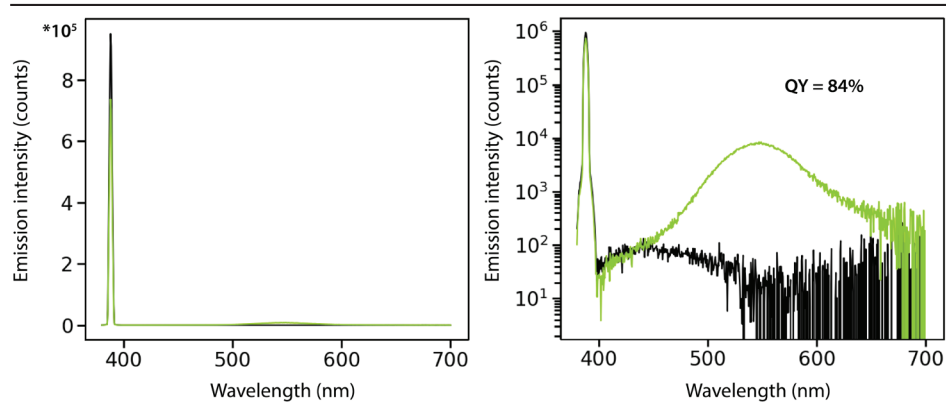
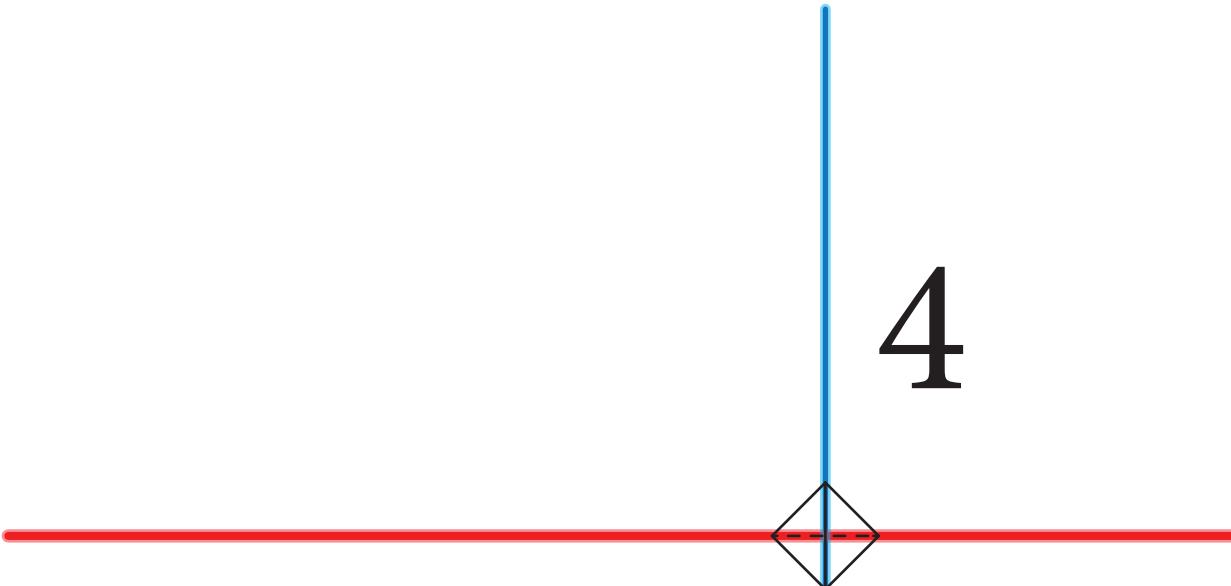


Figure A3.19. Integrating sphere PLQY measurement of a typical in-situ HF/ ZnCl_2 treated InP QD sample. A PLQY of 84% was observed.



Phosphorus Oxidation Controls Epitaxial Shell Growth in InP/ ZnSe Quantum Dots

This chapter is based on: Reinout F. Ubbink, Tom Speelman, Daniel Arenas Esteban, Mourijn van Leeuwen, Maarten Stam, Sara Bals, Gilles A. de Wijs, Ernst R. H. van Eck and Arjan J. Houtepen. *ACS Nano*, 2024, 1936-0851.



4.1 Introduction

Indium phosphide (InP) is the most promising ROHS-compliant material to produce quantum dots (QDs) for lighting applications.¹⁻³ Although InP QDs have significantly improved over the last 5 years⁴⁻⁶, their optical properties and stability leave much to be desired before InP QDs could be implemented as phosphors in high-intensity lighting applications such as ambient LED lamps or lasers.

One suspected source of both instability and trap states is the III-V/II-VI interface that is formed in InP/ZnSe/ZnS core/shell/shell particles. So far ZnSe and ZnS have been the most successful shelling materials for InP, leading to >90% photoluminescence quantum yields (PLQYs).^{4, 5, 7, 8} However, ZnSe and ZnS shelling results in an inherently charged interface due to the imbalance in charges of the lattice ions.^{9, 10} In addition, oxidized impurities have been identified at the InP/ZnSe interface.^{4, 5, 11-13} Surprisingly, the role of oxidative defects at this interface has remained a topic of debate, with reports of both detrimental^{4, 12, 13} and beneficial^{5, 11} effects on the quantum dot properties. The nature of the exact types of oxidative defects remains ambiguous, and a description of the atomistic structure of these defects is missing.

In this work, we use solid state nuclear magnetic resonance (ssNMR) and high-angle annular dark-field scanning transmission electrons microscopy (HAADF-STEM) techniques to improve the atomistic understanding of the InP/ZnSe QD interface. The chemical nature and location of various phosphorus species on InP/ZnSe QDs are revealed through ³¹P ssNMR measurements. ⁷⁷Se ssNMR experiments are then performed on QDs with enriched ⁷⁷Se in the whole ZnSe shell, the InP/ZnSe interface or the ZnSe shell surface. By combining these experiments with DFT calculations, we identify selenium at different positions in the shell, distinguishing interface, bulk shell and outer surface selenium based on its chemical shift. Specifically, the ⁷⁷Se peak at the interface is attributed to an In-Se-Zn environment at the epitaxial InP/ZnSe interface.

We then controllably oxidize the InP cores with labelled molecular ¹⁷O₂ before shelling with ZnSe. This results in PO₄³⁻ at the InP/ZnSe interface as the only reaction product. In the oxidized QDs, PLQY is significantly lower and the epitaxial In-Se-Zn ⁷⁷Se peak, which is clearly observed in the non-oxidized QDs, is missing. This indicates that excessive oxidation disrupts the development of an epitaxial InP/ZnSe interface. HAADF-STEM measurements reveal different crystal orientations of the core and shell when the interface is oxidized, supporting the idea of a disconnected interface between the InP and ZnSe for the oxidized particles.

We propose an atomistic picture of the InP/ZnSe interface in presence and absence of oxidation. When the amount of interface oxidation is low, an epitaxial interface is grown. Excessive oxidation however disrupts the epitaxial growth, as observed by a reduction in the amount of interface selenium and the different orientation core and shell crystals. The ZnSe is separated from the InP by the amorphous oxide layer.

4.2 Results and discussion

4.2.1 General properties of the QDs

Figure 4.1A schematically shows the protocol that was used to synthesize the InP/ZnSe QDs studied here. Zinc-free InP cores were prepared by a modified heat-up synthesis reported by Li and colleagues⁷ to minimize the surface oxidation present on the QDs.¹⁴ The purified cores were then heated up in the presence of zinc oleate (ZnOA_2), and selenium dissolved in trioctylphosphine (Se:TOP) was injected dropwise for 1 hour to grow the shell. As expected, the ZnSe shelling of InP particles results in a significant redshift of the absorption spectrum and an increase in the PLQY to 66% (Figure 4.1B). HAADF-STEM images reveal a truncated tetrahedral shape of the InP/ZnSe QDs (Figure 4.1C). The mean edge length of the particles increased from 3 nm to 6.5 nm after the shelling was completed (Figure A4.2). EDS analysis was performed to corroborate the core-shell atomic distribution of the QDs (Figure A4.3).

The synthesis method shown in Figure 4.1A was optimized specifically for ⁷⁷Se ssNMR measurements. To maximize the ⁷⁷Se signal from these samples, we did not grow an additional ZnS shell around the particles (which would “dilute” the effective density of selenium in the sample) and also applied extensive purification procedures to completely dry the samples for use in ssNMR. While this optimization results in excellent ssNMR signals from these samples, the PLQY of 66% after purification is modest compared to state-of-the-art InP core/shell/shell QDs.

To be able to generalize the results presented in this work, we also synthesized high-quality InP/ZnSe/ZnS QDs with PLQYs > 90% and compared the ³¹P ssNMR results between the two methods. For this we used a similar method as shown in Figure 4.1A, except the shelling was performed at 280 °C in octadecene, zinc chloride was added to be able to grow a thick ZnSe shell, and an additional ZnS shell was grown. While this synthesis method resulted in high PLQY values, the ssNMR signal of these samples is too weak to accurately measure ⁷⁷Se signal. As we will show below, there are no differences in the ³¹P measurements between these two samples, indicating the results presented here also hold for high-PLQY InP QDs. A complete comparison and analysis of the optical properties of all samples used in this study can be found in Figure A4.1.

To investigate the effect that oxidized interface species have on both the optical and structural properties of InP/ZnSe QDs, we introduced an oxidation step in the protocol (Figure 4.1A). We attempted to oxidize QDs in two ways: using either water or elemental oxygen at elevated temperatures. H_2O oxidation was successfully performed on aminophosphine-based InP to increase interface oxidation by van Avermaet and coworkers.⁵ We attempted the same protocol, but did not see any increase in oxidation of our InP QDs in ssNMR spectra (Figure A4.4). We speculate that the high concentration of strongly bound apolar ligands on our QDs as compared to aminophosphine InP QDs¹⁵ may prevent water from reaching the QD surface before it is evaporated from the solvent.

When exposing our InP QDs to elemental O_2 gas at elevated temperatures however we observed clear evidence of oxidation on the InP QDs, so we used isotopically enriched ¹⁷O₂ gas (allowing ssNMR analysis of the oxygen) to synthesize InP/ZnSe QDs with

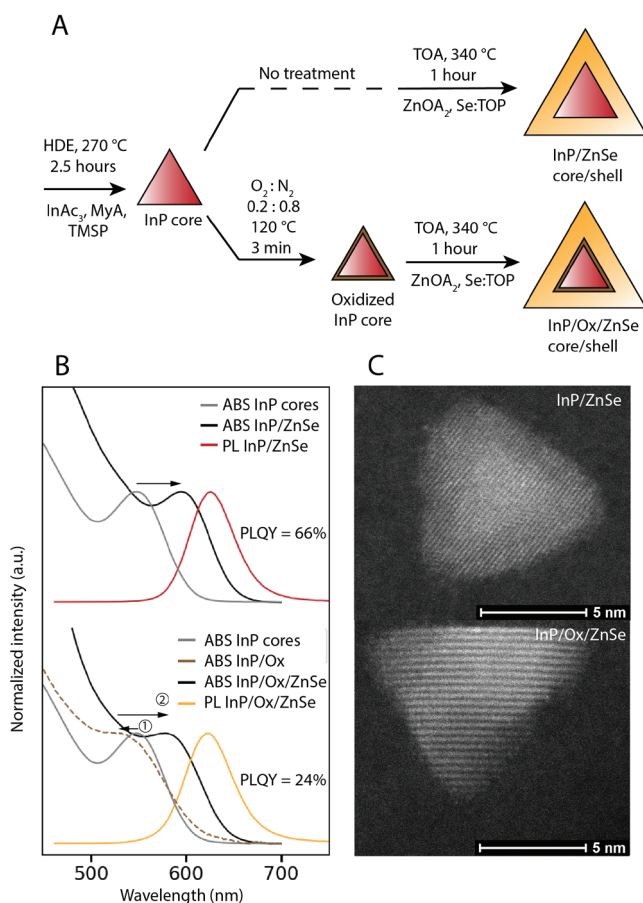


Figure 4.1. A) The synthesis scheme of the InP/ZnSe QDs with and without an interface oxidation step. B) Absorbance and photoluminescence spectra of the oxidized and unoxidized QDs. C) HAADF-STEM images of the oxidized and unoxidized QDs.

increased oxidation at the interface. This was done by placing the QD solution under an atmosphere of 0.21 $^{17}\text{O}_2/0.79 \text{ N}_2$, heating the solution to 120 °C for 3 minutes and then evacuating the oxygen/nitrogen mixture for 30 minutes (see methods section for details). After all oxygen had been removed, ZnSe shells were then grown following the same shelling procedure as used for the other ssNMR samples. The InP/ZnSe QDs that were obtained after treatment of the cores with O_2 are referred to as InP/Ox/ZnSe going forward.

Both the PL and absorbance of the InP/Ox/ZnSe QDs are blueshifted (absorbance maximum at 578 compared to 594 nm) and broadened compared to the unoxidized InP/ZnSe QDs (Figure 4.1B). As shown below, this effect is due to the conversion of some phosphorous in the cores to PO_4^{3-} during the oxidation, resulting in a net decrease of the InP particles size. A large difference in PLQY values is observed, as the InP/Ox/ZnSe show

a PLQY of only 24%, significantly lower than the 66% that was observed for unoxidized InP/ZnSe QDs. HAADF-STEM (Figure 4.1C, Figure A4.2) results indicate that the InP/Ox/ZnSe particles have a similar size as the unoxidized InP/ZnSe (mean edge length 7.1 nm vs. 6.5 nm). We will now first discuss the structural analysis of the unoxidized QDs and then evaluate the structural differences observed in the QDs with an oxidized interface.

4.2.2 Phosphorus ssNMR

Figure 4.2A shows quantitative single pulse ^{31}P ssNMR spectra of the InP core QDs before shelling, and of the InP/ZnSe QDs after shelling. The same 4 different species of phosphorous are distinguished in the ^{31}P ssNMR spectra of the core and core/shell QDs (Figure 4.2A): at around -185 ppm, the typical InP peak is observed, ascribed to P^{3-} in the InP crystal^{11, 16-18}. The peak around 0 ppm is ascribed to oxidized phosphorous in the form of PO_4^{3-} .^{11, 17, 18} We previously reported that using the heat-up synthesis it is possible to synthesize PO_4^{3-} -free InP cores¹⁹, however later observations suggest that this only holds true for short synthesis times. The cores used in this synthesis were grown at 270°C over a period of 2.5 hours. As was shown previously this prolonged exposure to high temperature results in a condensation reaction of the palmitic acid precursor. The produced water is suspected to cause oxidation of surface phosphorous,^{17, 18} leading to the observed PO_4^{3-} presence on the QDs (6.9% PO_4^{3-} out of total phosphorus). The relative integral of the PO_4^{3-} peak is also increased somewhat after shelling, which indicates that some additional oxidation may occur in the early stages of the shelling procedure by the same precursor condensation reaction as mentioned above (percentage PO_4^{3-} increases from 6.9% to 9.0%).¹² Two more peaks are observed, at 28 and 50 ppm, which we ascribe to the phosphorous-containing surface ligands dioctylphosphine oxide (DOPO) and triocetylphosphine oxide (TOPO) respectively.

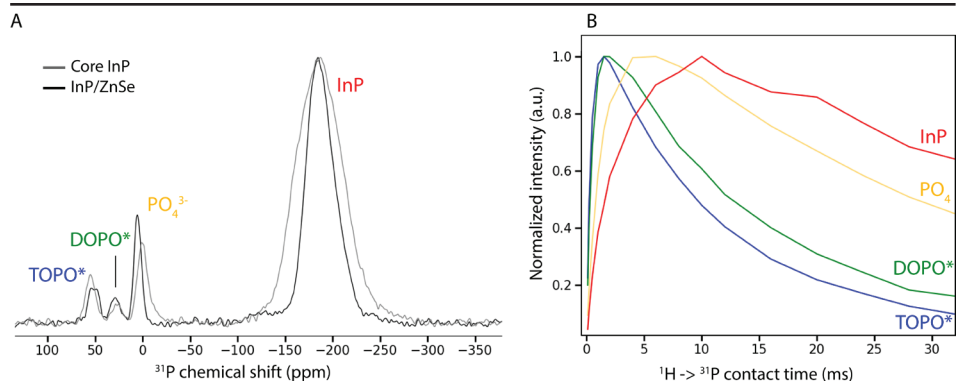


Figure 4.2. ^{31}P ssNMR measurements of InP QDs before and after ZnSe shelling. A) Single pulse ^{31}P measurements. The same 4 different phosphorous species are distinguished in the QDs before and after ZnSe shelling. B) Intensity of the 4 different species in the InP/ZnSe sample for different $^1\text{H} \rightarrow ^{31}\text{P}$ cross-polarization contact times. High intensities at short contact times indicate proximity to the hydrogen-rich ligands on the outer surface, while longer risetimes of the intensity indicate a position deeper inside the QD, removed from the surface ligands. *These peaks could also belong to other, similar organophosphorus species.



Both these compounds are already present as contaminants in as-purchased TOP that is used in the synthesis as confirmed by solution NMR (Figure A4.5).²⁰

¹H→³¹P cross-polarization experiments provide further insight into the identity and location of the 4 different phosphorous species in the core/shell QDs. In these measurements, spin polarization is transferred from hydrogen to phosphorous, increasing the ³¹P signal strength. By performing the measurement with different cross-polarization times, information can be obtained on the position of the phosphorous relative to the hydrogen in the ligands.²¹ Figure 4.2B shows the relative signal intensity of the 4 phosphorous species after different cross-polarization (CP) times in InP/ZnSe core/shell QDs. The intensity of the InP signal rises only with longer CP times (maximum at 12 ms), since the core is separated from the ligands by the ZnSe shell and the transfer of polarization is slow. This shows that, as expected, protons are only present in ligands on the surface of the shell, and not at the interface nor in the lattice. The peaks at 28 and 50 ppm both show very strong signal intensity even at short CP times (maximum at 1.5 ms), indicating fast polarization transfer and close proximity to hydrogen. This aligns with the assignment of these peaks to DOPO and TOPO, which are bound as ligands to the surface of the QDs. During the shelling, these ligands are easily detached from the InP surface at high temperature, then reattach to the outer ZnSe surface. The PO₄³⁻ signal reaches maximum intensity at intermediate times (6 ms) between the TOPO/DOPO and core InP peaks. This indicates that the PO₄³⁻ is present at the interface of the InP and ZnSe, closer to the ligands than the core P³⁻ in the core, but still separated from the ligands by the ZnSe shell. This confirms earlier reports that PO₄³⁻ species do not move to the outer ZnSe surface during the shelling procedure, but instead keep their position and are encased by the shell.^{11, 18}

4.2.3 Selenium ssNMR

Since the natural abundance of ⁷⁷Se is only 7.6%, InP/ZnSe QDs were synthesized with isotopically pure (>99%) elemental ⁷⁷Se (referred to as enriched ⁷⁷Se) to strongly enhance the ssNMR signal of the samples. Use of enriched ⁷⁷Se increases signal from the sample by a factor 13, reducing the NMR measurement time necessary to achieve the same signal/noise ratio by a factor 13² = 169. For all samples measured, ⁷⁷Se signals were observed in the range between -250 to -500 ppm, with a maximum around -350 ppm (Figure 4.3A and 4.3B). This is in accordance with measurements on bulk zinc blende ZnSe.²² Any signals of oxidized Se species would be expected at positive chemical shifts,²³ but were not observed, indicating that all Se in the samples was Se²⁻ in ZnSe.

Se²⁻ in different chemical environments can be distinguished by performing REDOR (Rotational Echo DOuble Resonance) measurements, correlating ⁷⁷Se with ¹H or ³¹P nuclei. In the REDOR sequence, the ⁷⁷Se signal is suppressed if it comes from nuclei that are close to the correlating nucleus (either ¹H or ³¹P). Figure 4.3A shows the results of both these correlation measurements compared to the ⁷⁷Se measurement with no correlation. Selenium at more negative chemical shifts (around -380 ppm) is suppressed when correlating with ¹H, which means that this signal corresponds to selenium atoms present at the outer surface of the shell, close to the hydrogen-rich ligands. This assignment is confirmed by ¹H → ⁷⁷Se cross-polarization measurements (Figure A4.6).

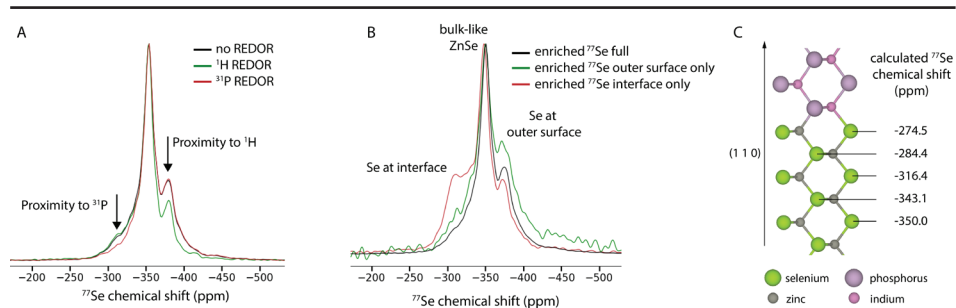


Figure 4.3. ^{77}Se ssNMR measurements of InP/ZnSe QDs. A) CPMG measurements, with REDOR coupling to ^1H and ^{31}P as well as no coupling. Signals from species close to the coupled nuclei will be suppressed in the REDOR experiment. B) CPMG measurements of QDs with enriched ^{77}Se at different locations in the shell. When isotopically pure ^{77}Se is placed only at the interface/outer surface of the shell, the corresponding signal at that location is strongly enhanced. C) Calculated ^{77}Se isotropic chemical shifts at the epitaxial [110] InP/ZnSe interface.

In contrast, signals around -310 ppm are suppressed when correlating with ^{31}P , indicating proximity to the phosphorus-rich core. We assign this peak to ^{77}Se at the epitaxial InP/ZnSe interface. The main peak at -350 ppm is assigned to “bulk-like” selenium, fully coordinated by 4 zinc atoms in the zinc blende ZnSe lattice. In summary, selenium attains more negative chemical shifts the closer the selenium atoms are to the outer shell surface.

With these assignments in mind, we explored the possibility of enhancing only specific parts of the selenium signal with enriched ^{77}Se . For the growth of the fully enriched ZnSe shell on our QDs, ^{77}Se :TOP is injected for 60 minutes (see methods section for further details). To create interface-labelled and outer-surface labelled particles, enriched ^{77}Se :TOP was instead injected for the first 5 minutes or last 10 minutes respectively, with regular Se:TOP being injected the remainder of the 60 minutes. The ^{77}Se ssNMR measurements of these 3 different samples are compared in Figure 4.3B. For the interface-labelled QDs, the signal at -310 ppm is strongly enhanced, while for the outer-surface labelled QDs the signal at -380 ppm is enhanced instead. Figure 4.3B also shows a significantly better resolved interface peak, clearly differentiated from the more bulk-like selenium at -350 ppm. Thus, our labelling experiment confirms the previous assignments.

To help interpret the different chemical shifts observed, we performed DFT chemical shielding calculations of various selenium-based crystal structures. We reference the DFT shieldings such that for bulk ZnSe the DFT and experimental ^{77}Se isotropic shift coincide, i.e. $\delta_{\text{calculated}} = \delta_{\text{experimental}} = -350$ ppm, for more details see Section S1 in the supporting information.

We first considered the formation of a layer of mixed (non-zinc blende) In-Zn-Se crystal phase at the InP/ZnSe interface, such as recently proposed for InAs/ZnSe QDs.^{24, 25} However, calculations of bulk ZnIn_2Se_4 and In_2Se_3 structures yielded shifts of -8.8 ppm and 356.1/472.3/732.3 ppm (for different selenium positions), respectively. These values



are several hundreds of ppm more positive than ZnSe (at -350 ppm), which does not align with ssNMR measurements on our samples, suggesting that no separate layer of mixed In-Zn-Se crystal phase is present in our samples.

We then performed chemical shift calculations on an epitaxial (110) InP/ZnSe interface, shown in Figure 4.3C. The calculated ^{77}Se chemical shifts of atoms next to the interface are ~ 75 ppm more positive compared to selenium atoms deeper in the ZnSe material. This resembles the 40 ppm chemical shift difference between interface and bulk-like selenium atoms from our experimental data and provides additional support for the assignment of the -310 ppm peak to Se at the InP/ZnSe interface.

4

4.2.4 Oxidation at the InP/ZnSe interface

The presence of PO_4^{3-} at the interface of InP/ZnSe as observed by ^{31}P NMR has been reported before, with claims of both beneficial^{4,12} and detrimental^{5,11} effects on the PLQY. To probe the structural effects of an oxidated interface on the QDs, we synthesized the aforementioned InP/Ox/ZnSe QDs (Figure 4.1) with ^{77}Se present only at the interface (injecting enriched ^{77}Se for the first 5 out of 60 minutes of shelling).

XPS measurements showed no difference between the oxidized and unoxidized QDs (Figure A4.7). Using ssNMR however, clear effects of the oxidation on the InP/ZnSe interface can be observed, as shown in Figure 4.4. From the ^{31}P spectra (Figure 4.4A), it is obvious that the amount of PO_4^{3-} of the QDs is significantly increased. This can be quantified by dividing the integral of the PO_4^{3-} peak by the total integral of the PO_4^{3-} and InP peaks, yielding an increase in ^{31}P in the PO_4^{3-} state from 9.0% for the as synthesized QDs to 32.2% for the oxidized QDs. ^{17}O ssNMR shows only one peak (Figure 4.4B), which is in the chemical shift range typically associated with phosphate species. Because there are no other peaks (except the zirconia artifact from the rotor), we conclude that all the molecular oxygen gas that reacted during our oxidation procedure ended up as phosphate species on the InP surface (which becomes the InP/ZnSe interface after shelling). In particular, we note that no In_3O_2 , In_3OH_3 , nor any other hydroxyl species are observed in the ^{17}O spectrum.²⁶ We propose a simple reaction for the oxidation of InP with molecular oxygen at 120 °C:



Selenium oxide species were again not observed. Looking at the ssNMR data of all investigated nuclei together, only one type of oxygen-containing species is actually observed at the InP/ZnSe interface: PO_4^{3-} .

4.2.5 Effects of interface oxidation on the properties of InP/ZnSe QDs

Earlier reports show that PO_4^{3-} does not directly cause trap states in the InP band gap: near unity PLQYs can be obtained even when a significant amount of phosphate is present on the surface/interface of the QDs.^{5,19} When running the synthesis optimized for high PLQY (in ODE with the addition of a ZnS shell, details in the method section), we were also able to obtain >90% PLQY on the same InP cores. While these QDs were not intentionally

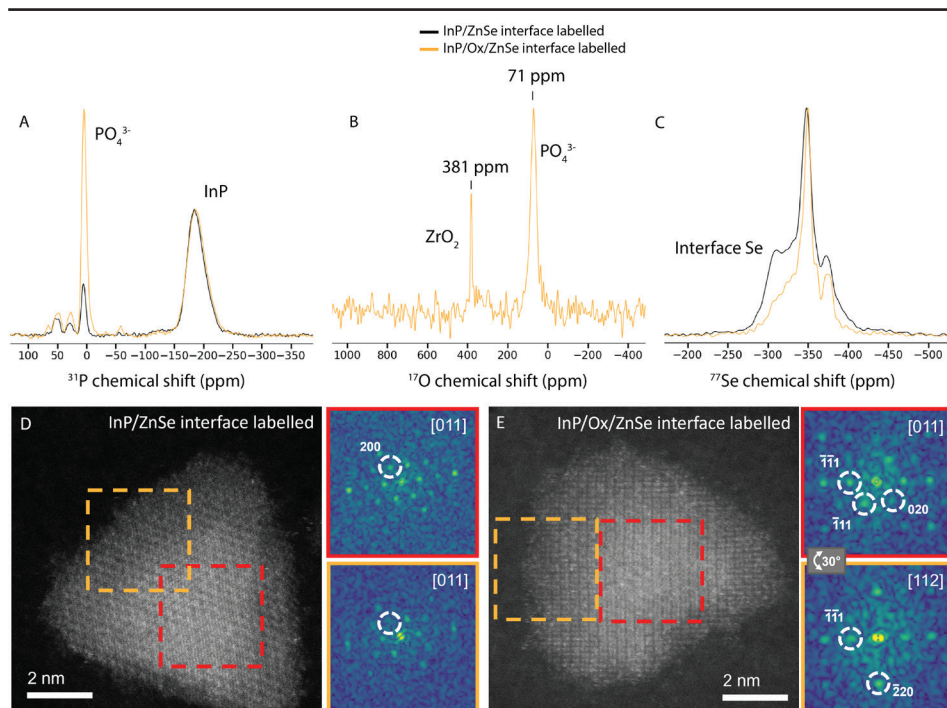


Figure 4.4. Comparison of ssNMR measurements of oxidized and non-oxidized InP/ZnSe QDs. A) Single pulse ^{31}P spectra. B) ^{17}O spectrum of the oxidized InP/Ox/ZnSe QDs. The peak at 381 ppm results from naturally abundant ^{17}O from zirconia in the rotor. Only one other peak is observed from the sample in the ^{17}O spectrum, assigned to PO_4^{3-} formed during the reaction with molecular oxygen. C) CMPG ^{77}Se spectra with enriched ^{77}Se at the InP/ZnSe interface. High-resolution HAADF-STEM images of non-oxidized D) and oxidized E) QDs. Inset shows FFT analysis of the central part (red) and external area (orange). In the non-oxidized quantum dot (QD), the crystal structures remain aligned along the [011] zone axis, displaying the characteristic fading of the (200) spacing for the ZnSe phase (white dashed circles). In contrast, the oxidized QD exhibits differing crystal orientations; the center is aligned along [011], while the outer region is aligned along [112]. These orientations are tilted at an angle of 30 degrees, indicating the coexistence of different crystal orientations in the QD.

oxidized, they did show a significant presence of PO_4^{3-} , even after shelling (Figure A4.4). This PO_4^{3-} was again confirmed to be situated at the InP/ZnSe interface by $^1\text{H} \rightarrow ^{31}\text{P}$ cross-polarization experiments (Figure A4.4C), as explained in Figure 4.2B. Through integration of ssNMR peaks and atom counting²⁷ it can be estimated that each QD, even when not intentionally oxidized, still contains an average of 5 PO_4^{3-} moieties. Since this sample still shows a PLQY of >90%, this demonstrates that the mere presence of interface PO_4^{3-} is not enough to cause carrier trapping and recombination. This is in line with our earlier DFT results that showed no addition of states in the bandgap when PO_4^{3-} is present on the surface. Rather, new orbitals associated to PO_4^{3-} reside inside the valence band.¹⁹ However, the presence of phosphate species on the interface could still lead to



in-gap states indirectly, by increasing disorder at the interface, which may result in *e.g.* undercoordinated interface atoms. Figure 4.4C shows the ^{77}Se spectra of the oxidized and unoxidized QDs. Both samples contain enriched ^{77}Se spectra only at the interface, strongly enhancing the signal of selenium nuclei that are closest the InP/ZnSe interface.

In the oxidized sample, a clear peak at -310 ppm is missing, even though the same amount of enriched ^{77}Se is present in this sample. Instead, only bulk-like ^{77}Se is present at -350 ppm, as well as Se at the outer ZnSe shell surface at -380 ppm. This indicates that the PO_4^{3-} layer interrupts the crystal at the InP/ZnSe interface, resulting in a decreased amount of selenium at epitaxial interface positions.

4

This interruption of the crystal is also supported by HAADF-STEM measurements of non-oxidized and oxidized QDs. Both InP and ZnSe have the same zinc blende cubic crystal structure with space group F-43m. However, a noticeable decrease in the intensity of the (200) crystal plane in the ZnSe system compared to InP makes it possible to distinguish between the crystal structures present in the same nanoparticle.²⁷ This difference is shown clearly in a HAADF-STEM image of a QD oriented along the [001] crystal direction in Figure A4.2 in the supporting information.

In Figure 4.4D, a non-oxidized QD is shown, with the crystal structure from the center and border area remaining oriented along the same [011] direction. When performing a fast Fourier transform (FFT) on the shell region (orange square), only a faint (200) crystal spacing is observed, highlighted by a white dashed circle in the FFT analysis, characteristic for the ZnSe phase. When performing the same analysis in the center of the particle (red square), the (200) spacing is much more clearly visible, indicating that InP is present in addition to the ZnSe shell in this part of the particle. The alignment of both crystal structures along the same zone axis indicates that the core and shell crystals have the same structure and orientation, pointing to epitaxial growth of the ZnSe on the InP core. In contrast, Figure 4.4E shows an oxidized QD, where the crystalline structure from the center of the particle exhibits a different crystal orientation of [011] compared with the shell crystal structure of [112]. This suggests a tilt of 30 degrees between the two structures. The center of the QD additionally shows a blurred effect most likely due to the oxide layer created between the core and the shell. This observation indicates that the shell was grown in a different orientation than the core InP. The excessive presence of PO_4^{3-} in the oxidized InP/ZnSe thus appears to disrupt the zinc blende lattice, interfering with epitaxial shell growth. While we showed that excessive interface oxidation is detrimental to the PLQY of our InP/ZnSe QDs, we were also able to obtain near-unity PLQY values with significant presence of interface phosphate (an average of 5 PO_4^{3-} moieties per QD, Figure A4.1 and Figure A4.4). Although it is difficult to imagine how these are incorporated in the zinc blende crystal at the InP/ZnSe interface, apparently their presence does not result in trap states. The disruption of epitaxy discussed above only seems to occur when even more interface oxidation occurs.

Figure 4.5 shows schematically the effects that excessive oxidation can have on the interface based on the results of this work. In this schematic, an amorphous phosphate layer is formed on top of the InP particles, in correspondence with the ssNMR observations.

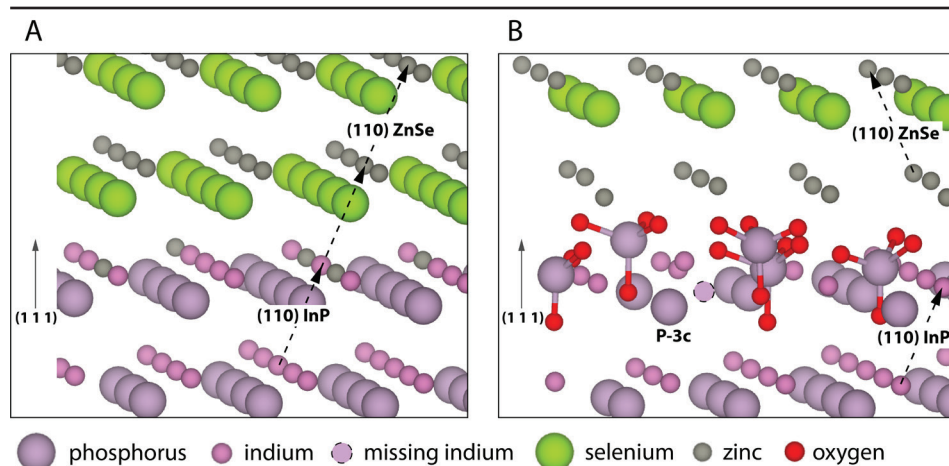


Figure 4.5. Sketches of the proposed structure of the InP/ZnSe interface with and without oxidation. A) Oxide-free InP/ZnSe (111) interface. The proposed oxide-free interface is an epitaxial InP/ZnSe interface, where the ZnSe crystal is oriented in the same direction as the InP crystal (dashed arrows). Selenium is present at the epitaxial interface, resulting in the characteristic NMR resonance observed around -310 ppm. B) Oxidized InP/ZnSe (111) interface. Most of the P³⁻ has been converted to PO₄³⁻, preventing the binding of selenium at the interface until a layer of positive zinc ions is present. The PO₄³⁻ layer disrupts the crystal lattice, which may result in trap states, for example an undercoordinated phosphorous (shown in B as P-3c) and growth of the ZnSe crystal in a different orientation (shown by dashed arrows) as observed in HAADF-STEM images. Bonds between phosphorus and oxygen are shown in B to highlight the phosphate units. Other bonds were omitted for visual clarity.

When shelling on the oxidized particles is performed, selenium ions cannot directly bind to indium. Instead, zinc binds first to the phosphate, and only then can selenium bind to begin the formation of the ZnSe lattice. The signal at -310 ppm that is observed from selenium at the epitaxial InP/ZnSe interface is thus suppressed.

4.3 Conclusion

This study elucidates the atomic structure of the InP/ZnSe QD interface with and without oxidation. It is shown how a high level of oxidation results in the presence of an amorphous phosphate layer at the InP/ZnSe quantum dot interface, which inhibits epitaxial shell growth. At the same time, it is shown that fully oxide-free interfaces are not required to obtain high-quality InP QDs, as epitaxial growth is still possible even when some phosphate is present. By providing insight in the effects of interface oxidation, these findings will aid the development of stable and high-quality QDs for lighting applications.

4.4 Methods

Materials

Anhydrous indium acetate (Thermo Fisher, 99.99%), anhydrous zinc acetate (Thermo Fisher, 99.9%), anhydrous zinc chloride (Merck Sigma, 99.999%), myristic acid (Merck



Sigma, >99%), tris(trimethylsilyl)phosphine (TMSP, Strem, >98% *caution: TMSP is a highly pyrophoric substance that can release toxic phosphine gas upon reaction with air*), selenium (Merck Sigma, 99.99%), selenium-77 (CortecNet, enrichment level 99.66%), sulphur (Alpha Aesar, 99.9995%), anhydrous acetone (VWR, max 0.01% H₂O), anhydrous toluene (VWR, 20 ppm H₂O) and anhydrous ethanol (VWR, 30 ppm H₂O) were used as received. Oleic acid (Merck Sigma, 90%), octadecene (ODE, Merck Sigma, 90%), trioctylamine (TOA, Merck Sigma >92.5%) and trioctylphosphine (TOP, Merck Sigma, 97%) were degassed *in vacuo* at 120 °C for at least 1 hour before use. All chemicals were stored inside a glovebox under inert N₂ atmosphere (concentration O₂ and H₂O < 0.1 ppm).

InP core QD synthesis

InP cores were synthesized according to a protocol by Li *et al.* 450 mg indium acetate (1.54 mmol), 1056 mg myristic acid (4.62 mmol) and 55 mL hexadecane were combined in a 3-neck roundbottomflask inside a nitrogen-filled glovebox (concentration O₂ and H₂O < 0.1 ppm). The flask was closed, taken outside and attached to a Schlenk line, where the mixture was degassed *in vacuo* for 30 minutes at room temperature under constant stirring. After purging, the flask was put under an atmosphere of Ar/2%H₂ and a needle was then added to bubble Ar/2%H₂ gas through the reaction mixture for the rest of the procedure (flow rate ~0.2 L/min). The mixture was raised to 150 °C and kept at that temperature for 30 minutes, during which the myristic acid and indium acetate reacted to form indium myristate and acetic acid, which was carried away by the bubbled gas. Then, 6750 mg of trioctylphosphine (TOP) was injected into the mixture. Once the temperature recovered to 150 °C, 9000 mg of 0.063 M tris(trimethylsilyl)phosphine (TMSP) in hexadecane was injected into the mixture as quickly as possible, using two syringes (*caution: TMSP is a highly pyrophoric substance that can release toxic phosphine gas upon reaction with air*). This led to an instant color change of the mixture from colorless to yellow as the InP nucleation took place. The temperature was raised to 270 °C. After 10 minutes, an additional 15 mL of 0.010 M TMSP in hexadecane was injected over 2.5 hours to grow the InP crystals. After cooling down, this yielded a dark red InP QD solution, which was returned under Ar/2%H₂ atmosphere to the glovebox. This crude mixture was purified by addition of 4 volume equivalents of anhydrous acetone, followed by centrifugation at 6000 rpm for 10 minutes. The clear supernatant was discarded, leaving a liquid residue which was redissolved in 24 mL of anhydrous toluene. Another 4 volume equivalents of anhydrous acetone was added, and after centrifugation at 6000 rpm for 40 minutes and discarding supernatant, the solid residue was redissolved in anhydrous toluene, yielding the InP core QD solution.

Treatment of InP cores with H₂O

126.5 µL of InP core solution (0.033 µmol InP QDs) was mixed with 3 mL of octadecene in a three-neck roundbottomflask inside a glovebox. The flask was taken outside, connected to a Schlenk line and degassed *in vacuo* for 10 minutes. The temperature was raised to 120 °C, and a drop of water (11 mg = 0.61 mmol, ratio indium atoms/water molecules = 65) was injected using a syringe. The mixture was stirred at 120 °C for 10 minutes under Argon bubbling, after which it was evacuated for 60 minutes at 110 °C to remove any excess water. The QD solution was purified three times by addition of 4 equivalents of anhydrous acetone, centrifugation at 6000 rpm for 10 minutes and redispersion in

anhydrous heptane.

Preparation of ZnOA₂

Zinc oleate precursor in octadecene (ZnOA₂ in ODE, 0.46 M) was synthesized by mixing 3.38 g zinc acetate (18.4 mmol), 10.4 g oleic acid (36.8 mmol) and 40 mL of ODE in a three-neck flask inside a nitrogen filled glovebox. The resulting solution was transferred to a Schlenk line, degassed for 10 minutes, then heated to 150°C and reacted for 60 minutes *in vacuo* until a clear solution was obtained. The solution was then transferred to a vial and stored in a nitrogen-filled glovebox.

ZnSe shelling of InP QDs

In a three-neck roundbottomflask in the glovebox, 957 µL of InP core solution (0.87 µmol InP QDs) was mixed with 2580 mg of ZnOA₂ solution (0.46M in ODE, heated to 150 °C, total ZnOA₂ ~ 1.8 mmol) and 80 mL trioctylamine (TOA). The flask was sealed, taken outside and attached to a Schlenk line. The mixture was degassed *in vacuo* for 30 minutes at room temperature and 30 minutes at 120 °C under constant stirring. If the oxidation was performed, the atmosphere was changed to 80%/20% N₂/isotopically enriched ¹⁷O₂ before heating (*caution: large hydrocarbons have low auto-ignition temperatures and care should be taken when heating these solvents in an oxygen-rich atmosphere*). The temperature was then raised to 120 °C over 18 minutes. Aliquots were regularly taken to check changes in the absorption spectrum of the QDs. A strong broadening was observed after 3 minutes at 120 °C, after which the mixture was cooled down and degassed *in vacuo* for another 30 minutes. After changing the atmosphere to pure Ar gas, the temperature was raised to 340 °C. Starting after 5 minutes, Se:TOP was injected into the mixture for 60 minutes using a syringe pump, during which the ZnSe shell growth took place. In total, 587 mg of 2.0 M Se in TOP solution was injected, diluted to 10 mL total volume in TOA (injection rate = 20.4 µmol selenium/min). Isotopically pure (enriched) ⁷⁷Se was injected for either the first 5 minutes, final 10 minutes or full 60 minutes and normal elemental selenium was used for the remaining duration. The mixture was cooled down and returned to the glovebox under inert atmosphere. Purification was performed by adding 3 volume equivalents of anhydrous ethanol, centrifugation at 6000 rpm for 10 minutes, discarding the clear supernatant and redissolving in toluene. This process was then repeated once. A very dry, deep red powder was obtained after 2 rounds of purification and drying under vacuum.

PLQY-optimized InP/ZnSe/ZnS synthesis

In a three-neck roundbottomflask in the glovebox, 360 µL of InP core solution (0.33 µmol InP QDs) was mixed with 1440 mg of ZnOA₂ solution (0.46M in octadecene, heated to 150 °C, total ZnOA₂ ~ 1.0 mmol), 60 mg ZnCl₂ (0.44 mmol) and 48 mL octadecene (ODE). In our experience, ZnCl₂ could not be used in conjunction with TOA, as this will cause the InP cores to accumulate and crash out of the solution. The flask was sealed, taken outside and attached to a Schlenk line. The mixture was degassed *in vacuo* for 30 minutes at room temperature and 30 minutes at 120 °C under constant stirring. After changing the atmosphere to pure Ar gas, the temperature was raised to 280 °C. Starting when the temperature reached 230 °C, Se:TOP was injected into the mixture for 60 minutes using a syringe pump, during which the ZnSe shell growth took place. In total, 220 mg of 2.0 M Se in TOP solution was injected, diluted to 5 mL total volume in ODE (injection rate



= 7.6 μmol selenium/min). The solution was kept at 280 $^{\circ}\text{C}$ for 15 minutes, then S:TOP was injected over 30 minutes using a syringe pump. In total, 110 mg of 2.0 M S in TOP solution was injected, diluted to 2.5 mL total volume in ODE (injection rate = 7.6 μmol sulphur/min). The mixture was cooled down, and purified 3 times using the same method as described above for the InP/ZnSe QDs. Despite extensive purification, a liquid residue was obtained, which was dried *in vacuo* to obtain a sticky red paste.

Optical characterization

UV-Vis absorption spectra were recorded on a Perkin-Elmer Lambda 365 spectrometer. Emission measurements were recorded on Edinburgh Instruments FLS980 spectrometer equipped with a PMT 750 detector. Photoluminescence quantum yields were measured against a fluorescein dye solution in 0.1 M NaOH in H_2O at an excitation wavelength of 465 nm. To calculate the quantum yield, the literature value of 92% is considered for the quantum yield of fluorescein.²⁹

Transmission electron microscopy

High-angle annular dark field scanning transmission electron microscopy (HAADF-STEM) and energy-dispersive X-ray spectroscopy (EDS) were performed using an aberration-corrected Thermo Fisher Titan G2 60-300 electron microscope equipped with a Super-X EDS detector operated at 300 keV. For the EDS analysis, 342 frames with a pixel size of 50.75 pm were acquired using a dwell time of 2 μs and a beam current of 150 pA, resulting in a total dosage of approximately 2.5 10^6 e- \AA^{-2} to ensure accurate element detection. X-ray diffraction relative intensity data was obtained from the Materials Project for InP (mp-20351) and ZnSe (mp-1190) from database version v2023.11.1.²⁷

X-ray diffraction

Powder X-ray diffraction samples were prepared by drop casting QD solutions onto low-reflection silicon wafers. XRD patterns were then collected on a Bruker D8 Advance diffractometer (Cu $\text{K}\alpha$, $\lambda=1.5418$ \AA).

Solid-state NMR

ssNMR analysis was performed at the Magnetic Resonance Research Center at the Radboud University Nijmegen. Samples were loaded into 4 mm zirconia rotors inside a nitrogen filled glovebox. Measurements not involving ^{77}Se or ^{17}O were performed using an Agilent 400 MHz magnet operating at ^1H and ^{31}P resonance frequencies of 399.9 and 161.9 MHz respectively, with a CMX 4.0mm T3 SPC400-550 probe, spinning at a MAS frequency of 10 kHz. Spectra were referenced to external H_3PO_4 in H_2O (= 0 ppm). Single Pulse ^{31}P measurements were collected with a recycle delay (d1) of 600 s and a ^{31}P $\pi/2$ 6 μs pulse width. Extremely long recycle delays are needed to obtain quantitative data since relaxation is very slow in these highly crystalline samples with core phosphorus separated from the surface by the ZnSe shell. $^1\text{H}\rightarrow^{31}\text{P}$ CPMAS measurements were performed with a ^1H $\pi/2$ pulse width of 6 μs and a recycle delay (d1) of 4 s. Proton decoupling was performed during the CP measurements using the Spinal-64 decoupling sequence. Measurements involving ^{77}Se or ^{17}O were performed using a Bruker 850 MHz magnet operating at ^{77}Se , ^1H , ^{31}P and ^{17}O resonance frequencies of 162.1, 849.7, 344.0 and 115.2 MHz respectively with an Agilent T3 4.0 mm probe, spinning at a MAS frequency of

10 kHz. All spectra were referenced to external H_3PO_4 in H_2O (= 0 ppm in the ^{31}P). ^{77}Se spectra were accumulated using a CPMG (Carr-Purcell-Meiboom-Gill) pulse sequence (see Figure A4.8 for the full pulse program), with a ^{77}Se $\pi/2$ pulse width of 6 μs and a recycle delay (d1) of 300 s. 64 CPMG cycles were recorded with each cycle consisting of 16 rotor periods. In the REDOR measurements, either ^1H , ^{31}P or no dephasing pulses were given at half and full rotor periods, while refocusing pulses were given on the selenium channel every 16 rotor periods. The REDOR dephasing was performed for 16 ms before the CPMG signal acquisition. ^{17}O spectra were accumulated using a CPMG pulse sequence with a ^{17}O $\pi/2$ pulse width of 6.25 μs and a recycle delay (d1) of 30 s.

ssNMR analysis of the water-treated InP was performed at the Reactor Institute Delft. Samples dried *in vacuo* were mixed with activated alumina and loaded into a 4 mm zirconia rotor. Measurements were then performed with a Bruker Ascend 500 magnet (11.7 T) with a NEO console operating at a ^{31}P resonance frequency of 202.45 MHz and a MAS spinning frequency of 8 kHz. Spectra were referenced to external H_3PO_4 (= 0 ppm). Single pulse measurements were performed with a recycle delay (d_1) of 50 s and a pulse width of 4.8 μs . Proton decoupling was performed during the measurement using the Spinal-64 decoupling sequence.

X-ray photoelectron spectroscopy (XPS)

Samples were prepared by drop casting the QD dispersions gold-plated glass substrates inside a nitrogen-filled glovebox and were vacuum-transferred to the instrument to avoid exposure to air. Measurements were performed under UHV ($<2\text{e-}7$ mbar) on a ThermoFisher K-Alpha equipped with Al K α source, radiating with an energy of 1486 eV. A flood gun (Ar) was active during all measurements to prevent charging of the samples. Samples were etched with an ion gun before measurement for 30 seconds to avoid surface bias and measure a representative average of the QD sample.

DFT calculations

Crystal structures were obtained from the Materials Project²⁷, specifics are available in table S1. Before calculating the chemical shieldings, all structures were optimized at the PBE level^{30, 31}. An epitaxial ZnSe/InP interface, featuring 10 atomic layers of each compound, was constructed based on ZnSe lattice parameters obtained from the previous geometry optimization. The interface model includes no vacuum, and is essentially an infinite repetition of alternating ZnSe/InP layers. Consecutively, we relaxed the atomic positions whilst varying the long direction of the unit cell to find the minimum energy structure (figure A4.9). All DFT calculations presented in this work were performed using VASP^{32, 33}, using the projector augmented-wave (PAW)^{34, 35} and gauge-including PAW methods.³⁶ Detailed input parameters are available in the supporting information section S1.

References

1. Almeida, G.; Ubbink, R. F.; Stam, M.; du Fossé, I.; Houtepen, A. J., InP colloidal quantum dots for visible and near-infrared photonics. *Nature Reviews Materials* **2023**, 8 (11), 742-758.
2. Chen, B.; Li, D.; Wang, F., InP quantum dots: synthesis and lighting applications. *Small* **2020**, 16 (32), 2002454.
3. Wu, Z.; Liu, P.; Zhang, W.; Wang, K.; Sun, X. W., Development of InP quantum dot-based light-emitting diodes. *ACS Energy Letters* **2020**, 5 (4), 1095-1106.



4. Won, Y.-H.; Cho, O.; Kim, T.; Chung, D.-Y.; Kim, T.; Chung, H.; Jang, H.; Lee, J.; Kim, D.; Jang, E., Highly efficient and stable InP/ZnSe/ZnS quantum dot light-emitting diodes. *Nature* **2019**, *575* (7784), 634–638.
5. Van Avermaet, H.; Schiettecatte, P.; Hinz, S.; Giordano, L.; Ferrari, F.; Nayral, C.; Delpech, F.; Maultzsch, J.; Lange, H.; Hens, Z., Full-Spectrum InP-Based Quantum Dots with Near-Unity Photoluminescence Quantum Efficiency. *ACS nano* **2022**, *16* (6), 9701–9712.
6. Jo, D.-Y.; Kim, H.-M.; Park, G. M.; Shin, D.; Kim, Y.; Kim, Y.-H.; Ryu, C. W.; Yang, H., Unity quantum yield of InP/ZnSe/ZnS quantum dots enabled by Zn halide-derived hybrid shelling approach. *Soft Science* **2024**, *4* (3), N/A–N/A.
7. Li, Y.; Hou, X.; Dai, X.; Yao, Z.; Lv, L.; Jin, Y.; Peng, X., Stoichiometry-controlled InP-based quantum dots: synthesis, photoluminescence, and electroluminescence. *Journal of the American Chemical Society* **2019**, *141* (16), 6448–6452.
8. Kim, Y.; Ham, S.; Jang, H.; Min, J. H.; Chung, H.; Lee, J.; Kim, D.; Jang, E., Bright and uniform green light emitting InP/ZnSe/ZnS quantum dots for wide color gamut displays. *ACS Applied Nano Materials* **2019**, *2* (3), 1496–1504.
9. Cui, Z.; Qin, S.; He, H.; Wen, Z.; Yang, D.; Piao, Z.; Mei, S.; Zhang, W.; Guo, R., Sequential Growth of InP Quantum Dots and Coordination between Interfacial Heterovalency and Shell Confinement: Implication for Light-Emitting Devices. *ACS Applied Nano Materials* **2023**.
10. Jeong, B. G.; Chang, J. H.; Hahm, D.; Rhee, S.; Park, M.; Lee, S.; Kim, Y.; Shin, D.; Park, J. W.; Lee, C.; Lee, D. C.; Park, K.; Hwang, E.; Bae, W. K., Interface polarization in heterovalent core–shell nanocrystals. *Nature Materials* **2021**.
11. Tessier, M. D.; Baquero, E. A.; Dupont, D.; Grigel, V.; Bladt, E.; Bals, S.; Coppel, Y.; Hens, Z.; Nayral, C.; Delpech, F., Interfacial oxidation and photoluminescence of InP-based core/shell quantum dots. *Chemistry of Materials* **2018**, *30* (19), 6877–6883.
12. Vikram, A.; Zahid, A.; Bhargava, S. S.; Jang, H.; Sutrisno, A.; Khare, A.; Trefonas, P.; Shim, M.; Kenis, P. J., Unraveling the origin of interfacial oxidation of InP-based quantum dots: implications for bioimaging and optoelectronics. *ACS Applied Nano Materials* **2020**, *3* (12), 12325–12333.
13. Choi, Y.; Hahm, D.; Bae, W. K.; Lim, J., Heteroepitaxial chemistry of zinc chalcogenides on InP nanocrystals for defect-free interfaces with atomic uniformity. *Nature Communications* **2023**, *14* (1), 43.
14. Stam, M.; Almeida, G.; Ubbink, R. F.; van der Poll, L. M.; Vogel, Y. B.; Chen, H.; Giordano, L.; Schiettecatte, P.; Hens, Z.; Houtepen, A. J., Near-Unity Photoluminescence Quantum Yield of Core-Only InP Quantum Dots via a Simple Postsynthetic InF₃ Treatment. *ACS nano* **2024**.
15. Dumbgen, K. C.; Leemans, J.; De Roo, V.; Minjauw, M.; Detavernier, C.; Hens, Z., Surface Chemistry of InP Quantum Dots, Amine–Halide Co-Passivation, and Binding of Z-Type Ligands. *Chemistry of Materials* **2023**, *35* (3), 1037–1046.
16. Tomaselli, M.; Yarger, J.; Bruchez Jr, M.; Havlin, R.; DeGraw, D.; Pines, A.; Alivisatos, A., NMR study of InP quantum dots: Surface structure and size effects. *The Journal of chemical physics* **1999**, *110* (18), 8861–8864.
17. Cros-Gagneux, A.; Delpech, F.; Nayral, C.; Cornejo, A.; Coppel, Y.; Chaudret, B., Surface chemistry of InP quantum dots: a comprehensive study. *Journal of the American Chemical Society* **2010**, *132* (51), 18147–18157.
18. Virieux, H.; Le Troedec, M.; Cros-Gagneux, A.; Ojo, W.-S.; Delpech, F.; Nayral, C.; Martinez, H.; Chaudret, B., InP/ZnS nanocrystals: coupling NMR and XPS for fine surface and interface description. *Journal of the American Chemical Society* **2012**, *134* (48), 19701–19708.
19. Ubbink, R. F.; Almeida, G.; Iziyi, H.; Du Fossé, I.; Verkleij, R.; Ganapathy, S.; Van Eck, E. R.; Houtepen, A. J., A Water-Free In Situ HF Treatment for Ultrabright InP Quantum Dots.

- Chemistry of Materials* **2022**, *34* (22), 10093-10103.
20. Wang, F.; Tang, R.; Buhro, W. E., The trouble with TOPO; identification of adventitious impurities beneficial to the growth of cadmium selenide quantum dots, rods, and wires. *Nano letters* **2008**, *8* (10), 3521-3524.
 21. Kolodziejski, W.; Klinowski, J., Kinetics of cross-polarization in solid-state NMR: a guide for chemists. *Chemical Reviews* **2002**, *102* (3), 613-628.
 22. Cadars, S.; Smith, B.; Epping, J.; Acharya, S.; Belman, N.; Golan, Y.; Chmelka, B., Atomic positional versus electronic order in semiconducting ZnSe nanoparticles. *Physical review letters* **2009**, *103* (13), 136802.
 23. Demko, B. A.; Wasylishen, R. E., Solid-state selenium-77 NMR. *Progress in Nuclear Magnetic Resonance Spectroscopy* **2009**, *54* (3-4), 208-238.
 24. Zhu, D.; Bellato, F.; Bahmani Jalali, H.; Di Stasio, F.; Prato, M.; Ivanov, Y. P.; Divitini, G.; Infante, I.; De Trizio, L.; Manna, L., ZnCl₂ Mediated synthesis of InAs nanocrystals with aminoarsine. *Journal of the American Chemical Society* **2022**, *144* (23), 10515-10523.
 25. Zhu, D.; Bahmani Jalali, H.; Saleh, G.; Di Stasio, F.; Prato, M.; Polykarpou, N.; Othonos, A.; Christodoulou, S.; Ivanov, Y. P.; Divitini, G., Boosting the Photoluminescence Efficiency of InAs Nanocrystals Synthesized with Aminoarsine via a ZnSe Thick-Shell Overgrowth. *Advanced Materials* **2023**, *35* (38), 2303621.
 26. Han, Q.; Gao, P.; Liang, L.; Chen, K.; Dong, A.; Liu, Z.; Han, X.; Fu, Q.; Hou, G., Unraveling the surface hydroxyl network on In₂O₃ nanoparticles with high-field ultrafast magic angle spinning nuclear magnetic resonance spectroscopy. *Analytical Chemistry* **2021**, *93* (50), 16769-16778.
 27. Jain, A.; Ong, S. P.; Hautier, G.; Chen, W.; Richards, W. D.; Dacek, S.; Cholia, S.; Gunter, D.; Skinner, D.; Ceder, G.; Persson, K. A., Commentary: The Materials Project: A materials genome approach to accelerating materials innovation. *APL Materials* **2013**, *1* (1).
 28. Almeida, G.; van der Poll, L.; Evers, W. H.; Szoboszlai, E.; Vonk, S. J.; Rabouw, F. T.; Houtepen, A. J., Size-dependent optical properties of InP colloidal quantum dots. *Nano Letters* **2023**, *23* (18), 8697-8703.
 29. Brouwer, A. M., Standards for photoluminescence quantum yield measurements in solution (IUPAC Technical Report). *Pure and Applied Chemistry* **2011**, *83* (12), 2213-2228.
 30. Perdew, J. P.; Burke, K.; Ernzerhof, M., Generalized gradient approximation made simple. *Physical review letters* **1996**, *77* (18), 3865.
 31. Perdew, J. P.; Burke, K.; Ernzerhof, M., Generalized Gradient Approximation Made Simple [Phys. Rev. Lett. *77*, 3865 (1996)]. *Physical Review Letters* **1997**, *78* (7), 1396-1396.
 32. Kresse, G.; Furthmüller, J., Efficient iterative schemes for ab initio total-energy calculations using a plane-wave basis set. *Physical Review B* **1996**, *54* (16), 11169-11186.
 33. Kresse, G.; Furthmüller, J., Efficiency of ab-initio total energy calculations for metals and semiconductors using a plane-wave basis set. *Computational materials science* **1996**, *6* (1), 15-50.
 34. Blöchl, P. E., Projector augmented-wave method. *Physical review B* **1994**, *50* (24), 17953.
 35. Kresse, G.; Joubert, D., From ultrasoft pseudopotentials to the projector augmented-wave method. *Physical review b* **1999**, *59* (3), 1758.
 36. Yates, J. R.; Pickard, C. J.; Mauri, F., Calculation of NMR chemical shifts for extended systems using ultrasoft pseudopotentials. *Physical Review B—Condensed Matter and Materials Physics* **2007**, *76* (2), 024401.

Appendix

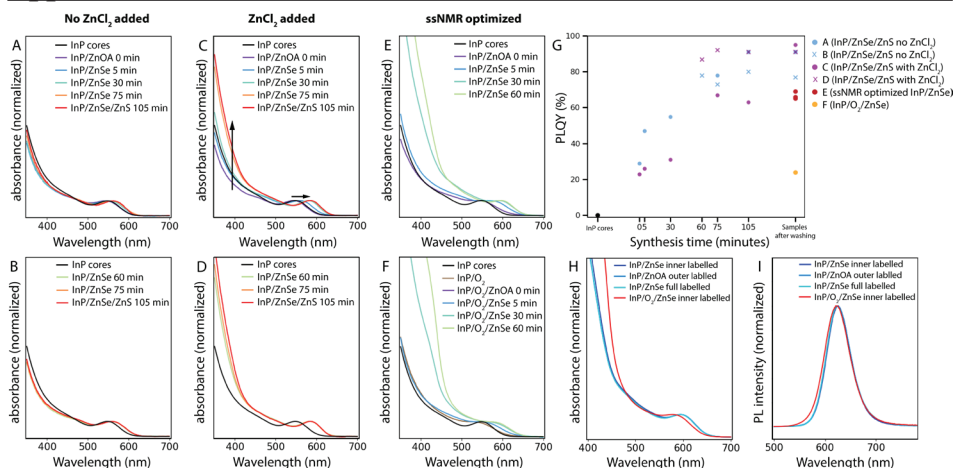


Figure A4.1. Overview of optical properties of the samples during synthesis and after purification. A), B) Absorption spectra of aliquots taken during shelling optimized for PLQY except no ZnCl_2 is added. C), D) Absorption spectra of aliquots taken during shelling optimized for PLQY where ZnCl_2 is added. Compared to shelling without ZnCl_2 , a stronger redshift of the 1S peak and a larger increase at lower wavelengths is observed (as indicated by the arrows in C). This indicates the growth of a thicker shell when ZnCl_2 is added. Sample D) was measured using ssNMR (Figure A4.5). E) Absorption spectra of aliquots taken during the synthesis of the interface- ^{77}Se labeled sample. By using TOA as the solvent (as opposed to ODE in the other samples), a thicker shell is grown, similar to the case where ZnCl_2 is added. The larger ZnSe shell allows more signal to be obtained from the samples in ssNMR. F) Absorption spectra of sample oxidized with molecular O_2 gas before the shelling procedure. The shelling procedure still works in the same way as for the non-oxidized samples. Compared to non-oxidized samples, the 1S peak of the final InP/ZnSe QDs is only slightly blueshifted and slightly broadened. G) PLQY values of all samples during the synthesis and after washing. The PLQY-optimized version of the protocol yields high-quality InP/ZnSe/ZnS QDs with PLQY values $>90\%$. ssNMR-optimized samples show lower PLQY values (around 66%), likely due to the missing ZnS outer shell in combination with the aggressive washing procedure used to prepare the samples for ssNMR analysis, which may increase surface defects.¹ The interface-oxidized sample shows significantly lower PLQY compared to ssNMR-optimized samples of 24% . H) Absorption spectra and I) photoluminescence spectra of all samples analyzed by ssNMR. All unoxidized InP/ZnSe particles synthesized have optical properties that are practically identical, regardless of the use of enriched ^{77}Se . Interface-oxidized InP/ O_2 /ZnSe particles show slightly broadened and redshifted emission and absorption compared to unoxidized ones. The increased intensity at lower wavelengths in the absorption spectrum of InP/ O_2 /ZnSe indicates that slightly thicker ZnSe shells are formed on that sample.

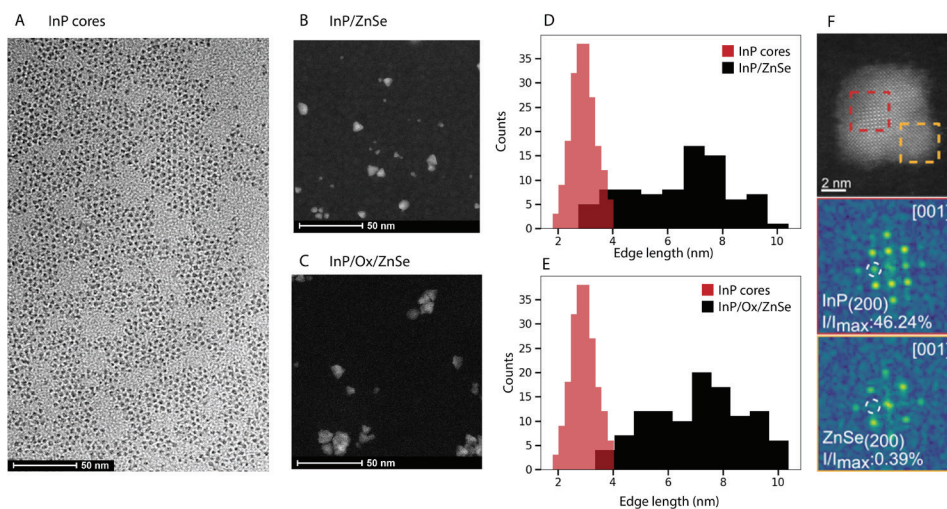


Figure A4.2. A) TEM images of InP core QDs. B), C) HAADF-STEM images of InP/ZnSe and InP/Ox/ZnSe QDs. D), E) Size histograms of InP core, InP/ZnSe and InP/Ox/ZnSe QDs edge lengths as measured from the TEM images. Mean edge lengths \pm 2 standard deviations were calculated from this distribution. InP cores: 2.9 ± 0.90 nm, InP/ZnSe: 6.5 ± 3.6 nm, InP/Ox/ZnSe: 7.1 ± 3.4 nm, indicating a slightly thicker shell on the InP/Ox/ZnSe sample in correspondence with absorption and XRD measurements. F) HAADF-STEM image of one the unoxidized QDs oriented along the 001 zone axis. The bottom insets show the FFT analysis in the center (red) and a corner (orange) of the QD, where a characteristic reduction in the intensity of the (200) spacing, highlighted with a dashed white circle, can be observed from the InP to the ZnSe cubic crystal structures.

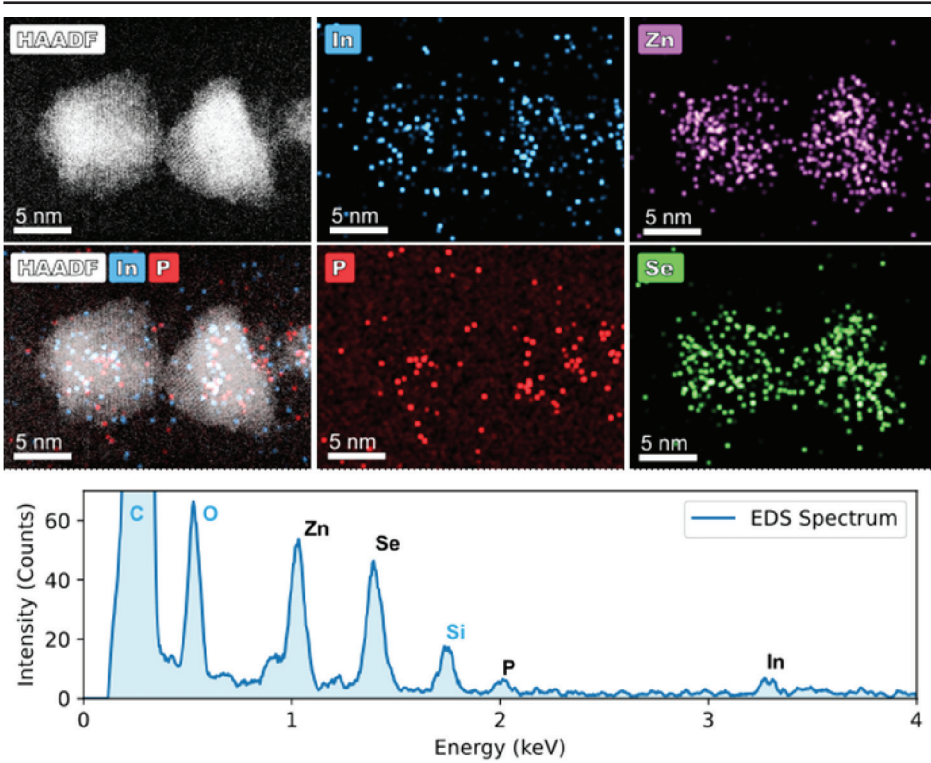
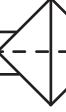


Figure A4.3. EDS analysis on 2 InP/ZnSe core-shell QDs. The elemental map distribution shows a concentration of In and P inside the nanoparticles as well as Zn and Se at the external parts. In, P, Zn, and Se peaks can be detected on the EDS spectrum together with C, O, and Si that can be ascribed to the specimen support.

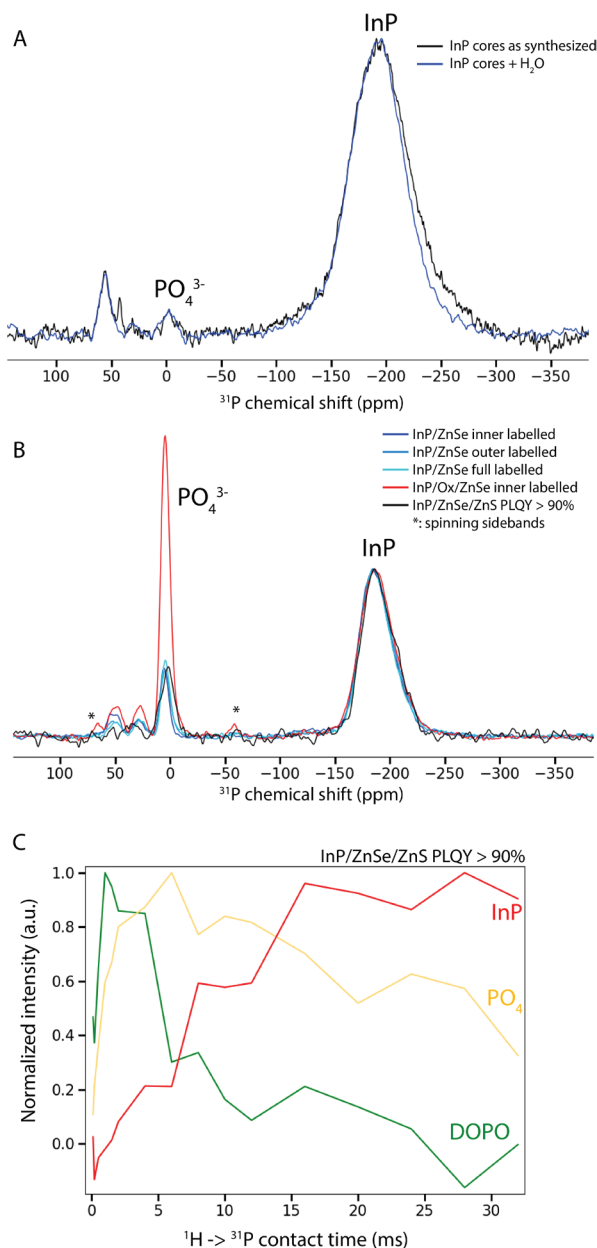


Figure A4.4. A) ³¹P ssNMR spectra of InP cores as synthesized and after attempted oxidation using water. Addition of water to the InP core solution at 120 °C did not result in an increase in PO₄³⁻ (peak around 0 ppm). B) ³¹P ssNMR spectra of various InP/ZnSe and InP/ZnSe/ZnS samples. Regardless of the shelling method, the ratio of integrals of PO₄³⁻/InP peaks is the same. Significant quantities of PO₄³⁻ are observed even on samples with PLQY > 90%. Only when the interface is oxidized on purpose using molecular O₂ is the amount of PO₄³⁻ significantly different.

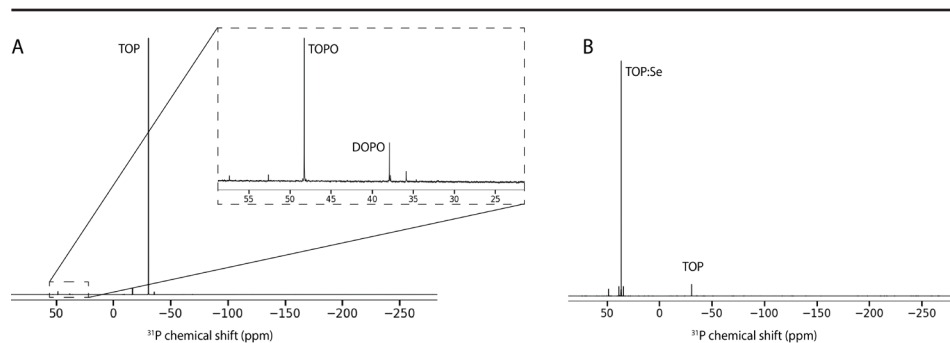


Figure A4.5. A) ^1H NMR of as-purchased TOP. TOPO and DOPO impurities can be observed.² B) ^1H NMR of elemental selenium dissolved in TOP. This compound is used as the Se precursor during shelling.

4

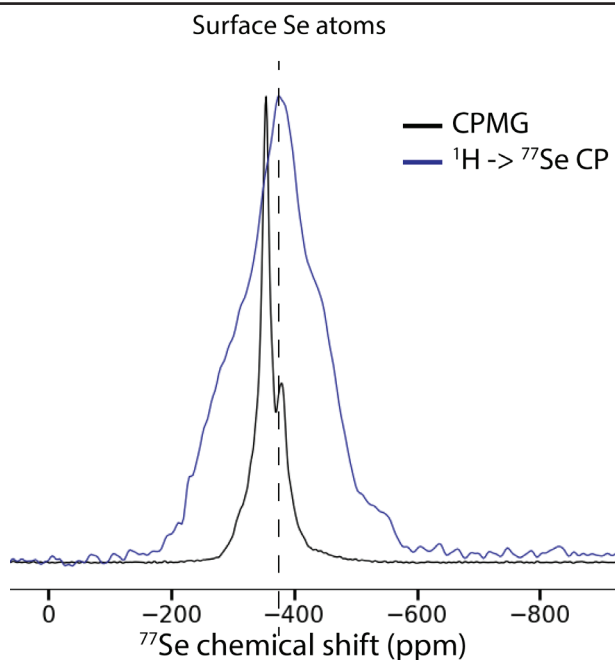


Figure A4.6. When $^1\text{H}\text{-}\rightarrow\text{}^{77}\text{Se}$ cross-polarization is employed (contact time = 5 ms), selenium signal of nuclei in close proximity to hydrogen (present only in surface ligands) is enhanced. It is observed that the signal around 380 ppm is enhanced, which is thus ascribed to selenium atoms at the outer ZnSe surface close the hydrogen-rich ligands. This is in agreement with REDOR measurements.

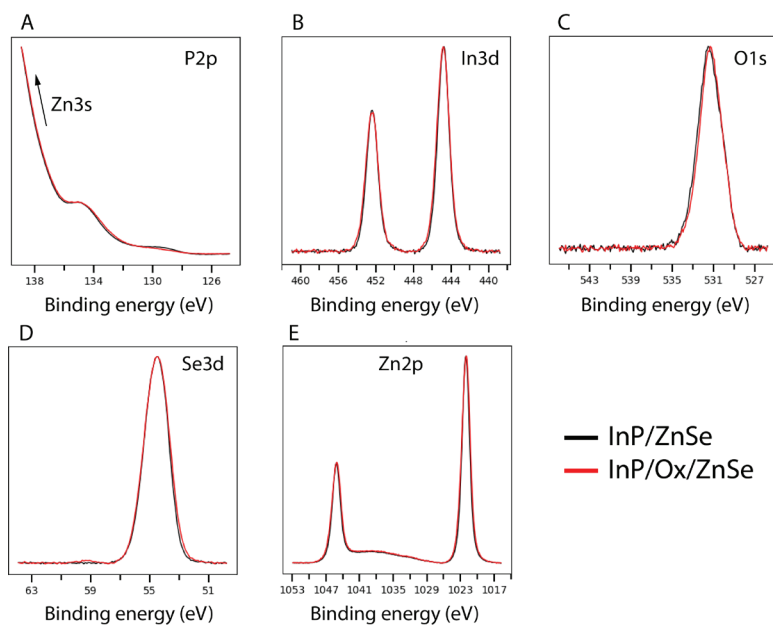


Figure A4.7. No difference is observed between the InP/ZnSe and InP/Ox/ZnSe in XPS data.

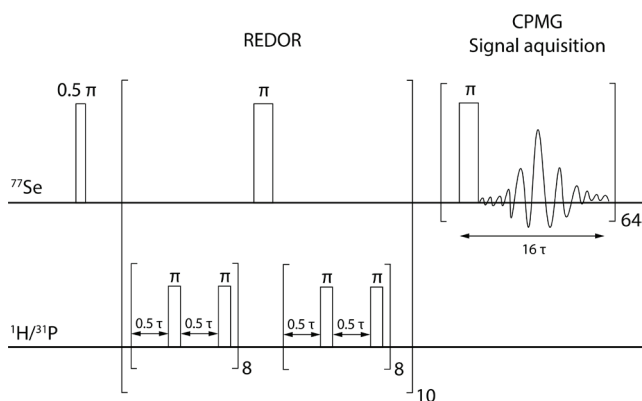


Figure A4.8. Pulse program employed to measure ^{77}Se in the InP/ZnSe QDs. All ^{77}Se measurements were performed using the CPMG detection sequence, employing 64 detection cycles with a 180° refocusing pulse in between. For the REDOR interaction measurements, the REDOR dephasing sequence was performed for 16 ms (160 rotor periods) before the signal acquisition was started. A long recycle delay (d1) of 300 s was always used in between scans.



A4.1: DFT calculations

This section describes the DFT calculations performed. First the bulk structures will be discussed, followed by the ZnSeInP interface model.

Calculations report chemical shieldings (σ), we relate these to experiment such that the bulk ZnSe chemical shifts (δ) coincide, i.e. $\delta_{calc} = \delta_{exp}$. We use the following formula:

$\delta_{calc} = \delta_{exp,ZnSe} - \sigma_{calc} + \sigma_{calc,ZnSe}$. For the bulk structures is obtained from an explicit calculation on ZnSe. However, for the interface we select the ^{77}Se shielding from the center of the ZnSe layer as instead.

A4.1.1: Bulk Structures

In addition to the k-point meshes specified below, for the geometry optimizations we used a cut-off energy of 520 eV with an electronic convergence criterion of 1E-07 eV (EDIFF) and ionic convergence of -1E-03 eV (EDIFFG). Pseudopotentials used were the VASP “Zn”, “In_d”, and “Se” PBE.54 POTCARs. Materials Project IDs of input structures and k-point meshes are listed below (table A4.1).

Chemical shieldings were calculated with a cut-off energy of 520 eV and electronic convergence criterion of 1E-10 eV, employing the same pseudopotentials as before.

Table A4.1. Input structures for geometry optimization and k-point meshes of geometry optimization and chemical shielding calculation for bulk structures.

Compound (Materials Project ID)	Space Group	k-point mesh (gamma-centered)	
		Geometry Optimization	Shielding Calculation
In ₂ Se ₃ (MP-612740)	$P6_1$	7×7×3	15×15×5
ZnIn ₂ Se ₄ (MP-22607)	$I\bar{4}$	8×8×4	20×20×10
ZnSe (MP-1190)	$F\bar{4}3m$	8×8×8	32×32×32

A4.1.2 ^{77}Se Chemical Shielding Tensors (including susceptibility)

We present the shielding tensors with the applied field direction along the columns and the induced field along the rows. For each tensor, the corresponding atom number in the compound’s POSCAR is mentioned along with its Wyckoff position.

In₂Se₃

Atom 13, Wyckoff 6a: x=0.68334, y=0.02465, z=0.63490

(ppm)	x	y	z
x	784.2	-716.0	-35.5
y	-357.0	1149.3	83.7
z	-164.7	-39.4	1315.6

Atom 14, Wyckoff 6a: x=0.62965, y=0.66687, z=0.45132

(ppm)	x	y	z
x	803.4	-576.7	-344.9
y	-436.6	781.3	-243.6
z	19.7	-87.4	1315.6

Atom 15, Wyckoff 6a: x=0.93650, y=0.27327, z=0.82881

(ppm)	x	y	z
x	300.4	-119.2	-40.4
yz	-286.4	475.8	-5.7
	3.5	8.1	1344.2

ZnIn₂Se₄

Atom 7, Wyckoff 8g: x=0.76082, y=0.28134, z=0.36989

(ppm)	x	y	z
x	1457.3	45.3	120.6
y	53.1	1473.3	-5.0
z	-4.9	-115.6	1413.1

ZnSe

Atom 5, Wyckoff 4d: x=0.75000, y=0.25000, z=0.25000

(ppm)	x	y	z
x	1789.1	0.0	0.0
y	0.0	1789.1	0.0
z	0.0	0.0	1789.1

A4.1.3: Interface

Starting from the optimized cubic ZnSe structure, an epitaxial [110] interface was constructed of 10 layers ZnSe and 10 layers of InP using the ZnSe lattice parameters.



Fixing the **b** and **c**-lattice vectors, we varied the length of the **a**-vector to find the optimal value. We used a cut-off energy of 520 eV with an electronic convergence criterion of $1\text{E-}07$ eV (EDIFF) and ionic convergence of $-1\text{E-}03$ eV (EDIFFG). Pseudopotentials used were the VASP “Zn”, “In_d”, and “Se” PBE.54 POTCARs. A $1\times 10\times 10$ Gamma-centered **k**-point mesh was used.

For the optimal structure, chemical shieldings were calculated with a cut-off energy of 520 eV and electronic convergence of $1\text{E-}10$ eV, employing the same pseudopotentials as before. The **k**-point sampling was increased to $2\times 16\times 16$.

The isotropic shieldings reported in the main text are obtained using averages of the xx , yy and zz components of the shielding tensors. In spite of the local cubic symmetry at the Se nuclei far from the interfaces their shielding tensors are not isotropic due to the presence of induced net interface currents at the ZnSe/InP interfaces.

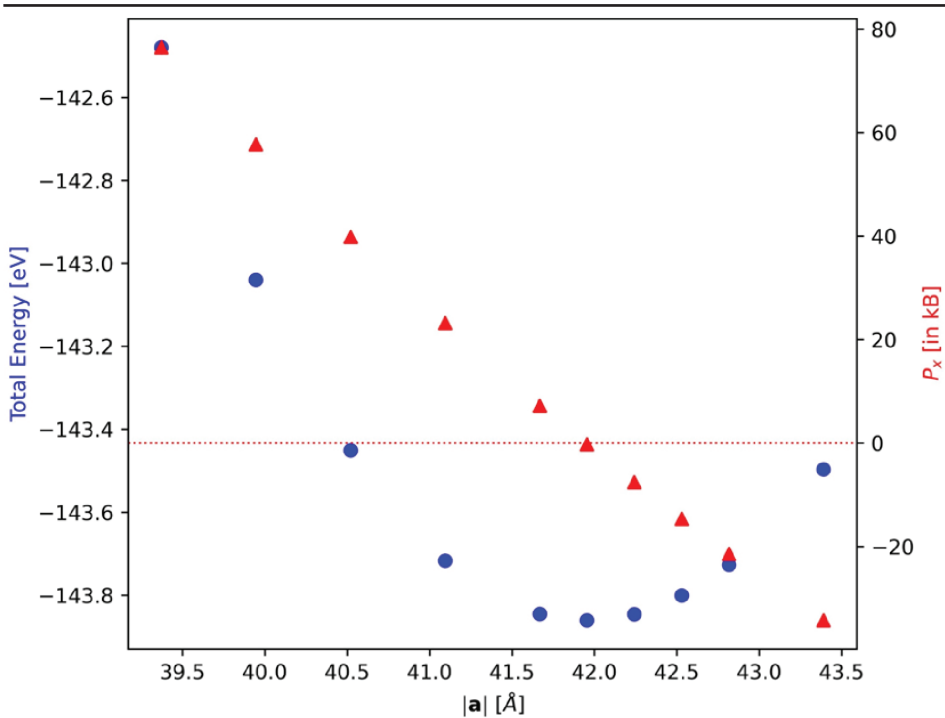


Figure A4.9. Total Energy [eV] (bullets) and xx component of the stress tensor P_x [kB] (triangles) versus **a**-vector length [Å] for the ZnSe/InP-interface model.

A4.1.4 ^{77}Se Chemical Shielding Tensors (excluding susceptibility)

Due to the net induced interface currents, we report the chemical shielding tensors below without susceptibility (i.e. $G=0$ component). We list only the first 5 Se atoms from the POSCAR.

Atom 11

(ppm)	x	y	z
x	1717.8	0.0	16.6
y	0.0	1625.2	0.0
z	38.6	0.0	1701.5

Atom 12

(ppm)	x	y	z
x	1679.9	0.0	18.5
y	0.0	1713.0	0.0
z	1.8	0.0	1681.5

Atom 13

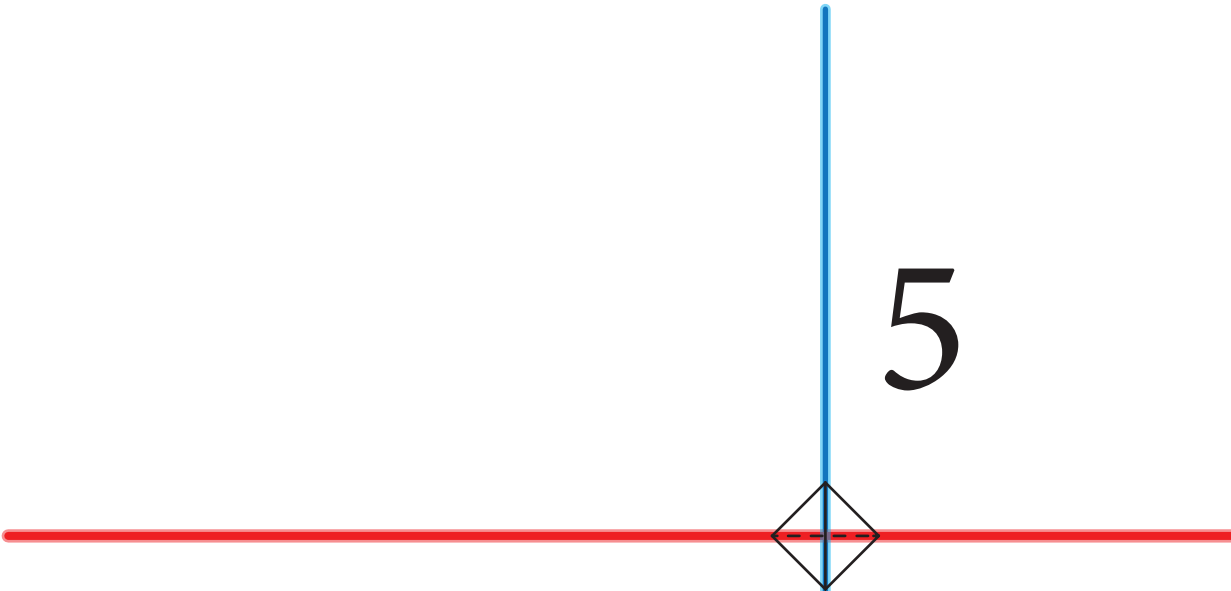
(ppm)	x	y	z
x	1749.8	0.0	2.4
y	0.0	1704.5	0.0
z	6.6	0.0	1716.1

Atom 14

(ppm)	x	y	z
x	1754.4	0.0	4.8
y	0.0	1750.9	0.0
z	1.7	0.0	1745.4

Atom 15

(ppm)	x	y	z
x	1760.2	0.0	-6.0
y	0.0	1758.4	0.0
z	0.0	0.0	1752.6



Electrochemically Doped
Quantum Dot Light-emitting
Electrochemical Cells without
Charge Injection Layers

This chapter is based on: Hua Chen, Reinout F. Ubbink, Rens A. Olsthoorn, Maarten Stam, Jesse 't Hoen, Tom J. Savenije and Arjan J. Houtepen. *Submitted*.

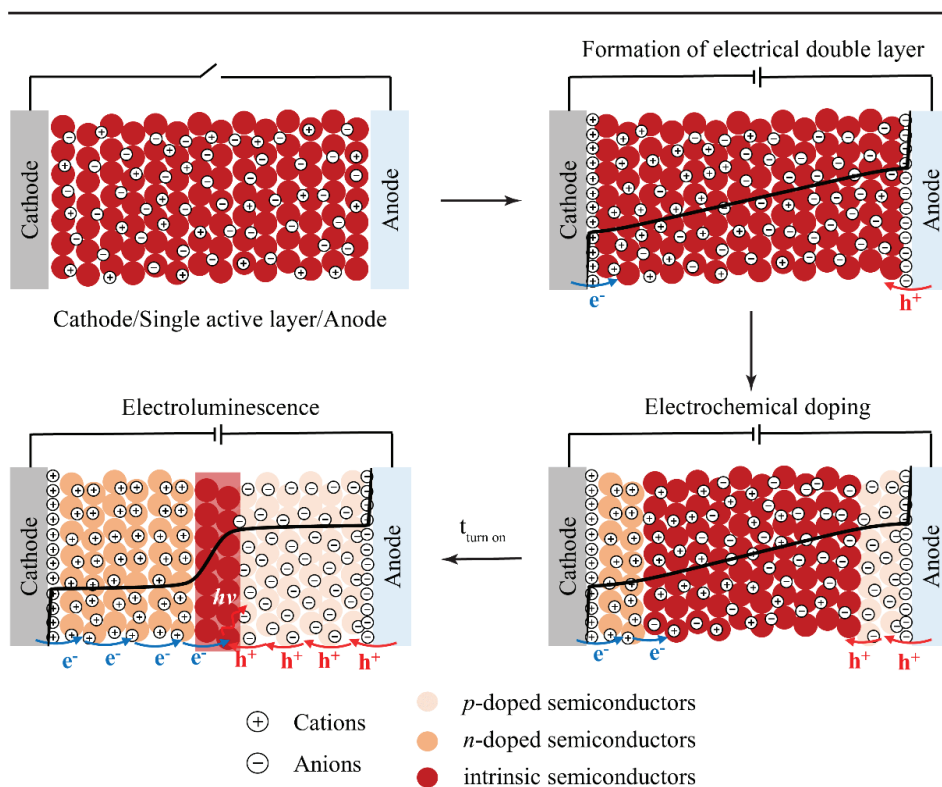


5.1. Introduction

Light-emitting electrochemical cells (LECs) offer distinct advantages over solid-state light-emitting diodes (LEDs).^{1,2} One of the benefits of LECs lies in their simple device architecture. An LEC consists of a two electrodes sandwiching a single active layer, which contains a light-emitting material mixed with mobile ions. As illustrated in Scheme 5.1, because of the mobile ions present in the LEC active layer, electrical double layers (EDLs) form at the interfaces between the metallic electrodes and the active layer. These EDLs significantly decrease, or even eliminate, the energy barriers for injection of electrons and holes into the active layer. When charges are injected into the light-emitting material, the additional charge is compensated by mobile ions. Electrons are compensated by a flow of cations towards the negative electrode, while holes are compensated by anions. This in situ electrochemical doping³ results in the formation of n-type and p-type regions, which readily facilitates charge transport. A p-i-n junction is formed in the middle of the device, where the injected carriers radiatively recombine to obtain electroluminescence (EL).^{4,5} The EDLs and electrochemical doping eliminate the need for complex multilayer structures, while in efficient solid-state LEDs, it is necessary to include several charge injection and transport layers.⁶⁻⁹ The simplicity of this device structure can lead to reduced manufacturing costs and improved device scalability. Furthermore, there are no inherent restrictions on the electrode materials of LECs, since the potential drop in the EDL eliminates injection barriers between the electrodes and the active material, offering opportunities to implement air-stable electrodes.

Polymers and ionic transition metal complexes (iTMC) have been the most widely chosen electroluminescent materials in LECs.¹⁰⁻¹³ However, relatively low photoluminescence quantum yield (PLQY), difficulty in tuning emission colors and poor stability impede the commercialization of LECs.¹⁴⁻¹⁶ Colloidal quantum dots (QDs) offer opportunities to address the aforementioned issues due to their size-dependent emission spectra, near-unity PLQY and high color purity for light-emitting applications.¹⁷⁻²¹ There have been attempts to fabricate QD-based LECs (QLECs) using CdSe/CdS, InP/ZnSeS and CuInS₂/ZnS QDs as electroluminescent materials in the active layer, by blending these QDs with poly-(N-vinylcarbazole) (PVK) as charge transporting matrix.²²⁻²⁴ PVK is widely used as a host to transport charges to the electroluminescent guest, which complicates the charge transfer.^{25,26} Emission from PVK also broadens the emission spectrum.²⁴ The additional charge transport materials result in extra voltage losses, since the PVK bandgap is much larger than that of the emitting QDs, hindering the development of LECs as simple, scalable and cheap light-emitting devices.

More importantly, due to the use of charge injection layers the working mechanism of QLECs has remained elusive. In the aforementioned studies, the addition of mobile ions to the devices resulted in shorter turn-on times and higher luminance. This demonstrates that the formation of EDLs facilitates charge injection.²³ However, in situ electrochemical doping of QDs, which facilitates charge transport and makes QLECs different from other light-emitting devices, has not been experimentally illustrated so far. The addition of charge injection and transport layers makes it difficult to directly probe the charge injection into QDs and confirm electrochemical doping of the material.



Scheme 5.1. Working mechanism of LECs, illustrating the formation of electric double layers (EDLs), electrochemical doping and EL. The potential distribution across the active layer is shown in black solid lines. EDLs are first formed by the accumulation of mobile ions at the electrodes. This reduces the injection barrier of charges, which are subsequently injected into the material. The additional charge is compensated by the flow of oppositely charged ions, resulting in net *n*- and *p*-type doped regions. These doped regions facilitate charge transport to the intrinsic region in the middle of the device, where holes and electrons recombine to emit light.

It is known that films of QDs can be electrochemically doped,²⁷⁻³⁰ that the doped QD films can transport charge efficiently if short enough ligands are used^{3, 31-36} and that they can exhibit efficient EL.^{6, 37, 38} In principle, dense QD films could play all roles needed in an LEC. However, until now, no EL has been obtained from QLECs where no additional charge injection or transport materials were employed.

In this work, we fabricated QLECs with a simple device structure of ITO/QD active layer/Al, without adding charge injection or transport layers. In the active layer, highly luminescent ligand exchanged CdSe/CdS/ZnS QDs were used, while lithium trifluoromethanesulfonate (LiCF_3SO_3) in polyethylene oxide (PEO) was used as electrolyte. These devices reproducibly show EL from the QDs. We find that there is only minor shift in the EL spectra at various voltages. The peak external quantum efficiency (EQE) is 0.024 %.



Cyclic voltammetry and operando PL measurement were used to investigate the working mechanism of our devices. We compare the experimental characteristics to drift-diffusion simulations and conclude that our devices operate as LECs rather than diodes. Reversible PL quenching during operation demonstrates that electrochemical doping takes place, which is typical of LECs.

Although our devices can be charged from both sides, no EL is obtained when Al is the anode. We hypothesize that the p-type doping is inefficient, and thus the recombination zone is close to the anode, where EL is quenched by metallic Al electrode. To gain further understanding of charge injection and transport, we performed spectroelectrochemical (SEC) measurements on the QD films deposited on the ITO electrode. The results indicate that electrons can be injected into QDs to form the n-type region in QLECs while there is no clear spectroscopic evidence of hole injection. Therefore, even though hole injection is achieved in the devices through the EDL, achieving sufficient hole injection is the main challenge to improve the device performance in QLECs.

5

2. Results and Discussion

Highly luminescent red-emitting core/shell/shell QDs were synthesized by sequential shelling of approximately 6 monolayers of CdS and 2 monolayers of ZnS on CdSe QDs (see appendix for details). The thin ZnS shell is essential to remove trap states localized on the CdS surface and enhance the electrochemical stability of the QDs against cathodic degradation.³⁹ During the shelling, sulfur-octadecene (S-ODE) was used as sulfur source instead of thiols to have only oleate (OA) ligands on the surface of QDs, simplifying the ensuing ligand exchange procedure. The photoluminescence quantum yield (PLQY) of the as-synthesized QDs is 87% with an emission peak maximum at 649 nm (Figure 5.1A). The broadened peak in the NMR spectrum of the as-synthesized QDs, observed at 5.3–5.4 ppm is typical for the protons of the double bond in bound oleate ligands (Figure 5.1B).⁴⁰ The X-ray diffractogram of QDs demonstrates a zinc blende crystal structure (Figure 5.1C). TEM images reveal that QDs are octahedral with a size of around 10 nm (Figure 5.1D).

To realize efficient charge transfer between QDs in LECs, the long-chain insulating ligands on the surface of the as-synthesized QDs must be removed or replaced by shorter ligands. A ligand exchange (LE) is also necessary to transfer QDs into polar solvents to ensure the miscibility of QDs and electrolyte. However, LE often results in the formation of new traps on the surface of the QDs and therefore a drop in PLQY.^{41–45} To maintain the PLQY after LE as much as possible, we used $\text{In}(\text{NO}_3)_3$ to perform the LE, a method recently developed by Talapin et al.⁴⁶ The original oleate ligands are removed, leaving a positively charged QD surface, which together with loosely bound NO_3^- ions ensures stable dispersion in polar system, as demonstrated by a two-phase LE, where QDs are transferred from hexane (top phase) to N,N-dimethylformamide (DMF) (bottom phase) (inset of Figure 5.1A).

The stripping of oleate ligands was confirmed by ^1H NMR spectroscopy. After LE, this peak is hardly observed, indicating the complete removal of oleate ligands (Figure 5.1B). The absorption and PL spectra remain the same after LE, while the PLQY is reduced to 75% (Figure 5.1A).

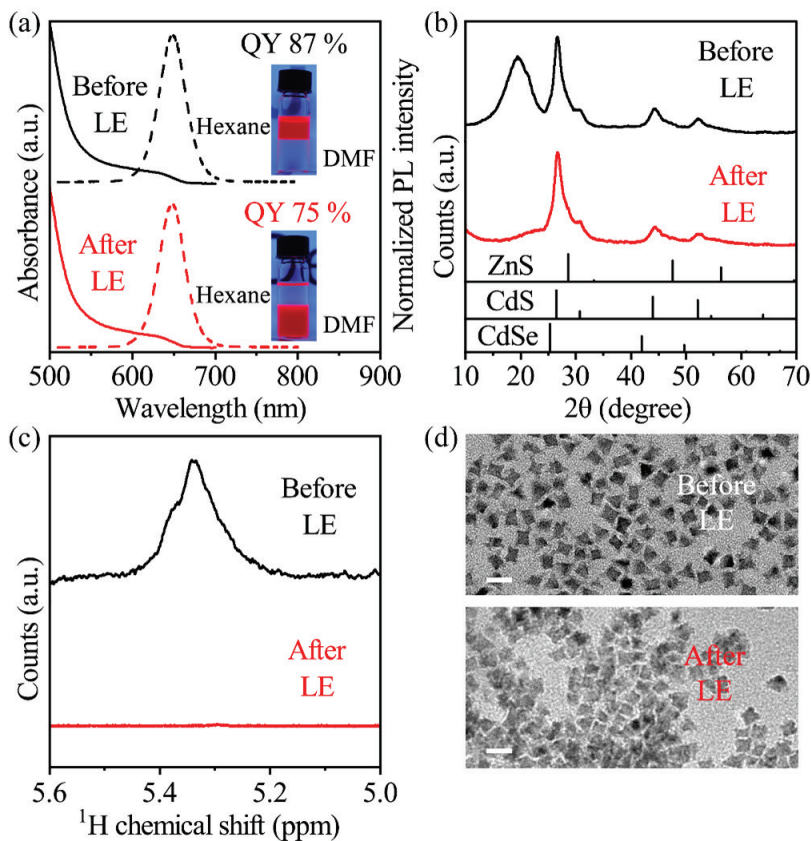


Figure 5.1. A) Absorption (solid lines) and PL (dash lines) spectra, B) ^1H NMR spectra, C) X-ray diffraction patterns, and D) TEM images of CdSe/CdS/ZnS QDs before and after ligand exchange. Inset in A): Photographs of QDs transferred from hexane (top) to DMF (bottom) after two-phase ligand exchange. Scale bars in D): 20 nm.

We ascribe the drop in PLQY to the possible removal of Z-type zinc oleate ligands from the surface, resulting in some trap states on the surface.⁴⁶ The full width at half-maximum (FWHM) of the PL spectra are 36 nm before and after the treatment, indicating an unchanged narrow size distribution and high color purity.

The X-ray diffractogram reveals no changes in crystal structure after LE. The peak located at around 19° is assigned to the ordered oleate ligands on QDs, which disappears after the ligand exchange, indicating the removal of organic ligands (Figure 5.1C).⁴⁷ As shown in the TEM images, the morphology of QDs is retained while the distance between QDs is decreased due to the removal of long-chain ligands (Figure 5.1D). In conclusion, after ligand exchange, QDs are highly luminescent and form stable colloidal dispersions in DMF, after which they are ready for the fabrication of QLECs.

QLECs with a device structure of ITO/QD active layer/Al were fabricated (Figure 5.2A).



In the active layer, ligand exchanged QDs were combined with PEO and LiCF_3SO_3 ions. The active layer was directly spin coated onto an ITO substrate. The Al back contact with a thickness of 100 nm was thermally evaporated onto the QD active layer (see section 5.4 for details). EL was obtained from this simple three-layered QLEC, as shown in the inset of Figure 5.2B.

The current density-voltage-luminance (J-V-L) characteristics of the red-emitting QLEC, with ITO as the positive electrode, can be divided into three stages: Below 1.5 V only a low background current is observed (first stage, marked green). The current density then increases exponentially between 1.5 and 2.5 V applied potential (second stage, marked blue). Above 2.5 V, the current density is almost constant (third stage, marked orange) until it starts increasing exponentially again at potentials $> 5\text{V}$.

To understand this behavior we have also modelled the J-V response of the QLECs using drift-diffusion simulations, based on those by van Reenen *et al.*⁴⁸ In these simulations, given a voltage program, the current response of the device is calculated based on drift-diffusion movement of electrons, holes, anions and cations. Simulations were performed using any known parameters obtained from the experiments, then fitted to the experimental data to optimize the mobilities of the charge carriers for this specific case. The simulated J-V response is shown in Figure 5.2B and exhibits the same 3 stages. Concentration profiles from the simulation (Figure 5A.1) provide insight into the mechanisms underlying these 3 stages.

Below 1.5 V, the potential is not high enough to inject any carriers into the QDs. The only current is from formation of the EDLs. When the potential is higher than 1.5 V, electrochemical doping starts to occur, which results in a significant increase in current density over a short potential range. Above 2.5 V, the electrochemical doping process is completed, and the current density levels off. At this point the p-i-n junction is formed, and EL is observed due to charge recombination in the intrinsic zone. At 5 V, the luminance and the external quantum efficiency (EQE) reaches the maxima of 0.1 cd/m^2 and 0.024%, respectively (Figure 5.2C). In the simulations, the current density above 2.5 V increases only very slightly for higher applied potential, due to slight redistribution of the electrochemical doping at higher potentials. In the experimental device, current density is also nearly constant up to a potential of 5V. Above 5V, current density increases exponentially again while the luminance stays constant, resulting in a drop-off of the EQE. This implies leakage channels are opened by non-ideal processes above 5V.

When the device is scanned from 0 V to 9 V, the EL spectra are 9-12 nm red shifted compared to PL spectrum. The FWHM of EL spectra is increased to 45 nm (Figure 5.2D). In quantum dots light-emitting diodes (QLEDs), a red shift of EL spectrum has been reported due to inter-dot interactions and electric-field-induced Stark effects.^{49, 50} However, we also consider that electrochemical doping results in the preferential charging of the larger QDs in the ensemble, which subsequently emit slightly red shifted compared to the PL, where all QDs are excited. This does however not explain the increasing redshift with increasing bias. Rather we tentatively attribute the latter to a changing position of the emission zone in the active layer, leading to the varying enhancement of the emission in

the cavity that is formed by the Al and ITO contact. This so-called micro-cavity effect, is often invoked to explain shifts in EL in polymer based LECs, where it is so severe that the EL spectrum changes significantly compared to PL spectrum due to the wide emission spectra of polymers.^{51, 52} Due to the narrow emission of QDs, the high color purity is maintained in QLECs even with the micro-cavity effect. This makes QDs promising candidate for LECs, compared to electroluminescent polymers.

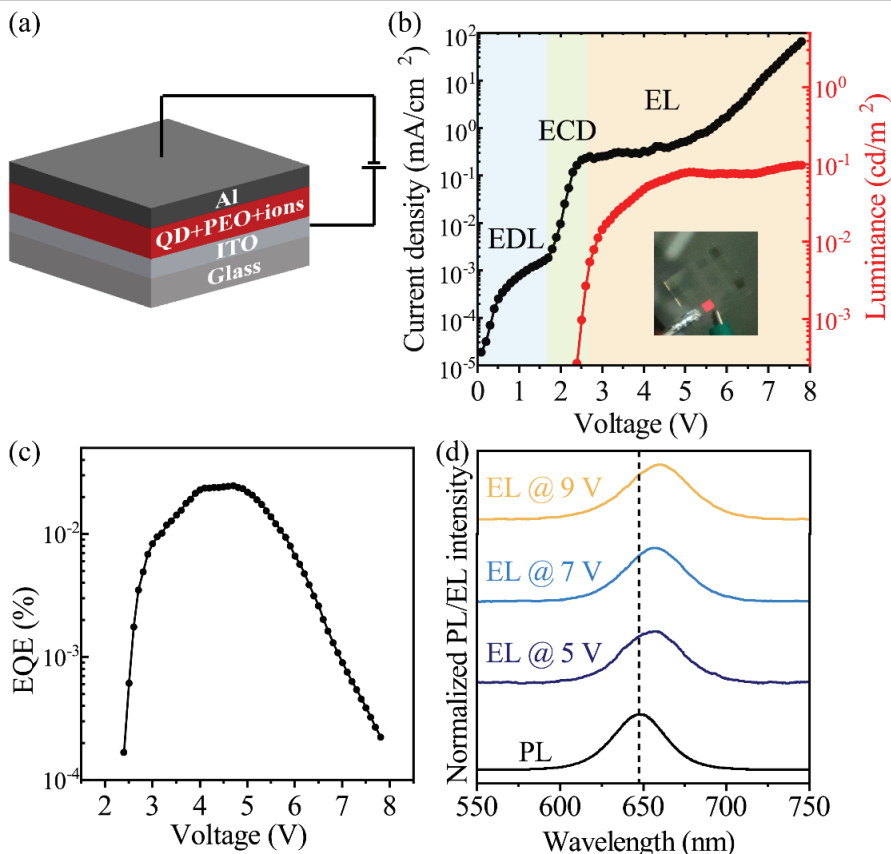


Figure 5.2. A) Device structure the QLECS: ITO/QD active layer/Al. B) Current density-voltage-luminance curves. EDL, ECD and EL denote electrical double layer, electrochemical doping and electroluminescence, respectively. Inset: photograph of a red-emitting QLECS in operation. C) EQE and D) normalized PL spectrum of QDs dispersion and normalized EL spectra of QLECS at various voltages. ITO were biased positively in these measurements.

To investigate the working mechanism of the QLECS we performed both constant bias chronoamperometry and cyclic voltammetry experiments. Figure 5.3A shows an experimental cyclic voltammogram (CV) of the QLECS, where a negative potential denotes that ITO is biased positively while a positive potential denotes that ITO is biased negatively. Significant current density can be observed that for both negative and positive



applied bias, unlike in a diode. This symmetrical voltage dependence is also characteristic of LECs, because the in-situ p-i-n junction can be formed in both directions. When the device is scanned to negative bias, the n-doped region is formed near the Al electrode, while the p-doped region is formed on the side of the ITO electrode. When the bias is scanned back to 0 V, the device returns to its intrinsic state as ions diffuse back across the whole device. Then when the bias becomes positive, the p-i-n junction is formed again with a reversed orientation.

The constant bias measurement, shown in the top panel of Figure 5.3B, shows three distinct parts. First, a quick rise of the current density is observed. Second, the current density drops, and finally, current density reaches a steady state value. This characteristic current response to constant applied bias (observable rise, peak and steady state) indicates that the device undergoes electrochemical doping and is indeed working as an LEC. The simulated results of the constant bias response at -5 V, shown in the bottom panel of Figure 5.3B, shows the same three contributions as observed in the experiment.

5

Snapshots of concentration profiles taken during the drift-diffusion simulations (Figure 5.3C) provide insight into the subsequent processes occurring during the constant-bias experiment. Before electron and hole injection into the active layer occurs, EDLs first need to be formed next to the electrodes. However, even when ion mobilities are low, EDL formation takes place on timescales of $< 10 \mu\text{s}$ in the simulations, too fast to observe in the experiment. As soon as the potential drops in the EDLs are large enough to allow charge injection, the doping process starts. The speed of this process is limited by the mobility of the slowest charge carrier, which determines the response time of the device. The current density increases quickly, then reaches a maximum as the n and p doping fronts meet. After this, the doping process still continues, as the concentration profiles have not yet achieved the optimal charge distribution. During this period, increased electron-hole recombination is observed, since some drift transport of electrons and holes still occurs due to remaining electric fields, which results in a peak in the current density. Only after the doping process is fully completed and the steady-state doping profile is achieved does the current density reach a steady state value.

In the steady state situation, the current density is limited by diffusion of the electrons and holes in the doped zones. Since the current is constant over the device, this implies a constant gradient of the doping (to allow an equal diffusion current everywhere) and hence a linear concentration profile of ions and electrons and holes. The position of the junction at steady state is dependent only on the ratio of electron/hole mobilities. The ion mobility determines the response time of the device, but is irrelevant to the steady state current. The concentration profile snapshots in Figure 5.3C show a simulated device where the anion mobility is much lower than the cation mobility, but this affects the junction position only while the doping process is incomplete. After completion of the doping process, the junction is positioned in the middle of the device since the electron and hole mobility are equal in the simulation.

The occurrence and speed of in-situ electrochemical doping in LECs can also be confirmed experimentally by analysis of the PL intensity as a function of the applied bias.

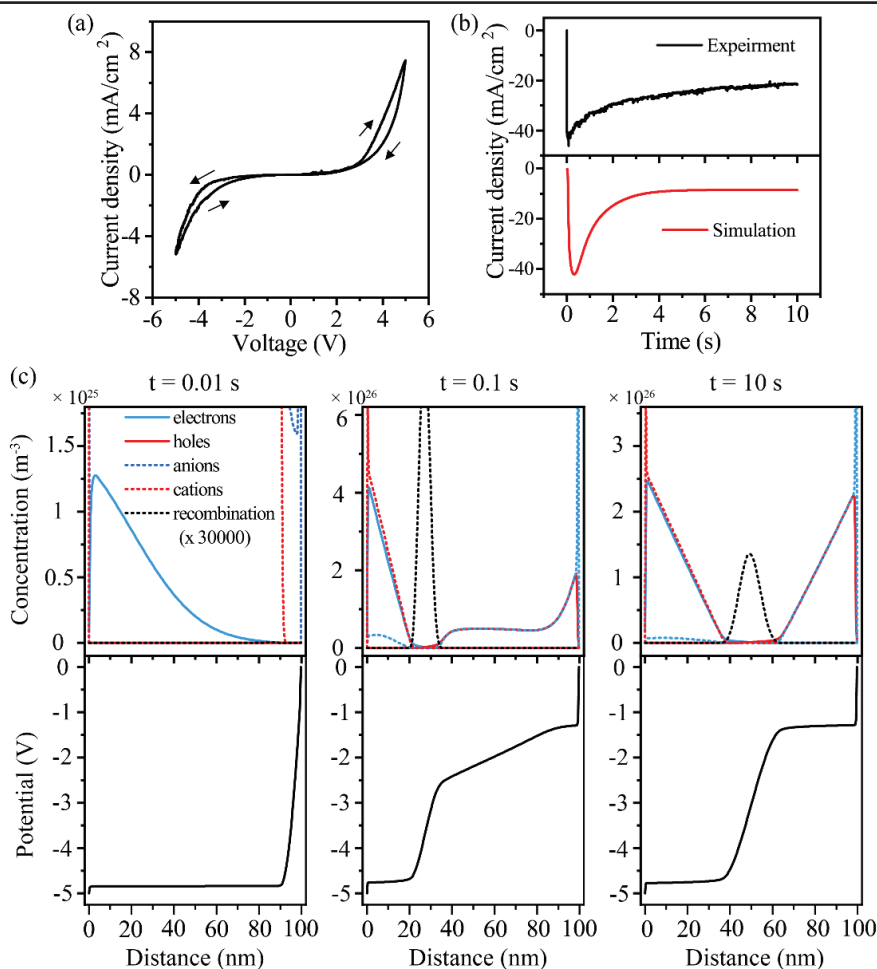


Figure 5.3. A) Cyclic voltammogram of a QLEC. B) Experimental and simulated electrical response of the device under a constant bias of -5 V. The ITO electrode was biased positively. C) Development of the n-i-p junction in an LEC under a constant bias of -5 V. Top panel: Distribution of carriers, ions and recombination concentrations from cathode to anode. Bottom panel: Distribution of electrostatic potential from cathode to anode.

Upon doping, the absorption of QDs is bleached and the PL is simultaneously quenched due to Auger recombination.^{27, 39, 53} To observe if electrochemical doping takes place in our devices, we therefore measured the PL of the QDs in a QLEC device in operation. In these measurements, a laser with a wavelength of 405 nm was used to illuminate the device from the glass substrate side and the PL intensity was monitored by a fiber-coupled spectrometer, synchronized with the device operation (Figure 5.4A, section 5.4). In this measurement, the device was driven by cyclic voltammetry.

We firstly carried out operando PL and EL measurement when ITO electrode was biased positively. A typical EL evolution under cyclic potential sweep is shown in Figure 5.4B.



EL starts around 2.5 V and increases with increasing potential up to the turning point of 5 V. PL was measured for 3 cycles. The onset of quenching in PL is around 1.3 V and the PL intensity is decreased to 11 % of the original intensity at 5 V. The quenching in PL can be divided into two regions as indicated by the slope. From 1.3 V to 2.5 V, the PL is rapidly quenched due to electrochemical doping. Beyond 2.5 V, the doping density does not increase much and the injected carriers radiatively recombine in the emission zone. This clearly proves that QDs become electrochemically doped in the biased QLEC. When scanning back, the PL intensity is slowly recovered. After 3 cycles, the devices were biased at 0 V for 30 minutes. The PL intensity recovers to 96 % of the original value, indicating that electrochemical doping is reversible (Figure 5.4C). The long recovery time can be ascribed to the slow emptying of charges in deep trap states or an overpotential of electrochemical reactions on the surface.³⁹

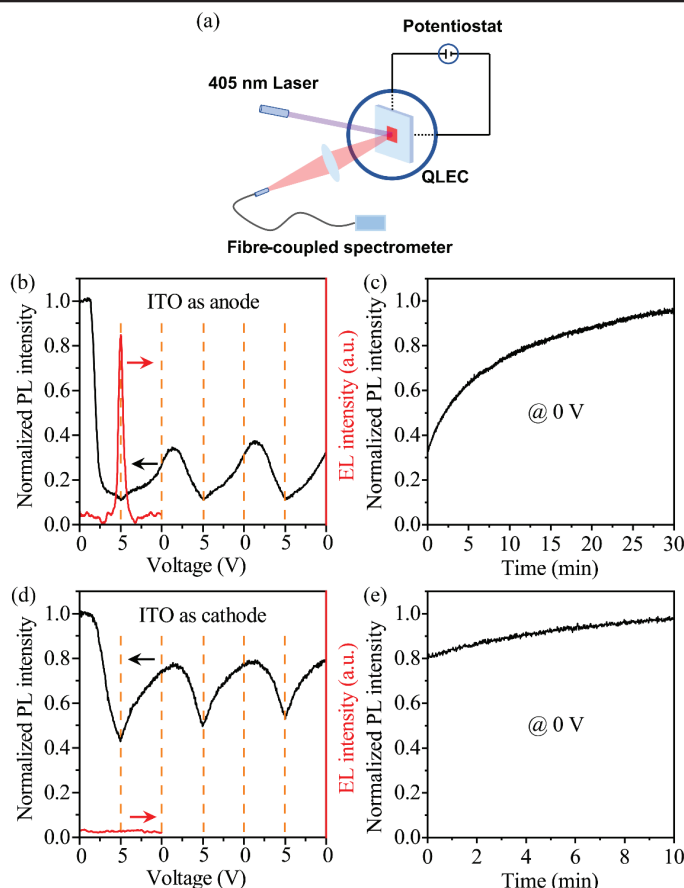


Figure 5.4. A) Scheme of experimental setup for operando PL measurement. Operando PL (black solid lines) and EL (red solid lines) measurement when B-C) the ITO electrode was the positive anode and D-E) the ITO electrode was the negative cathode. During the measurement, the devices were electrically scanned from 0 V to 5 V and back to 0 V for three cycles and then connected at 0 V for 10-30 min.

In an ideal LEC, the device performance does not depend on the Fermi levels of the contacts, since the EDLs that form can provide the required potential drop for electron and hole injection. There is in principle no limit to the magnitude of the potential drop in the EDLs, hence any metal could be used as anode or cathode. This also implies that the electrical and optical response of LECs should be symmetric with respect to positive or negative biasing. In our devices however, EL was not measurable when the ITO electrode was biased negatively (Figure 5.4D), even though significant current passed through the device as observed in Figure 5.3A. The electrochemical doping in this case was investigated by monitoring PL intensity during operation. The onset of PL quenching is found at 1.6V, which is larger than that when the ITO electrode is charged positively. The PL intensity is only quenched to 43 % of the original intensity at 5 V in the first cycle (vs. 11 % PL left at 5 V when ITO electrode is biased positively). The electrochemical doping process is similarly reversible and 98% of the original PL intensity is recovered when the device is biased at 0 V for 10 min (Figure 5.4E). Apparently the device does not respond fully symmetric to the electrical bias.

We hypothesize that because of difficulties with hole injection (see below) the emission zone is close to the anode. Therefore, when the ITO electrode is charged negatively, the emission zone is closer to Al electrode. The emission of photons depends on the density of optical modes in the surroundings, which is much higher in the metal, than that in the active layer and the ITO electrode, as the dielectric constants of metals are infinite. We will come back to this point below.

In a QLEC device, the formation of both n- and p-type doped regions are crucial for device operation. Although the operando PL measurements illustrated in Figure 5.4 indicate electrochemical doping of the QDs, PL quenching resulting from electron doping and hole doping are hard to separate. To distinguish between electrochemical p- and n-type doping, we instead, investigated the electrochemical doping process in QDs separately for electrons and holes using SEC measurements.^{28,39,54} Here a three-electrode electrochemical cell is used where the working electrode and counter-electrode (anode and cathode) are physically separated by the electrolyte solution. By manipulating the Fermi level of the working electrode, either electrons or holes can be injected into the QD film.

For these SEC measurements, ligand exchanged CdSe/CdS/ZnS QDs were drop cast on ITO electrodes. To probe the electrochemical doping in our devices, we tried to use the same electrolyte environment for the SEC measurements. However, due to the high melting point of the PEO (Mv ~ 5000000 g/mol) used in the LEC device, it is not possible to perform the SEC measurements. Instead, we chose PEO with a smaller molecular weight of 600 g/mol as the solvent, ensuring chemical similarity while allowing liquid electrochemical measurements at room temperature. During cyclic voltammetry, a white light source and a laser with a wavelength of 405 nm were used to probe and excite the QD film alternately and the corresponding absorption and PL spectra were collected by a spectrometer (section 5.4, Figure A5.3). When a negative potential is applied to the working electrode, the absorption bleaching of CdSe 1S transition (around 633 nm) and CdS localized transitions (around 500 nm) is observed, clearly indicating the electron injection into QDs (Figure 5.5B). A corresponding quenching in PL due to non-radiative



Auger recombination is also present (Figure 5.5C). The absorption bleaching is reversible since it fully recovers when the potential is scanned back to the open circuit potential, demonstrating that the QDs are not degraded in three cycles (Figure 5.5D).

At positive potentials, no clear and reversible absorption bleaching or PL quenching of the 1S absorption is observed (Figure 5.5F-H). There are some fluctuations in the differential absorption and PL spectra during the cyclic voltammetry. However these do not correlate with the expected onset of hole injection (i.e. the valence band potential). Moreover the absorption changes appear over the entire recorded spectrum, rather than showing a bleach of the band edge absorption, as expected for hole injection. Therefore, the changes in the spectra we observe here are not due to hole injection. Rather, we tentatively ascribe it to a change in the refractive index of the QD film in the electrolyte solution during charging. We also performed the SEC measurements in 0.1 M LiClO₄ acetonitrile electrolyte solution, one of the most widely used electrolyte solutions for electrochemical doping of QDs. As shown in Figure 5A.3, electron injection under cathodic current is clearly observed in absorption and PL spectra, but there is no clear spectroscopic indication of hole injection. It appears that the absence of hole injection does not depend on the electrolyte solution, but that it is an intrinsic property of CdSe-based QDs.

Both electron and hole injections are required for LECs to exhibit EL. In polymer-based LECs, electron injection is typically less efficient than hole injection, causing the emissive intrinsic zone to be close to the cathode. In that case the electrode-induced quenching limit the device performance. Similarly, inefficient hole injection in QLECs will cause the emission zone to be close to the anode. Since we are not using any hole injection (i.e. electron blocking) layer, this could result in electron leak currents when electrons pass through the junction directly into the positive electrode. Thus, although the EDL facilitates some hole injection in QLECs, as evidenced by the observation of EL, boosting hole injection further is suggested to be the most promising avenue to increase device performance, by increasing the width of the p-doped region of the film and thereby moving the junction further away from the positive electrode, reducing electron leak currents.

5.3. Conclusion

In conclusion, this proof-of-concept work highlights the possibility of employing QDs as the only active material in LECs, wherein they combine the roles of electrochemical doping, charge transfer and electroluminescence. Simple three-layered QLECs were fabricated without any charge injection and transport layers using highly luminescent, ligand-exchanged CdSe/CdS/ZnS QDs. These devices reproducibly show band edge EL. The shift of EL spectra with changing voltage is minor and a high color purity is maintained. Experimental and simulated I-V curves indicate that our devices work as LECs rather than diodes. Operando PL measurements demonstrate the occurrence of electrochemical doping. The external quantum efficiency of the QLECs is so far limited to 0.024%. Spectro-electrochemical measurements demonstrate that electrochemical electron doping is efficient, but hole doping is nearly absent in these CdSe/CdS/ZnS QDs, significantly limiting the efficiency of the QLECs. Improvements in the efficiency and stability of hole injection are needed to enhance the efficiency of QLECs to a level where they may become relevant for lighting applications.

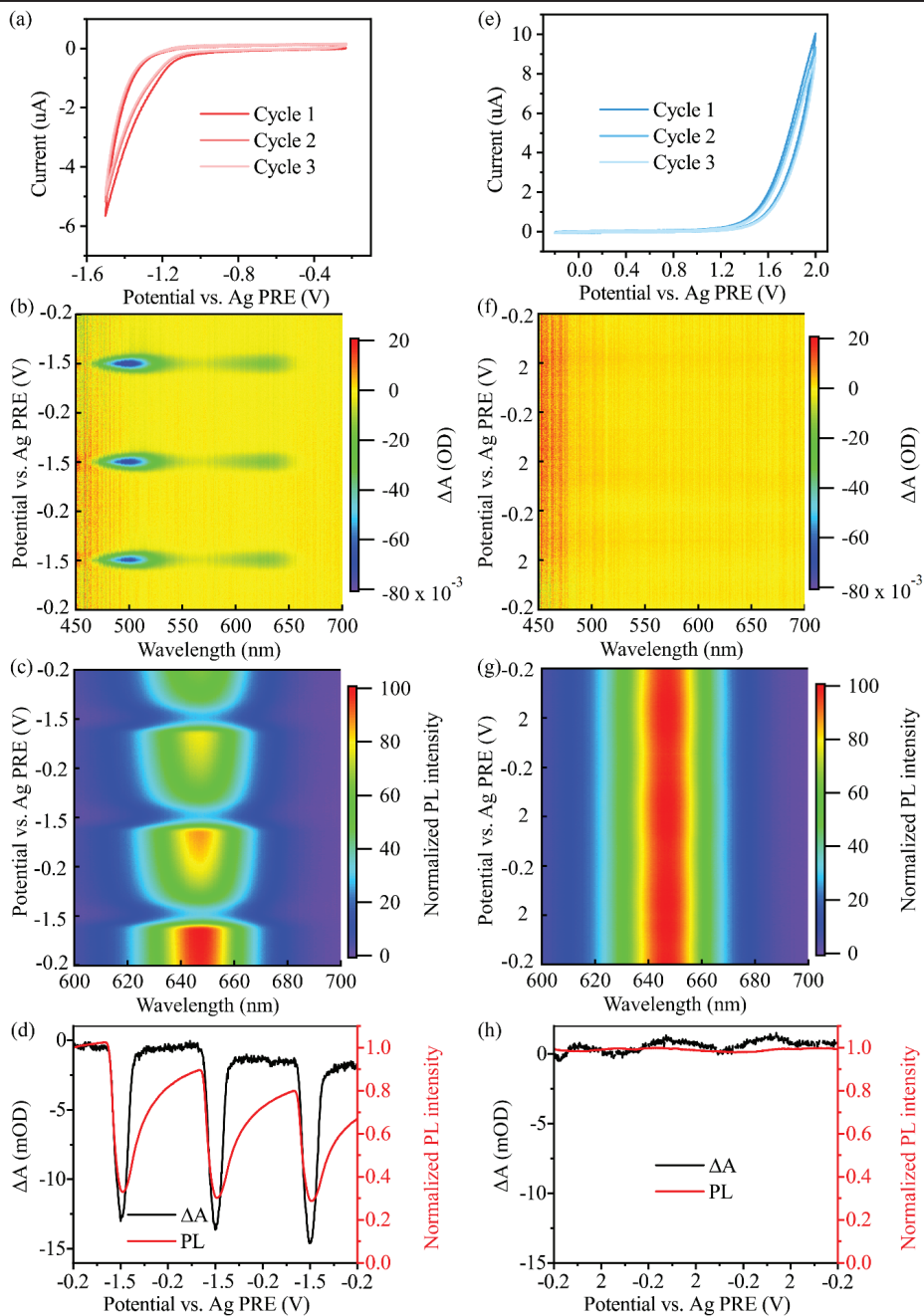


Figure 5.5. Cyclic voltammograms, 2D differential absorbance, 2D normalized PL and 1D plot of differential absorbance at the CdSe 1S transition and PL maxima of QD films/ITO scanned A-D) negatively and E-H) positively in the 0.1 M LiCF₃SO₃ PEO (Mn ~ 600 g/mol) solution. The scan rate was 5 mV/s.



5.4. Methods

Materials

Indium nitrate hydrate ($\text{In}(\text{NO}_3)_3$, 99.999%), poly(ethylene oxide) (PEO, $M_v \sim 5 \times 10^6$ g mol^{-1} and $M_n \sim 600$ g mol^{-1}), lithium trifluoromethanesulfonate (LiCF_3SO_3 , 99.995 %), lithium perchlorate (LiClO_4 , battery grade), ferrocenium hexafluorophosphate (FcPF_6 , 98 %, BLDpharm), and anhydrous *N,N*-dimethylformamide (DMF), 99.8 %, anhydrous acetonitrile (MeCN, 99.8 %) were all purchased from Sigma-Aldrich unless otherwise stated and used as received. Aluminum (Al) pellets (99.99 %) for thermal evaporation were purchased from Kurt J. Lesker Company. Indium-doped tin oxide (ITO)/glass substrates (7-10 Ω/m^2) for QLECs and spectroelectrochemistry (SEC) measurements were purchased from MSE Supplies.

Ligand exchange

The ligand exchange of QDs was based on the method reported by Talapin *et al.*⁴⁶ The ligand exchange solution was prepared by heating the mixture of $\text{In}(\text{NO}_3)_3$ in DMF to 120 °C for 20 min with a concentration of 0.1 M. In a one-phase ligand exchange system, 1 mL $\text{In}(\text{NO}_3)_3$ solution (0.1 M) was added to 10 mL QDs solution (10 mg/mL). The mixture was vigorously stirred at room temperature until a precipitate was clearly observed. The mixture was purified twice by adding excessive toluene and centrifuging at 1937 g. The resulting precipitate was dispersed in 1 mL DMF and filtered through cellulose acetate syringe filters with a pore size of 0.2 μm . The QDs solution was stored in a nitrogen-purged glovebox for future use. A two-phase ligand exchange system was selected for the illustration images in the inset of Figure 5.1A. In a 4 mL vial, 1.5 mL 10 mg/mL QDs solution (in hexane) and 1.5 mL 0.01 M $\text{In}(\text{NO}_3)_3$ DMF solution were mixed and vigorously stirred until QDs were transferred from the hexane phase to the DMF phase.

Device Fabrication and Characterization

The master solution was prepared by mixing 1 mL QDs solution (OD~1.2 at 633 nm in DMF), 0.5 mL 10 mg/mL PEO solution (in DMF) and 0.1 mL 10 mg/mL LiCF_3SO_3 solution (in DMF). It was stirred at 90 °C for 3 h. The patterned ITO/glass substrates were ultrasonically cleaned with acetone and isopropanol, followed by the ozone treatment. The QLECs with a structure of ITO/active layer/Al were fabricated by spin coating an active layer (~100 nm) at 700 r.p.m. for 120 s onto the ITO/glass substrates, followed by drying at 4000 r.p.m. for 60 s. The films were subsequently annealed at 60 °C for 3 h. Afterwards, Al electrodes (100 nm) were deposited using a thermal evaporation system through a shadow mask under a high vacuum of $\sim 1 \times 10^{-6}$ mbar. The device area was 3 mm \times 3 mm as defined by the overlapping area of the ITO and Al electrodes.

The current density-voltage measurements were performed using a PGSTAT128N Autolab potentiostat. The emission from QLECs was measured using a calibrated Si switchable gain photodetector (PDA100A2, Thorlabs). The luminance was calculated assuming Lambertian emission. The electroluminescence spectra were recorded using a fiber-coupled USB2000+ spectrometer (Ocean Optics). The operando photoluminescence measurement was performed by exciting the QLECs from the glass side and simultaneously recording the photoluminescence spectra during cyclic voltammetry, as is illustrated in Figure 5.4A. The excitation light source was a collimated laser diode with a wavelength

of 405 nm and a power of 4.5 mW. The laser beam dimension was decreased by adding an iris (ID25Z/M, Thorlabs) between the laser and the device, to ensure that QDs outside the actual area weren't illuminated to contribute to the signals. The photoluminescence spectra were recorded simultaneously using a fiber-coupled USB2000+ spectrometer.

SEC Measurements

The SEC experiments were performed using a PGSTAT128N Autolab potentiostat to regulate the potential and measure the current. A three-electrode electrochemical cell was used, consisting of a platinum (Pt) plate counter electrode, a Ag wire pseudoreference electrode (PRE) and an QDs/ITO/glass working electrode. The working electrode was prepared by drop casting ligand exchanged QDs solution onto the ITO/glass substrate. Measurements were carried out in 0.1 M LiCF_3SO_3 PEO solution and 0.1 M LiClO_4 MeCN solution, as specified in the captions of the figures. All the experiments were performed inside a nitrogen-purged glovebox. A scheme of the SEC measurement setup can be found in Figure 5A.2. Cyclic voltammograms were obtained with a scan rate of 0.005 V/s. The Ag PRE was calibrated with a ferrocene/ferrocenium redox couple. During the electrochemical doping, simultaneous differential absorption spectra and photoluminescence spectra were recorded on a fiber-coupled USB2000+ spectrometer (Ocean Optics). The white excitation light for absorbance measurement was a DH-2000 deuterium halogen UV-VIS-NIR light source (Ocean Optics).

Simulations

The drift-diffusion simulator was based on work by van Reenen et al.⁴⁸ The 1-dimensional simulated space encompasses both electrodes and the active layer in between. The space is split into $N=250$ individual cells, with the outermost cells representing the electrodes, and the cells in between representing the active layer. The active layer is modelled as a mixture of a semiconductor and an electrolyte, and the concentrations of electrons, holes, cations and anions are tracked over time as a function of space. At time = 0, anions and cations are distributed equally over the active layer cells, and a small thermal population of both holes and electrons is present (concentrations also constant over space). The concentrations of ions in and the ion current into the electrodes is always kept at zero. The simulator then starts iterating timesteps. During each time step, a midpoint method is used to solve the Poisson equation (Table 5A.1) and to determine the spatial profile of the electrostatic potential for the next step. The boundary conditions for the Poisson equation are the potential values of the two electrodes, with the difference in these potential being equal to the applied voltages at that timestep. The applied voltage can either be constant or follow some program as a function of time (e.g. a linear scan). After the potential profile in space is determined, the movement of all carriers is calculated based on drift-diffusion equations (see Table 5A.1 for all equations used in the simulation). Electron and hole concentration in the cells adjacent to both electrodes is calculated by the Boltzmann approximation, assuming chemical equilibrium between the electrodes and the cells directly adjacent to them. Recombination of electrons and holes is governed by a second-order function. Table 5A.2 shows the employed parameters in the simulation that were found to best match experimental data and were used for the simulations shown in this work. Electron and hole currents are recorded by counting the number of electrons/holes that flow from the electrodes into the respective adjacent cells of the active layer.



References

1. Pei, Q.; Yu, G.; Zhang, C.; Yang, Y.; Heeger, A. J., Polymer light-emitting electrochemical cells. *Science* **1995**, *269* (5227), 1086-1088.
2. Youssef, K.; Li, Y.; O'Keeffe, S.; Li, L.; Pei, Q., Fundamentals of Materials Selection for Light-Emitting Electrochemical Cells. *Advanced Functional Materials* **2020**, *30* (33), 1909102.
3. Yu, D.; Wang, C.; Guyot-Sionnest, P., n-Type conducting CdSe nanocrystal solids. *Science* **2003**, *300* (5623), 1277-1280.
4. Matyba, P.; Maturova, K.; Kemerink, M.; Robinson, N. D.; Edman, L., The dynamic organic p-n junction. *Nature materials* **2009**, *8* (8), 672-676.
5. Hu, Y.; Gao, J., Direct imaging and probing of the p-n junction in a planar polymer light-emitting electrochemical cell. *Journal of the American Chemical Society* **2011**, *133* (7), 2227-2231.
6. Cho, H. H.; Gorgon, S.; Hung, H. C.; Huang, J. Y.; Wu, Y. R.; Li, F.; Greenham, N. C.; Evans, E. W.; Friend, R. H., Efficient and bright organic radical light-emitting diodes with low efficiency roll-off. *Advanced Materials* **2023**, *35* (45), 2303666.
7. Feng, Q.; Zhu, S.; Wang, B.; Yu, F.; Li, H.; Yu, M.; Xu, M.; Xie, L., Thermally Activated Delayed Fluorescence Macrocycles for Organic Light-Emitting Diodes. *Advanced Functional Materials* **2024**, *34* (14), 2312622.
8. Deng, Y.; Peng, F.; Lu, Y.; Zhu, X.; Jin, W.; Qiu, J.; Dong, J.; Hao, Y.; Di, D.; Gao, Y., Solution-processed green and blue quantum-dot light-emitting diodes with eliminated charge leakage. *Nature Photonics* **2022**, *16* (7), 505-511.
9. Zhu, Y.; Deng, Y.; Bai, P.; Wu, X.; Yao, Y.; Liu, Q.; Qiu, J.; Hu, A.; Tang, Z.; Yu, W., Highly Efficient Light-Emitting Diodes Based on Self-Assembled Colloidal Quantum Wells. *Advanced Materials* **2023**, *35* (49), 2305382.
10. Tang, S.; dos Santos, J. M.; Ràfols-Ribé, J.; Wang, J.; Zysman-Colman, E.; Edman, L., Introducing MR-TADF emitters into Light-Emitting Electrochemical Cells for narrowband and efficient emission. *Advanced Functional Materials* **2023**, *33* (42), 2306170.
11. Fresta, E.; Mahoro, G. U.; Cavinato, L. M.; Lohier, J. F.; Renaud, J. L.; Gaillard, S.; Costa, R. D., Novel Red-Emitting Copper (I) Complexes with Pyrazine and Pyrimidinyl Ancillary Ligands for White Light-Emitting Electrochemical Cells. *Advanced Optical Materials* **2022**, *10* (3), 2101999.
12. Tang, S.; Lundberg, P.; Tsuchiya, Y.; Ràfols-Ribé, J.; Liu, Y.; Wang, J.; Adachi, C.; Edman, L., Efficient and Bright Blue Thermally Activated Delayed Fluorescence from Light-Emitting Electrochemical Cells. *Advanced Functional Materials* **2022**, *32* (44), 2205967.
13. Giobbio, G.; Cavinato, L. M.; Fresta, E.; Montrieul, A.; Umuhire Mahoro, G.; Lohier, J. F.; Renaud, J. L.; Linares, M.; Gaillard, S.; Costa, R. D., Design Rule Hidden from The Eye in S/N-Bridged Ancillary Ligands for Copper (I) Complexes Applied to Light-Emitting Electrochemical Cells. *Advanced Functional Materials* **2023**, *33* (50), 2304668.
14. Filate, T. T.; Tang, S.; Genene, Z.; Edman, L.; Mammo, W.; Wang, E., Hydrophilic Conjugated Polymers for Sustainable Fabrication of Deep-Red Light-Emitting Electrochemical Cells. *Advanced Materials Technologies* **2024**, *9* (3), 2301696.
15. Costa, R. D.; Ortí, E.; Bolink, H. J.; Monti, F.; Accorsi, G.; Armaroli, N., Luminescent ionic transition-metal complexes for light-emitting electrochemical cells. *Angewandte Chemie International Edition* **2012**, *51* (33), 8178-8211.
16. Tang, S.; Edman, L., Light-emitting electrochemical cells: a review on recent progress. *Photoluminescent Materials and Electroluminescent Devices* **2017**, 375-395.
17. Chen, O.; Zhao, J.; Chauhan, V. P.; Cui, J.; Wong, C.; Harris, D. K.; Wei, H.; Han, H.-S.; Fukumura, D.; Jain, R. K., Compact high-quality CdSe-CdS core-shell nanocrystals with narrow emission linewidths and suppressed blinking. *Nature materials* **2013**, *12* (5), 445-451.
18. Almeida, G.; Ubink, R. F.; Stam, M.; du Fossé, I.; Houtepen, A. J., InP colloidal quantum dots for visible and near-infrared photonics. *Nature Reviews Materials* **2023**, *8* (11), 742-758.

19. Almeida, G.; van der Poll, L.; Evers, W. H.; Szoboszlai, E.; Vonk, S. J.; Rabouw, F. T.; Houtepen, A. J., Size-dependent optical properties of InP colloidal quantum dots. *Nano Letters* **2023**, *23* (18), 8697-8703.
20. Xu, H.; Song, J.; Zhou, P.; Song, Y.; Xu, J.; Shen, H.; Fang, S.; Gao, Y.; Zuo, Z.; Pina, J. M., Dipole-dipole-interaction-assisted self-assembly of quantum dots for highly efficient light-emitting diodes. *Nature Photonics* **2024**, *18* (2), 186-191.
21. Stam, M.; Almeida, G.; Ubbink, R. F.; van der Poll, L. M.; Vogel, Y. B.; Chen, H.; Giordano, L.; Schiettecatte, P.; Hens, Z.; Houtepen, A. J., Near-Unity Photoluminescence Quantum Yield of Core-Only InP Quantum Dots via a Simple Postsynthetic InF₃ Treatment. *ACS nano* **2024**.
22. Qian, G.; Lin, Y.; Wantz, G.; Davis, A. R.; Carter, K. R.; Watkins, J. J., Saturated and Multi-Colored Electroluminescence from Quantum Dots Based Light Emitting Electrochemical Cells. *Advanced Functional Materials* **2014**, *24* (28), 4484-4490.
23. Frohleihs, J.; Wefers, F.; Wepfer, S.; Hong, A. R.; Jang, H. S.; Nannen, E., CuInS₂-Based quantum dot light-emitting electrochemical cells (QLECs). *Advanced Materials Technologies* **2017**, *2* (11), 1700154.
24. Park, S.; Yang, J.; Kim, S.; Hahm, D.; Jo, H.; Bae, W. K.; Kang, M. S., Light-Emitting Electrochemical Cells with Polymer-Blended InP/ZnSeS Quantum Dot Active Layer. *Advanced Optical Materials* **2020**, *8* (24), 2001535.
25. Tang, S.; Murto, P.; Wang, J.; Larsen, C.; Andersson, M. R.; Wang, E.; Edman, L., On the Design of Host-Guest Light-Emitting Electrochemical Cells: Should the Guest be Physically Blended or Chemically Incorporated into the Host for Efficient Emission? *Advanced Optical Materials* **2019**, *7* (18), 1900451.
26. Tang, S.; Buchholz, H. A.; Edman, L., On the selection of a host compound for efficient host-guest light-emitting electrochemical cells. *Journal of Materials Chemistry C* **2015**, *3* (31), 8114-8120.
27. Pinchetti, V.; Lorenzon, M.; McDaniel, H.; Lorenzi, R.; Meinardi, F.; Klimov, V. I.; Brovelli, S., Spectro-electrochemical probing of intrinsic and extrinsic processes in exciton recombination in I-III-VI₂ nanocrystals. *Nano Letters* **2017**, *17* (7), 4508-4517.
28. Gudjonsdottir, S.; Houtepen, A. J., Permanent electrochemical doping of quantum dots and semiconductor polymers. *Advanced Functional Materials* **2020**, *30* (49), 2004789.
29. Mulder, J. T.; Du Fossé, I.; Alimoradi Jazi, M.; Manna, L.; Houtepen, A. J., Electrochemical p-Doping of CsPbBr₃ Perovskite Nanocrystals. *ACS Energy Letters* **2021**, *6* (7), 2519-2525.
30. Ashokan, A.; Hutchison, J. A.; Mulvaney, P., Spectroelectrochemistry of CdSe/CdS Core-Shell Quantum Dots. *Chemistry of Materials* **2024**, *36* (4), 1810-1817.
31. Houtepen, A. J.; Kockmann, D.; Vanmaekelbergh, D., Reappraisal of variable-range hopping in quantum-dot solids. *Nano letters* **2008**, *8* (10), 3516-3520.
32. Gao, Y.; Aerts, M.; Sandeep, C. S.; Talgorn, E.; Savenije, T. J.; Kinge, S.; Siebbeles, L. D.; Houtepen, A. J., Photoconductivity of PbSe quantum-dot solids: dependence on ligand anchor group and length. *ACS nano* **2012**, *6* (11), 9606-9614.
33. Boehme, S. C.; Wang, H.; Siebbeles, L. D.; Vanmaekelbergh, D.; Houtepen, A. J., Electrochemical charging of CdSe quantum dot films: dependence on void size and counterion proximity. *ACS nano* **2013**, *7* (3), 2500-2508.
34. Gudjonsdottir, S.; Van Der Stam, W.; Kirkwood, N.; Evers, W. H.; Houtepen, A. J., The role of dopant ions on charge injection and transport in electrochemically doped quantum dot films. *Journal of the American Chemical Society* **2018**, *140* (21), 6582-6590.
35. Grimaldi, G.; Van Den Brom, M. J.; Du Fossé, I.; Crisp, R. W.; Kirkwood, N.; Gudjonsdottir, S.; Geuchies, J. J.; Kinge, S.; Siebbeles, L. D.; Houtepen, A. J., Engineering the band alignment in QD heterojunction films via ligand exchange. *The Journal of Physical Chemistry C* **2019**, *123* (49), 29599-29608.
36. Vogel, Y. B.; Stam, M.; Mulder, J. T.; Houtepen, A. J., Long-Range Charge Transport via



- Redox Ligands in Quantum Dot Assemblies. *ACS nano* **2022**.
37. Pu, C.; Dai, X.; Shu, Y.; Zhu, M.; Deng, Y.; Jin, Y.; Peng, X., Electrochemically-stable ligands bridge the photoluminescence-electroluminescence gap of quantum dots. *Nature Communications* **2020**, *11* (1), 937.
 38. Deng, Y.; Lin, X.; Fang, W.; Di, D.; Wang, L.; Friend, R. H.; Peng, X.; Jin, Y., Deciphering exciton-generation processes in quantum-dot electroluminescence. *Nature communications* **2020**, *11* (1), 2309.
 39. Van Der Stam, W.; Grimaldi, G.; Geuchies, J. J.; Gudjonsdottir, S.; Van Uffelen, P. T.; Van Overeem, M.; Brynjarsson, B.; Kirkwood, N.; Houtepen, A. J., Electrochemical modulation of the photophysics of surface-localized trap states in core/shell/(shell) quantum dot films. *Chemistry of Materials* **2019**, *31* (20), 8484-8493.
 40. Fritzing, B.; Capek, R. K.; Lambert, K.; Martins, J. C.; Hens, Z., Utilizing self-exchange to address the binding of carboxylic acid ligands to CdSe quantum dots. *Journal of the American Chemical Society* **2010**, *132* (29), 10195-10201.
 41. Dong, A.; Ye, X.; Chen, J.; Kang, Y.; Gordon, T.; Kikkawa, J. M.; Murray, C. B., A generalized ligand-exchange strategy enabling sequential surface functionalization of colloidal nanocrystals. *Journal of the American Chemical Society* **2011**, *133* (4), 998-1006.
 42. Zhang, H.; Jang, J.; Liu, W.; Talapin, D. V., Colloidal nanocrystals with inorganic halide, pseudohalide, and halometallate ligands. *ACS nano* **2014**, *8* (7), 7359-7369.
 43. Boles, M. A.; Ling, D.; Hyeon, T.; Talapin, D. V., The surface science of nanocrystals. *Nature materials* **2016**, *15* (2), 141-153.
 44. Kovalenko, M. V.; Bodnarchuk, M. I.; Zaumseil, J.; Lee, J.-S.; Talapin, D. V., Expanding the chemical versatility of colloidal nanocrystals capped with molecular metal chalcogenide ligands. *Journal of the American Chemical Society* **2010**, *132* (29), 10085-10092.
 45. Nag, A.; Kovalenko, M. V.; Lee, J.-S.; Liu, W.; Spokoynny, B.; Talapin, D. V., Metal-free inorganic ligands for colloidal nanocrystals: S²⁻, HS⁻, Se²⁻, HSe⁻, Te²⁻, HTe⁻, TeS₃²⁻, OH⁻, and NH₂⁻ as surface ligands. *Journal of the American Chemical Society* **2011**, *133* (27), 10612-10620.
 46. Xiao, P.; Zhang, Z.; Ge, J.; Deng, Y.; Chen, X.; Zhang, J.-R.; Deng, Z.; Kambe, Y.; Talapin, D. V.; Wang, Y., Surface passivation of intensely luminescent all-inorganic nanocrystals and their direct optical patterning. *Nature Communications* **2023**, *14* (1), 49.
 47. Calvin, J. J.; Kaufman, T. M.; Sedlak, A. B.; Crook, M. F.; Alivisatos, A. P., Observation of ordered organic capping ligands on semiconducting quantum dots via powder X-ray diffraction. *Nature communications* **2021**, *12* (1), 1-8.
 48. van Reenen, S.; Matyba, P.; Dzwilewski, A.; Janssen, R. A.; Edman, L.; Kemerink, M., A unifying model for the operation of light-emitting electrochemical cells. *Journal of the American Chemical Society* **2010**, *132* (39), 13776-13781.
 49. Mashford, B. S.; Stevenson, M.; Popovic, Z.; Hamilton, C.; Zhou, Z.; Breen, C.; Steckel, J.; Bulovic, V.; Bawendi, M.; Coe-Sullivan, S., High-efficiency quantum-dot light-emitting devices with enhanced charge injection. *Nature photonics* **2013**, *7* (5), 407-412.
 50. Kagan, C.; Murray, C.; Bawendi, M., Long-range resonance transfer of electronic excitations in close-packed CdSe quantum-dot solids. *Physical Review B* **1996**, *54* (12), 8633.
 51. Diethelm, M.; Schiller, A.; Kawecki, M.; Devižis, A.; Blülle, B.; Jenatsch, S.; Knapp, E.; Grossmann, Q.; Ruhstaller, B.; Nüesch, F., The Dynamic Emission Zone in Sandwich Polymer Light-Emitting Electrochemical Cells. *Advanced Functional Materials* **2020**, *30* (33), 1906803.
 52. Lindh, E. M.; Lundberg, P.; Lanz, T.; Edman, L., Optical analysis of light-emitting electrochemical cells. *Scientific Reports* **2019**, *9* (1), 10433.
 53. Geuchies, J. J.; Brynjarsson, B.; Grimaldi, G.; Gudjonsdottir, S.; Van Der Stam, W.; Evers, W. H.; Houtepen, A. J., Quantitative electrochemical control over optical gain in quantum-dot solids. *ACS nano* **2020**, *15* (1), 377-386.

54. Vogel, Y. B.; Pham, L. N.; Stam, M.; Ubbink, R. F.; Coote, M. L.; Houtepen, A. J., Solvation Shifts the Band-Edge Position of Colloidal Quantum Dots by Nearly 1 eV. *Journal of the American Chemical Society* **2024**, *146* (14), 9928-9938.

Appendix



Synthesis and Characterization of CdSe/CdS/ZnS QDs

Materials

Cadmium oxide (CdO, 99.99 %), oleic acid (OA, 90 %), 1-octadecene (ODE, 90 %), selenium powder (Se, 99.99 %), trioctylphosphine (TOP, 90 %), trioctylphosphine oxide (TOPO, 90 %), sulfur flake (S, 99.99 %), zinc acetate ($\text{Zn}(\text{OAc})_2$, 99.99 %, anhydrous), oleylamine (OLAM, 80-90 %), octadecylamine (ODA, 99 %), deuterated dimethyl sulfoxide ($\text{DMSO}-d_6$, 99.9 atom %), deuterated chloroform (CDCl_3 , 99.5 atom %, Cortecnet), rhodamine 6G (99 %) and anhydrous solvents (toluene, 99.8 %, methyl acetate, 99 %, methanol, 99.8 %, ethanol, 99.8 % and acetonitrile (MeCN), 99.8 %) were all purchased from Sigma-Aldrich unless otherwise stated and used as received, except for OA, ODE and OLAM, which were degassed *in vacuo* at 100 °C before being stored in the glovebox.

Precursor Preparation

0.077 M Cadmium oleate (Cd-oleate) solution was synthesized by dissolving 0.367 g CdO in 3.68 g OA and 25.9 g ODE. The mixture was firstly degassed *in vacuo* at 110 °C for 1 h and then heated to 250 °C until a transparent solution was formed. Then it was cooled down to 110 °C and degassed again for 1 h. Afterwards, the reaction was cooled to room temperature and the Cd-oleate solution was stored in a nitrogen-purged glovebox for future use.

0.209 M zinc oleate (Zn-oleate) solution was synthesized by dissolving 0.367 g $\text{Zn}(\text{OAc})_2$ in 1.13 g OA, 1.07 g OLAM and 5.523 g ODE in a 40 mL vial. Inside a nitrogen-purged glovebox, the vial was heated up to 130 °C until a transparent solution was formed and stored there for future use. OLAM stabilizes the Zn-oleate to prevent solidification at room temperature.⁵³

0.75 M selenium precursor (Se-TOP) was prepared by heating up a mixture of 1.42 g Se, 7.5 g TOP and 11.9 g ODE to 60 °C until the complexation was completed.

0.5 M sulfur precursor (S-ODE) was prepared by heating up a mixture of 0.32 g S and 15.78 g ODE to 90 °C until the complexation was completed.

Synthesis of CdSe Core QDs

In a 100 mL three-neck round bottom flask, 3.2 g ODA and 1.11 g TOPO was heated up to 140 °C and degassed for 1.5 h. Afterwards, 5.2 g 0.75 M Se-TOP solution was added into the flask and the reaction was heated up to 300 °C. 4.9 g 0.077 M Cd-oleate solution was swiftly injected into the flask. The temperature was subsequently kept at 280 °C for 4 min. The reaction was quenched to 60 °C. To purify the CdSe core QDs, methyl acetate and methanol with a ratio of 5:1 was added to the reaction mixture, followed by centrifugation at 3354 g and redispersed in toluene. This purification procedure was repeated once. The corresponding diameter of CdSe core QDs was around 4 nm.

Synthesis of Core/shell/shell QDs

he shelling of CdSe core QDs was based on a method described in the work of Hanifi *et al.* with some modifications.^[2] In this synthesis, S-ODE was used as sulfur source instead of thiols for the following ligand exchange. Using the methods below, CdSe/6CdS/2ZnS

core/shell/shell QDs were synthesized and used in this work.

For the synthesis of 6 monolayers of CdS shell, 100 nmol CdSe core QDs in toluene, 4 mL 0.077 M Cd-oleate solution and 4 mL ODE were added to a 100 mL three-neck round bottom flask. The mixture was kept at 60 °C *in vacuo* for 1 h to remove toluene. Afterwards, the reaction mixture was heated up under nitrogen atmosphere. Upon the temperature reached 230 °C, 12 mL 0.04 M Cd-oleate solution and 12 mL 0.05 M S-ODE solution were dropwise injected into the flask using two syringe pumps with a rate of 4 mL/h. During the injection, the temperature was kept at 310 °C. After the reaction was cooled down to room temperature, the crude product was purified by adding methyl acetate and methanol with a ratio of 5:1 and centrifuging at 8586 g. The precipitate was redispersed in toluene. The purification procedure was repeated once.

For the synthesis of 2 monolayers of ZnS shell, CdSe/CdS core/shell QDs synthesized above in toluene, 1.875 mL 0.209 M Zn-oleate solution and 3 mL ODE were added into a 100 mL three-neck round bottom flask. Toluene was removed by keeping the mixture at 60 °C *in vacuo* for 1 h. Afterwards, the mixture was heated up and when the temperature reached 230 °C, 12 mL 0.032 M Zn-oleate solution and 12 mL 0.064 M S-ODE solution were dropwise injection into the flask using two syringe pumps with a rate of 12 mL/h. The temperature was 280 °C during the injection of shelling precursors. CdSe/CdS/ZnS QDs were purified three times by adding methyl acetate:methanol (5:1) and centrifuging at 3354 g. The final precipitate was dispersed in toluene and stored in a nitrogen-purged glovebox for future use.

Characterization of QDs

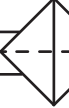
The steady-state UV-vis absorption spectra were recorded using a PerkinElmer Lambda 365 spectrometer. The steady-state photoluminescence spectra were obtained using an Edinburgh Instruments FLS980 spectrofluorometer equipped with a 450 W Xenon lamp as the excitation source and double grating monochromators. PLQY of QDs were determined with respect to the rhodamine 6G reference dye in ethanol (PLQY 95 %). The PLQY was calculated using the following equation:

$$PLQY = PLQY_{rhodamine\ 6G} \times \frac{I_{QD\ solution}^{PL}}{I_{rhodamine\ 6G}^{PL}} \times \frac{f_{rhodamine\ 6G}}{f_{QD\ solution}} \times \left(\frac{n_{QD\ solution}}{n_{ethanol}} \right)^2$$

Where I is the integrated intensity of the photoluminescence spectra of either the QD solution or the rhodamine 6G solution, n is the refractive index of solvents used for either QD solutions or rhodamine 6G solution, f is the fraction of absorbed light of samples, calculated as $f = 1 - 10^{-OD}$, where OD is the optical density of the samples at the excitation wavelength (500 nm). All the samples were diluted until the OD at 500 nm was around 0.1.

Powder X-ray diffraction patterns were collected using a Bruker D8 Advance diffractometer (Cu K α , $\lambda = 1.5418$ Å). The samples were prepared by drop casting QD solutions onto the silicon substrates.

Solution nuclear magnetic resonance (NMR) spectra were recorded on an Agilent 400-



MR DD2 equipped with a 5 mm ONE NMR probe and operating at 25 °C. ^1H NMR (399.7 MHz) spectra were collected with a recycle delay of 1 s in CDCl_3 for oleate-capped QDs and $\text{DMSO}-d_6$ for ligand exchanged QDs, respectively. Spectra were all calibrated with respect to the peak of tetramethylsilane (0 ppm).

Transmission electron microscopy (TEM) images were acquired using a JEOL JEM1400 transmission electron microscope which was operated at 120 kV. The TEM samples were prepared by drop casting QDs solution onto the carbon-coated copper TEM grids.

Table 5A.1. List of formulas employed in the simulator.

Formula	Name and purpose	Explanation of parameters
$J_n = nq\mu_n \frac{dV}{dx} - kT\mu_n \frac{dn}{dx}$ $J_p = pq\mu_p \frac{dV}{dx} + kT\mu_p \frac{dp}{dx}$ $J_c = cq\mu_c \frac{dV}{dx} + kT\mu_c \frac{dc}{dx}$ $J_a = aq\mu_a \frac{dV}{dx} - kT\mu_a \frac{da}{dx}$	Drift-diffusion equations Calculate the currents of electrons (n), holes (p), cations (c) and anions (a).	J: current density q: elementary charge V: electrostatic potential level vs vacuum μ : carrier mobility
$\frac{d^2V}{dx^2} = \frac{q}{\epsilon_0\epsilon_r} (n - h + a - c)$	1D Poisson equation Calculate the potential profile over the space of the simulation.	ϵ_0, ϵ_r : vacuum and relative electric permittivity.
$n = N_C * e^{\frac{E_f - E_C}{kT}}$ $p = N_V * e^{\frac{E_V - E_f}{kT}}$	Boltzmann approximation Calculate the equilibrium concentration of electrons and holes at the interface between the electrodes and the active layer.	E: energy N_C, N_V : effective density of states of the conduction, valence band E_C, E_V : conduction, valence band level E_f : Fermi level (= intrinsic Fermi level - electrostatic potential)
$R = k_R * n * p$	Recombination Calculate the amount of recombination in each cell	k_R : recombination rate constant

Table 5A.2. List of parameters used in this work. Parameters used in simulations were chosen to reflect those expected for QD-based active layers, then the mobilities were optimized to achieve a good fit with experimental results.

Parameter	Value (* = based on experimental data)
Active layer thickness	100 nm *
Number of lamella	250
Time step length	100 ns (1e-7 s)
Electron mobility	1.5e-12 m ² V ⁻¹ s ⁻¹
Hole mobility	1.5e-12 m ² V ⁻¹ s ⁻¹
Anion mobility	1e-15 m ² V ⁻¹ s ⁻¹
Cation mobility	1.5e-12 m ² V ⁻¹ s ⁻¹
Recombination rate constant	1e-11 m ³ s ⁻¹
Conduction band level	-3.9 eV vs vacuum (CdSe QDs) *
Valence band level	-5.9 eV vs vacuum (CdSe QDs) *
Work function of left electrode	-4.1 eV vs vacuum (Aluminum) *
Work function of right electrode	-4.7 eV vs vacuum (ITO) *
Effective density of states (holes and electrons)	1e26 m ⁻³
Ion concentration	5e25 m ⁻³ (0.08 M) *
Temperature	300 K*
Relative permittivity of the active layer	4

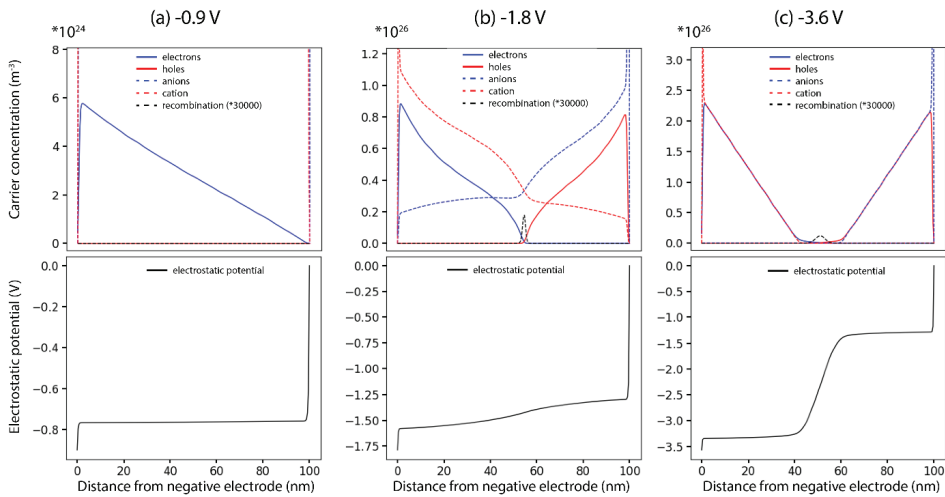


Figure 5A.1. Concentration and potential profiles during the simulated J-V curve of the QLEC. A) below 1.5 V, EDL are formed at the electrodes, as evidenced by the potential drops at the side of the device. A small leak current of electrons occurs, but no electrochemical doping has taken place. B) between 1.5 and 2.5 V, the electrochemical doping process takes place. Electrons and holes are injected into the active layer, and separation of ions occurs to compensate for the added charge. An n-type doped region develops at the left of the device and a p-type doped region at the right. C) At -3.6 V, complete separation of cations and anions has taken place and the doped regions have completely developed. In the middle of the device a potential drop marks the position of the p-i-n junction.

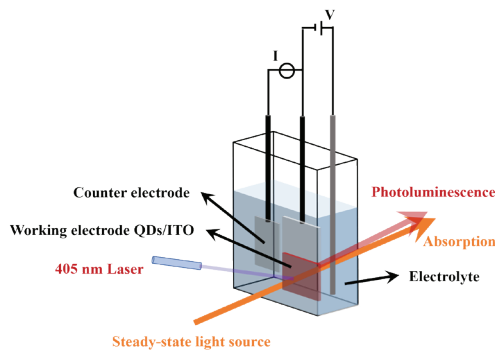


Figure 5A.2. Illustration of spectroelectrochemistry measurement setup, including a Pt sheet as the counter electrode, a Ag wire as the reference electrode and a QD film on ITO substrate as the working electrode in the electrolyte solution. A laser with a wavelength of 405 nm and a steady-state white light source were used as the excitation light source for PL and absorption measurements.

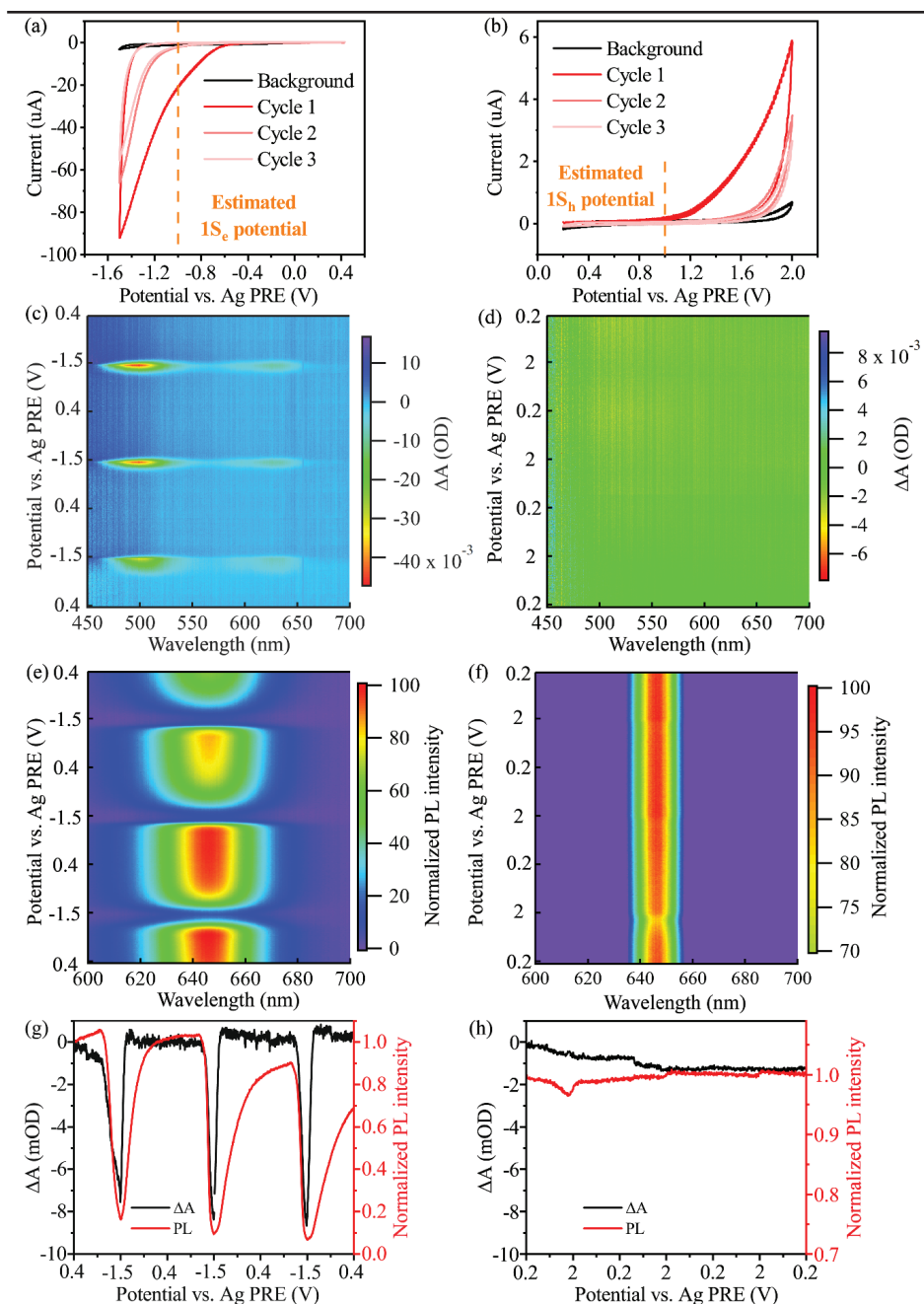
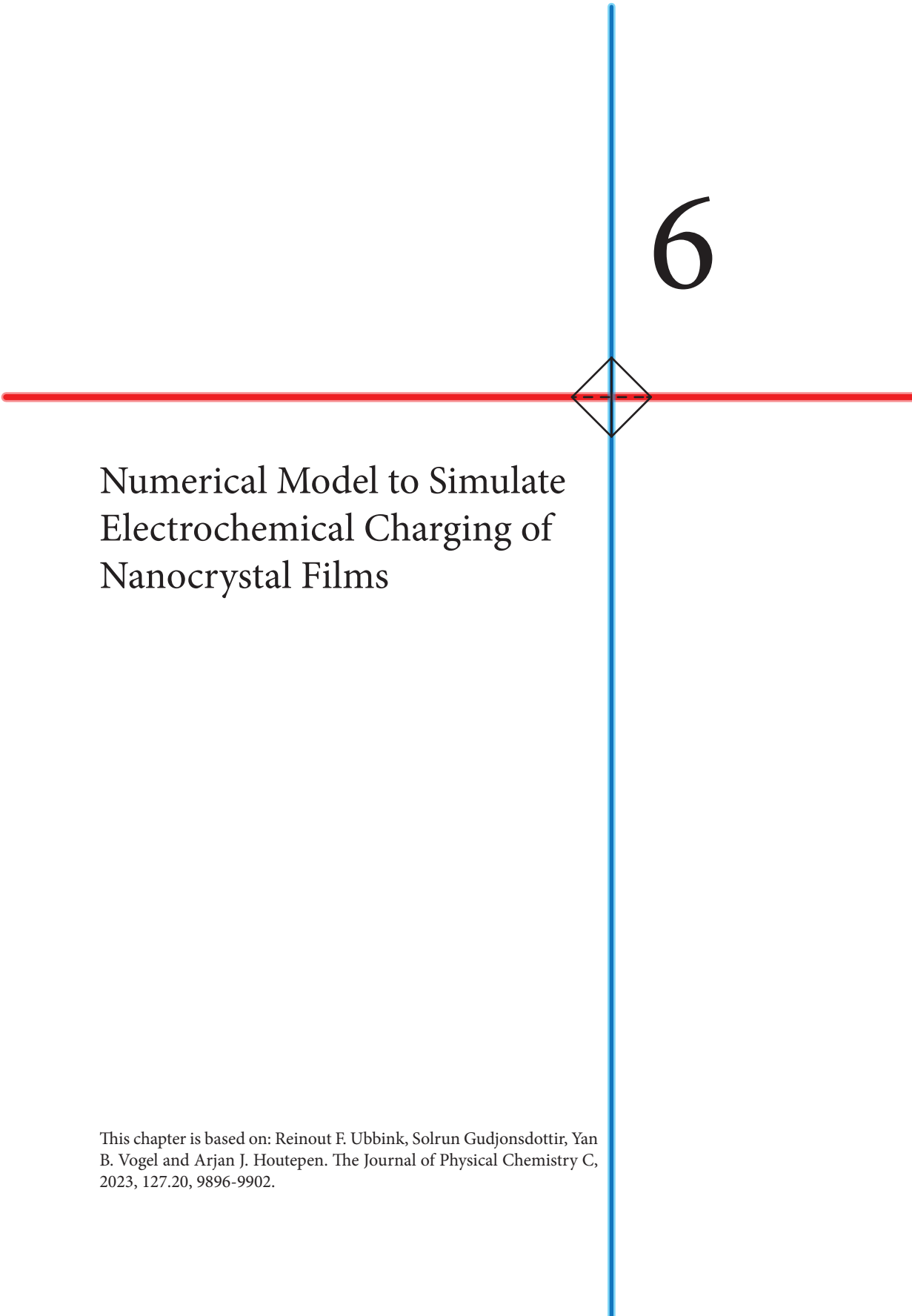


Figure 5A.3. Cyclic voltammograms, 2D differential absorbance, 2D normalized PL and 1D plot of differential absorbance at CdSe $1S$ transition peak and PL peak maxima of QD films/ITO scanned a,c,e,g) negatively and b,d,f,h) positively in the 0.1 M LiClO_4 acetonitrile solution. The scan rate was 5 mV/s.



Numerical Model to Simulate Electrochemical Charging of Nanocrystal Films

This chapter is based on: Reinout F. Ubbink, Solrun Gudjonsdottir, Yan B. Vogel and Arjan J. Houtepen. *The Journal of Physical Chemistry C*, 2023, 127.20, 9896-9902.



6.1 Introduction

Semiconductor nanocrystals, also called quantum dots (QDs) show promise in various optoelectronic applications, such as displays, LEDs, photodetectors and lasers.¹⁻⁴ The ability to control doping density in QDs is an important tool for the design of these applications as it can be used to increase the conductivity of QD films, lower the gain threshold of QD-based lasers or create p-n junctions inside the films.⁵ Compared to traditional bulk semiconductors, impurity doping of QDs is challenging due to the formation of lattice defects and charged surface states, making precise control over the doping density hard to achieve.⁶⁻⁸ Electrochemical doping of QD films has been shown to be a viable alternative to impurity doping,⁹⁻¹¹ and can be used to simply and precisely control the Fermi level in a QD film. Additionally, no lattice distortion takes place as dopants are drawn from the electrolyte solution and are present externally in the voids between QD in the nanoporous film.

While electrochemical doping of QD films has been successfully performed, a solid understanding of the process is still lacking. Various assumptions that hold true for electrochemistry on flat electrodes are often made for experiments on nanoporous electrodes such as QD films and battery electrode materials¹²⁻¹⁶, but their validity for these systems is not obvious. In this work, we present a drift-diffusion simulator that is able to simulate a broad range of electrochemical measurements on nanoporous electrode materials. Using this simulator, we test the validity of some commonly made assumptions regarding the charging of these materials.

The first assumption that is often made is that the charge carrier concentration inside the nanoporous films is constant and that the Fermi-level is equal to the applied electrochemical potential. Through steady state simulations, we show the presence of two sharp potential drops at the interfaces of electrochemically doped semiconductor films. The first is due to an electrical double layer at the working electrode/QD film interface and is responsible for the change in Fermi level in the QD film. The second however forms at the QD film/solution interface. The presence of this potential drop implies that not all of the applied potential changes the Fermi-level inside the QD film. At an electrolyte concentration of 0.01 M, the film-solution potential drop can be as large as 10% of the total potential. At high electrolyte concentrations (> 1M), this potential drop can be minimized to < 1% of the applied potential.

We then compare simulated cyclic voltammograms (CVs) to experimentally obtained CVs of ZnO QD films. At high scan rates, a square root relation between the scan rate and the current density is observed, indicating that the current is limited by mass transport of the cations inside the QD film. Analysis of the concentration gradient reveals that, unlike in flat electrode systems, the Randles-Ševčík equation does not hold when considering charging of a nanoporous electrode. Specifically, when an electrode material is permeable to ions, using the Randles-Ševčík equation to calculate the diffusion coefficient of these ions leads to an underestimation of 1-2 orders of magnitude.

6.2 Results and discussion

6.2.1 The drift-diffusion simulator

For most QD materials, experimental n-doping of QD films has proven more successful than p-doping.^{10, 17-21} For this reason, we have only considered negative applied potentials (relative to the open circuit potential), electron injection and n-type doping, while neglecting the presence of holes, although extension to hole injection would be straightforward. Since the movement of both electrons and ions is predicted by drift-diffusion theory, this is an ideal basis for simulating the electrical behavior of QD films in an electrochemical cell.

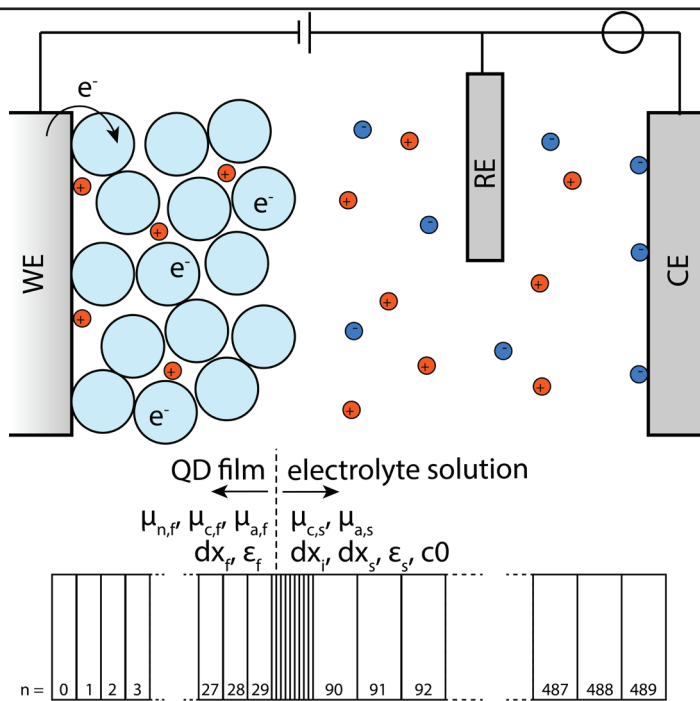


Figure 6.1. Schematic of the experimental 3-electrode setup and the 1-dimensional model used in the simulations. The working electrode (WE) and counter electrode (CE) mark the edge of the simulated space, while the reference electrode (RE) is placed in the middle of the electrolyte solution between the film/solution interface and the CE.

We designed the 1-dimensional simulator to mirror a 3-electrode electrochemical cell, as shown in Figure 6.1. The simulator consists of three sections: the QD film, the film/solution interface and the electrolyte solution. The QD film is in contact with the working electrode (WE), while the electrolyte solution is in contact with both the reference electrode (RE) and the counter electrode (CE). The film/solution interface plays a critical role in determining the electrical response and is therefore deserving of its own separate section. Cations and anions can freely flow anywhere in the simulation according to drift-diffusion theory, but electrons are confined to the QD film. When negative potentials relative to the open



circuit potential are applied to the WE cations migrate towards it and an electrical double layer (EDL) develops at the WE/QD film interface. In the EDL (typically ~ 1.5 nm wide), the electrostatic potential (ϕ) drops as the excess of cations shields the negative charge of the working electrode. This potential drop at the working electrode/film interface ($\Delta\phi_{E/F}$) increases as the applied potential becomes more negative. The presence of $\Delta\phi_{E/F}$ leads to band bending in the QD film (see Figure A6.1 in the appendix) and a decrease of the QD conduction band edge relative to the work function of the electrode. In other words, the Fermi level of electrons in the QD film is raised (Figure A6.1). If the applied potential is negative enough to raise the Fermi level above the conduction band edge, electrons will be injected from the working electrode into the conduction band of the QDs, while additional cations will flow from the solution into the voids of the QD film to compensate the excess negative charge.

6.2.2 Steady state concentration and potential profiles

Steady state solutions of the 3-electrode system were obtained by running the simulator at an applied potential of -1.2 V vs. the RE until the current was $<0.1\%$ of the maximum current. The electrostatic potential profile and electron concentration profile obtained for 3 different electrolyte concentrations in this way are depicted in Figure 6.2.

6

At steady state, the electron concentration in the film is constant and equal to the excess cation concentration in the film: electrochemical n-doping has been achieved at a constant concentration throughout the film. The electrostatic potential over the film is also constant, but two sharp drops of the electrostatic potential are observed at the interfaces of the film (Figure 6.2A). The aforementioned potential drop at the working electrode-film interface develops as cations are attracted to the negative charge in the electrode and accumulate in an electric double layer. This potential drop is the reason electrons can be injected, as it provides the potential energy necessary to overcome the injection barrier between the electrode work function and the conduction band of the quantum dots. As $\Delta\phi_{E/F}$ grows larger, electrons can be injected into higher energy states, thus increasing the equilibrium concentration of electrons in the film (Figure A6.1).

The second potential drop, at the film-electrolyte solution interface ($\Delta\phi_{F/S}$), is responsible for providing the excess concentration of cations in the film that is necessary to compensate the charge of the electrons. Without $\Delta\phi_{F/S}$ ions would diffuse back into the solution and no steady state would be achieved. Migration due to $\Delta\phi_{F/S}$ balances this diffusion at steady state. High spatial resolution ($dx_i < 0.5$ nm) is needed to simulate $\Delta\phi_{F/S}$ accurately. Low resolution leads to an overestimation of the potential drop: as the entire drop will be contained in one lamella, increasing dx_i will result in the same electric field being considered over a longer distance during integration and thus an unphysically high interface drop. A comparison of interface potential drops calculated from simulations at different resolutions can be found in Figure A6.2. Increasing the resolution from 0.3 nm to 0.2 nm leads to only a 3% change in $\Delta\phi_{F/S}$.

To achieve high spatial resolution at the interface without increasing the number of lamella, a variable lamella thickness was employed in the simulations (each of the three sections has its own dx value). For the steady state simulations in Figure 6.2, an interface

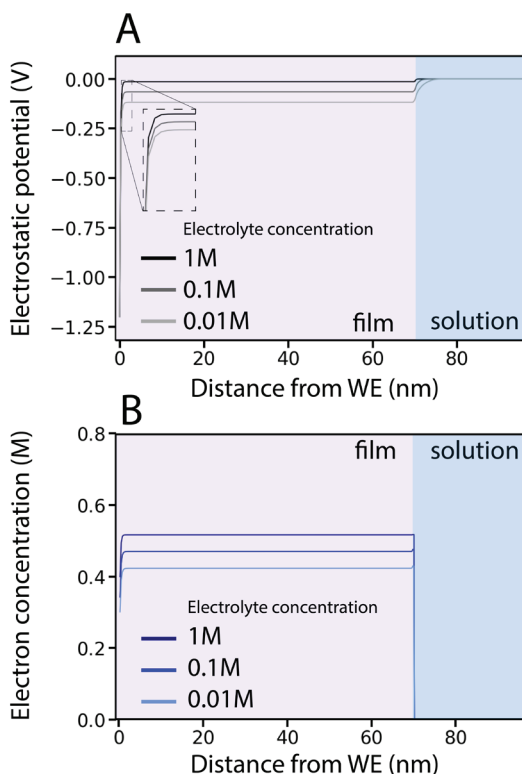


Figure 6.2. A) Simulated steady state potential and B) simulated electron concentration profiles for electrolytes with different ion concentrations for an applied potential of -1.2 V. The film-solution interface is indicated at 70 nm. Both the potential and electron concentration are constant over the remainder of the electrolyte solution, which has been omitted for clarity. Electron concentration is constant throughout the bulk of the film, but deviates slightly at the edges due to the EDLs.

resolution of 0.1 nm was used, while for the transient simulations below a resolution of 0.3 nm was used, achieving good accuracy without compromising the performance of the simulations.

As can be seen in Figure 6.2A, for a 1M concentration of ions in the electrolyte solution, $\Delta\phi_{F/S}$ is $\sim 1\%$ of the total applied potential and practically the entire potential drops at the WE-film interface. This means that the Fermi level in the semiconductor film is raised from the intrinsic level by an amount roughly equal to the applied potential.

At lower electrolyte concentrations however, a larger potential drop is observed. At 0.01 M about 10% of the potential drops at the electrolyte solution interface. In these low concentration conditions, the increase in Fermi level in the film is no longer equal to the applied potential. If $\Delta\phi_{F/S}$ is larger, $\Delta\phi_{E/F}$ is smaller for the same applied potential, thus resulting in a lower electron concentrations and lower doping density (Figure



6.2B). Doping densities in these simulations range from 0.51 M to 0.42 M for electrolyte concentrations of 1 M and 0.01M respectively (Figure A6.3), a difference of 21%.

To achieve maximum doping density in QD films, it is therefore favorable to increase the concentration of the electrolyte solution. This is also important when thermodynamic properties are derived from electrochemical measurements, such as the density of electron states. This effect of the QD-film/solution interface has previously been overlooked.

As long as steady state systems are considered, it is possible to calculate the minimum electrolyte concentration needed to charge a nanoporous film to a certain doping density while keeping $\Delta\phi_{F/S}$ below a chosen threshold (see also derivation A6.1 in the appendix). When steady state has been reached, the concentration of cations in the system follows the Boltzmann distribution:

$$c = c_0 \exp\left(-\frac{q\phi}{kT}\right) \quad (6.1)$$

Where c is the cation concentration, c_0 is the bulk electrolyte concentration (assuming an infinite supply of bulk cations), q is the elementary charge, ϕ is the electrostatic potential, k is the Boltzmann constant and T is the temperature. This relation is observed in the steady state simulations shown in Figure 6.2. Rewriting this distribution yields:

$$c_0 = \frac{n}{p * \exp\left(\frac{q\Delta\phi_{F/S}}{kT}\right)} \quad (6.2)$$

Where n is the electron concentration in the nanoporous film and p is the porosity of that film. For example for a film (porosity = 50%) of QDs with a diameter of 3.5 nm (QD volume = 22 nm³, QD “concentration” = 0.0742 M), if one wants to charge the film with 8 electrons per QD while keeping $\Delta\phi_{F/S} < 2$ kT (= 0.052 eV at RT), this would require a minimum electrolyte concentration of 0.16 M:

$$c_0 = \frac{0.594 \text{ M}}{0.5 * \exp(2)} = 0.16 \text{ M} \quad (6.3)$$

6.2.3 Cyclic voltammetry simulations of QD films

To acquire information on the dynamics of charge injection into QD films, cyclic voltammetry is commonly employed. Figure 6.3A shows such experimental CVs on a film of ZnO QDs at different scan rates, collected and shown in prior work by Godjunsdottir *et al.*⁹ To analyze these CVs, the scans were also simulated. The applied potential was changed over time and the current was recorded by counting the amount of electrons that entered the QD film from the WE. Parameters were chosen to mirror those of the experiments on ZnO QD films, and then optimized to fit to the experimental data (Table A6.1). A set of simulated CVs at different scan rates is shown in Figure 6.3B. With a single

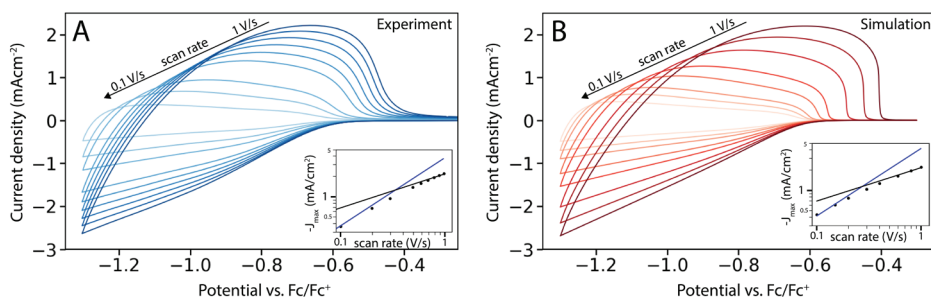


Figure 6.3. Comparison of experimental A) and simulated B) cyclic voltammograms of QD films. Experimental data were collected in a 3-electrode cell, employing a ZnO QD film (thickness = 700 nm) on top of an ITO working electrode, and a 0.1 M LiClO₄ acetonitrile electrolyte solution. For more experimental details see reference ⁹. Excellent agreement between simulation and experiment is observed for a range of scan rates. Insets show the relationship between the maximum current and the scan rate. In the insets a transition from capacitance-limited charging (slope = 1, blue line) to mass transport-limited charging (slope = 0.5, black line) is observed as the scan rate is increased in both the experimental and simulated CVs.

parameter set, excellent agreement with experimental data is achieved across a wide range of scan rates.

In a typical CV of a QD film, the current density is small ($<1 \mu\text{A}/\text{cm}^2$) until the applied potential is high enough to inject electrons into the conduction band of the QDs (around $-0.6 \text{ V vs. Fc/Fc}^+$ in these simulations). Before this point, the Fermi level is still in the band gap of the QDs and any current that flows is attributed to the formation of the EDLs at the electrodes. Once the Fermi level is raised above the conduction band edge, significant n-type doping starts to occur, and a negative current starts to flow. After the applied potential has reached its minimum and the scan direction is inverted, a positive current is observed as electrons are extracted from the QDs and flow back into the WE.

The electrical response of a QD film during a CV is strongly dependent on the scan rate. When a low enough scan rate is used (for example, 0.1 V/s for a film thickness of 700 nm), the current density is determined by the capacitance of the film. In this case, a linear relationship between the peak current density and scan rate is expected, since the same amount of charge is injected regardless of the scan rate.⁹ In both the experiments and simulations, this linear relation is observed for low scan rates (insets Figure 6.3A and 6.3B). Under these conditions the simulations show that the concentration profiles of electrons and cations over the film are nearly constant, indicating that the film is charged with electrons in near-steady state conditions. When low scan rates are applied, the shape of the CV is expected to almost perfectly trace the density of states (DOS) of the QDs (save for the potential drop over the film solution interface discussed above). This can be simulated by adjusting the DOS function.

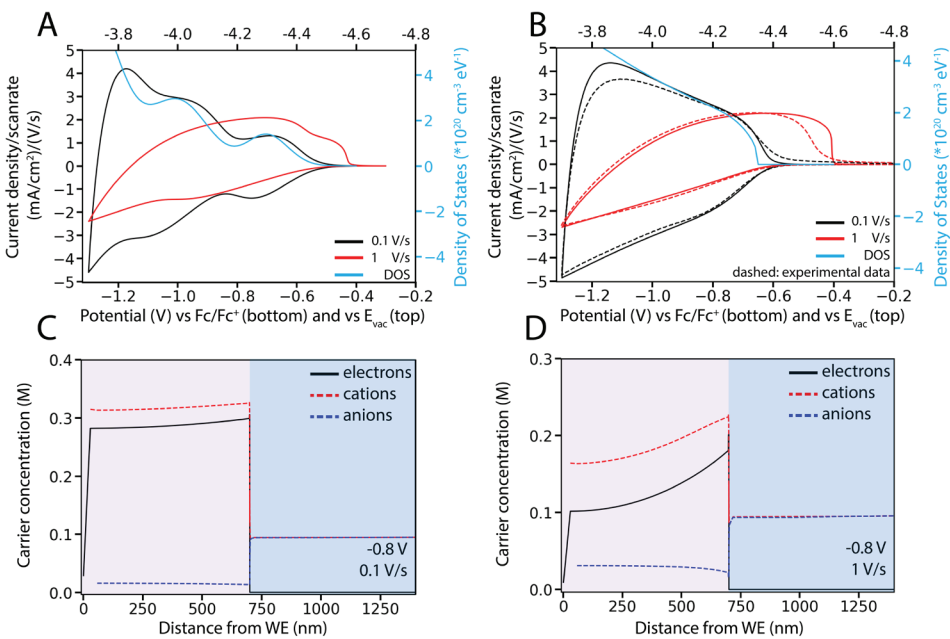


Figure 6.4. A-B) Comparison of simulated cyclic voltammograms and corresponding concentration profiles of QD films with different scan rates and the corresponding density of state (DOS) functions (blue) that were used in the simulation, at an electrolyte concentration of 0.1 M. At a scan rate of 0.1 V/s, the CV shape is mostly determined by the shape of the DOS. The concentration profile that is observed in this near-steady state regime is visible in C). At higher scan rates, the current density is limited by carrier mobility and the CV shape is mostly independent of the DOS function of the material. In this case the current is limited by cation transport, and an accompanying concentration profile is observed D).

Figure 6.4A and 4B depict simulated CVs of materials using a different DOS function. At a scan rate of 0.1 V/s the two CVs differ significantly, tracing the shape of the corresponding DOS function. The DOS used in Figure 6.4A was chosen to resemble a typical QD DOS function, featuring 3 Gaussian peaks for the s, p and higher energy levels. The corresponding simulated CV resembles experimental CVs observed for CdSe QDs.¹¹ However, experiments on ZnO QD films result in CVs with a distinctly different shape.⁹ ¹⁰ To best fit the experimentally observed results, we chose a DOS function that resembled that of a bulk semiconductor (square root function of energy) combined with some minor quantum dots features (Gaussian peaks). Using this DOS we were able to closely reproduce experimental CV shapes (Figure 6.4B). This is in accordance with earlier results from Brovek and colleagues, which indicated that discrete energy levels were not visible in the ensemble capacitance of ZnO QD films²², and generally shows that in these dropcasted and mildly annealed ZnO QD films quantum confinement is weak.

As long as low enough scan rates are applied, the shape of simulated and experimental CVs show a strong correlation with the DOS function of the material that is used, and

simulations can be used to extract information on the DOS function of QD materials. Qualitative DOS functions of QD materials can be extracted by fitting experimental CVs as shown in Figure 6.4, and even quantitative DOS values can be obtained from CVs at low scan rates if the number of QDs in the film or the film thickness and porosity are known. In Figure 6.4B, the quantitative DOS function that was fitted for a ZnO QD film is plotted in $\text{cm}^{-3} \text{eV}^{-1}$.

At higher scan rates however (1 V/s for a film thickness of 700 nm is used in Figure 6.4), the shape of the CV is mostly independent of the DOS function of the material. The current density is limited instead by the mobility of one of the charge carriers. Charge carrier mobility is related to the diffusion coefficient through the Einstein relation:

$$\mu = \frac{D}{kT} \quad (6.4)$$

Where μ is the mobility of a charge carrier and D is its diffusion coefficient. Earlier work showed that electrons are typically very mobile in ZnO QD films (electron mobility of $\sim 0.1 \text{ cm}^2/\text{Vs}$), while cation movement through the pores of the film is slow (mobility of Li^+ is $\sim 10^{-7} \text{ cm}^2/\text{Vs}$) and limits the speed of charge injection.^{9,23}

In Figure 6.4C, it is shown that at low scan rates, the concentration profiles of cations, anions and electrons in the film resemble those obtained in the steady state simulations: the concentration of both electrons and cations is almost constant throughout the QD film. At low scan rates (0.1 V/s), the film is charged in near-steady state conditions.

When faster scan rates are applied (1 V/s), cation transport is too slow to achieve constant concentrations, resulting in the concentration profile shown in Figure 6.4D. This concentration profile that develops is quite different from the concentration profile that develops in electrochemical experiments on redox active molecules in solution using flat electrodes. For such flat electrode systems, it is well-known that the peak current in the CV, i_p , can be related to the mobility of the electrochemical species through the Randles-Ševčík equation²⁴⁻²⁶:

$$i_p = 0.4463nFAC^* \left(\frac{nFv\mu}{N_A} \right)^{1/2} \quad (6.5)$$

Where n is the number of electrons involved in the reaction, F is the Faraday constant, A is the area of the working electrode, C^* is the concentration of the redox active molecule, v is the scan rate, and μ is the mobility of the redox active molecule. If the Randles-Ševčík equation holds, a square root-relationship between scan rate and peak current density is expected. Such a relationship is indeed observed at faster scan rates in both the experimental and simulated scan rate series presented in Figure 6.3 (black line in the insets). For this reason we have earlier used the Randles-Ševčík equation to estimate the mobility of cations in the quantum dot film.^{9,19} The Randles-Ševčík equation is also commonly used to determine diffusion coefficients in e.g. battery research, where a



similar process is considered: the diffusion of ions into an electrode material where their charge is compensated by electrons.^{12, 14-16} Using the drift-diffusion simulator, we can now assess the validity of this equation for the case of charge-compensated electron injection into nanoporous electrodes, such as a battery electrode or a QD film.

In Figure A6.4 a series of mobilities as calculated by the Randles-Ševčík equation is compared with the actual mobilities as they were set at the start of the simulation. Using the equation on the CVs obtained in the simulation yields a cation mobility that is a factor 10-300 lower than the real mobility, showing that the Randles-Ševčík equation is not valid for the charging of a nanoporous film system.

This can be explained by considering the cation and electron concentration profiles more closely: since the movement of cations into the film is limiting, the cation concentration must be higher near the film/solution interface and lower near the working electrode. In order to maintain local charge neutrality, electron concentrations must necessarily follow the same profile. By solving the drift-diffusion equations for this system, it can be shown that the concentration profile of cations and electrons increases quadratically with distance from the working electrode/film interface (see Table A6.3 and derivation A6.2 in the appendix), which is different from the concentration profile observed in flat-electrode electrochemistry.

Furthermore, since both cations and electrons follow the same concentration profile (Figure 6.4D), mass transport cannot be completely diffusion controlled: if only diffusion currents were present in the film, both cations and electrons would diffuse towards the WE, while the direction of total electron flux must be towards the film/solution interface during electrochemical charging. In the simulations electric fields are indeed observed, which result in a drift current inside the film that is 11 times stronger than the diffusion current (Figure A6.6). While charging is still limited by the transport of the cations, drift currents dominate in the film, rather than diffusion.

An assumption necessary for application of the Randles-Ševčík equation is that drift current is negligible and transport of redox species is fully diffusion-controlled. This is a reasonable assumption for flat-electrode systems as long as the concentration of the supporting electrolyte is significantly higher than that of the redox species. In that case, the supporting electrolyte will form a thin EDL at the electrode surface, and transport of the redox species takes place outside the EDL and is completely diffusion-controlled. Because of the electric fields present inside the film during electrochemical charging of nanoporous films, the system is significantly different and the Randles-Ševčík equation is not applicable.

We note that the analysis given here only holds when considering the electrochemical charging of an electrode material, i.e. charged ions and electrons or holes enter and remain in the electrode material itself. Purely heterogeneous electrochemical reactions on (nano) porous electrodes are subtly different, and the Randles-Ševčík equation is applicable in those cases when a supporting electrolyte is present as shown in earlier simulations by Henstridge *et al.*²⁷

6.3 Conclusion

1-dimensional drift-diffusion simulations were found to accurately reproduce electrochemical experiments on the charging of QD films, showing that drift-diffusion theory is an excellent model to describe the movement of charge carriers in these systems. Through steady state simulations, it was revealed that the electrostatic potential drop is distributed over the film/electrode interface and the film/solution interface, with a ratio that depends on the electrolyte concentration. This implies that the doping density that can be achieved in nanoporous films through electrochemical charging depends both on the applied potential and the concentration of electrolyte ions. It was further shown that the density of states function of QD materials can be obtained by combining simulations and experimental cyclic voltammograms at low scan rates. When QD films are charged at high scan rates, cation transport in the QD film limits the charging speed. Contrary to earlier discussions on this topic we show that this cation transport is dominated by drift, rather than diffusion, and that the concentration profile of ions is very different from for electrochemical reactions in solution. We show that the often-used Randles-Ševčík equation does not hold for the charging of nanoporous electrodes, but underestimates the actual ion mobility by 1-2 orders of magnitude.

6.3 Methods

The simulator was inspired by work on light-emitting electrochemical cells by van Reenen et al.,²⁸ but was redesigned to mirror a 3-electrode electrochemical cell. An electrochemical cell with QD films on the working electrode (WE) is treated as a 1-dimensional system, divided numerically in multiple (~500) lamella, as shown in Figure 6.1. The 1-dimensional simulated space starts at the WE, encompasses the QD film and the electrolyte solution, and ends at the counter electrode (CE). The reference electrode (RE) is positioned halfway between the film/solution interface and the CE. To achieve high spatial resolution in the film/solution interface region without sacrificing computational performance, the space was divided in lamella non-linearly. The simulator considers an initial state, which contains starting values of the concentrations of electrons, anions and cations for each lamella. It then determines the movement of these three charge carriers over small time steps based on the drift-diffusion equations (see Table A6.2, appendix). The hole concentration is assumed to be zero as only negative applied potentials relative to the open circuit potential are considered in this work. During each time step, a midpoint method is used to solve the Poisson equation (Table A6.2) and to determine the spatial profile of the electrostatic potential for the next step. Boundary conditions of a regular 3-electrode system are enforced, i.e., ϕ_{WE} minus $\phi_{RE} = V_{applied}$ and $\phi_{RE} = 0$ (with ϕ the electrostatic potential at a certain position), while the electrostatic potential at the counter electrode is allowed to float. The true potential at the RE (and thus the initial Fermi level) at open circuit potential is arbitrary for the simulation, but for comparison with experiments was set to -4.7 V vs. vacuum = 0.26 V vs. SHE = -0.3 V vs. ferrocene/ferrocenium (Fc/Fc⁺) in acetonitrile. This value corresponds to the work function of ITO (used as working electrode) and is in accordance with the open circuit potential of experimental ZnO QD films (Figure A6.7 in the appendix).^{9, 10} The proficiency of the program in simulating electrochemical behavior of 3-electrode systems was confirmed by simulating a cyclic voltammogram of a simple reductant/oxidant pair in Nernst equilibrium (Figure A6.8 in the appendix). In the actual QD film simulations, the initial state of the simulation always consisted of an uncharged



QD film, where the concentration of electrons was zero, and an electrolyte solution with a certain concentration of cations and anions, c_0 . An infinite supply of ions was achieved by setting the concentration of both ions at the RE constant at c_0 during the simulation. The QD film was considered to have a porosity of 50%, with the pores filled with electrolyte solution at concentration c_0 . The electron concentration in the first lamella of the film, in contact with the ITO electrode, is governed by a Fermi-Dirac equilibrium with the electrode:

$$n = \int_{E=E_c}^{\infty} g_c(E) \frac{1}{1 + e^{\frac{E-E_F}{kT}}} dE \quad (6.6)$$

Where n is the concentration of electrons in the first lamella, $g_c(E)$ is the density of states (DOS) function of the material, E_c is the conduction band energy level and E_F is the Fermi level in the first lamella, which is equal to the intrinsic Fermi level minus the electrostatic potential (ϕ) in the first lamella. Thus, as the applied potential becomes more negative, the value of the Fermi level, Fermi-Dirac integral and the concentration of electrons all increase in the first lamella. Any DOS function can be used as input in the simulator. The simulation parameters, including the DOS function, were set at the start of the simulation, after which only the applied potential was altered to obtain the CV curves shown in this work. Parameters used were optimized to most closely fit experimental data of electrochemical charging of ZnO films (see Table A6.1, appendix). Parameters used here were kept consistent for every Figure shown unless otherwise noted, but any set of input parameters can be used. For performance reasons, the simulator was written in C++ and compiled using Microsoft Visual Studio. Simulations were typically completed in a few minutes (for a scan rate of 1 V/s) to an hour (for a scan rate of 0.1 V/s and steady-state simulations) on a single core of a personal computer. Additional computational details, equations, DOS functions, and a list of parameters that were used in these simulations can be found in the appendix. The simulator source code and accompanying instructions are available at github.com/RFUbbink/QDfilmsim.

References

1. Coe-Sullivan, S.; Liu, W.; Allen, P.; Steckel, J. S., Quantum dots for LED downconversion in display applications. *ECS Journal of Solid State Science and Technology* **2012**, *2* (2), R3026.
2. Wu, Z.; Liu, P.; Zhang, W.; Wang, K.; Sun, X. W., Development of InP quantum dot-based light-emitting diodes. *ACS Energy Letters* **2020**, *5* (4), 1095-1106.
3. Yin, X.; Zhang, C.; Guo, Y.; Yang, Y.; Xing, Y.; Que, W., PbS QD-based photodetectors: future-oriented near-infrared detection technology. *Journal of Materials Chemistry C* **2021**, *9* (2), 417-438.
4. Park, Y.-S.; Roh, J.; Diroll, B. T.; Schaller, R. D.; Klimov, V. I., Colloidal quantum dot lasers. *Nature Reviews Materials* **2021**, *6* (5), 382-401.
5. Shim, M.; Wang, C.; Norris, D. J.; Guyot-Sionnest, P., Doping and charging in colloidal semiconductor nanocrystals. *Mrs Bulletin* **2001**, *26* (12), 1005-1008.
6. Makkar, M.; Viswanatha, R., Frontier challenges in doping quantum dots: synthesis and characterization. *RSC advances* **2018**, *8* (39), 22103-22112.
7. Mikulec, F. V.; Kuno, M.; Bennati, M.; Hall, D. A.; Griffin, R. G.; Bawendi, M. G., Organometallic synthesis and spectroscopic characterization of manganese-doped CdSe

- nanocrystals. *Journal of the American Chemical Society* **2000**, *122* (11), 2532-2540.
8. Erwin, S. C.; Zu, L.; Haftel, M. I.; Efros, A. L.; Kennedy, T. A.; Norris, D. J., Doping semiconductor nanocrystals. *Nature* **2005**, *436* (7047), 91-94.
 9. Gudjonsdottir, S.; Van Der Stam, W.; Kirkwood, N.; Evers, W. H.; Houtepen, A. J., The role of dopant ions on charge injection and transport in electrochemically doped quantum dot films. *Journal of the American Chemical Society* **2018**, *140* (21), 6582-6590.
 10. Gudjonsdottir, S.; Van Der Stam, W.; Koopman, C.; Kwakkenbos, B.; Evers, W. H.; Houtepen, A. J., On the stability of permanent electrochemical doping of quantum dot, fullerene, and conductive polymer films in frozen electrolytes for use in semiconductor devices. *ACS applied nano materials* **2019**, *2* (8), 4900-4909.
 11. Guyot-Sionnest, P., Charging colloidal quantum dots by electrochemistry. *Microchimica Acta* **2008**, *160* (3), 309-314.
 12. Li, L.; Liu, X.; Tang, L.; Liu, H.; Wang, Y.-G., Improved electrochemical performance of high voltage cathode Na₃V₂(PO₄)₂F₃ for Na-ion batteries through potassium doping. *Journal of Alloys and Compounds* **2019**, *790*, 203-211.
 13. Kim, T.; Choi, W.; Shin, H.-C.; Choi, J.-Y.; Kim, J. M.; Park, M.-S.; Yoon, W.-S., Applications of voltammetry in lithium ion battery research. *Journal of Electrochemical Science and Technology* **2020**, *11* (1), 14-25.
 14. Takahashi, Y.; Yamashita, T.; Takamatsu, D.; Kumatani, A.; Fukuma, T., Nanoscale kinetic imaging of lithium ion secondary battery materials using scanning electrochemical cell microscopy. *Chemical Communications* **2020**, *56* (65), 9324-9327.
 15. Li, D.; Dai, L.; Ren, X.; Ji, F.; Sun, Q.; Zhang, Y.; Ci, L., Foldable potassium-ion batteries enabled by free-standing and flexible SnS 2@ C nanofibers. *Energy & Environmental Science* **2021**, *14* (1), 424-436.
 16. Shen, J.; Wang, H.; Zhou, Y.; Ye, N.; Li, G.; Wang, L., Anatase/rutile TiO₂ nanocomposite microspheres with hierarchically porous structures for high-performance lithium-ion batteries. *RSC advances* **2012**, *2* (24), 9173-9178.
 17. Guyot-Sionnest, P., Charging colloidal quantum dots by electrochemistry. *Microchimica Acta* **2008**, *160*, 309-314.
 18. Chen, M.; Guyot-Sionnest, P., Reversible electrochemistry of mercury chalcogenide colloidal quantum dot films. *ACS nano* **2017**, *11* (4), 4165-4173.
 19. Van Der Stam, W.; Gudjonsdottir, S.; Evers, W. H.; Houtepen, A. J., Switching between plasmonic and fluorescent copper sulfide nanocrystals. *Journal of the American Chemical Society* **2017**, *139* (37), 13208-13217.
 20. Van Der Stam, W.; Grimaldi, G.; Geuchies, J. J.; Gudjonsdottir, S.; Van Uffelen, P. T.; Van Overeem, M.; Brynjarsson, B.; Kirkwood, N.; Houtepen, A. J., Electrochemical modulation of the photophysics of surface-localized trap states in core/shell/(shell) quantum dot films. *Chemistry of Materials* **2019**, *31* (20), 8484-8493.
 21. Gudjonsdottir, S.; Houtepen, A. J., Permanent electrochemical doping of quantum dots and semiconductor polymers. *Advanced Functional Materials* **2020**, *30* (49), 2004789.
 22. Brozek, C. K.; Hartstein, K. H.; Gamelin, D. R., Potentiometric Titrations for Measuring the Capacitance of Colloidal Photodoped ZnO Nanocrystals. *Journal of the American Chemical Society* **2016**, *138* (33), 10605-10610.
 23. Vogel, Y. B.; Stam, M.; Mulder, J. T.; Houtepen, A. J., Long-Range Charge Transport via Redox Ligands in Quantum Dot Assemblies. *ACS nano* **2022**, *16* (12), 21216-21224.
 24. Bard, A. J.; Faulkner, L. R., *Fundamentals and applications*. 2001; Vol. 2, p 580-632.
 25. Randles, J. E., A cathode ray polarograph. Part II.—The current-voltage curves. *Transactions of the Faraday Society* **1948**, *44*, 327-338.
 26. Ševčík, A., Oscillographic polarography with periodical triangular voltage. *Collection of Czechoslovak Chemical Communications* **1948**, *13*, 349-377.
 27. Henstridge, M. C.; Dickinson, E. J.; Compton, R., Mass transport to and within porous



- electrodes. Linear sweep voltammetry and the effects of pore size: The prediction of double peaks for a single electrode process. *Russian Journal of Electrochemistry* **2012**, 48, 629-635.
28. van Reenen, S.; Matyba, P.; Dzwilewski, A.; Janssen, R. A.; Edman, L.; Kemerink, M., A unifying model for the operation of light-emitting electrochemical cells. *Journal of the American Chemical Society* **2010**, 132 (39), 13776-13781.

Appendix

Table A6.1. List of parameters used in this work. Parameters used in CV simulations were chosen to reflect those of a ZnO QD film, then optimized to achieve a good fit with experimental results. Parameters for the steady-state simulations were chosen to achieve steady state quickly at a high spatial resolution.

Parameter	Value (CVs)	Value (steady-state)
QD film thickness	700 (nm)	70 (nm)
Number of lamella (film)	25	245
Lamella thickness (film)	27.94 (nm)	0.2837 (nm)
Number of lamella (film/solution interface)	65	
Lamella thickness (film/solution interface)	0.3 (nm)	0.1 (nm)
Distance between WE and CE	0.1 (mm)*	0.03 (mm)
Number of lamella (solution)	400	
Lamella thickness (solution)	~249 (nm)	~75 (nm)
Electron mobility	3e-10 (m ² V ⁻¹ s ⁻¹)**	3e-11 (m ² V ⁻¹ s ⁻¹)
Ion mobility (film)	3.5e-12 (m ² V ⁻¹ s ⁻¹)	
Ion mobility (solution)	5e-10 (m ² V ⁻¹ s ⁻¹)*	5e-11 (m ² V ⁻¹ s ⁻¹)
Ion concentration (solution)	0.1 (M)	
Film porosity	50%	
Temperature	300 (K)	
Open circuit potential	-4.7 eV vs vacuum = 0.26 V vs SHE	
Relative permittivity electrolyte solution	37 [#]	
Relative permittivity QD film	10	

* In reality, the ion mobility in the solution is expected to be higher, while the distance between the WE and CE is larger. For performance reasons, the mobility of ions was reduced. The distance between the WE and CE is lowered in accordance to avoid the formation of a large Ohmic drop over the solution. The mobility of the ions in solution is not limiting the injection of electrons, and thus increasing it further will not affect the results of the simulation. Performing the simulation with both 10 times increased ion mobility and distance between the WE and CE gave the same results, but took 10 times longer.

** It has been shown that electrons have a much higher mobility in ZnO QD films than the one used here.⁹ Increasing the electron mobility higher than ~2 orders of magnitude above the ion mobility in the film does not affect the results of the simulation however, as cation mass transport in the film quickly becomes the limiting factor. For performance reasons, the electron mobility was therefore kept at an unphysically low level.

[#] Based on acetonitrile. The QD films is assumed to be a mixture of a QD material and the electrolyte solution, so an arbitrary in-between value was picked for its relative permittivity. The relative permittivity of either the film of solution does not affect the results of the simulation as long as the spatial resolution is sufficient and can be put to any desired value.



Table A6.2. List of formulas employed in the simulator.

Formula	Name and purpose	Explanation of parameters
$J_n = nq\mu_n \frac{dV}{dx} - kT\mu_n \frac{dn}{dx}$ $J_c = cq\mu_c \frac{dV}{dx} + kT\mu_c \frac{dc}{dx}$ $J_a = aq\mu_a \frac{dV}{dx} - kT\mu_a \frac{da}{dx}$	Drift-diffusion equations Calculate the currents of electrons (n), cations (c) and anions (a).	J: current density q: elementary charge V*: electrostatic potential level vs vacuum μ: carrier mobility
$\frac{d^2V}{dx^2} = \frac{q}{\epsilon_0\epsilon_r} (n + a - c)$	1D Poisson equation Calculate the potential profile over the space of the simulation.	ε ₀ , ε _r : vacuum and relative electric permittivity.
$n = \int_{E=E_c}^{\infty} g_c(E) \frac{1}{1 + e^{\frac{E-E_F}{kT}}} dE$	Fermi-Dirac distribution Calculate the equilibrium concentration of electrons at the interface between the WE and the QD film.	E: energy E _c : conduction band level E _F : current Fermi level (= intrinsic Fermi level - electrostatic potential) g _c (E): density of states function of the material

* For electrons, the total potential relative to vacuum is instead used, i.e. *energy level in the DOS* vs. *vacuum + electrostatic potential*. In this way, the extra energy needed for electrons to occupy higher levels in the DOS at higher energies is taken into account in calculating the drift current. The position of electrons in the DOS is calculated from the electron concentration.

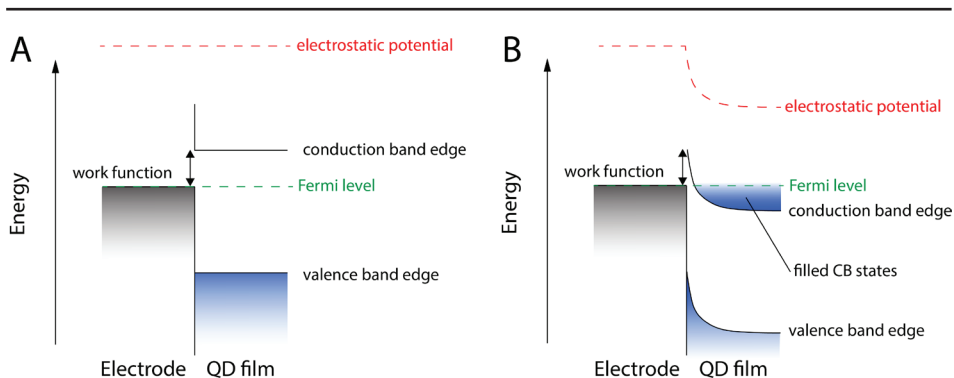


Figure A6.1. Energy level diagrams of the electrode and QD film at A) open circuit potential and B) negative applied potential $>$ electron injection barrier. As the applied potential is increased, an electric double layer (EDL) develops at the QD film/electrode interface, causing the electrostatic potential to drop over the interface. This potential profile causes band bending. When the applied potential is larger than the electron injection barrier (= conduction band edge – electrode work function), electrons can tunnel through the EDL into the conduction band states. The energy cost of entering a higher energy state (the semiconductor environment) is compensated by the gain in energy through the electrostatic potential.

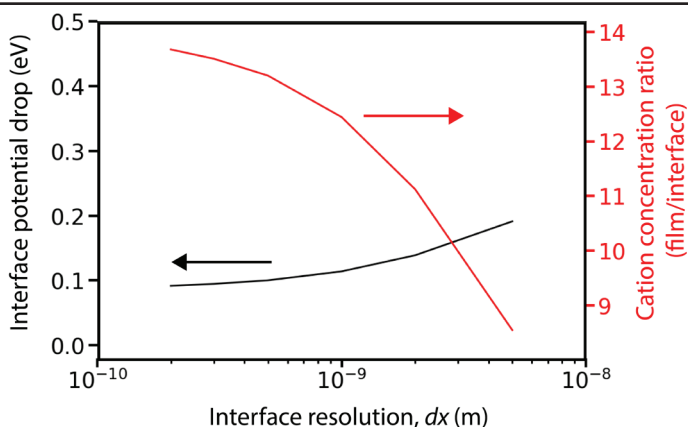


Figure A6.2. Steady-state interface potential drops and cation concentration ratios for different interface resolutions. The cation concentration ratio is calculated by dividing the concentration of cations in the film by the electrolyte concentration. When the resolution across the interface is insufficient, the simulator overestimates the interface potential drop and underestimates the cation concentration and thus doping density in the QD film. A resolution of 0.3 nm was deemed precise enough while still allowing for reasonable performance and was used in CV simulations.

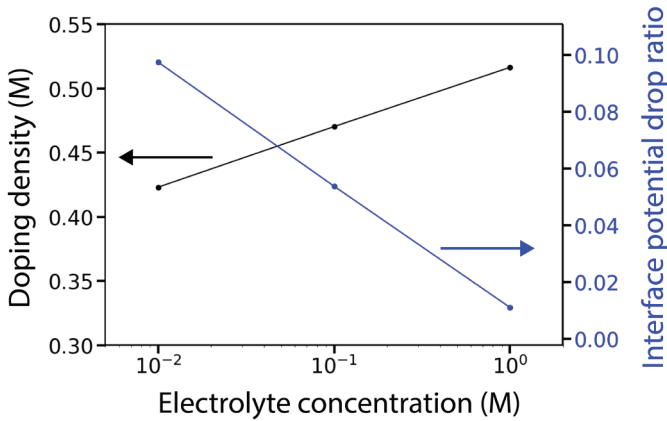


Figure A6.3. Steady-state interface potential drops and doping densities for different electrolyte concentrations. The interface potential drop is plotted as the ratio of the total potential drop (potential drop over the film/solution interface)/(voltage at WE vs RE). For lower electrolyte concentrations, the interface drop is larger and the steady state doping density of the QD film is lower.

6

Derivation A6.1: relation between the interface potential drop and the concentration of excess charge in the film.

Starting from the Boltzmann distribution:

$$c = c_0 \exp\left(\frac{-q\phi}{kT}\right) \quad (\text{A6.1})$$

$$\text{and } \frac{c_{film}}{c_0} = \exp\left(\frac{q\Delta\phi_{F/S}}{kT}\right) \quad \text{with } c_{film} = \frac{n}{p}, \text{ assuming no anions are left in the film}$$

Where c is the cation concentration, c_0 is the bulk electrolyte concentration (assuming an infinite supply of bulk cations), q is the elementary charge, ϕ is the electrostatic potential, k is the Boltzmann constant, T is the temperature, $\Delta\phi_{F/S}$ is the electrostatic potential drop over the film/solution interface, c_{film} is the concentration of cations in the electrolyte in the nanoporous film, n is the concentration of electrons in the film (for a QD film this is equal to the number of additional electrons per QD/the QD volume*the porosity of the film), and p is the porosity of the film. We can then define a minimum bulk concentration to keep $\Delta\phi_{F/S}$ below a certain threshold:

$$c_0 = \frac{n}{p * \exp\left(\frac{q\Delta\phi_{F/S}}{kT}\right)} \quad (\text{A6.2})$$

For example for a film (porosity = 50%) of QDs with a diameter of 3.5 nm (QD volume

$= 22 \text{ nm}^3$, QD “concentration” $= 0.0742 \text{ M}$, if we wish to charge the film with 8 electrons per QD while keeping $\Delta\phi_{F/S} < 2 \text{ kT}$ ($= 0.052 \text{ eV}$ at RT), this would require a minimum electrolyte concentration of 0.16 M :

$$c_0 = \frac{0.594 \text{ M}}{0.5 * \exp(2)} = 0.16 \text{ M} \quad (\text{A6.3})$$

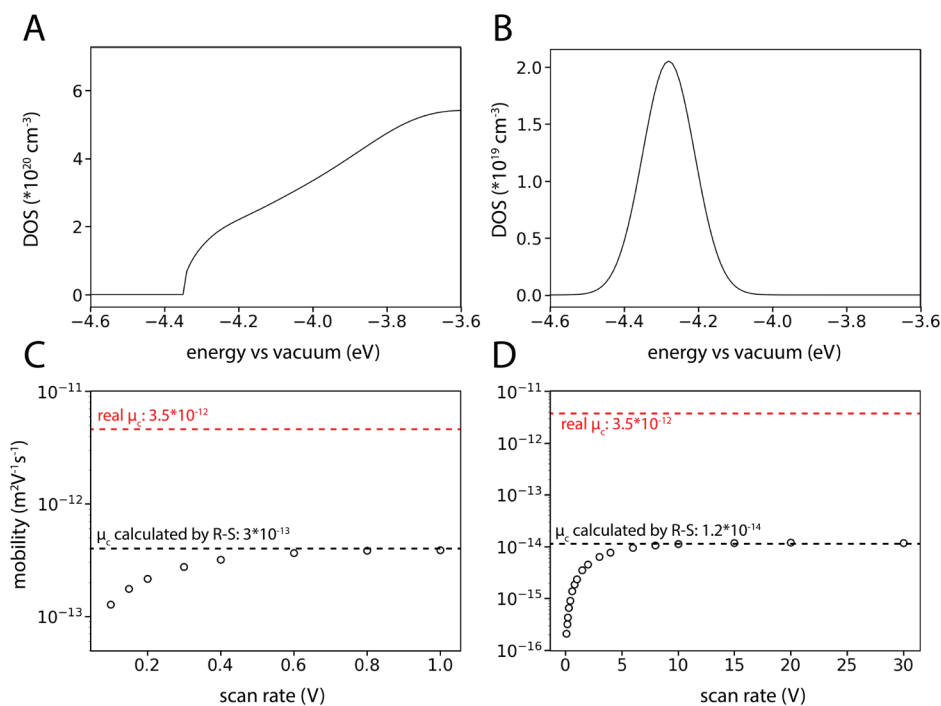


Figure A6.4. Cation mobilities (μ_c) in the QD film as calculated by the Randles-Ševčík equation compared to the mobility that was set at the start of the simulation, using two different density of states (DOS) functions. A) The typical ZnO DOS function that was used in all other simulations. B) A DOS function that more closely resembles a simple electrochemical reaction (single Gaussian peak), such as may be observed when charging a battery electrode. Note the scaling, as B) has a much lower total amount of states available. Because of this a higher scan rate is needed to enter the cation transport-limited regime. C) and D) show the respective scan rates series of simulations using A) and B) as DOS functions. As the scan rate increases, the calculated mobilities converge, showing that the current density becomes limited by the cation mass transport in the film at these scan rates. Depending on the specific DOS function, the Randles-Ševčík equation underestimates the mobility by a factor 10-300 for these systems.



Derivation A6.2: Solution of drift-diffusion equations for the charging of a nanoporous film

Table A6.3. Assumptions to solve the concentration profile during cation mobility-limited charging.

- (1) Charge neutrality is preserved locally in the film.
- (2) The current density in the film is constant over distance (follows from (1)).
- (3) The electron mobility is much higher than the cation mobility ($\mu_n \gg \mu_c$).
- (4) $n(x) = c(x)$ and thus $dn/dx = dc/dx$, where x is the distance, n is the electron concentration and c is the excess hole concentration.
- (5) Boundary condition 1: No cations flow into the WE ($J_c(x=WE) = 0$)
- (6) Boundary condition 2: No electrons flow out of the film ($J_n(x=IF) = 0$)
- (7) dn/dt is independent of x .

First we consider assumption (7). Since the amount of electrons is increasing at the same rate throughout the whole film, the current density of electrons across the film must show a linear profile with distance. This is always observed in typical charging simulations and can also be understood intuitively as any non-linear profile of electron current would lead to the accumulation of electrons at certain positions in the film. That accumulation would lead to increased diffusion away from those positions, until a stable concentration profile is obtained, where the concentration of electrons increases at the same rate everywhere in the film and assumption (7) is satisfied. The same is true for cations, except their flow direction is reversed. In combination with assumption (2) and boundary conditions (5) and (6) we find linear current density profiles for electrons (J_n) and cations (J_c) across the film, as depicted in Figure A6.5.

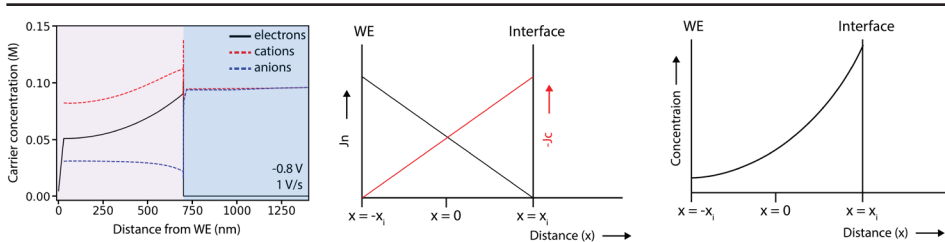


Figure A6.5. Concentration and current profiles in the QD film during cation-mobility limited charging.

Taking the midpoint between the WE and the IF as $x = 0$, so that $x_{IF} = x_i$ and $x_{WE} = -x_p$, we can then express the current density of electrons and holes as follows:

$$J_n(x) = \frac{J_{tot}}{2} + \frac{J_{tot} * x}{2x_i} \quad (\text{A6.4A})$$

$$J_c(x) = \frac{J_{tot}}{2} - \frac{J_{tot} * x}{2x_i} \quad (\text{A6.4B})$$

Where J_{tot} is the total current density over the film. We can then start from the drift-diffusion equations for electrons and excess cations:

$$J_n = nq\mu_n \frac{dV}{dx} - kT\mu_n \frac{dn}{dx} \quad (\text{A6.5A})$$

$$J_c = cq\mu_c \frac{dV}{dx} + kT\mu_c \frac{dc}{dx} \quad (\text{A6.5B})$$

Where n and c are the concentrations of electrons and cations, μ_i is the mobility of the respective carrier, V is the electric field, q is the elementary charge, k is Boltzmann's constant and T the temperature. We can substitute the current density profiles A6.4A and A6.4B to and rearrange to obtain:

$$nq\mu_n \frac{dV}{dx} + kT\mu_n \frac{dn}{dx} = \frac{J_{tot}}{2} - \frac{J_{tot} * x}{2x_i}$$

$$nq\mu_n \frac{dV}{dx} + = \frac{J_{tot}}{2} - \frac{J_{tot} * x}{2x_i} - kT\mu_n \frac{dn}{dx} \quad (\text{A6.6A})$$

$$cq\mu_c \frac{dV}{dx} - kT\mu_c \frac{dc}{dx} = \frac{J_{tot}}{2} + \frac{J_{tot} * x}{2x_i}$$

$$cq\mu_c \frac{dV}{dx} = \frac{J_{tot}}{2} + \frac{J_{tot} * x}{2x_i} + kT\mu_c \frac{dc}{dx} \quad (\text{A6.6B})$$

When we divide A6.6A and A6.6B, then apply assumption (4) we find:



$$\frac{\frac{J_{tot}}{2} - \frac{J_{tot} * x}{2x_i} - kT\mu_n \frac{dn}{dx}}{\frac{J_{tot}}{2} + \frac{J_{tot} * x}{2x_i} + kT\mu_c \frac{dc}{dx}} = \frac{nq\mu_n \frac{dV}{dx}}{cq\mu_c \frac{dV}{dx}}$$

$$\frac{\frac{J_{tot}}{2} - \frac{J_{tot} * x}{2x_i} - kT\mu_n \frac{dc}{dx}}{\frac{J_{tot}}{2} + \frac{J_{tot} * x}{2x_i} + kT\mu_c \frac{dc}{dx}} = \frac{cq\mu_n \frac{dV}{dx}}{cq\mu_c \frac{dV}{dx}} = \frac{\mu_n}{\mu_c} \quad (\text{A6.7})$$

$$\left(\frac{J_{tot}}{2} - \frac{J_{tot} * x}{2x_i} - kT\mu_n \frac{dc}{dx} \right) \mu_c = \left(\frac{J_{tot}}{2} + \frac{J_{tot} * x}{2x_i} + kT\mu_c \frac{dc}{dx} \right) \mu_n$$

$$\mu_c J_{tot} \left(\frac{1}{2} - \frac{x}{2x_i} \right) + kT\mu_c \mu_n \frac{dc}{dx} = \mu_n J_{tot} \left(\frac{1}{2} - \frac{x}{2x_i} \right) - kT\mu_c \mu_n \frac{dc}{dx}$$

$$\mu_c J_{tot} \left(\frac{1}{2} - \frac{x}{2x_i} \right) - \mu_n J_{tot} \left(\frac{1}{2} - \frac{x}{2x_i} \right) = 2kT\mu_c \mu_n \frac{dc}{dx}$$

$$\frac{J_{tot}}{2} \left((\mu_c - \mu_n) - \frac{x}{x_i} (\mu_c - \mu_n) \right) = 2kT\mu_c \mu_n \frac{dc}{dx}$$

$$\frac{dc}{dx} = \frac{\frac{J_{tot}}{2} \left((\mu_c - \mu_n) - \frac{x}{x_i} (\mu_c - \mu_n) \right)}{2kT\mu_c \mu_n} = x \frac{J_{tot}(\mu_c - \mu_n)}{4x_i kT\mu_c \mu_n} + \frac{J_{tot}(\mu_c - \mu_n)}{4kT\mu_c \mu_n} \quad (\text{A6.8})$$

After integration of c to dx we find a quadratic concentration profile for cations and thus also for electrons because of assumption (4) (Figure A6.5C):

$$c(x) = -x^2 \frac{J_{tot}(\mu_c - \mu_n)}{8x_i kT\mu_c \mu_n} + x \frac{J_{tot}(\mu_c - \mu_n)}{4kT\mu_c \mu_n} + c_0 \quad (\text{A6.9})$$

Furthermore by calculating $\Delta c = c(x_p) - c(-x_p)$ we find:

$$\Delta c = -x_i^2 \frac{J_{tot}(\mu_c - \mu_n)}{8x_i kT\mu_c \mu_n} + 2x_i \frac{J_{tot}(\mu_c - \mu_n)}{4kT\mu_c \mu_n} + x_i^2 \frac{J_{tot}(\mu_c - \mu_n)}{8x_i kT\mu_c \mu_n} = 2x_i \frac{J_{tot}(\mu_c - \mu_n)}{4kT\mu_c \mu_n} \quad (\text{A6.10})$$

$$J_{tot} = \frac{4kT}{2x_i \Delta c} \mu_c \mu_n$$

Considering $2x_i =$ film thickness L , we come to the following expression for the current density at any given point in the QD film during diffusion-limited charging:

$$J_{tot} = \frac{4kT}{L\Delta c} \frac{\mu_c \mu_n}{(\mu_c - \mu_n)} \quad (\text{A6.11})$$

As expected, the current density is inversely proportional to the concentration gradient and the thickness of the film. If one of the charge carriers is limiting (as in this case the cations are), the expression reduces to:

$$J_{tot} = -\frac{4kT\mu_c}{L\Delta c} \quad (\text{A6.12})$$

And a simple linear relationship between current density and charge carrier mobility is observed. Unfortunately, since Δc (or Δn) is unknown during an experiment and depends on many factors, we cannot directly use this expression to determine the limiting mobility during a CV scan. It should be noted that while the charge transport in this case is limited by the mobility of the cations and charging of the film is in a diffusion-limited regime, drift current cannot be neglected. This follows logically from assumptions (2), (3) and (4): since the concentration profile of both carriers is the same, their diffusion fluxes point in the same direction (both electrons and cation diffuse towards the WE). However, electrons necessarily must move in the opposite direction as cations during film charging. To achieve this, an electric field is needed, which is always present in the film during charging. Thus both drift and diffusion are contributing to the overall current in the film.

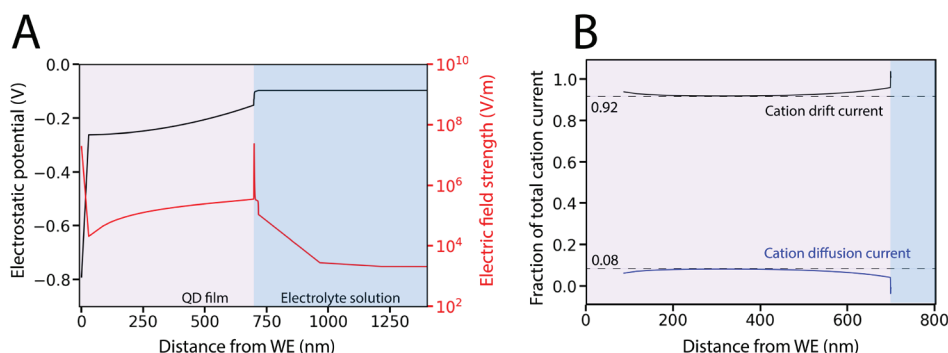


Figure A6.6. A) The potential and electric field in the QD film during cation transport-limited charging. A strong electric field is present in the QD film even during cation transport-limited charging, which leads to drift currents in the film. B) The individual components of the cation current. The drift current accounts for ~92% of the total cation current during cation transport-limited charging of the QD films.

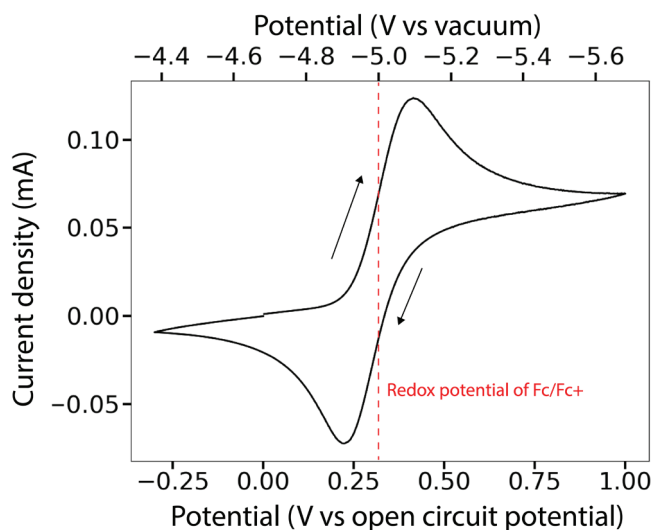


Figure A6.7. Experimental CV of the ferrocene/ferrocenium (Fc/Fc⁺) pair in acetonitrile used for referencing in this work.⁹ The redox potential of Fc/Fc⁺ is at ~5.0 V vs. the vacuum level.²⁴

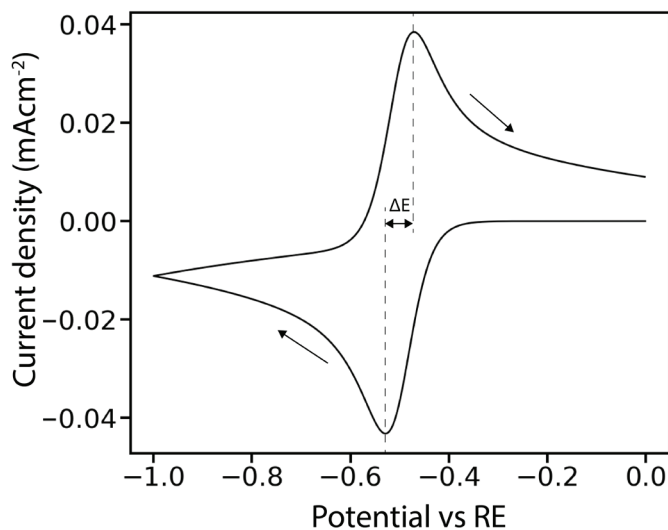
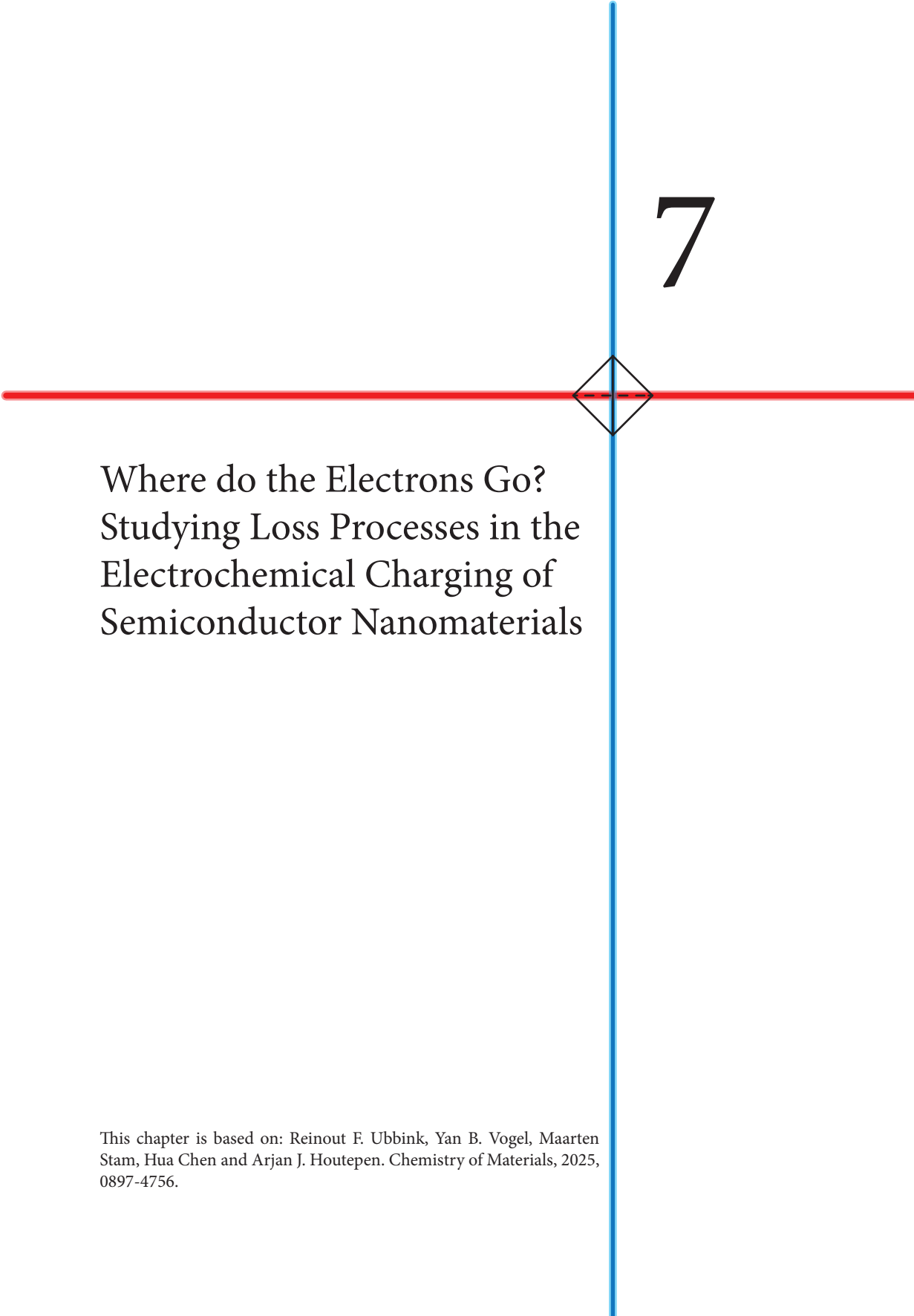


Figure A6.8. Simulated CV of a simple reductant/oxidant pair, $E^0 = -0.5$ V vs RE. As expected, ideal reversible behavior is observed with $\Delta E = 57$ mV.





Where do the Electrons Go? Studying Loss Processes in the Electrochemical Charging of Semiconductor Nanomaterials

This chapter is based on: Reinout F. Ubbink, Yan B. Vogel, Maarten Stam, Hua Chen and Arjan J. Houtepen. *Chemistry of Materials*, 2025, 0897-4756.



7.1 Introduction

The ability to controllably charge films of semiconductor nanocrystals like quantum dots (QDs), nanoplatelets or nanowires with electrons or holes opens up possibilities for use of these materials in light-emitting electrochemical cells, photodetectors and lasers.¹⁻⁵ Through electrochemical methods, the Fermi energy and thus charge density in semiconductor nanocrystal (NC) films can be controlled with great precision.⁶⁻⁹ When charging a semiconductor NC film electrochemically, a potential is applied to the film while it is submerged in an electrolyte solution containing free ions.¹⁰ The application of the potential leads to a flow of electrons or holes into the semiconductor NC film, depending on the sign of the applied potential. The charge of the additionally injected electrons/holes is compensated by ions flowing into the pores in the film from the electrolyte solution, resulting in electrochemical charging of the semiconductor NC film. In the ideal case, electrochemical charging of semiconductor NCs is fully reversible, meaning every electron/hole that is injected into the film remains there and can subsequently be extracted by returning the potential back to the open circuit potential and letting the charges flow back into the electrode.

Charging of semiconductor NC films is rarely fully reversible however, and large differences in reversibility of charging are observed between different materials. For nanocrystals of materials like indium phosphide, cadmium selenide¹¹ or lead halide perovskites¹², charges injected in the NCs are often lost, after which they cannot be extracted again. We have shown previously for ZnO and PbS NCs that even if charges can be recovered in a fast cyclic voltammetry experiment, they are lost on longer timescales.^{9, 13, 14} Methods have been developed to improve the stability of the injected charges^{8, 15}, but these are hampered by the fact that it is not well understood what processes are responsible for the loss of charge density in doped semiconductor NC film. While electrochemical measurements on semiconductor NCs are typically executed under stringent oxygen- and water-free conditions, contaminations of these molecules in the electrolyte cannot be fully excluded, and both can be reduced at high enough negative potentials, resulting in loss of electrons. On the other hand, we can also not exclude that other redox active impurities are present, for instance on the surface of the semiconductor NCs, such as ligands, adsorbed water or OH⁻ ions or unknown reaction products from the semiconductor NC synthesis and processing. Indeed, Pu *et al.* have shown that metal-carboxylate ligands are likely reduced in QLEDs, resulting in a drop in efficiency.¹⁶

In order to improve the stability of electrochemically injected charges into semiconductor NC films, we aim to identify which processes are most likely to result in loss of charges, and to what extent they occur in films of different semiconductor NC materials. To tackle this problem systematically, in this work we start by examining one-electron transfer reactions between the semiconductor NCs and redox molecules with variable reduction potential. Although there is no theoretical difference between charging the conduction band (CB) with electrons or the valence band with holes, we will focus on electron injection into the conduction band and loss of electrons, since this process is much more readily achieved in most semiconductor NC materials and hence better understood. The question 'where do the holes go?' is even harder to answer. This will be the topic of future publications. Since ZnO QD films can show nearly reversible charging behavior, we use them as a model

experimental system to show how the charging is affected by electrochemical reactions between electrons in the QDs and different redox-active species in solution. We model the same systems using drift-diffusion simulations. In previous work we showed that the electrochemical charging of semiconductor NC films can be accurately simulated by tracking the movement of all mobile species using drift-diffusion simulations¹⁷, however only ideal charging of semiconductor NC films was considered. Here we extend the simulations by including electrochemical reactions using the Gerischer kinetic theory¹⁸.

First we show how the redox potential (E^0) of the redox-active species determines the reversibility of one-electron transfer reactions in both simulation and experiment. Species with a reduction potential in the bandgap of the semiconductor NCs lead to irreversible loss of charges from the semiconductor NCs. While species with a reduction potential inside the conduction band also partake in electrochemical side-reactions, these are fully reversible and thus do not lead to irreversible loss of charges. This is shown experimentally by comparing cyclic voltammograms on ZnO QD films with either cobaltocenium (E^0 inside the CB) or ferrocenium (E^0 in the bandgap) added to the solution. Simulations show that when E^0 is well below the CB, the reverse reaction (the oxidation of cobaltocene/ferrocene) is impeded, because it would only occur at much more positive potentials, resulting in irreversible loss of electrons.

Subsequently we address the more complicated case of reactions with molecular oxygen, which may give rise to subsequent chemical reactions between the formed superoxide molecules and ligands or protic impurities. Experiments show charging of ZnO QDs in oxygen-saturated solution are fully irreversible, even though the reduction potential of oxygen reduction is in the ZnO conduction band. Through simulations we show that this can be explained if the reduction of molecular oxygen to superoxide is followed by an irreversible chemical reaction in a reversible electrochemical-irreversible chemical ($E_r C_i$) mechanism.

Finally we model reactions where the semiconductor NC material itself is reduced. While this could include bulk decomposition of the materials, bulk decomposition is rarely observed in the potential ranges discussed here. More likely are reactions with ligands or surface ions on the surface of the NCs, as the most reactive species reside on the surface. It is found that the ability to reversibly charge a material depends on the energy of the CB edge compared to the lowest E^0 of the available reduction reactions that can occur in that material. Simulations of material reduction reactions closely resemble experimental data of InP and CdSe QDs, marking material reduction reactions as a likely candidate for electron loss in these materials.

Taken together, these results show that the stability of electrochemical charges in semiconductor NC materials is determined by electrochemical side reactions and their reduction potentials in relation to the energy of electrons in the CB. All of these reactions must be suppressed to achieve stable and reversible electrochemical charging of semiconductor NCs. Based on experiments and simulations, we provide strategies for improving the reversibility and stability of electrochemical charging of semiconductor NCs.



7.2 Results and discussion

Reversible and irreversible charging of QD films

The electrochemical setup of both experiments and simulations is shown schematically in Figure 7.1A. semiconductor NCs are deposited on a working electrode (WE), which is submerged in an electrolyte solution containing ions and optionally redox-active species which can react with charges in the semiconductor NC film. A three-electrode setup is used, where a voltage is applied to the WE with respect to a known reference electrode (RE), while the potential at the counter electrode (CE) is allowed to float to complete the circuit.

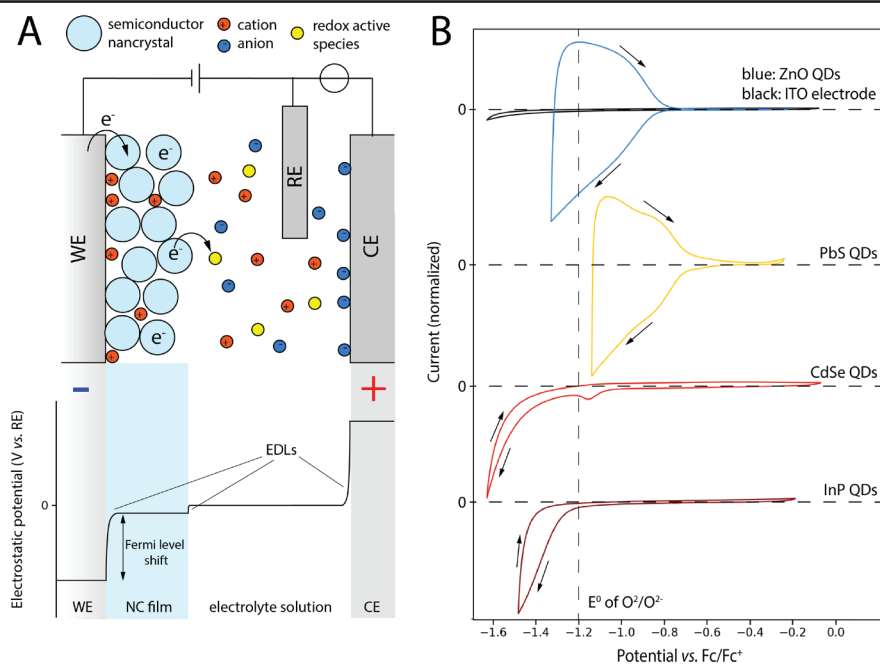


Figure 7.1. A) Schematic of the setup used for electrochemical charging of semiconductor NCs. semiconductor NCs are deposited on the working electrode (WE) and placed in an electrolyte solution containing ions in a three-electrode system with a reference electrode (RE) and counter electrode (CE). The electrostatic potential drops due to the formation of electric double layers (EDLs) at the interfaces between WE/film, film/solution and solution/CE. B) Cyclic voltammograms of QD films, normalized to the peak cathodic current. QD sizes, film thickness and ligand types can be found in the Table A7.1 in the appendix and in the methods section. All materials are measured with 0.1 M LiClO_4 in acetonitrile as the electrolyte, at a scan speed of 50 mV/s. Scan directions are indicated by arrows. Almost reversible charging is observed for ZnO (blue) and PbS (yellow) QDs (extraction ratios of 0.85 and 0.87 respectively), while CVs of CdSe (red) and InP (dark red) are almost fully irreversible (extraction ratios 0.1 and 0.08 respectively). Any observed positive current is ascribed to the formation and breakdown of the EDL on the electrode, which can also be observed for the bare indium tin oxide (ITO) WE (black).

When applying a potential to the semiconductor NC film in the presence of a sufficiently concentrated electrolyte solution, the ions will form an electric double layer (EDL) at the WE/NC film interface (Figure 7.1A), which will cause an increase of the electrochemical potential (μ) inside that semiconductor NC film by an amount approximately equal to the applied potential.¹⁷ Electrons will start to transfer into the semiconductor NC film if it is raised higher than the first available empty state in the CB of the semiconductor NCs. This results in an injection current into the semiconductor NCs. Counterions (cations in the case of electron injection) will migrate from the solution into the pores of the semiconductor NC film to compensate for the added charge, resulting in a net doping of the semiconductor NCs. In the ideal case, raising the applied potential further above the CB edge will cause any states available in the density of states (DOS) of the material up to μ to fill up. Then when the applied potential is reduced again, drops, electrons (or holes in case of positive potentials) will leave the QDs and ions will diffuse back into the solution. In the ideal case, electrons/holes would flow back into the electrode, resulting in an extraction current with opposite sign to the injection current.

This process of raising and lowering the potential can be done experimentally by recording a cyclic voltammogram (CV), where the potential is swept back and forth with a certain set scan rate. Figure 7.1B shows CVs performed on ZnO, PbS, CdSe and InP NC films. The CVs start at open circuit potential (OCP) and are scanned to the negative vertex first and then back to OCP (indicated with arrows) at a scan rate of 50 mV/s. In the experimental CV on ZnO QDs, the aforementioned injection and subsequent extraction of electrons can clearly be observed: as the applied potential becomes more negative, a negative current is observed, because electrons are injected into the material. The more negative the potential becomes, the higher in the QDs is, and the more conduction states are filled with electrons. When scanning back, a positive extraction current is observed. By integrating the negative and positive parts of the scan, the extraction ratio can be determined for this material, defined as extracted charge/injected charge. For ZnO and PbS QD films (blue and yellow lines in Figure 7.1B), extraction ratios of > 0.85 are observed, which indicates that the doping of the QDs is almost fully reversible. However, for other materials, extraction ratios are typically much lower. For films of CdSe and InP QDs (red and dark red lines in Figure 7.1B), very little or no extraction current is observed from these experiments (extraction ratios < 0.1). Even though electrochemical doping takes place in these films, the process is irreversible. These results are typical. In the literature charge extraction from CdSe core-only QDs is rarely observed¹⁹, and extraction ratios are low unless the temperature is reduced to $-60\text{ }^{\circ}\text{C}$ ²⁰. For InP QDs, no charge extraction in cyclic voltammograms has been reported to the best of our knowledge.

Figure 7.1 shows only CVs to negative applied potentials. While electrochemical injection of holes into QDs should in theory be possible by applying positive potentials, this has been very challenging to achieve and has hardly been investigated except for a small number of studies on lead chalcogenide and CsPbBr₃ perovskite nanocrystals.²¹⁻²³ We will therefore focus on results of electron injection in this work and extend our discussion to hole injection later on.



Loss of electrons

When no extraction current is observed this implies that the injected electrons are no longer available for extraction, indicating 'loss' of electrons from the semiconductor NCs. In CdSe and InP QDs the conduction band is higher in energy than in ZnO and PbS QDs. This means higher potentials need to be applied to achieve electron doping in these materials, and it becomes more likely that the reduction potential of reactions with impurities or on the surface of the semiconductor NC material itself is below the CB edge. To achieve reversible or even permanent^{8,9} doping in CdSe and InP QD films, it is important to understand what loss reactions can occur during the electrochemical doping of films. By simulating various electrochemical loss reactions and comparing to experimental data, we gain insight in what kinds of loss processes are occurring, and how to explain the discrepancies in doping reversibility of different QD materials. For this reason, we extended our earlier reported drift-diffusion simulations of electrochemical doping of QD films to include electrochemical side-reactions based on Gerischer kinetics (Figure 7.2, see appendix for a full derivation and implementation).

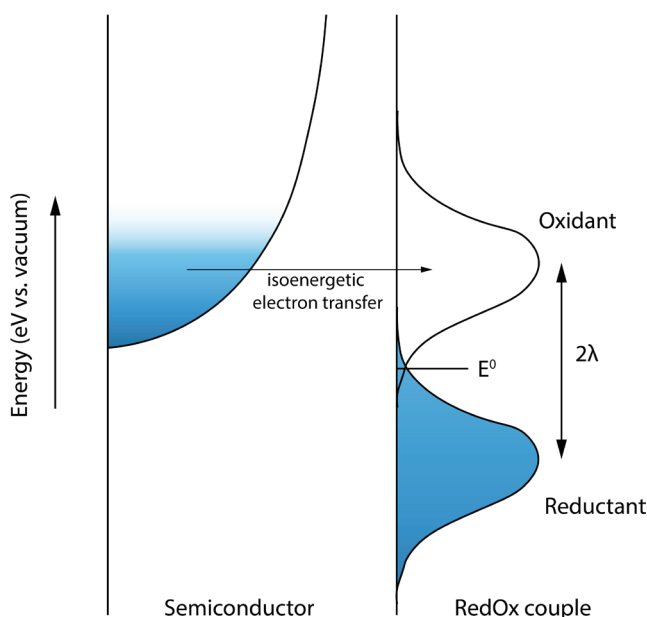


Figure 7.2. Example energy state distribution in the Gerischer kinetic model, filled states are blue and empty states white. The semiconductor conduction band is modelled using a density of states function. The energy states of the redox couple are modelled using a redox potential E^0 and a reorganization energy λ . The total electron transfer rate is calculated by integrating the rates of isoenergetic electron transfer over all energies.

In the Gerischer model¹⁸, the rate of isoenergetic electron transfer between the semiconductor NCs and the redox-active species is calculated for each energy level separately. The total rate is then calculated by integrating over all energy levels, correcting for the occupancy

of states in the semiconductor NC DOS using the Fermi-Dirac distribution. While for metallic working electrodes this is not always important, it is essential to take into account the DOS for semiconductors, as no reactions can take place from the energies in the band gap range. The energy states of the oxidant/reductant couple are modelled as Gaussian distributions using a redox potential E^0 and a reorganization energy λ , as shown in Figure 7.2. The final parameter in the Gerischer model is the prefactor of the reaction rate k^0 , which includes the transfer attempt frequency and dimension correction factors (detailed explanation in the appendix). By adjusting the value of these parameters, different types of redox species are modelled. The Gerischer model is identical to the Marcus model for transfer of an electron from a single energy state to an oxidant/reductant couple. However, since the Gerischer model takes into account electron transfer from all available energy states in the semiconductor NC DOS it is a better fit for semiconductor materials.

Loss of electrons to reversible oxidant in solution

To systematically investigate the effect of oxidants present in the electrolyte solution, we first investigate loss of electrons to an ideal dissolved oxidant. Cobaltocenium is known to undergo ideal one-electron reduction to cobaltocene, with an E^0 at around -1.2 eV vs. Fc/Fc⁺ in acetonitrile, well inside the conduction band of the ZnO QDs (CB edge at -0.7 eV vs. Fc/Fc⁺). Figure 7.3A shows the experimental CV of a ZnO QD film submerged in an electrolyte solution containing 1 mM cobaltocenium (blue line). In addition to a charging current of electrons entering the ZnO CB starting around -0.7 V vs. Fc/Fc⁺, a clear reduction peak of cobaltocenium is observed at -1.1 V vs. Fc/Fc⁺. Oxidation of cobaltocene back to cobaltocenium is also observed on the backward scan as a positive peak, confirming that the reaction is reversible.

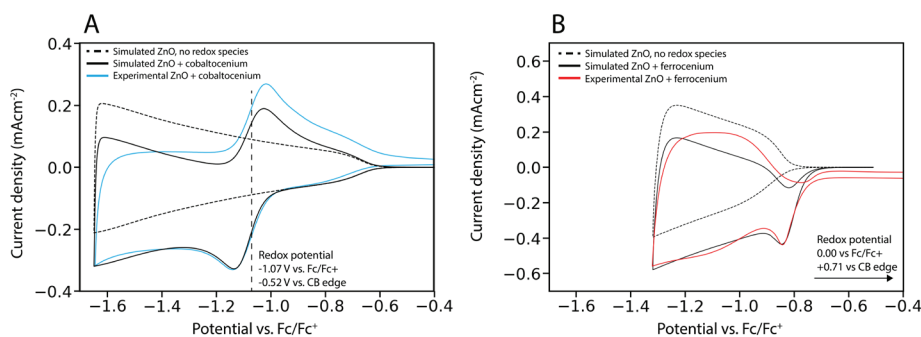


Figure 7.3. Experimental and simulated CVs of ZnO QD films in the presence of a redox couple at a scan rate of 50 mV/s. In experiment the electrolyte was acetonitrile containing 0.1 M LiClO₄ and 1 mM of cobaltocenium/ferrocenium hexafluorophosphate. QD diameter is 2.5 nm. A) If the reduction potential is in the CB of the ZnO QDs a reversible redox reaction is observed. The total current is the sum of the charging current into the ZnO QD film (dashed line) and the resulting redox current of the reduction reaction. B) If the reduction potential is in the band gap of the ZnO QDs, an irreversible reduction current is observed as soon as the applied potential is raised beyond the conduction band edge.



We performed simulations of the same system both with and without the inclusion of side-reactions with cobaltocenium, which are shown in Figure 7.3A (black lines). In the simulated scan without any oxidant present, perfect cyclical charging and discharging of ZnO is observed, with an extraction ratio of unity. The scan with the oxidant present in the simulation shows an additional reduction (negative current) and oxidation (positive current) peak around the reduction potential of the oxidant.

The resulting CV is the sum of the charging of the ZnO film and the expected ideal reduction/oxidation current of the redox couple. Although both processes are ideally reversible, the observed extraction ratio in both the experiment and simulation is less than unity (0.37 for simulation, 0.61 for experiment) because of a leak current: cobaltocene is formed at the working electrode, transported to the counter electrode through diffusion, and subsequently oxidized to form back cobaltocenium. This results in a net transport of electrons from the WE to the CE and a leakage current when the applied bias is higher than the reduction potential of the redox couple.

Figure 7.3B shows simulations and experiment of another ZnO QD film, but with ferrocenium present in solution, which has a reduction potential that is inside the band gap of ZnO. In this case, a reduction peak is observed as soon as the applied potential is high enough to inject electrons into the conduction band (around -0.85 V in Figure 3B). Once electrons can be injected into the ZnO, they can reach any ferrocenium species that are present in the film and reduce them, resulting in a sharp peak at the CB edge, as we reported before.²⁴ However, no oxidation peak is observed, since the reduction potential is inside the bandgap the material. In terms of the Gerischer model (Figure 7.2), all the filled reductant energy states are below the CB edge of the ZnO, so no electrons would be transferred back to the ZnO even if the conduction band is completely empty. This means that the reduction of ferrocenium to ferrocene is also irreversible in this case. At potentials above the CB edge, an additional irreversible leak current is observed for the same reasons as mentioned for the cobaltocene system in Figure 7.3A. The reversibility of the redox reaction thus depends on the reduction potential compared to the conduction band edge of the QDs.

While this shows that irreversible CVs can be due to kinetically facile reactions with redox impurities with an E^0 in the bandgap, it is unlikely that this explains the loss of electrons shown in Figure 7.1 for 2 reasons. First, the sharp peak at the CB edge that is due to the oxidation of such ideal impurities is not observed in experiments. Secondly, as shown below addition of oxygen makes CVs on ZnO films completely irreversible in experiment, even though its reduction potential is in the conduction band. To explain these observations, we next consider what happens if an electron transfer reaction to a redox impurity is coupled to an irreversible chemical reaction in an reversible electrochemical-irreversible chemical (E_rC_i) mechanism.

Loss of electrons to oxidant, followed by irreversible reaction

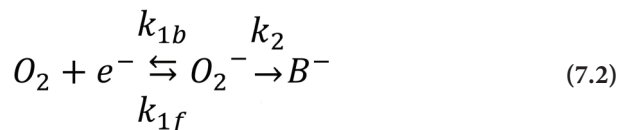
The most relevant potential oxidant molecule in real systems is molecular oxygen itself, especially when permanent electrochemical doping is considered.¹⁴ Indeed, adding oxygen to the electrolyte solution makes CVs on ZnO QDs irreversible. In Figure 7.4A, two

CVs on ZnO QD films are presented, after bubbling either argon or O₂/N₂ 0.21/0.79 gas through the electrolyte solution. The addition of molecular oxygen reduces the extraction ratio from 0.92 to 0.0. This shows that molecular oxygen acts as an oxidant and makes charge injection into QDs irreversible; it does not necessarily mean that the reason CVs on QDs are typically irreversible is due to oxygen.

In aprotic media, reduction of oxygen occurs through single electron reduction to the superoxide radical:



Under strict anhydrous conditions this reaction has been shown to be ideally reversible in acetonitrile, with a reduction potential very similar to cobaltocene/cobaltocenium at ~ -1.2 V vs. Fc/Fc⁺.²⁵ Based on this it would be expected that the ZnO CV with bubbled oxygen would resemble those with cobaltocenium in solution, but we instead observe irreversible behavior. To investigate this difference, we performed CVs on bare ITO and bare glassy carbon (GC) electrodes after bubbling O₂/N₂ 0.21/0.79 through the electrolyte in order to saturate the oxygen concentration. These CVs are shown in Figure A7.1 in addition to the same scans but with argon bubbled to remove any oxygen from solution. Rather than reversible reduction and oxidation of oxygen, we observe only a fully irreversible reduction peak when oxygen is present in the solution, with a width of >0.3 V. This is likely explained by reactions of the oxygen radical that is formed upon reduction with impurities in the solvent, for example trace amounts of water that are present in as-purchased solvents (~ 10 ppm even for anhydrous solvents), or contaminations on the electrodes.^{26, 27} To observe fully reversible reduction of oxygen, both a very clean (water-free) solvent and electrode are required, since O₂⁻ is known to react further with H₂O and H⁺ impurities.²⁷ When considering reactions with QD films, many different contaminations can be present which can react with superoxide radicals, especially ligands (hydroxides on ZnO, carboxylates/amines on CdSe, PbS and InP). Ideal reversible reduction of oxygen is therefore unlikely, so we model the oxygen reduction as a reversible electrochemical-irreversible chemical (E_rC_i) reaction, as shown in the reaction scheme below.



The first step is a reversible single-electron reduction with forward and backward rate (k_{1f} , k_{1b}) dependent on the applied potential, modelled using Gerischer kinetics. The second step is irreversible chemical conversion of the reduced species. For the second step we used a constant rate k_2 as an input parameter for the simulation.

Figure 7.4B shows an example of a simulation incorporating E_rC_i reaction kinetics for different values of k_2 . When the irreversible rate constant is low, the result is comparable to



the simulation shown in Figure 7.3A, with a reversible redox couple in the conduction band. As k_2 increases, the reaction becomes more irreversible. The oxidation peak disappears (marked by 1 in Figure 7.4B), as all the reduced species are consumed before they can be oxidized again. The reduction peak also shifts to lower potentials with increasing k_2 (marked by 2). This occurs when the irreversible part of the reaction becomes so fast that any reduced species that are formed are immediately reacted away, disturbing the equilibrium of the reversible step. These results resemble those on E_rC_i reaction kinetics on flat electrodes.²⁸ The simulations with the E_rC_i reaction mechanism at a high k_2 closely resemble the results from the experimental oxygen reduction on bare electrodes (Figure A7.1).

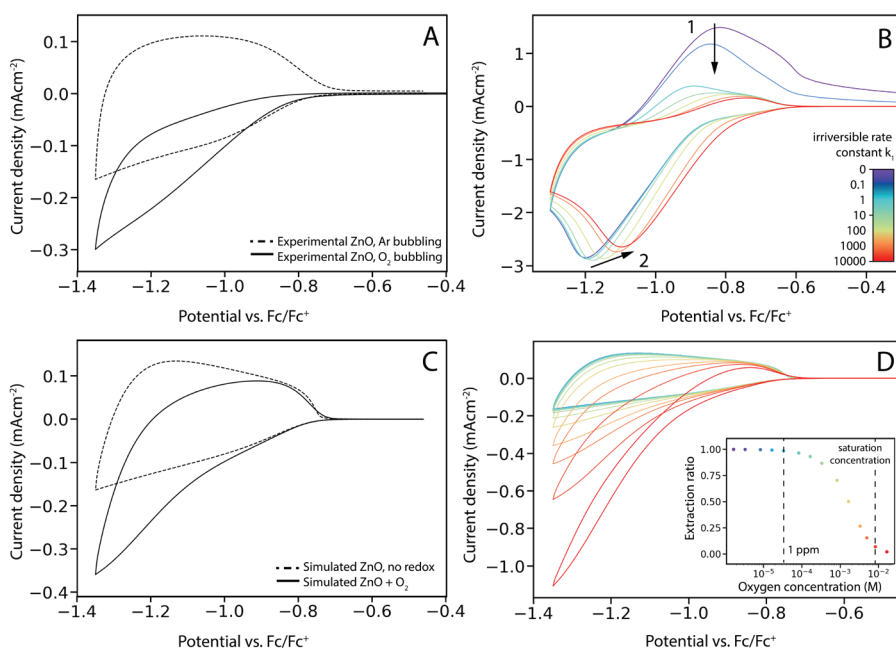


Figure 7.4. A) Experimental CVs of a ZnO QD film with and without oxygen in the electrolyte solution (0.1 LiClO_4 in acetonitrile) at a scan rate of 100 mV/s. QD diameter is 2.5 nm. B) Simulated CVs of a ZnO QD film in the presence of an oxidant molecule following the coupled reversible-irreversible mechanism. As the rate of the irreversible reaction increases, reaction with the oxidant becomes more irreversible. This results in reduction of the oxidation peak (1) as well as a shift of the reduction peak to lower energies (2). C) Simulated ZnO CVs with and without the addition of oxygen. Reduction of oxygen can only be successfully modelled by adjusting the Gerischer model to include a distribution of E^0 values around the experimentally observed value of $E^0 = -1.2$ V vs. Fc/Fc^+ . Simulated oxygen concentration = 3.3 mM, diffusion coefficient = $2.6 \times 10^{-6} \text{ cm}^2\text{s}^{-1}$). D) Simulated ZnO CVs with oxygen at different concentrations, ranging from 1.6×10^{-6} M (purple) to 1.6×10^{-2} M (red), diffusion coefficient = $2.6 \times 10^{-6} \text{ cm}^2\text{s}^{-1}$.

However, even employing the $E_r C_i$ reaction mechanism, the simulations do not yet fully resemble the experimental CVs of ZnO in oxygenated electrolyte. In the simulations in Figure 7.4B, a clear peak is observed in the cathodic current, which is not seen in the experiments in Figure 7.4A. A similar effect is observed when comparing the experimental CVs in oxygenated electrolyte on the glassy carbon and ITO electrodes, as the reduction peak on the ITO electrode appears at more negative potentials and is also much broader than on the glassy carbon. Using simulations with a wide range of parameters, we show that this widening of peaks cannot be explained with only the Gerischer model of charge transfer. An extended discussion of these simulations can be found in Figure A7.2 in the appendix. In short, a broad reduction peak is observed in the experiments (both on bare ITO and on the ZnO QD film), which implies a wide distribution of oxidant states and thus a large reorganization energy λ . However, a large λ value in the Gerischer model would also push up the oxidant states to higher energy values, since the separation between the peaks of the oxidant/reductant states distribution is governed by λ as well (Figure 7.2). This would entail that the reduction would be observed only at much higher energy values and thus much more negative applied potential, around 2.5 V *vs.* Fc/Fc⁺, while this is clearly not the case in the experimental data. It thus follows that the experimental reduction of oxygen on ZnO and ITO cannot be modelled by 1-electron transfer Gerischer kinetics. One reason for this observed broad reduction peak could be that oxygen is reduced at different reaction sites on the ZnO QD or ITO surface, leading to a distribution of E^0 and k^0 values. Another reason could be an electrostatic potential variation on the ITO surface, due to the relatively high sheet resistance of the electrode material, which has been known to induce peak broadening in ITO electrodes. We simulated this peak broadening by considering a distribution of E^0 values around -1.2 V *vs.* Fc/Fc⁺ instead of just one single E^0 value, resulting in an increase of the width of the Gaussian distribution of energy states of the oxidant molecule. This results in the simulations shown in Figure 7.4C which fit the experimental data reasonably well. Choosing a range of k^0 values would have the exact same effect on the distribution of energy states, leading to the same results.

Based on our experiments and simulations, the irreversible charging response of semiconductor NC films in the presence of oxygen can thus best be explained by the reversible reduction of molecular oxygen, followed by an irreversible chemical reaction of the formed superoxide radical.

Reduction of the semiconductor NC material

The loss processes discussed are dependent on the presence of contaminations, which can feasibly be avoided. In fact, reducing the concentration of contaminants to below 1 ppm practically eliminates side reactions, as shown by simulations in Figure 7.4D. However, some electrochemical side reactions are intrinsic to the material, for example reduction of lattice ions, surface ions, or ligands. If these reactions are irreversible and occur with the ions in the crystal lattice they may lead to cathodic decomposition of the materials. If they are limited to the surface²⁹, they may change the photoluminescence by inducing trap states without fully decomposing the materials.^{30, 31}

A likely candidate for cathodic decomposition reactions is the reduction of the metal ion in semiconductor materials to neutral metal. For example, this reaction probably occurs



in lead-perovskite and PbS nanocrystals, resulting in clear deposition of metallic lead.^{12, 23} Similarly, DFT calculations have suggested that indium reduction can take place in InP QDs when they are charged.³⁰ The addition of a shell around QDs helps protect them against cathodic decomposition if the ions in the shell have more negative standard reduction potentials (e.g. Zn^{2+} is more stable than Cd^{2+}), and may allow (semi-)stable electron injection into QD materials.^{30,31} Especially ZnS shells greatly improve the stability under negative potentials.¹¹ Surface modifications also have a large influence on the reduction potential of the cations of QDs.¹⁶ Since the surface ions are the first to undergo reduction, increasing their reduction potential can improve the stability of the QDs to cathodic decomposition.

To model how such material reduction reactions influence CV measurements we again invoke Gerischer-kinetics and the $E_r C_i$ mechanism, but now considering species are not mobile ($\mu = 0$) and with a high concentration (0.5 M). We model the effect of a reduction reaction on different materials by setting a constant E^0 value for the reduction (-0.8 V vs. Fc/Fc^+), while varying the energy of the CB. These simulations are shown in Figure 7.5.

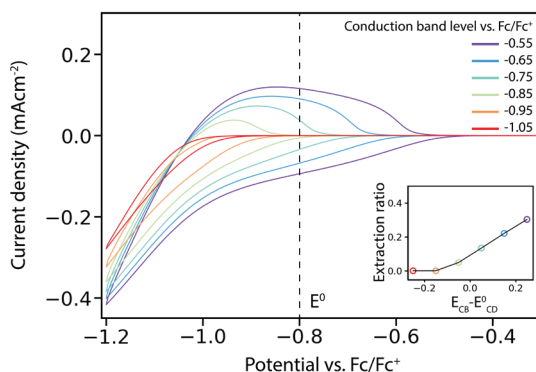


Figure 7.5. Simulated CVs of the charging of a QD film in the presence of a material reduction reaction with $E_{CD}^0 = -0.8$ V vs. Fc/Fc^+ . Different conduction band edges were used ranging from -0.5 to -1 V vs. Fc/Fc^+ . The inset shows the extraction ratios for different the conduction band edge levels compared to the E_{CD}^0 . As the conduction band edge becomes more negative in energy, the charging becomes less reversible.

As the conduction band edge becomes higher in energy than E_{CD}^0 , the charging of the QDs becomes less reversible. When the CB edge is more than > 0.1 eV higher in energy than the decomposition potential, fully irreversible charging is observed (extraction ratio = 0). In this case the simulated curves closely resemble experimental CVs on CdSe and InP QD films shown in Figure 7.1. Since the amount of oxidant contaminations in the electrolyte is typically low (which can be measured by running a CV on a blank electrode such as in Figure A7.1), material reduction is the most likely cause of irreversible behavior in experimental charging of semiconductor NC films. The simulations in Figure 7.5 confirm that material reduction can indeed lead to the observed irreversible charging in CVs on CdSe and InP QD films. Since the optical properties of these materials are

often not permanently changed by electrochemical charging, the most likely candidate for reduction reactions are surface species (ligands or surface ions)²⁹, while the inside of the semiconductor NCs remains unaffected.

Strategies to improve the stability of charges in the semiconductor NCs (and thereby the reversibility) therefore include surface modifications¹⁶ and/or the growth of shells. Another way to improve stability may be to shift the energy levels of the semiconductor NCs.²³ Figure 7.5 shows that even if E_{CD}^0 is inside the conduction band, when the electrochemical potential becomes too negative, material reduction can still occur. When the CB is filled up beyond the CB edge, the higher-energy electrons can still partake in electrochemical reduction reactions. The lowest available E_{CD}^0 will therefore put an upper limit on the concentration of charges that can stably be injected into a semiconductor NC material.

In many semiconductor NC materials, (electrochemical) hole injection has proven much more challenging than electron injection. This can mostly be ascribed to anodic decomposition reactions, as the E_0 of anodic decomposition is above the valence band level in many materials³², and thus anodic decomposition happens as soon as holes are injected into the semiconductor NCs. In devices such as QD-LEDs, hole injection is also generally more difficult than electron injection, even with the help of hole injection layers.^{33, 34} With the simulations presented here, hole injection could be modelled in the same way as electron injection, providing more insight into this topic. In addition, similar analysis and arguments can be made for the processes resulting in loss of holes from semiconductor NCs. These types of simulations and analyses could help improve stability of semiconductor NC devices.

7.3 Conclusion

In this work we model loss processes in electrochemically charged semiconductor nanocrystal films using drift-diffusion simulations and Gerischer kinetics. We consider both reactions with redox-active impurities and with the semiconductor NC materials themselves. The results are compared to experimental cyclic voltammetry on films of InP QDs, CdSe QDs, PbS QDs and ZnO QDs. The latter serve as an experimental model system, where to we added controlled amounts of redox species. We show that the presence of oxidant molecules in solution results in an additional reduction peak observed in CVs. If the reduction potential is above the conduction band of the semiconductor NC material, the reduced species can be oxidized again, and charging of the semiconductor NC remains reversible. When the reduction potential resides in the semiconductor NC band gap however, reduction of the oxidant is irreversible and leads to loss of electrons from the semiconductor NCs. Loss of electrons to oxygen is best modelled using a reversible electrochemical-irreversible chemical reaction mechanism, because oxygen reduction is irreversible due to chemical reactions of the superoxide radical that is formed upon reduction. Reduction reactions of the semiconductor NC materials themselves are modelled by introducing a high concentration of immobile redox species in the semiconductor NC film. We show that material reduction reactions on the nanocrystal surface are the most likely candidate to explain the irreversible electrochemical behavior of InP and CdSe QD films, while for ZnO and PbS QD films, a small amount of dissolved oxygen (~1 ppm) is responsible for the loss of electrons on longer timescales.



7.4 Methods

All experimental procedures and measurements were performed in a nitrogen-filled glovebox ($O_2 < 0.5$ ppm, $H_2O < 0.5$ ppm) unless otherwise noted.

Materials

Zinc acetate (99.99%), potassium hydroxide (KOH, 99.99%), anhydrous ethanol (max. 0.01% H_2O), anhydrous methanol ($\geq 99.8\%$), and anhydrous hexane (95%), Lead(II) oxide (PbO, 99.999%), 1-octadecene (ODE, 90%, degassed *in vacuo* at 120 °C for 1 hour), bis(trimethylsilyl) sulfide (TMSS, synthesis grade), cadmium oxide (CdO, 99.99%), selenium powder (Se, 99.99%), trioctylphosphine (TOP, 97%, degassed *in vacuo* at 120 °C for 1 hour), octadecylamine (ODA, 99%), trioctylphosphine oxide (TOPO, 90%), anhydrous methyl acetate (99%), anhydrous toluene (99.8%), indium(III) chloride (99.999%), zinc(II) chloride ($>98\%$), tris(diethylamino)-phosphine (97%), lithium perchlorate ($LiClO_4$, 99.99%, dry), 1,2-ethanedithiol (EDT, 98%), 1,7-diaminoheptane (7DA, 98%) ferrocenium hexafluorophosphate (97%, dried under vacuum), anhydrous acetonitrile (99.8%) and anhydrous methanol (99.8%) were purchased from Sigma Aldrich. Oleic acid (OA, extra pure) was purchased from Thermo Fischer Scientific. Anhydrous oleylamine (80–90%) was purchased from Acros Organics. 1-carboxycobaltocenium hexafluorophosphate (dried under vacuum) was purchased from MCAT.

ZnO QD synthesis

The ZnO QDs were synthesized by a previously reported procedure.²⁴ Zinc acetate (0.628 g) was dissolved in anhydrous ethanol (50 mL) by heating the solution to 60 °C while stirring. When dissolved, a solution of KOH (0.351 g) in anhydrous methanol (5 mL) was added dropwise (ca. 1 drop per second), and the solution was taken off the heat. The ZnO QDs were isolated from the reaction mixture by adding hexane until the solution became turbid. The mixture was centrifuged, the supernatant removed, and the QDs redispersed in 6 mL of ethanol. The QD dispersion was stored at –20 °C. The diameter of ZnO QDs used in experiments presented in Figures 3 and 4 was determined by transmission electron microscopy (TEM, Figure A7.3) to be 2.5 nm. The diameter of ZnO QDs used in experiments presented in Figure 7.1 was determined to be 3.8 nm by use of a sizing curve (ABS peak at 340 nm).³⁵

PbS QD synthesis

PbS QDs were synthesized following a previously described procedure.³⁶ Lead(II) oxide (90 mg) was dissolved in OA (0.25 mL) and ODE (3 mL) by heating *in vacuo* to 100 °C for 1 h. The temperature was then set to 150 °C, and a solution of TMSS (42 μ L) in ODE (0.75 mL) was injected under a nitrogen atmosphere. The heating mantle was lowered away from direct contact with the reaction flask immediately after injection of the TMS solution and allowed to cool to room temperature. The PbS QDs were isolated from the reaction mixture by adding acetone until the solution became turbid, centrifuging the mixture, removing the supernatant and redispersing in 8 mL of hexane. The diameter of the PbS QDs was determined to be 5.5 nm by TEM imaging (Figure A7.3).

CdSe synthesis

CdSe QDs were synthesized according to a previously reported procedure.¹¹ 0.077 M

Cadmium oleate (Cd-oleate) solution was synthesized by dissolving 0.367 g CdO in 3.68 g OA and 25.9 g ODE. The mixture was first degassed *in vacuo* at 110 °C for 1 h and then heated to 250 °C under nitrogen atmosphere until a transparent solution was formed. Then it was cooled down to 110 °C and degassed again for 1 h. Afterwards, the reaction was cooled to room temperature. 0.75 M selenium precursor (Se-TOP) was prepared by heating up a mixture of 1.42 g Se, 7.5 g TOP and 11.9 g ODE to 60 °C until the complexation was completed. In a 100 mL three-neck round bottom flask, 3.2 g ODA and 1.11 g TOPO was heated to 140 °C and degassed for 1.5 h under vacuum. The mixture was placed under nitrogen atmosphere, and 5.2 g 0.75 M Se-TOP solution was added into the flask and the reaction was heated up to 300 °C. 4.9 g 0.077 M Cd-oleate solution was swiftly injected into the flask. The temperature was subsequently kept at 280 °C for 4 min. The reaction was quenched to 60 °C. To purify the CdSe QDs, anhydrous methyl acetate and anhydrous methanol with a ratio of 5:1 was added to the reaction mixture, followed by centrifugation at 3354 g. The supernatant was discarded and the residue redispersed in anhydrous toluene. This purification procedure was repeated once. The diameter of the CdSe QDs was determined to be 4 nm by TEM imaging (Figure A7.3).

InP synthesis

InP QDs were synthesized as reported previously.³⁷ 100 mg (0.45 mmol) of indium(III) chloride and 300 mg (2.20 mmol) of zinc(II) chloride were mixed in 3 mL (9.10 mmol) of anhydrous oleylamine in a 25 mL flask. The mixture was stirred and degassed at 120°C for an hour and then heated to 180°C under inert atmosphere. Upon reaching 180°C, 0.50 mL (1.83 mmol) of tris(diethylamino)phosphine, transaminated with 2 mL (6.07 mmol) of anhydrous oleylamine, was quickly injected in the reaction mixture described above and the InP nanocrystal synthesis proceeded for 30 min. The synthesized InP QDs were purified using anhydrous ethanol. The edge length of the QDs was determined to be 2.7 nm using a sizing curve (ABS maximum = 530 nm).³⁸

Transmission electron microscopy (TEM) imaging

Transmission electron microscopy images were acquired using a JEOL JEM1400 transmission electron microscope operating at 120 keV.

Experimental cyclic voltammograms

Experimental cyclic voltammogram measurements were performed using an Autolab PGSTAT128N potentiostat. A three-electrode setup was used, with a platinum sheet as the counter electrode, a silver wire as the pseudo reference electrode and an indium tin oxide (ITO)-coated glass plate as the working electrode. The pseudo reference electrode was referenced relative to 1 mM ferrocenium hexafluorophosphate in 0.1 M LiClO₄ in acetonitrile (at -5.0 vs. vacuum level), which is used as the reference potential for all measurements. The electrolyte was 0.1 M LiClO₄ in anhydrous acetonitrile for all experiments.

Cyclic voltammograms of different materials

QDs were deposited on the ITO working electrode using different techniques: ZnO QDs were dropcast on top of ITO-coated glass (film thickness = 700 nm) and annealed at 60 °C for 1 hour before the measurement. PbS QDs were dropcast on top of ITO-coated



glass (film thickness = 2400 nm) and dried at room temperature. The films were then immersed in a ligand exchange solution (0.1 M EDT in anhydrous acetonitrile) for 1 minute to replace the isolating oleate ligands and rinsed with anhydrous acetonitrile.²³ CdSe QDs were spincoated on ITO-coated glass (film thickness = 40 nm). The QD films were then immersed in a ligand exchange solution (0.1 M 1,7-diaminoheptane in anhydrous methanol) for 1 minute to replace the oleate ligands on the surface. Films were washed with anhydrous methanol to remove any excess 7DA.¹¹ InP QDs were spincoated on ITO-coated glass substrates. Films were then submerged in anhydrous acetonitrile with 0.1 M EDT overnight to completely exchange the native ligands. Films were rinsed with anhydrous acetonitrile to remove any excess EDT. When quantum dots are covered in long apolar ligands, on-film ligand exchange is crucial to allow electrochemical charge injection and movement of charge through the film. Replacing long apolar ligands by shorter ligands such as EDT or 7DA both removes the isolating ligand barrier and brings the QDs closer together, greatly increasing charge transport between quantum dots through charge hopping.¹⁰ A comparison of the film parameters can also be found in Table A7.1 in the appendix.

Cyclic voltammograms on ZnO QDs with ferrocene/cobaltocene

ZnO QDs were dropcast on top of ITO-coated glass and annealed at 60 °C for 1 hour before the measurement. Anhydrous acetonitrile with 0.1 M LiClO₄ and 1 mM of either ferrocenium hexafluorophosphate or 1-carboxycobaltocenium hexafluorophosphate was used as the electrolyte solution.

Cyclic voltammograms on ZnO with oxygen

ZnO QDs were dropcast on top of ITO-coated glass and annealed at 60 °C for 1 hour before the measurement. A solution of 0.1 M LiClO₄ in anhydrous acetonitrile was prepared. Through this solution either pure Argon (99.9999%) or dry O₂/N₂ (21%/79%) was bubbled for 20 minutes. The ZnO films on ITO, bare ITO electrode or bare glassy carbon electrodes were then submerged in the electrolyte solution and measurements were performed. Measurements involving oxygen-bubbled solutions were performed outside the glovebox.

Drift-diffusion simulations

The drift-diffusion simulations used are an extension of earlier work.¹⁷ Full computational details can be found in the appendix. In short, a 3-electrode electrochemical cell is modelled as a 1-dimensional system, divided numerically in 250-490 lamella. The cell consists of a working electrode (WE) with a semiconductor NC film (porosity = 50%²⁴), an electrolyte which contains mobile ions and can also contain electrochemically reactive species, a counter electrode (CE) which is treated as a capacitor with infinite capacitance and a reference electrode (RE) in the middle of the cell (schematic in Figure 7.1A). To model the electron injection into the semiconductor NCs, we assume that the NCs in the first lamella are in Boltzmann equilibrium with the WE (Table A7.2). This assumption implies this step is never rate-limiting. The Poisson equation is solved for each time step, then the movement of all mobile species is calculated using drift-diffusion equations (Table A7.2). Reactions between electrons that are in the conduction band of the semiconductor NCs and electrochemically reactive species are governed by the Gerischer kinetic model¹⁸

(appendix). The Gerischer model is a better fit than the Marcus model for this scenario, since it considers reactions involving all energy states in the semiconductor NCs, instead of considering only a single energy level. All parameters used in the various simulations presented here are listed in Table A7.3. Experimentally known parameters like the temperature, scan speed and electrolyte and reductant/oxidant concentration were set in the simulations mirroring the experiments that they correspond with. Other parameters (most notably the effective mobilities of species inside the QD film) were optimized while being restrained to their expected range by running multiple simulations (such as in Figure 7.4D) to fit the experimental data. When simulating the same film with and without the presence of oxidant/reductant, these parameters were first optimized to fit the experiment performed without oxidant/reductant, then kept the same for the simulation with the oxidant/reductant. Simulations were performed on the DelftBlue cluster.³⁹ The C++ source code underlying the simulations as well as accompanying instructions are available on Github: github.com/RFUbbink/QDfilmsim.

References

1. Coe-Sullivan, S.; Liu, W.; Allen, P.; Steckel, J. S., Quantum dots for LED downconversion in display applications. *ECS Journal of Solid State Science and Technology* **2012**, *2* (2), R3026.
2. Wu, Z.; Liu, P.; Zhang, W.; Wang, K.; Sun, X. W., Development of InP quantum dot-based light-emitting diodes. *ACS Energy Letters* **2020**, *5* (4), 1095-1106.
3. Yin, X.; Zhang, C.; Guo, Y.; Yang, Y.; Xing, Y.; Que, W., PbS QD-based photodetectors: future-oriented near-infrared detection technology. *Journal of Materials Chemistry C* **2021**, *9* (2), 417-438.
4. Park, Y.-S.; Roh, J.; Diroll, B. T.; Schaller, R. D.; Klimov, V. I., Colloidal quantum dot lasers. *Nature Reviews Materials* **2021**, *6* (5), 382-401.
5. Schlingman, K.; Chen, Y.; Carmichael, R. S.; Carmichael, T. B., 25 Years of Light-Emitting Electrochemical Cells: A Flexible and Stretchable Perspective. *Advanced Materials* **2021**, *33* (21), 2006863.
6. Gooding, A. K.; Gómez, D. E.; Mulvaney, P., The effects of electron and hole injection on the photoluminescence of CdSe/CdS/ZnS nanocrystal monolayers. *ACS nano* **2008**, *2* (4), 669-676.
7. Schimpf, A. M.; Knowles, K. E.; Carroll, G. M.; Gamelin, D. R., Electronic doping and redox-potential tuning in colloidal semiconductor nanocrystals. *Accounts of chemical research* **2015**, *48* (7), 1929-1937.
8. Gudjonsdottir, S.; Houtepen, A. J., Permanent electrochemical doping of quantum dots and semiconductor polymers. *Advanced Functional Materials* **2020**, *30* (49), 2004789.
9. Gudjonsdottir, S.; Van Der Stam, W.; Koopman, C.; Kwakkenbos, B.; Evers, W. H.; Houtepen, A. J., On the Stability of Permanent Electrochemical Doping of Quantum Dot, Fullerene, and Conductive Polymer Films in Frozen Electrolytes for Use in Semiconductor Devices. *ACS applied nano materials* **2019**, *2* (8), 4900-4909.
10. Guyot-Sionnest, P., Charging colloidal quantum dots by electrochemistry. *Microchimica Acta* **2008**, *160* (3), 309-314.
11. Van Der Stam, W.; Grimaldi, G.; Geuchies, J. J.; Gudjonsdottir, S.; Van Uffelen, P. T.; Van Overeem, M.; Brynjarsson, B.; Kirkwood, N.; Houtepen, A. J., Electrochemical modulation of the photophysics of surface-localized trap states in core/shell/(shell) quantum dot films. *Chemistry of Materials* **2019**, *31* (20), 8484-8493.
12. Mulder, J. T.; Monchen, J. O.; Vogel, Y. B.; Lin, C. T.; Drago, F.; Caselli, V. M.; Saikumar, N.; Savenije, T. J.; Houtepen, A. J., Orthogonal Electrochemical Stability of Bulk and Surface in Lead Halide Perovskite Thin Films and Nanocrystals. *Journal of the American Chemical*



- Society* **2024**, *146* (35), 24415-24425.
13. Gudjonsdottir, S.; Van Der Stam, W.; Kirkwood, N.; Evers, W. H.; Houtepen, A. J., The role of dopant ions on charge injection and transport in electrochemically doped quantum dot films. *Journal of the American Chemical Society* **2018**, *140* (21), 6582-6590.
 14. Gudjonsdottir, S.; Koopman, C.; Houtepen, A. J., Enhancing the stability of the electron density in electrochemically doped ZnO quantum dots. *The Journal of Chemical Physics* **2019**, *151* (14).
 15. Eren, H.; Bednarz, R. J.-R.; Alimoradi Jazi, M.; Donk, L.; Gudjonsdottir, S.; Bohländer, P.; Eelkema, R.; Houtepen, A. J., Permanent electrochemical doping of quantum dot films through photopolymerization of electrolyte ions. *Chemistry of Materials* **2022**, *34* (9), 4019-4028.
 16. Pu, C.; Dai, X.; Shu, Y.; Zhu, M.; Deng, Y.; Jin, Y.; Peng, X., Electrochemically-stable ligands bridge the photoluminescence-electroluminescence gap of quantum dots. *Nature Communications* **2020**, *11* (1), 937.
 17. Ubbink, R. F.; Gudjonsdottir, S.; Vogel, Y. B.; Houtepen, A. J., Numerical Model to Simulate Electrochemical Charging of Nanocrystal Films. *The Journal of Physical Chemistry C* **2023**, *127* (20), 9896-9902.
 18. Gerischer, H., Electron-transfer kinetics of redox reactions at the semiconductor/electrolyte contact. A new approach. *The Journal of Physical Chemistry* **1991**, *95* (3), 1356-1359.
 19. Guyot-Sionnest, P.; Wang, C., Fast voltammetric and electrochromic response of semiconductor nanocrystal thin films. *The Journal of Physical Chemistry B* **2003**, *107* (30), 7355-7359.
 20. Yu, D.; Wang, C.; Guyot-Sionnest, P., n-Type conducting CdSe nanocrystal solids. *Science* **2003**, *300* (5623), 1277-1280.
 21. Wehrenberg, B. L.; Guyot-Sionnest, P., Electron and hole injection in PbSe quantum dot films. *Journal of the American Chemical Society* **2003**, *125* (26), 7806-7807.
 22. Mulder, J. T.; Du Fossé, I.; Alimoradi Jazi, M.; Manna, L.; Houtepen, A. J., Electrochemical p-Doping of CsPbBr₃ Perovskite Nanocrystals. *ACS Energy Letters* **2021**, *6* (7), 2519-2525.
 23. Vogel, Y. B.; Pham, L. N.; Stam, M.; Ubbink, R. F.; Coote, M. L.; Houtepen, A. J., Solvation Shifts the Band-Edge Position of Colloidal Quantum Dots by Nearly 1 eV. *Journal of the American Chemical Society* **2024**, *146* (14), 9928-9938.
 24. Vogel, Y. B.; Stam, M.; Mulder, J. T.; Houtepen, A. J., Long-range charge transport via redox ligands in quantum dot assemblies. *ACS nano* **2022**, *16* (12), 21216-21224.
 25. Vasudevan, D.; Wendt, H., Electroreduction of oxygen in aprotic media. *Journal of Electroanalytical Chemistry* **1995**, *392* (1-2), 69-74.
 26. Li, Q.; Batchelor-McAuley, C.; Lawrence, N. S.; Hartshorne, R. S.; Compton, R. G., Anomalous solubility of oxygen in acetonitrile/water mixture containing tetra-n-butylammonium perchlorate supporting electrolyte; the solubility and diffusion coefficient of oxygen in anhydrous acetonitrile and aqueous mixtures. *Journal of Electroanalytical Chemistry* **2013**, *688*, 328-335.
 27. Dvoranová, D.; Barbieriková, Z.; Brezová, V., Radical intermediates in photoinduced reactions on TiO₂ (an EPR spin trapping study). *Molecules* **2014**, *19* (11), 17279-17304.
 28. Nicholson, R. S.; Shain, I., Theory of stationary electrode polarography. Single scan and cyclic methods applied to reversible, irreversible, and kinetic systems. *Analytical chemistry* **1964**, *36* (4), 706-723.
 29. Hartley, C. L.; Dempsey, J. L., Electron-promoted X-type ligand displacement at CdSe quantum dot surfaces. *Nano Letters* **2019**, *19* (2), 1151-1157.
 30. Stam, M.; du Fossé, I.; Infante, I.; Houtepen, A. J., Guilty as Charged: The Role of Undercoordinated Indium in Electron-Charged Indium Phosphide Quantum Dots. *ACS nano* **2023**, *17* (18), 18576-18583.
 31. Du Fossé, I.; Ten Brinck, S.; Infante, I.; Houtepen, A. J., Role of surface reduction in the

- formation of traps in n-doped II–VI semiconductor nanocrystals: How to charge without reducing the surface. *Chemistry of Materials* **2019**, *31* (12), 4575-4583.
32. Smith, W. A.; Sharp, I. D.; Strandwitz, N. C.; Bisquert, J., Interfacial band-edge energetics for solar fuels production. *Energy & Environmental Science* **2015**, *8* (10), 2851-2862.
 33. Qian, G.; Lin, Y.; Wantz, G.; Davis, A. R.; Carter, K. R.; Watkins, J. J., Saturated and Multi-Colored Electroluminescence from Quantum Dots Based Light Emitting Electrochemical Cells. *Advanced Functional Materials* **2014**, *24* (28), 4484-4490.
 34. Deng, Y.; Lin, X.; Fang, W.; Di, D.; Wang, L.; Friend, R. H.; Peng, X.; Jin, Y., Deciphering exciton-generation processes in quantum-dot electroluminescence. *Nature communications* **2020**, *11* (1), 2309.
 35. Meulenkamp, E. A., Synthesis and growth of ZnO nanoparticles. *The journal of physical chemistry B* **1998**, *102* (29), 5566-5572.
 36. Hines, M. A.; Scholes, G. D., Colloidal PbS nanocrystals with size-tunable near-infrared emission: observation of post-synthesis self-narrowing of the particle size distribution. *Advanced materials* **2003**, *15* (21), 1844-1849.
 37. Tessier, M. D.; Dupont, D.; De Nolf, K.; De Roo, J.; Hens, Z., Economic and Size-Tunable Synthesis of InP/ZnE (E= S, Se) Colloidal Quantum Dots. *Chemistry of Materials* **2015**, *27* (13), 4893-4898.
 38. Almeida, G.; van der Poll, L.; Evers, W. H.; Szoboszlai, E.; Vonk, S. J.; Rabouw, F. T.; Houtepen, A. J., Size-dependent optical properties of InP colloidal quantum dots. *Nano Letters* **2023**, *23* (18), 8697-8703.
 39. *Delft High Performance Computing Centre (DHPC), DelftBlue Supercomputer (Phase 2), 2024, <https://www.tudelft.nl/dhpc/ark:/44463/DelftBluePhase2>, Accessed 17th december 2024.*



Appendix

Additional computational details

A 3-electrode electrochemical cell is modelled as a 1-dimensional system. The 1-dimensional simulated space starts at the working electrode (WE), encompasses the semiconductor NC film and the electrolyte solution, and ends at the counter electrode (CE). The reference electrode (RE) is positioned halfway between the film/solution interface and the CE. To achieve high spatial resolution in the film/solution interface region without sacrificing computational performance, the space was divided in lamella non-uniformly (see Table A7.3 for resolution parameters). The simulator considers an initial state, which contains starting values of the concentrations of electrons, anions, cations, and oxidant and reductant species for each lamella. It then determines the movement of these species over small time steps (dt , in the order of $1e-9$ to $1e-7$ s) based on the drift-diffusion equations (Table A7.2). The hole concentration is assumed to be zero as only negative applied potentials relative to the open circuit potential are considered in this work. During each time step, a midpoint method is used to solve the Poisson equation (Table A7.2) and to determine the spatial profile of the electrostatic potential for the next step. Boundary conditions of a regular 3-electrode system are enforced, so $\phi_{WE} - \phi_{RE} = V_{applied}$ and $\phi_{RE} = 0$ (with ϕ the electrostatic potential at a certain position), while the electrostatic potential at the counter electrode is allowed to float. The true potential at the RE (and thus the initial Fermi level of the system) at open circuit potential is arbitrary for the simulation, but for comparison with experiments was set to -4.7 V *vs.* vacuum = 0.26 V *vs.* SHE = -0.3 V *versus* ferrocene/ferrocenium (Fc/Fc⁺) in acetonitrile. This value corresponds to the work function of ITO (used as working electrode) and is in accordance with the open circuit potential of experimental ZnO QD films.^{9, 13} The initial state of the simulation always consisted of an uncharged semiconductor NC film, where the concentration of electrons was zero, and an electrolyte solution with a certain concentration of cations and anions, c^0 . An infinite supply of ions was simulated by setting the concentration of both ions at the RE constant at c^0 during the simulation. This most closely mirrors the much larger 3-dimensional volume of electrolyte solution that is available in experiments. The semiconductor NC film was considered to have a porosity of 50%, with the pores filled with electrolyte solution at concentration c^0 . An initial concentration of uncharged oxidant species can also be set. The initial concentration of oxidant species is considered to be constant throughout the simulated space, including the semiconductor NC film. Oxidant species can react with electrons in the semiconductor NC film, becoming negatively charged reductant species in the process. Similar to the ions, an infinite supply of oxidant species is artificially created by setting its concentration at the reference electrode to a constant value. Reactions between the electrons in the semiconductor NC s and the oxidant and reductant species were modelled using Gerischer kinetics, explained in detail below.

The electron concentration in the first lamella of the film, in contact with the ITO electrode, is governed by a Fermi-Dirac equilibrium with the electrode (Table A7.2). As the applied potential becomes more negative, the value of the Fermi level, Fermi-Dirac integral and the concentration of electrons all increase in the first lamella. Any DOS function can be used as input in the simulator. The simulation parameters, including the DOS function, were set at the start of the simulation, after which only the applied potential was altered

to obtain the CV curves shown in this work. Parameters used were optimized to most closely fit the corresponding experimental electrochemical data (see Table A7.3). For performance reasons, the simulator was written in C++ and compiled using Microsoft Visual Studio. The simulator source code and accompanying instructions are available at [github: github.com/RFUbbink/QDfilmsim](https://github.com/RFUbbink/QDfilmsim).

Table A7.1. Comparison of properties of QD films used in experimental CVs of this work. QD diameter determination method is indicated for each material. Either average diameters were measured from TEM images, or a sizing curve was used to calculate the diameter from an absorbance measurement, in which case the sizing method is referenced.

Material (Figure)	ZnO (Figure 7.1)	PbS (Figure 7.1)	CdSe (Figure 7.1)	InP (Figure 7.1)	ZnO (Figures 7.3-7.5)
QD diameter	3.8 nm (ABS = 340 nm) ³⁵	5.5 nm (TEM)	4 nm (TEM)	2.7 nm (ABS = 530 nm) ³⁸	2.5 nm (TEM)
Ligands after ligand exchange	OH ⁻	1,2-ethane-dithiol	1,7-heptane-diamine	1,2-ethane-dithiol	OH ⁻
Film thickness	700 nm	2400 nm	40 nm	Unknown	Unknown



Table A7.2. List of formulas employed in the simulator.

Formula	Name and purpose	Explanation of parameters
$J_n = nq\mu_n \frac{dV}{dx} - kT\mu_n \frac{dn}{dx}$ $J_c = cq\mu_c \frac{dV}{dx} + kT\mu_c \frac{dc}{dx}$ $J_a = aq\mu_a \frac{dV}{dx} - kT\mu_a \frac{da}{dx}$ $J_o = kT\mu_o \frac{dO}{dx}$ $J_R = Rq\mu_R \frac{dV}{dx} - kT\mu_R \frac{dR}{dx}$	Drift-diffusion equations Calculate the currents of electrons (n), cations (c), anions (a), oxidant (O) and reductant (R).	J: current density q: elementary charge V*: electrostatic potential level vs vacuum μ: carrier mobility
$\frac{d^2V}{dx^2} = \frac{q}{\epsilon_0\epsilon_r} (n + a - c + R)$	1D Poisson equation Calculate the potential profile over the space of the simulation.	ε ₀ , ε _r : vacuum and relative electric permittivity.
$n = \int_{E=Ec}^{\infty} g_c(E) \frac{1}{1 + e^{\frac{E-E_F}{kT}}} dE$	Fermi-Dirac distribution Calculate the equilibrium concentration of electrons at the interface between the WE and the QD film.	E: energy E _c : conduction band level E _F : current Fermi level (= intrinsic Fermi level - electrostatic potential) g _c (E): density of states function of the material

* For electrons, the total potential relative to vacuum is instead used, i.e. *energy level in the DOS* vs. *vacuum + electrostatic potential*. In this way, the extra energy needed for electrons to occupy higher levels in the DOS at higher energies is taken into account in calculating the drift current. The energy level of electrons in the DOS is calculated from the electron concentration.

Gerischer kinetic model employed in the simulator

We are considering the reaction of an electron residing in the conduction band (CB) of a semiconductor material with some oxidant in solution. The effective transfer of the electron is from an energy state in the CB to the HOMO of the oxidant molecule. If the CB consisted of only one energy level, a Marcus rate could be calculated, however there are many different energy levels in the CB at varying levels of occupancy. For this reason,

we calculate the reaction rate using the Gerischer kinetic model.¹⁸ The oxidant molecule is modelled using a redox potential E^0 and a reorganization energy λ . The reorganization energy of a molecule is determined by the reorganization of solvent molecules around the oxidant once it accepts an electron and becomes charged. Reorganization energy is typically large (order of 2 eV) for molecules where the charge is localized, as the solvent will reorganize a lot in reaction to the charge. For instance the reduction of O_2 to the O_2^- radical is associated with a large reorganization energy. Delocalized or shielded charges, such as in the ferrocene/ferrocenium couple, are associated with much smaller reorganization energies (order of 0.5 eV). The reorganization energy of solvent molecule orientation can be calculated with the following formula:

$$\lambda = \left(\frac{1}{2r_O} + \frac{1}{2r_W} - \frac{1}{r_O + r_W} \right) * \left(\frac{1}{\epsilon_{opt}} + \frac{1}{\epsilon_s} \right) \quad (7.3)$$

With r_O and r_W the radii of reductant and oxidant, and ϵ_{opt} and ϵ_s the optical and static dielectric constants of the solvent. In our case r_O is the radius of the semiconductor NC, while r_W is the radius of the redox-active species.

Using these two parameters, an effective “density of states” can be calculated for the oxidant/reductant pair. Both the empty states W_O (corresponding to the oxidant) and filled states W_R (reductant) are modelled as a Gaussian distribution according to the formulas:

$$W_O(E, \lambda) = \frac{1}{\sqrt{4\pi kT\lambda}} e^{-\frac{(E-E^0-\lambda)^2}{4kT\lambda}} \quad (7.4)$$

$$W_R(E, \lambda) = \frac{1}{\sqrt{4\pi kT\lambda}} e^{-\frac{(E-E^0+\lambda)^2}{4kT\lambda}} \quad (7.5)$$

Figure 7.2 in the main text shows an example energy distribution next to an example DOS function of a semiconductor. Transfer of electrons can take place between states in the semiconductor and the redox couple that have the same energy (isoelectronic energy transfer). Electrons can thus transfer both from filled states in the CB to the oxidant molecule as well as from filled states in the reductant back to empty CB states. The conduction band occupancy is determined by the Fermi-Dirac distribution. The rate of electron transfer from semiconductor to oxidant k_f is then given by the integral over the product of filled CB states and (empty) oxidant states:

$$k_f = \frac{4\pi}{3} \rho \tau_O \nu \int_{-\infty}^{\infty} W_{oxidator}(E, \lambda) DOS(E) f(E) dE \quad (7.6)$$



And the rate of reverse process k_b , electron transfer from reductant to semiconductor, is given by the integral over the product of empty CB states and filled reductant states:

$$k_b = \frac{4\pi}{3} \rho \tau_o \nu \int_{-\infty}^{\infty} W_{reductor}(E, \lambda) DOS(E) (1 - f(E)) dE \quad (7.7)$$

With $f(E)$ being the Fermi-Dirac function. For a given number of electrons in the CB, as can be obtained from the simulation at each point in space, the Fermi level can be calculated, which in combination with the DOS function, E^0 and λ is enough to calculate the rate of electron transfer. In practice, given the DOS function, E^0 and λ (which are all input parameters to the simulation), the reaction rate was calculated for a range of possible electron concentrations and saved in a lookup table before the simulation was started. This allowed quick lookup for the reaction rate through interpolation, avoiding the calculation of the complex integral (which would need to be performed separately for each lamella in space as electron concentration can vary throughout the semiconductor). This is critical for simulation performance.

The prefactor of the integral contains 3 components. First a unit conversion factor that accounts for the fact that not all molecules can partake in the reaction, only those close to the semiconductor surface. We consider that an electron in a semiconductor NC can react with any molecules on the surface, where ρ is the semiconductor NC diameter. Second the overlap integral τ_o between the wave function of electrons in the semiconductor and oxidant molecule. Third the “attempt frequency” ν , i.e. the amount of times per second that an electron can make the transfer. The last two components vary between systems and are essentially unknowable until they are measured for a specific redox couple/ semiconductor pair. The prefactor was thus left as a variable in the simulations, essentially serving as a base rate similar to k^0 in the Arrhenius equation. The effect of the prefactor on the reaction rate is explained in Figure A7.2. Since the E^0 of a redox couple can be determined experimentally and the λ can be calculated or estimated quite accurately, this leaves the prefactor as the only unknown variable in the simulation.

Table A7.3. Parameters used in the simulations.

Parameter	Fig. 7.3A	Fig. 7.3B	Fig. 7.4B	Fig. 7.4A/C/D	Fig. 7.5
semiconductor NC film thickness	350 (nm)	700 (nm)	700 (nm)	300 (nm)	
Number of lamella (film)	25				
Lamella thickness (film)	13.92 (nm)	27.92 (nm)	27.94 (nm)	11.94 (nm)	
Number of lamella (film/solution interface)	65				
Lamella thickness (film/solution interface)	0.4 (nm)		0.3 (nm)		
Distance between WE and CE	0.3 (mm)*	0.1 (mm)*	0.1 (mm)*		
Number of lamella (solution)	160			400	
Lamella thickness (solution)	~1875 (nm)	~625 (nm)	~625 (nm)	~250 (nm)	
Electron mobility	3e-10 (m ² V ⁻¹ s ⁻¹)**				
Ion mobility (film)	3.5e-12 (m ² V ⁻¹ s ⁻¹)			2e-13 (m ² V ⁻¹ s ⁻¹)	
Ion mobility (solution)	5e-9 (m ² V ⁻¹ s ⁻¹)		5e-10 (m ² V ⁻¹ s ⁻¹)		
Ion concentration (solution)	0.1 (M)				
Reductant/oxidant mobility (film)	2e-10 (m ² V ⁻¹ s ⁻¹)	2e-9 (m ² V ⁻¹ s ⁻¹)	1e-10 (m ² V ⁻¹ s ⁻¹)	2e-10 (m ² V ⁻¹ s ⁻¹)	0
Reductant/oxidant mobility (solution)	6e-8 (m ² V ⁻¹ s ⁻¹)*	2e-8 (m ² V ⁻¹ s ⁻¹)*	1e-10 (m ² V ⁻¹ s ⁻¹)*	1e-8 (m ² V ⁻¹ s ⁻¹)*	0
Reductant starting concentration	1.2 (mM)	1.9 (mM)	200 (mM)	3.3 (mM)	500 (mM)
Film porosity	50% ²⁴				
Temperature	300 (K)				
Relative permittivity electrolyte solution	37 [†]				
Relative permittivity QD film	10				

* The distance between the counter and working electrodes in the experimental setup is on the mm scale (1-3 mm), but this is too large to accurately simulate. We instead reduced this distance to 0.1-0.3 mm. To compensate for this and still simulate the Ohmic drop correctly, the ion mobility in the solution was reduced by a factor of ~10 from the expected values.

** It has been shown that electrons have a much higher mobility in ZnO QD films than the one used here.¹³ Increasing the electron mobility higher than ~2 orders of magnitude above the ion mobility in the film does not affect the results of the simulation however, as cation mass transport in the film quickly becomes the limiting factor. For performance reasons, the electron mobility was therefore kept at an unphysically low level.



*Based on acetonitrile. The semiconductor NC film is assumed to be a mixture of a semiconductor NC material and the electrolyte solution, so an arbitrary in-between value was picked for its relative permittivity. The relative permittivity of either the film or solution does not affect the results of the simulation as long as the spatial resolution is sufficient and can be put to any desired value.

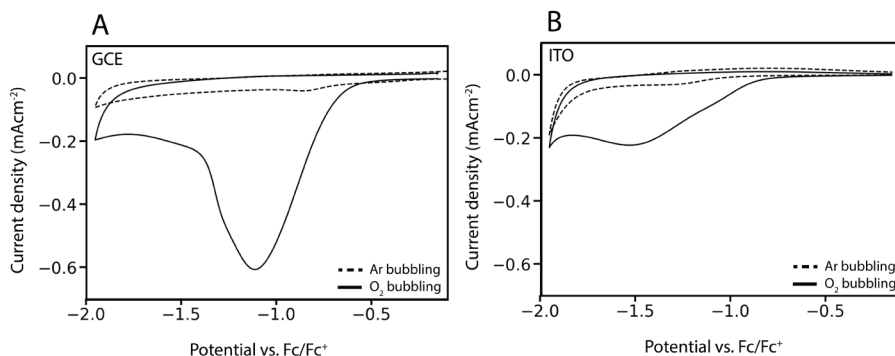


Figure A7.1. Experimental cyclic voltammograms performed on bare electrodes with either argon or O₂/N₂ 0.21/0.79 bubbled through the electrolyte for 20 minutes. A) Glassy carbon electrode (GCE) and B) indium tin oxide (ITO) electrode. In both cases, an irreversible reduction peak is observed when oxygen is present. The reduction peaks observed for the ITO is broadened and shifted to more negative potentials compared to the glassy carbon.

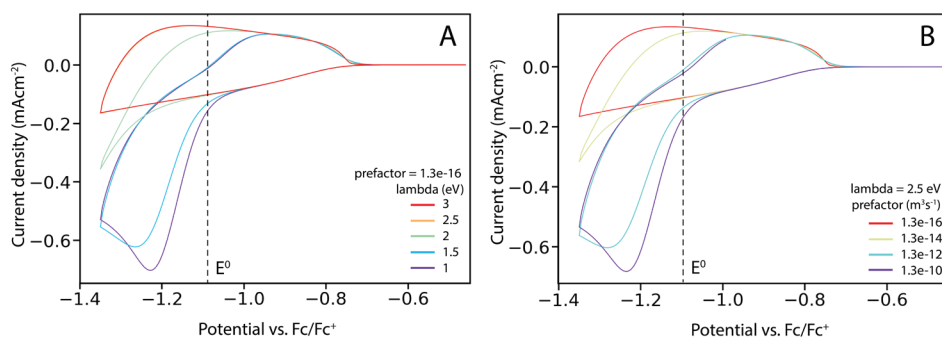


Figure A7.2. Simulated cyclic voltammograms of a semiconductor NC film in the presence of an oxidant following the coupled reversible-irreversible mechanism. The reduction potential is constant at -1.1 eV vs Fc/Fc^+ , which is roughly where the oxygen to superoxide standard potential would be expected. It is impossible to simulate the experimental oxygen CVs (Figure 7.4A in the main text) with this reduction potential using only the unmodified Gerischer model. The expected parameters for the reorganization energy λ and prefactor would be 2.5 eV and 1.3×10^{-16} m^3s^{-1} respectively. This results in no additional oxidative current, as the overpotential required to see significant current with these parameters is too large. Since the parameters are hard to determine/calculate based on experiments, both parameters were adjusted over a range of values to see if a fit could be obtained to the experiment. Increasing the prefactor or decreasing λ both results in lowering of the overpotential needed for reduction and thus an observed reduction current at low applied potentials. However, this reduction current increases exponentially, as is expected for the Gerischer model, and quickly reaches the point where diffusion limitation starts, leading to a peak in the current. This diffusion limitation is never observed in the experiments, which means that the reduction current there does not increase exponentially. This means the experimental data cannot be fit with a Gerischer model.

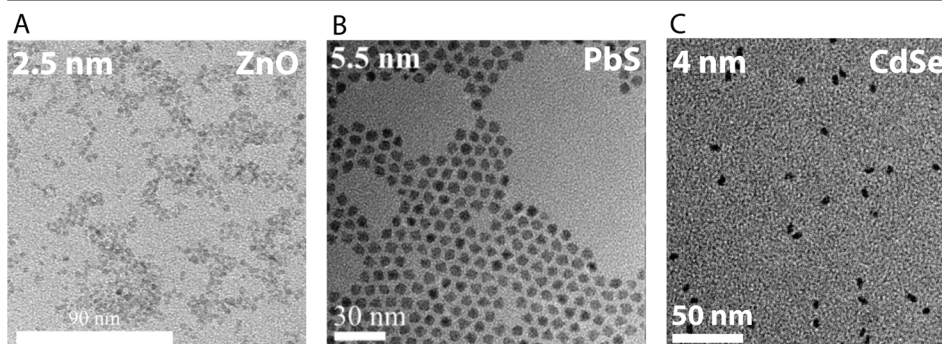


Figure A7.3. TEM images of A) ZnO, B) PbS and C) CdSe QDs used in this work. QD diameters were determined from these images by averaging over many particles.



Summary and outlook

Semiconductor nanocrystals, known as quantum dots (QDs), have unique optical properties that makes them useful for application in various light-emitting devices, such as LEDs, displays and lasers. For actual application of QDs, energy efficiency of their light emission and material stability are crucial. To achieve high energy efficiency, it must be understood which types of atomic defects on the nanocrystals lead to energy losses and how to prevent them. To achieve stable QDs, it is important to understand which kinds of chemical reactions the QDs can undergo, if these reactions lead to the formation of new defects and how to prevent this.

The motivation behind the research performed in this thesis is provided in Chapter 1. The unique properties of QDs are discussed. Loss mechanisms and their effects on the energy efficiency and stability are also explained.

Chapter 2 then provides an extensive literature overview of InP QDs. The properties of InP QDs are compared to other QD materials. Different synthesis methods of InP QDs and their resulting properties are explained. An overview is presented of the currently known and suspected atomic defects on InP QDs, as well as strategies to remove or prevent them. Current and future strategies for InP shelling are then examined. Finally, the many different current and future possible applications of InP QDs are discussed.

In Chapter 3, we provide a safe, water-free in-situ HF treatment that can be used to increase the photoluminescence quantum yield (PLQY) of InP QDs from <0.1% to up to 70%, and up to 85% when additional Z-type ZnCl_2 ligands are provided. We show through optical analysis the underlying chemical reactions of the process, where in-situ generated HF etches InP QDs to produce InF_3 and PH_3 . Through the use of solid state nuclear magnetic resonance (ssNMR) we show that the in-situ HF treatment does not remove all oxidized phosphorus from the QD surface, but converts polyphosphate species to H_xPO_4 , and results in exchange of surface $\text{In}(\text{PA})_3$ for InF_3 . By comparing these results with DFT calculations, we suggest phosphorus dangling bonds and the presence of polyphosphates on the surface are the sources of traps that cause non-radiative recombination in InP QDs. Removing these traps results in core-only InP QDs with PLQY that is comparable to the best available InP/ZnSe/ZnS core/shell/shell QDs.

In Chapter 4 we extend the structural analysis of InP QDs to InP/ZnSe core/shell nanocrystals. Using ssNMR, we find significant presence of PO_4^{3-} on the InP/ZnSe interface. However, these defects do not directly result in trap states, as we are still able to obtain >90% PLQYs for samples with on average 5 PO_4^{3-} moieties per QD. However, when we oxidize the interface further on purpose using molecular oxygen, the PLQY of the InP/ZnSe samples is significantly reduced. Using ^{77}Se ssNMR, we find that after excessive oxidation, the interface selenium signal is absent. This suggests that the layer of PO_4^{3-} that is formed after oxidation prevents binding of selenium to the interface until a layer of

zinc is bound to the oxidized layer. In addition, using transmission electron microscopy (TEM), we find a different orientation of core and shell crystals in oxidized particles. Both these measurements suggest that excessive oxidation disrupts the epitaxial growth of ZnSe on InP cores QDs.

From these studies, it is clear that InP quantum dots are generally more sensitive to defects than traditional CdSe-based materials. A prime example of this is the fact that CdSe core-only QDs reliably show significant photoluminescence (PLQY of 10-20%), while as-synthesized InP core QDs never have more than a few percent PLQY, and often show none at all. Based on the results from Chapter 3, my best theory for this difference is that due to the trivalent nature of indium and phosphide ions, it is difficult to fit enough indium ions on the InP surface to passivate all trap states due to dangling phosphorous bonds, since 3 negatively charged ligands are needed for each indium ion. Because it is so small, InF_3 z-type ligands may be able to provide sufficient ligand coverage to passivate most trap states. It also appears more difficult to achieve near-unity PLQY values in InP/ZnSe/ZnS compared to CdSe-based core/shell/shell particles. This may be due to the III-V/II-VI interface present between the InP/ZnSe, which is inherently charged and thus more prone to defects. Additionally, the increased sensitivity of InP to oxidation compared to CdSe (as measured with the ssNMR experiments in Chapters 3 and 4) could contribute to the difficulty of obtaining high-quality core and core/shell/shell InP-based QDs. Recent developments in the QD field do however show that it is possible to overcome these difficulties and obtain high-quality InP-based QD devices such as QLEDs.

The work in this thesis identifies important structural defects found on InP QDs and their effects on the optical properties, but questions about them still remain. We have shown that PO_4^{3-} defects on the interface do not result in trap states as long as their concentration is sufficiently low, but the exact quantitative relationship between the PO_4^{3-} defects and the amount of trap states is not fully clear. Is there a critical amount of PO_4^{3-} defects after which trap states and thus a low PLQY are guaranteed? Or is there a linear relationship between the amount of defects and the PLQY? Would this relationship hold for single quantum dots as well or only for the ensemble? Is the relationship different for in-situ HF-treated InP core-only particles compared to InP/ZnSe core-shell ones? To answer these questions, the oxidation method using molecular oxygen, explained in Chapter 4, is a great way to precisely control the amount of PO_4^{3-} by adjusting the treatment time. Ideally, completely oxygen-free cores should be used as the basis for these oxidation treatments. We have shown it is possible to synthesize small oxygen-free InP cores in Chapter 3, but were not able to make larger oxygen-free cores. It has however been shown that oxygen-free cores can be produced using aminophosphine-based syntheses, which could be a good starting material for a thorough analysis of the quantitative relationship between PO_4^{3-} defects and the quantum yield of larger InP QDs. Single-particle spectroscopy could provide insight into the effects of defects on the individual QD level, showing whether QDs become completely dark when the defect level increases, or still show photoluminescence occasionally (blinking).

We also have not investigated the effect of PO_4^{3-} defects on the stability of the QDs. A series of tests comparing the stability of oxidized and non-oxidized QDs under different



conditions such as high temperature and high photon flux could provide more insight. In general, the stability of QDs is not often investigated, even though it is crucial for QDs to be applied in actual devices. Studies of stability of high-PLQY core and core/shell InP QDs to heat, light of different energies, water and oxygen can provide valuable information for the application of InP QDs. These kinds of experiments would work best when combining optical and structural analysis, for example with ssNMR. In this way the formation of new structural defects may be linked to changes in optical properties.

We investigate the possibility of making quantum dot based light-emitting electrochemical cells (QDLEC) in Chapter 5. Using CdSe/CdS/ZnS QDs, we are able to produce a QDLEC without any use of transport or injection layers. This shows that both electron and hole injection can be performed electrochemically in these QDs. Through analysis of the device using both experimental methods and drift-diffusion simulations, we identify improving electrochemical hole injection as the most important strategy for improving QDLECs in the future.

In Chapter 6 we use drift-diffusion simulations to model the electrochemical charging of QDs. We show that drift-diffusion simulations can be used to reproduce experimental cyclic voltammetry measurements with great accuracy. Using the simulation data we challenge some common beliefs about the electrochemical charging of QDs. First we find that in a charged QD film, the electrostatic potential drops over the film/electrolyte solution interface in addition to the known potential drop at the working electrode/film interface. The presence of this second potential drop leads to the conclusion that the amount of charge added to the QD film is dependent not only on the total applied potential, but also the ion concentration in the electrolyte solution. Second by simulating cyclic voltammograms under different measurement conditions and comparing to experiments, we show that the commonly used Randles-Ševčík equation cannot be used to calculate the mobility of charges in a QD film. Charging of the QD film system differs from traditional electrochemical experiments on flat electrodes (where the Randles-Ševčík equation is valid) because charges flow through and are stored throughout the entire QD film.

In Chapter 7 we extend the drift-diffusion simulation of electrochemical charging of QDs by including chemical side reactions. We show how reactions of electrons in the QDs with redox-active molecules can be modelled with the Gerischer model for electron transfer. One-electron reactions with redox molecules are reversible if the redox potential of the molecule is in the conduction band of the QDs, but irreversible if the redox potential is in the band gap of the QDs. Through experiments we show that loss of electrons to molecular oxygen is always irreversible even when its redox potential is in the conduction band. We explain this effect by considering a coupled reversible-irreversible reaction mechanism, which allows a good fit of simulations on experimental data. Finally we model redox reactions with the QD material itself, such as reduction of ligands or surface ions. These reactions are irreversible and are shown to be a likely candidate for non-ideal charging behaviour of CdSe and InP-based QDs.

Combining drift-diffusion simulations with experimental electrochemistry on QDs allows a much better overall understanding of the system. Even if the results of simulations

and experiments do not match perfectly, the difference between the two can give an indication where the experiments differentiate from the theoretical predictions, and provide new directions or insights. InP and CdSe particles are inherently more difficult to charge electrochemically than ZnO and PbS, because of the higher energy level of their conduction band. This means electrons need more energy to enter the QDs, which in turn means that they are more likely to partake in other (electro)chemical reactions once they reside in the QD conduction band or even before they are injected.

Electrochemical experiments and drift-diffusion simulations may provide additional insight into the types of degradation reactions that occur in QDs, which can help to devise strategies to prevent them. Comparing the electrochemical stability of (in-situ HF treated) core InP QDs with particles shelled with ZnSe or ZnS is a good starting point. Shelled QDs are expected to be more stable because the indium ion is more readily reduced than the zinc ion. Additionally, it would be very interesting to compare (core-only and core/shell) QDs with different types of ligands, to see how these affect the electrochemical stability. Since the surface species are the first to react electrochemically, the stability of QDs may be controlled by adjusting the ligands. Ligands like thiolates or amines are promising candidates for improving stability, although care should be taken that any ligand exchanges performed do not reduce the PLQY of the particles. If the scientific community manages to combine high PLQY values and long-term stability under harsh conditions, the future of InP-based quantum dots will indeed be bright.



Samenvatting en vooruitzicht

Nanokristallen gemaakt van halfgeleider-materialen, ook bekend als kwantumstippen, hebben unieke optische eigenschappen, waardoor ze nuttig zijn in lichtgevende apparaten zoals LED-lampen, beeldschermen en lasers. Om kwantumstippen daadwerkelijk toe te kunnen passen in deze applicaties zijn een goede efficiëntie van hun lichtemissie en stabiliteit cruciaal. Om een hoge emissie-efficiëntie te behalen moet er begrepen worden welke atomische defecten in de nanokristallen leiden tot verlies van energie, en hoe deze defecten voorkomen kunnen worden. Om stabiele kwantumstippen te kunnen maken, is het belangrijk te begrijpen welke chemische reacties de kwantumstippen kunnen ondergaan, of deze reacties leiden tot nieuwe defecten, en zo ja, hoe ze voorkomen kunnen worden.

De motivatie voor het onderzoek in dit proefschrift wordt uiteengezet in Hoofdstuk 1. De unieke eigenschappen van kwantumstippen worden behandeld en verliesmechanismen en hun effect op de emissie-efficiëntie en stabiliteit wordt uitgelegd.

Hoofdstuk 2 geeft een uitgebreid overzicht van de literatuur op het gebied van kwantumstippen gemaakt van indium fosfide (InP). Verschillende synthesesmethodes van InP kwantumstippen en de resulterende eigenschappen worden uitgelegd. Er wordt een overzicht gegeven van de verscheidene bekende en vermoedde atomische defecten die op InP kwantumstippen aanwezig kunnen zijn, net als strategieën om deze defecten te voorkomen of verwijderen. Huidige en toekomstige strategieën voor het maken van een schil rond InP kwantumstippen worden uitgelicht. Tot slot worden de verscheidene huidige en mogelijke toekomstige toepassingen van InP kwantumstippen geanalyseerd.

In Hoofdstuk 3 presenteren we een veilige, watervrije in-situ waterstofluoride-behandeling die kan worden gebruikt om de fotoluminescentie-kwantumopbrengst (FLKO) van InP kwantumstippen van <math><0.1\%</math> naar 70% te verhogen, en zelfs tot 85% als ook Z-type liganden toe worden gevoegd. Door middel van optische analyse laten we zien welke chemische reacties aan de basis van de behandeling liggen. Tijdens de behandeling wordt in-situ waterstoffluoride (HF) gemaakt, wat de InP kwantumstippen etst, waarbij InF_3 en PH_3 worden gevormd. Met behulp van vastestof-kernspinresonantie-metingen tonen we aan de in-situ HF behandeling niet alle geoxideerde fosfor van de oppervlakte van het nanokristal verwijdert, maar wel polyfosfaten omzet in H_xPO_4 , en ervoor zorgt dat indiumpalmitaat (InPA_3) op het oppervlak deels wordt vervangen door indiumfluoride (InF_3). Na deze resultaten vergeleken te hebben met density functional theory (DFT) berekeningen, stellen we dat ongebonden fosfor-orbitalen en de aanwezigheid van polyfosfaten op het oppervlak de oorzaak zijn van valkuiltoestanden die non-radiatieve recombinatie veroorzaken in InP kwantumstippen. Het verwijderen van deze valkuiltoestanden resulteert in kern-InP kwantumstippen met een FLKO die vergelijkbaar is met de best beschikbare InP/ZnSe/ZnS kern/schil/schil kwantumstippen.

In Hoofdstuk 4 breiden we de structurele analyse van InP kwantumstippen uit naar InP/

ZnSe kern/schil nanokristallen. Uit kernspinresonantie-metingen blijkt er een significante hoeveelheid fosfaat (PO_4^{3-}) aanwezig te zijn op het grensvlak van InP en zinkselenide (ZnSe). Dit type grensvlakdefect leidt echter niet direct tot valkuiltoestanden, aangezien we nog steeds FLKO-waardes van boven de 90% kunnen waarnemen voor monsters met gemiddeld 5 fosfaatgroepen per nanodeeltje. Wanneer we echter het grensvlak expres nog verder oxideren met behulp van moleculair zuurstof, wordt de FLKO van de InP/ZnSe deeltjes significant verlaagt. Met behulp van ^{77}Se kernspinresonantie zien we dat na deze oxidatieprocedure het signaal van selenium aan het grensvlak afwezig is. Dit lijkt te betekenen dat de dikke laag fosfaat die wordt gevormd tijdens de oxidatie voorkomt dat selenium bindt aan het grensvlak totdat eerst een afdoende hoeveelheid zink is gebonden aan de fosfaatlaag. Met behulp van transmissie-elektron-microscopie (TEM) zien we daarnaast een verschillende kristaloriëntatie tussen de kern en de schil in de geoxideerde deeltjes. Deze metingen wijzen er allebei op dat excessieve oxidatie de kristalgroei van ZnSe schillen op InP nanodeeltjes verstoort.

Uit deze experimenten blijkt dat InP kwantumstippen over het algemeen gevoeliger zijn voor atomische defecten dan traditionele materialen gemaakt van cadmiumselenide (CdSe). Een goed voorbeeld hiervan is het feit dat CdSe kern-kwantumstippen direct na de synthese al zichtbaar sterke fotoluminescentie vertonen (FLKO van 10-20%), terwijl net gesynthetiseerde InP kristallen nooit meer dan een paar procent FLKO hebben, en vaak zelfs helemaal geen fotoluminescentie vertonen. Op basis van onze bevindingen uit Hoofdstuk 3, denk ik dat de meest waarschijnlijke verklaring voor dit verschil tussen materialen gevonden wordt in de lading van de ionen: indium is een driewaardig ion, terwijl cadmium tweewaardig is. Hierdoor zijn er 3 liganden per indiumion nodig voor ladingsneutraliteit, waardoor het moeilijker wordt om genoeg indiumionen op het oppervlak van de kwantumstippen te plaatsten om alle ongebonden fosfororbitale te verwijderen. Enige overgebleven ongebonden fosforionen veroorzaken valkuiltoestanden. Omdat fluorideionen zo klein zijn, is het met InF_3 -liganden wel mogelijk om genoeg liganden op het oppervlak te plaatsen, waardoor alle fosforatomen gebonden worden. Het lijkt ook moeilijker te zijn om hoge FLKO-waardes te behalen met InP/ZnSe/ZnS kern/schil/schil nanodeeltjes vergeleken met kern/schil/schil deeltjes gemaakt van CdSe. Dit zou kunnen komen door het III-V/II-VI grensvlak tussen InP en ZnSe, wat altijd een ladingsbalans heeft en waar daardoor makkelijker defecten ontstaan. Daarnaast kan de hogere gevoeligheid van InP voor oxidatie vergeleken met CdSe (zoals blijkt uit kernspinresonantiemetingen in Hoofdstuk 3 en 4) bijdragen aan het moeilijke om InP kern- en kern/schil/schil-deeltjes van hoge kwaliteit te maken. Recente vorderingen in het kwantumstippen-veld tonen echter aan dat het mogelijk is om deze uitdagingen te overkomen en met InP nanodeeltjes lichtgevende applicaties zoals QLEDs te maken met uitstekende eigenschappen.

Met het werk in dit proefschrift worden belangrijke structurele defecten van InP kwantumstippen geïdentificeerd en hun effect op de optische eigenschappen uitgelicht, maar er blijven nog vragen bestaan rondom structurele defecten. Hoewel we hebben aangetoond dat fosfaatdefecten op het InP/ZnSe grensvlak geen valkuiltoestanden hoeven te veroorzaken als hun concentratie laag genoeg is, is het nog niet duidelijk wat het exacte (kwantitatieve) verband is tussen de hoeveelheid fosfaat en de FLKO van InP



kwantumstippen. Is er een kritische hoeveelheid fosfaat waarboven valkuiltoestanden en dus een lagere FLKO gegarandeerd zijn? Of is er een lineair verband tussen de hoeveelheid defecten en de FLKO? Is dit verband anders als er wordt gekeken naar individuele kwantumstippen in plaats van het ensemble? En is dit verband verschillende voor in-situ behandelde InP kernen vergeleken met InP/ZnSe kern/schil deeltjes? Om deze vragen te beantwoorden kan de oxidatieprocedure met moleculaire zuurstof, zoals beschreven in Hoofdstuk 4, een goede manier zijn om de hoeveelheid fosfaat met precisie te controleren. Idealiter zouden volledig fosfaatvrije InP kernen de basis moeten zijn om deze oxidatiebehandelingen op uit te voeren. Hoewel we succesvol kleine fosfaatvrije InP kernen konden maken in Hoofdstuk 3, is het ons niet gelukt om grotere kernen te maken zonder fosfaat. Het is echter wel aangetoond dat dit mogelijk is met behulp van een synthesemethode waarin aminofosfines als reactant worden gebruikt. Kernen uit deze synthese zouden dus een goed startmateriaal zijn voor een uitgebreide analyse van het verband tussen fosfaatdefecten en de FLKO van grote InP kwantumstippen. Spectroscopie op individuele deeltjes zou inzicht kunnen geven van de invloed van defecten op een enkel nanodeeltje en laten zien of een kwantumstip geheel stopt met licht uitstralen wanneer er meer defecten aanwezig zijn, of dat er gedurende korte tijd nog wel fotoluminescentie plaatsvindt (ook wel “knipperen” genoemd).

We hebben ook het effect van fosfaatdefecten op de stabiliteit van de kwantumstippen niet onderzocht. Een set van experimenten om de stabiliteit van geoxideerde en niet-geoxideerde InP kwantumstippen te testen onder verschillende omstandigheden zoals hoge temperatuur en hoge fotonflux zou hierin inzicht kunnen bieden. Over het algemeen wordt de stabiliteit van kwantumstippen te weinig onderzocht, hoewel deze cruciaal is om kwantumstippen daadwerkelijk toe te passen in applicaties. Onderzoek dat de stabiliteit van InP kwantumstippen met hoge FLKO bestudeert onder verhoogde temperatuur, licht van verschillende golflengtes, water en zuurstof kan waardevolle informatie bieden op het gebied van het toepassen van InP kwantumstippen. Dit soort experimenten zouden het best tot hun recht komen als ze optische en structurele analyse zoals kernspinresonantie combineren. Op deze manier kan de formatie van structurele defecten gelinkt worden aan veranderingen in optische eigenschappen.

We onderzoeken de mogelijkheid om lichtgevende electrochemische cellen (LECs) te maken op basis van kwantumstippen in Hoofdstuk 5. We maken kwantumstip-LECs op basis van CdSe/ZnSe/ZnS kwantumstippen zonder het gebruik van ladingstransport- of ladingsinjectielagen. Hiermee tonen we aan dat zowel electrochemische elektron- als gateninjectie in kwantumstippen mogelijk is. Na analyse van de LEC met zowel experimenten als drift-diffusiesimulaties, identificeren we het verbeteren van de electrochemische gateninjectie als de belangrijkste strategie om kwantumstip-LECs in te toekomst te verbeteren.

In Hoofdstuk 6 gebruiken we drift-diffusiesimulaties om het electrochemisch opladen van kwantumstippen te modelleren. We tonen aan dat drift-diffusiesimulaties gebruikt kunnen worden om experimentele cyclische voltammogrammen met goede precisie te reproduceren. Met de simulatiedata kunnen we twee veel voorkomende aannames over het electrochemisch opladen van kwantumstippen verleggen. Ten eerste zien we dat in

een opgeladen laag kwantumstippen de elektrostatische potentiaal ook vervalt over het grensvlak tussen de kwantumstiplaag en de elektrolytoplossing, niet alleen tussen de elektrode en de kwantumstippen zoals eerder werd aangenomen. De aanwezigheid van deze tweede potentiaalval betekent dat de hoeveelheid lading die in kwantumstippen geïnjecteerd wordt niet louter afhankelijk is van de aangelegde potentiaal, maar ook van de concentratie van ionen in de elektrolytoplossing. Daarnaast zien we door het vergelijken van simulaties en experimentele metingen van cyclische voltammogrammen onder verschillende omstandigheden, dat de veelgebruikte Randles-Ševčík-vergelijking niet van toepassing is voor het berekenen van mobiliteiten in een kwantumstiplaag. Het elektrochemisch opladen van kwantumstippen verschilt van normale elektrochemische experimenten op vlakke elektrodes (waar de Randles-Ševčík-vergelijking wel toe kan worden gepast) omdat ladingen door de kwantumstiplaag heen en weer kunnen bewegen en worden opgeslagen in de gehele laag.

In Hoofdstuk 7 breiden we de drift-diffusiesimulaties uit door elektrochemische nevenreacties toe te voegen. We laten zien hoe reacties tussen elektronen in de kwantumstippen met redox-actieve moleculen gemodelleerd kunnen worden met het Gerischer model voor elektronoverdracht. 1-elektron-reacties met redox-actieve moleculen zijn reversibel als de reactiepotentiaal van het molecuul zich in de geleidingsband van de kwantumstippen bevindt, maar is irreversibel als deze zich in de bandkloof bevindt. Met behulp van experimentele metingen tonen we aan dat verlies van elektronen uit de kwantumstippen aan moleculair zuurstof altijd irreversibel is, zelfs als de reactiepotentiaal zich in de geleidingsband bevindt. We verklaren dit effect met behulp van een gekoppelde reversibel-irreversibel reactiemechanisme, waardoor er een goede overeenkomst tussen simulatie en experiment wordt bereikt. Tenslotte modelleren we reacties tussen elektronen en het kwantumstipmaterial zelf, zoals de reductie van liganden of oppervlakte-ionen. Deze reacties zijn irreversibel en aannemelijke kandidaatreacties om het niet-ideale opladingsgedrag van InP en CdSe kwantumstippen te verklaren.

Het combineren van drift-diffusiesimulaties met experimentele elektrochemie van kwantumstippen maakt het mogelijk om het systeem in zijn geheel beter te begrijpen. Zelfs als de resultaten van de simulaties en experimenten niet overeenkomen, kunnen de verschillen tussen de twee een indicatie geven waar de experimenten afwijken van theoretische voorspellingen, en zo nieuwe onderzoeksrichtingen of inzichten bieden. InP en CdSe nanodeeltjes zijn inherent moeilijker elektrochemisch op te laden dan zinkoxide (ZnO) en loodsulfide (PbS), dankzij de energetisch hoger gelegen geleidingsband van InP en CdSe. Dit betekent dat elektronen meer energie moeten hebben om in de geleidingsband te komen, wat weer betekent dat ze een grotere kans hebben om deel te nemen in (elektro)chemische reacties als ze eenmaal in de kwantumstippen geïnjecteerd zijn of zelfs al voordat injectie plaatsvindt.

Elektrochemische experimenten en drift-diffusiesimulaties kunnen verder inzicht geven in de degradatiemechanismen die plaatsvinden in kwantumstippen, wat vervolgens kan helpen om strategieën te ontwikkelen om deze te voorkomen. Het vergelijken van de elektrochemische stabiliteit van (met in-situ HF behandelde) InP kernen met dezelfde deeltjes na het toevoegen van een ZnSe- of ZnS-schil is een goed startpunt. Er wordt



verwacht dat deeltjes met een schil stabiel zijn, omdat indiumionen makkelijker worden gereduceerd dan zinkionen. Daarnaast zou het zeer interessant zijn om kwantumstippen (zowel kern als kern/schil) met verschillende typen liganden te vergelijken, om uit te vinden hoe deze de stabiliteit beïnvloeden. Aangezien oppervlaktegroepen de eerste zijn die elektrochemisch reageren, zou de stabiliteit van kwantumstippen verbeterd kunnen worden door de liganden aan te passen. Liganden als thiolen of amines zijn veelbelovende kandidaten, al moet er worden opgepast dat liganduitwisselingen de FLKO van de deeltjes niet beïnvloeden. Als het de wetenschappelijke gemeenschap lukt om hoge FLKO-waarden te combineren met lange-termijnstabiliteit, is de toekomst van InP kwantumstippen zeker lumineus.





Acknowledgements

A PhD thesis is never written alone, and I have received a lot of help and support from a great number of great people over the years. It is amazing to realize how much I have learned in 4 years, and I mostly learned it from the people below.

First of all, I'd of course like to thank **Arjan**. My interest in materials science was first peaked during the solar cells course that you gave together with Tom, so you influenced my student career earlier than you knew. I am really glad you offered me the opportunity to do a PhD in the NCFun group. Since I did my master thesis in the NCFun group, I already knew that there was a great atmosphere and nice people here, which really gave me the confidence to start my PhD project in the group. Over the years, I valued your input and directions for the project and appreciated the trust you placed in me.

Tom, I valued your input into the project through your feedback and at the yearly progress meetings, as your non-nonsense attitude really helps to create and stick to a good schedule, which we all know is essential for completing a PhD project.

Ernst, you acted almost as another promotor for my project. Without your great expertise and guidance in solid state NMR measurements, this thesis would never have been possible. Working in the magnetic resonance research center was always a nice change of pace and often re-invigorated my love for scientific experiments. Thank you for welcoming us so enthusiastically and all the time and effort you put into getting the very best signal/noise ratios together.

Maarten, it was a pleasure to have you as a close colleague in the InP project. It was always nice to talk to you during lunch or coffee breaks, either about our research or non-scientific topics. I think you really managed to bring the NCFun group together, and made it an especially nice place to work for everyone with your humor and compassion. I am also really happy to have had you as a companion on conferences and summer schools.

Hua, you continued the LEC project were Jesse and I let of. Due to your hard work in optimizing and standardizing our device production line, in addition to CdSe synthesis and electrochemistry experiments, we were able to write Chapter 5 of this thesis. It may not always have been an easy task, but I believe you did very well, and want to thank you for your great effort. It was nice to have you as my officemate for the last 2 years, I enjoyed your enthusiasm, stories and discussions.

Yan, your amazing experience in and knowledge of electrochemistry was instrumental in crafting Chapter 7 of this thesis. I could always count on your insights to discuss how to best implement complicated theoretical concepts into my simulations. And your crisp and clean electrochemical measurements provided a solid basis for me to optimize the simulations on. You also were a great colleague to hang out with during breaks, contributing to the pleasant atmosphere in the group with your jokes and stories.

Maryam, without your encouragement I might not have started this PhD journey. As my master thesis supervisor you convinced me to consider this role, and I am really grateful that you did. Although we unfortunately did not work long as colleagues, I will certainly remember your warm and enthusiastic personality.

Michael, It was great to have you as an officemate. Not only did you give me valuable advice about the more hardcore chemistry aspects of the research, you also had great non-science related stories and opinions on almost any issue which I loved to hear. And your introduction of the office coffee machine was much appreciated, although it is probably unwise of me to mention it here.

Jence, I learned so much from you about quantum dots, ligands and synthesis. You were always willing to assist and the lab. You also contributed greatly to the nice atmosphere in our office.

Guilherme, you laid very important groundwork for the InP project by painstakingly optimizing the synthesis methods of our quantum dots. You thought me a lot about synthesis, and that reading tons of literature is a great way to get better at experiment design. It was a pleasure to work with you on the in-situ HF treatment of Chapter 3. I also want to especially thank you for your contributions in Chapter 2, which you by far had the biggest hand in out of the InP team.

Ferdinand, I really enjoyed helping to teach the numerical techniques course, and learned a lot from it myself as well. My CPU is also very grateful for your help in getting my simulations running on the Delftblue cluster.

Solrun, thank you for providing a lot of useful electrochemistry data, without which I would not have been able to optimize the simulations so well for Chapter 6. You thought me a lot about setting up good experiments as well during my master thesis.

Lara, you did some important work on the synthesis of core-InP together with Guilherme. I'm really glad you joined Tom's group as a PhD after your master project, as it is always nice to chat with you at the weekly cookie and lunch breaks.

Jasmeen, you were always great to have around as your energy really enhanced the group spirit. I think you also have some cool views and opinions. Thank you for helping me with the setups in the upstairs lab as well.

Often underappreciated, there were many students who provided crucial contributions to this research. **Hodayfa**, although you were not my own student, you laid the groundwork for Chapter 3 of this thesis with Guilherme. Your hard work and impressive planning provided a great basis for us, and practically guaranteed that we could publish this work before we started on the complicated structural analysis. **Jesse**, you continued my master thesis work on light-emitting electrochemical cells. You worked really hard to make quantum-dots based LECs work and impressively, managed to do so. Without your work Chapter 5 of this thesis would not exist and I would always be wondering whether



QD-based LECs could work or not. I really appreciated the energy and enthusiasm you brought to the project. **Jay**, you continued the work on LECs. Although we did not manage to produce working InP-based devices, through your work we learned a lot about the stability of InP/ZnSe/ZnS and how to perform ligand exchanges on these particles. **Mourijn**, your work on InP shelling was crucial for developing the synthesis techniques used in Chapter 4 of this thesis. **Jim**, you took up the challenge of learning the transient absorption laser setup and data analysis. Your project was probably more complicated than most of the work in this thesis, and I tip my hat to your persistence, dedication and independence. **Gina**, you continued my streak of LEC-focussed students, expanding on the drift-diffusion simulations presented in Chapters 5. I was impressed by your coding skills and your ability to independently convert complex theory to simulations. Because of your good organisation and planning, I barely had any work to do in supervision.

Adinda, you made sure everything in the OM group was properly arranged and running, and made my work a lot easier and smoother. You also had the important job of organising group outings and cookie breaks, thereby greatly increasing group morale. In order to perform the many measurements I needed to for this thesis, I had a lot of help operating the machinery. **Bahiya** and **Nick**, you had the important job of keeping the lab running. Thank you for all your help over the years in teaching me new techniques and making sure everything worked properly. **Wiel**, you taught me how to use the TEM, but also assisted in many more areas where our own expertise ran short, such as fixing gloveboxes, making sure the evaporation setup worked and many more. **Pierre**, I appreciated your enthusiasm and willingness to face any problem head-on and come up with solutions fast. I hope you will keep spicing up OM breaks with amazing stories and discussion. **Swapna**, your help in doing the ssNMR measurements in the RID was instrumental to the structural analysis in Chapter 3. Thanks a lot for the effort you put in measuring so many of our samples. Thanks to **Stephen** for the help with solution NMR measurements. **Jos**, you are the best laser technician in the Netherlands. Thanks to you the TA setup always did what it needed to. **Bart**, thanks a lot for your help in mastering the XPS. Thanks to your care measuring was a smooth and consistent experience, exactly what researchers need most of all.

I would like to thank all current and past OM group members for the good times and useful discussions: **Laurens, Jaco, Indy, Hamit, Reinder, Jiashang, Jin, Valentina, Michelle, Goutam, Lennart, Maria, Magnus, Zimu and Deepika**. I enjoyed my time in OM group so much due to the positive and accepting atmosphere, and that is thanks to all of you.

Millicent, thank you for always being there for me when I needed you. You inspired my love for writing and storytelling, very important but often underestimated requirements for being a good scientist.

Marcellus, you inspired my love for science in general and chemistry specifically at a very young age. Thank you for always trying to answer any weird questions that I asked, that helped bolster my curiosity for the rest of my life.

And last but not least, **Denise**. You have been by my side since the start of my PhD, and have always supported me. You were always proud of my achievements and made sure that we celebrated them, which was extremely valuable to me. During the rougher periods you gave me great advice, were able to put things in perspective and were always on my side. You were able to remind me what was really important and to not take everything too seriously all the time. Your energy, creativity and resolution to make the best out of every moment make you the perfect counterbalance to me. I'm so glad to have you here, and I would like to embark on many more adventures together.



List of publications

Ubbink, R. F.; Almeida, G.; Iziyi, H.; Du Fossé, I.; Verkleij, R.; Ganapathy, S.; Van Eck, E. R.; Houtepen, A. J., A Water-Free In Situ HF Treatment for Ultrabright InP Quantum Dots. *Chemistry of Materials* 2022, 34 (22), 10093-10103.

Ubbink, R. F.; Gudjonsdottir, S.; Vogel, Y. B.; Houtepen, A. J., Numerical Model to Simulate Electrochemical Charging of Nanocrystal Films. *The Journal of Physical Chemistry C* 2023, 127 (20), 9896-9902.

Almeida, G.; Ubbink, R. F.; Stam, M.; du Fossé, I.; Houtepen, A. J., InP colloidal quantum dots for visible and near-infrared photonics. *Nature Reviews Materials* 2023, 8 (11), 742-758.

Vogel, Y. B.; Pham, L. N.; Stam, M.; Ubbink, R. F.; Coote, M. L.; Houtepen, A. J., Solvation Shifts the Band-Edge Position of Colloidal Quantum Dots by Nearly 1 eV. *Journal of the American Chemical Society* 2024, 146 (14), 9928-9938.

Stam, M.; Almeida, G.; Ubbink, R. F.; van der Poll, L. M.; Vogel, Y. B.; Chen, H.; Giordano, L.; Schiettecatte, P.; Hens, Z.; Houtepen, A. J., Near-Unity Photoluminescence Quantum Yield of Core-Only InP Quantum Dots via a Simple Postsynthetic InF₃ Treatment. *ACS nano* 2024.

Ubbink, R. F.; Speelman, T.; Esteban, D. A.; van Leeuwen, M.; Stam, M.; Bals, S.; De Wijs, G. A.; van Eck, E. R.; Houtepen, A. J., Phosphorus Oxidation Controls Epitaxial Shell Growth in InP/ZnSe Quantum Dots. *ACS Nano* 2024.

Ubbink, R. F.; Vogel, Y. B.; Stam, M.; Chen, H.; Houtepen, A. J., Where Do the Electrons Go? Studying Loss Processes in the Electrochemical Charging of Semiconductor Nanomaterials. *Chemistry of Materials* 2025.

Curriculum vitae

Reinout Floris Ubbink was born in Cambridge, United Kingdom on the 17th of October in 1995. In 2014 he started his bachelor programme “Molecular Science and Technology”, a shared programme of the universities of Leiden and Delft. Although he completed his bachelor thesis entitled “Effects of surface modification and growth time on the growth of [Fe(bapbpy)(NCS)₂] single crystals” in the MCBIM group of Leiden University, he went back to Delft to start his master programme in Materials Science and Engineering. During this time, he tried to share some of his love for chemistry and physics with the next generation, to varying success, by tutoring and supervising high school students. For his master thesis, he returned to the Chemical Engineering department to work on the



edge of chemistry and materials science, completing his master thesis, “Experimental and computational devices on the way to quantum-dot based light-emitting electrochemical cells”, in 2020. In that same year he started his PhD project in the Optoelectronic Materials group at the TU Delft, same research group he completed his master thesis in, under the supervision of Prof. Dr. Arjan J. Houtepen.

When not doing science, he enjoys playing the piano, running and playing various video games. He also likes reading and writing his own science fiction stories.

